THE PERFORMANCES AND MECHANISMS OF CD(II) AND CR(VI) REMOVAL BY A LOW-COST FILAMENTOUS FUNGAL BIOMASS

LO LAI SHAN

Ph.D

The Hong Kong Polytechnic University

2015

The Hong Kong Polytechnic University

Department of Applied Biology and Chemical Technology

The Performances and Mechanisms of Cd(II) and Cr(VI) Removal by a Low-Cost Filamentous Fungal Biomass

Lo Lai Shan

A thesis submitted in partial fulfillment of the requirements for the degree of Doctor of Philosophy

February, 2013

CERTIFICATE OF ORIGINALITY

I hereby declare that this thesis is my own work and that, to the best of my knowledge and belief, it reproduces no material previously published or written, nor material that has been accepted for the award of any other degree or diploma, except where due acknowledgement has been made in the text.

Lo Lai Shan

Abstract

Wastewater laden with toxic heavy metals must first be treated to minimize the amounts of metal ions in water before being discharged into the environment. Conventional treatment technologies, such as ion-exchange, membrane separation and chemical precipitation, have their inherent limitations and constraints. A promising, cost-effective and environmentally friendly alternative is to utilize microbial biomass as a biosorbent to remove and recover toxic metals from wastewater. In this study, the performances and mechanisms of Cd(II) and Cr(VI) removal by a low-cost filamentous fungal biomass were examined.

The cultivation temperature and duration of the fungal biomass were found to be important parameters governing not only the growth yield but also its metal removal abilities. Results showed that the optimum incubation temperature and incubation duration were 30℃ and 3 days, respectively. The fungal biomasses cultivated at 25, 30 and 37℃ demonstrated similar biosorption capacities towards Cr(VI) while a significant decrease was observed in the Cd(II) uptake ability of the biomass incubated at 37ºC. The biomasses harvested after 2 and 7 days exhibited lower biosorption capacities towards Cr(VI) and Cd(II), respectively.

The surface properties of the biomass were then characterized by zeta potential measurement, high resolution potentiometric titration and spectroscopic

techniques. The point of zero charge (PZC) of the fungal biomass was 3.5. The integrated results of potentiometric titration, energy dispersive analysis of X-rays (EDAX), fourier transform infrared spectroscopy (FTIR) and X-ray photoelectron spectroscopy (XPS) indicated the presence of phosphodiester (pK_a = 3.22±0.52), carboxyl (pK_a = 4.92±0.43), amino (pK_a = 6.79±0.21) and hydroxyl (pK_a = 8.77±0.31) groups on the fungal biomass surface with the corresponding site concentrations of 0.55±0.09, 0.30 ±0.09, 0.37±0.05 and 1.44±0.20 mmol/g-biomass, respectively.

Batch biosorption studies were conducted to evaluate the effects of pH, biomass concentration, initial metal concentration, contact time, agitation speed and temperature on Cd(II) and Cr(VI) removal by the fungal biomass. Results showed that the optimum pH values for Cd(II) and Cr(VI) removal were 7.5 and 2.0, respectively. The equilibrium data were simulated by the Langmuir, Freundlich, Sips, Redlich-Peterson, Temkin and Dubinin-Radushkevich isotherm models. The kinetic data were analyzed by the pseudo-first order, pseudo-second order, Elovich, fractional power and intraparticle diffusion equations. Results showed that the Sips model provided the best correlation of the Cd(II) equilibrium data, while the non-linearized Langmuir, Sips and Redlich-Peterson models presented the best simulation of the isotherm data of

total Cr and Cr(VI) at 6 and 24 h contact times. The pseudo-second order equation and intraparticle diffusion equation well simulated the kinetic data of removal of Cd(II) and Cr(VI), respectively. The intraparticle diffusion may not be the only rate-determining step in the Cd(II) and Cr(VI) biosorption processes, while the external mass transfer may control the processes to some extent. Three thermodynamic parameters (ΔH°, ΔS° and ΔG°) were determined from the slope and intercept of ln K_d versus 1/T. Results suggested that the Cd(II) biosorption process was endothermic, thermodynamically feasible and spontaneous under the examined conditions.

The surface characteristics of the fungal biomass before and after Cd(II) and Cr(VI) removal were examined with scanning electron microscopy equipped with energy dispersive X-ray spectroscopy (SEM/EDAX), FTIR and XPS. In EDAX analysis, no alkali or alkaline earth metal ions were observed on the pristine biomass surface, indicating that Cd(II) adsorption process might not be due to ion exchange between Cd(II) ions and the alkali or alkaline earth metal ions. Results from the FTIR and XPS studies demonstrated that phosphodiester, carboxyl and amino groups were involved in the Cd(II) binding process. On the other hand, the Cr(VI) removal from aqueous solution by the fungal biomass was through adsorption-coupled reduction. XPS was employed to determine the oxidation

state of the Cr bound onto the biomass surface; it revealed that most of the chromium bound on it was in trivalent form, showing that most of the Cr(VI) ions were reduced to Cr(III) by the fungal biomass. The integrated results of FTIR and XPS demonstrated that amine, carboxyl and phosphodiester groups might be involved in the Cr(VI) removal process. These results show that the anionic Cr(VI) ions bound onto the positively-charged biomass surface by electrostatic attraction and the electron donating groups on the biomass surface were capable of reducing Cr(VI) to Cr(III). The bio-reduced Cr(III) ions appeared in the aqueous solution or were partly bound onto the biomass surface.

This research has demonstrated that the filamentous fungal biomass shows great potential to be applied in developing low-cost and effective biosorbents for removing Cd(II) and Cr(VI) ions from contaminated water and wastewater.

Acknowledgements

I wish to express my sincere gratitude to my supervisor Dr. LO Wai-hung for his kind guidance, supervision and suggestions throughout the entire period of this study.

I am also grateful to Dr. NG Lau-mei, Dr. LI Chun-chiu, Miss LAM Yan-yan and my research colleagues for their continuous support and valuable suggestions.

I would like to thank my family and friends for their supports and encouragements.

Finally, I would like to thank the Research Committee of the Hong Kong Polytechnic University and the Research Grants Council (RGC) of Hong Kong SAR (China) for funding this project.

Table of Contents

List of Abbreviations

α_E	Initial adsorption rate (mg $g^{-1}min^{-1}$)
α_R	Redlich-Peterson constants (L mg^{-1})
β_D	Activity coefficient related to mean biosorption energy (mol^2 kJ^{-2})
β_E	Related to the extent of surface coverage (g mg^{-1})
β_R	Exponent which lies between 0 and 1
ε	Polanyi potential (kJ mol^{-1})
ΔS°	Change in free entropy (kJ $mol^{-1}K^{-1}$)
ΔH°	Change in free enthalpy (kJ mol^{-1})
ΔG°	Change in Gibbs free energy (kJ mol^{-1})
A	Arrhenius factor
AAS	Atomic absorption spectrophotometer
a_T	Temkin isotherm constant (L mg^{-1})
B_t	Boyd value
b_L	Langmuir isotherm constant (L mg^{-1})
b_T	Heat adsorption constant (J mol^{-1})
C	Concentration of the metal ions in aqueous solution (mg L^{-1})
C_e	Equilibrium metal concentration (mg L^{-1})
C_o	Initial metal concentration (mg L^{-1})

CCM	Constant capacitance model
c	Related to the thickness of boundary layer
DDI water	Distilled and deionized water
E	Mean biosorption energy (kJ mol^{-1})
E_a	Activation energy (kJ mol^{-1})
EDAX	Energy dispersive X-ray analysis
F	Faraday constant (C mol^{-1})
FTIR	Fourier transform infrared spectroscopy
G	Gran function
K	Equilibrium constant
K_1	Rate constant of pseudo-first order reduction equation (h^{-1})
K_2	Rate constant of pseudo-second order reduction equation (L mg^{-1} h^{-1})
k	Fractional power kinetic model constant (mg $g^{-1}h^{-\nu}$)
k_{diff}	Intraparticle diffusion rate constant (mg $g^{-1}min^{-1/2}$)
k_F	Freundlich constants (L g^{-1})
k_R	Redlich-Peterson constants (L g^{-1})
k_p	Rate constant of Park model (L/mmol h)
k_1	Rate constant of pseudo-first order equation (min^{-1})
k_2	Rate constant of pseudo-second order equation (g $mg^{-1}min^{-1}$)

m	Number of observations in the experimental isotherm
n_F	Exponent in Freundlich isotherm
n_S	Exponent in Sips isotherm
PZC	Point of zero charge
p	Number of parameters in the regression model
Q_i	Estimated value
q	Amount of metal ions adsorbed per unit weight of the biomass (mg g^{-1})
q_e	Amount of metal ions adsorbed per unit weight of the biomass at equilibrium (mg g^{-1})
q_i	Experimental value
q_{max}	Maximum biosorption capacity (mg g^{-1})
q_t	Amount of metal ions adsorbed at time t (mg g^{-1})
R	Gas constant (8.314 J $mol^{-1}K^{-1}$)
RMSE	Root mean square error
r^2	Correlation coefficient
SCM	Surface complexation model
SE	Standard error
SEM	Scanning electron microscopy
SSE	Sum of squares error

T	Absolute temperature (K)
ν	Fractional power kinetic model constant
XPS	X-ray photoelectron spectroscopy

List of Figures

List of Tables

Chapter 1

Introduction

1.1 Motivations

Heavy metal pollution is a worldwide and momentous problem, especially in developing countries. Effluents laden with heavy metal ions such as Cd(II) and Cr(VI) are discharged from various economic activities, such as electroplating industries, printed circuit-board factories, leather tanning and battery industries. The heavy metal ions are mostly toxic, water soluble and non-biodegradable, thus they can be absorbed by aquatic organisms and tend to accumulate to high concentrations along the food chain. Excessive uptake of these ions can cause various health problems (Table 1.1) (Kurniawan et al. 2006b). Cadmium is a by-product of zinc mining and smelting and it is commonly used for the production of Ni-Cd batteries. The sources of cadmium pollution include atmospheric deposition, domestic wastewater, non-ferrous metal processing and production of chemicals (Nordic Council of Ministers 2003). Cadmium is considered as one of the most hazardous heavy metal ions and carcinogenic by the inhalation route (World Health Organization 2003). It enters the human body via inhalation or food diet and tends to accumulate in the internal organ especially kidney. The reabsorption of glucose and amino acids in the kidney is weaken due to the cadmium accumulation. Cadmium exposure can also cause lung

cancer, prostate cancer, bone damage and hypercalciuria (Nordic Council of Ministers 2003). Chromium is widely used in electroplating, tanning, petroleum refining processes and wood preservation. The effluents from these industries contain considerable Cr(III) and Cr(VI) ions. Cr(VI) exhibits one hundred fold more toxic than Cr(III) due to its high solubility, mobility and oxidizing ability. The ingested Cr(VI) enters red blood cells via the phosphate and sulfate anion-exchange carrier pathway and can be reduced to Cr(III) by glutathione, cysteine or ascorbate. The reduced Cr(III) can bind to DNA and cause mutagenesis. In addition, unstable intermediates such as Cr(IV), Cr(V) and radicals are formed during the reduction of Cr(VI) to Cr(III), which leads to DNA damage (Water Research Foundation 2012; United States Environmental Protection Agency 1998). On the other hand, Cr(III) is toxic to plant at high concentrations and less toxic to human since Cr(III) can only enter cell through slow diffusion (Water Research Foundation 2012; Park et al. 2005a). In Hong Kong, the maximum effluent discharge standards for cadmium and chromium are 0.001 and 0.1 mg/L in a flow rate of 5000-6000 m^3/day, respectively (Environmental Protection Department 1997). According to the guidelines set by the World Health Organization, the maximum permissible limit in drinking water for cadmium and total chromium are 0.003 and 0.05 mg/L, respectively

(Dhankhar and Hooda 2011).

Various conventional methods like chemical precipitation, membrane separation, electrochemical treatment, ion-exchange and coagulation-flocculation are used to treat metal-laden industrial wastewaters. However, these treatments have their inherent disadvantages and limitations. Chemical precipitation can be used to remove Cd(II) from industrial wastewaters. However, Cr(VI) cannot precipitate in any forms and must first be reduced to Cr(III) before chemical precipitation can be applied. Additionally, chemical precipitation produces large amounts of metal bearing hazardous sludge which are difficult to dispose. In addition, these methods are inefficient to treat wastewater containing low levels of metal ions. Membrane separation, electrochemical treatment and ion-exchange do not appear to be economically attractive because of the high material and operational costs (Ahluwalia and Goyal 2007; Kurniawan et al. 2006b). Adsorption is an alternative technology for removal of heavy metals. Some commercial adsorbents such as activated carbon can be employed to adsorb metal ions in wastewater, but these adsorbents are not very cost-effective and efficient for the removal of Cd(II) and Cr(VI). Therefore, there is an urgent need to develop effective and inexpensive alternative methods for treating industrial wastewaters laden with Cd(II) and Cr(VI) ions.

Biosorption has been shown to be a very promising technology for the removal of toxic heavy metal ions from industrial wastewaters and contaminated waters (Davis et al. 2003; Volesky 2001; Volesky and Holan 1995). It is a process in which metal uptake occurs through adsorption, reduction, ion exchange, co-ordination and/or complexation in the presence of biosorbents (Bingol et al. 2004). Several functional groups, for example, carboxylate, hydroxyl, phosphate, amide and amine groups on the biomass surface, are suggested to be responsible for the metal removal (Arief et al. 2008). A potential biosorbent is generally considered to be available in large amount, non-pathogenic, low-cost or easily grown. Different types of bacteria, algae, fungi and agricultural byproducts have been investigated to evaluate their potentiality in treating metal-laden waters and wastewaters (Patron-Prado et al. 2011; Ramrakhiani et al. 2011; Tan et al. 2011; Arief et al. 2008; Deng et al. 2007; Lo et al. 2003a; Wong et al. 2001). Some fungal species exhibit high adsorption capacities towards heavy metal ions and it may be obtained from waste byproduct of large-scale industrial processes. The conversion of the biomass waste into effective biosorbent is an eco-friendly alternative for treating metal-laden wastewaters.

Mucor rouxii is a filamentous fungal biomass which was reported to be an effective and inexpensive biosorbent for Pb(II) removal by our research group (Lo

et al., 1999). This fungal biomass has demonstrated great potential to be applied in developing effective and low-cost biosorbents for removing toxic heavy metal ions from wastewaters and contaminated waters. Novel, eco-friendly as well as low-cost materials and processes for removal and recovery of heavy metals from metal-laden wastewaters can be developed from the biomass. However, there are very few studies on the performances and mechanisms of metal removal by *Mucor rouxii* (Majumdar et al. 2010; Yan and Viraraghavan 2008). Thus, little is known about the surface properties and metal removal mechanisms of *Mucor rouxii*. Such knowledge is essential for developing effective materials and processes for removal and recovery of toxic metals from industrial wastewaters and natural waters. In view of this, it is worthwhile and very useful to investigate in depth the performances and mechanisms of metal removal by *Mucor rouxii.*

Results of screening experiments have shown that this particular fungal biomass is a potent biosorbent for Cd(II) and Cr(VI) ions, which are commonly present in industrial effluents. The performances and mechanisms of Cd(II) and Cr(VI) removal have been studied in details in this study. Various types of biomasses are able to remove Cr(VI) ions from aqueous solution. Some researchers have reported that the Cr(VI) removal by biomasses was solely due to

anionic biosorption (Gupta and Rastogi 2009; Bayramoglu et al. 2005; Karthikeyan et al. 2005), while others have suggested that it was through adsorption coupled with reduction (Chen et al. 2012; Ramrakhiani et al. 2011; Shen et al. 2010; Wang et al. 2010; Elangovan et al. 2008). The gaps in the literature have therefore motivate us to study and unravel if the anionic Cr(VI) ions bind onto the biomass surface solely by electrostatic attraction or reduction is also involved.

Table 1.1 The toxicities and maximum effluent discharge standards of heavy metal ions (Kurniawan et al. 2006a).

Heavy metal	Toxicities	Maximum effluent discharge standards in Hong Kong (ppm)
Cd(II)	Kidney damage, renal disorder, human carcinogen	0.001 – 0.05
Cr(VI)	Headache, vomiting, human carcinogen	0.05 – 0.10
Cu(II)	Liver damage, Wilson disease	0.05 – 0.10
Zn(II)	Depression, lethargy	0.60 – 1.00
Ni(II)	Chronic asthma, coughing, nausea	0.10 - 0.20

1.2 Objectives

In this research, the Cd(II), Cr(VI) and Cr(III) biosorption capacities of *Mucor rouxii* were compared with other studies. The fungal biomass exhibited outstanding removal abilities towards Cd(II) and Cr(VI) ions compared with other studies. Therefore, the present work focuses on the removal of Cd(II) and Cr(VI) ions from aqueous solution by the fungal biomass. The main objectives of this study are to examine the cell surface properties of *Mucor rouxii*, evaluate the effects of experimental parameters on biosorption performances of the fungal biomass and elucidate the removal mechanisms of Cd(II) and Cr(VI) by the biomass.

The detailed works of this research are listed below:

1.) To investigate the Cd(II), Cr(VI) and Cr(III) removal abilities of *Mucor rouxii* and to compare its metal removal abilities with other studies.

2.) To optimize the growth conditions of *Mucor rouxii* for the removal of Cd(II) and Cr(VI).

3.) To characterize the surface properties of *Mucor rouxii* by zeta potential measurement, high-resolution potentiometric titration, scanning electron microscopy (SEM), energy dispersive analysis of X-rays (EDAX), Fourier

transform infrared spectroscopy (FTIR) and X-ray photoelectron spectroscopy (XPS).

4.) To evaluate the effect of pH, biomass concentration, initial metal concentration, contact time, temperature and agitation speed on Cd(II) and Cr(VI) removal abilities of *Mucor rouxii*.

5.) To mathematically simulate the equilibrium and kinetic data of Cd(II) and Cr(VI) removal by *Mucor rouxii* with different isotherm and kinetic models.

6.) To evaluate the applicability of surface complexation model for simulating the biosorption of Cd(II) by *Mucor rouxii*.

7.) To elucidate the Cd(II) and Cr(VI) removal mechanisms of *Mucor rouxii* using high-resolution potentiometric titration, SEM-EDAX, FTIR and XPS and through biosorption behavior.

1.3 Organization of thesis

There are a total of eight chapters in this dissertation. The chapters of the dissertation are organized as follows:

Chapter 1 Introduction: the current chapter.

Chapter 2 Literature Review: this reviews the literature related to the technologies for treating metal-laden wastewaters, spectroscopic techniques for the elucidation of biosorption mechanism, and factors affecting the performance of biosorption.

Chapter 3 Materials and Methods: this describes the materials and instruments used in the experiment, and states the experimental procedures used for data collection.

Chapter 4 Optimization of Growth Conditions and Surface Characterization of *Mucor rouxii*: this presents, discusses and interprets the optimization of growth conditions of *Mucor rouxii* and the surface properties of the fungal biomass.

Chapter 5 Biosorption of Cd(II) by *Mucor rouxii*: this presents, discusses and interprets the Cd(II) batch biosorption experiments and the

Cd(II) binding mechanisms.

Chapter 6 Removal of Cr(VI) by *Mucor rouxii*: this presents, discusses and interprets the Cr(VI) batch biosorption experiments and the Cr(VI) removal mechanisms.

Chapter 7 Conclusions: this summarizes the major findings of this research.

Chapter 8 Future Studies: this lists the limitations of this research and gives recommendations for future studies.

Chapter 2

Literature Review

2.1 Traditional methods for treating metal-laden wastewater

Different physical and chemical traditional treatments are commonly used to treat metal-laden industrial effluents. Chemical precipitation, electrochemical treatment, and reverse osmosis are used for the treatment of cadmium(II)-laden wastewater (Ghosh et al. 2015). Hexavalent chromium removal can be achieved by reducing the highly toxic Cr(VI) to the less toxic Cr(III) ions in the presence of reducing agents such as ferrous sulphate, sodium sulfite, sodium bisulfate and sulfur dioxide under acidic condition. The reduced Cr(III) ions can then be removed by chemical precipitation (Saha et al. 2011). The ion-exchange method is another traditional method used for the removal of chromium(VI) ions (Mohan and Pittman 2006). However, a number of these methods possesses inherent disadvantages (Cesur and Balkaya 2007; Deng et al. 2007). For instance, in the chemical precipitation process, lime and calcium hydroxide are commonly used for the precipitation of metal ions in aqueous solution. Usually, solution pH 11 is the optimum pH for chemical precipitation. In the presence of lime/calcium hydroxide, the metal ions in aqueous solution can form an insoluble metal hydroxide. Thus, large amounts of hazardous sludge are produced, which require further treatment before disposal (Ahluwalia and Goyal 2007; Kurniawan

et al. 2006b). In coagulation-flocculation treatment, the operating costs are high due to the high costs of chemicals and the handling and disposal of the precipitate (Kurniawan et al. 2006b). With the membrane separation process, although the metal removal efficiency is high, fouling may occur. Additionally, the maintenance of constant flux rate and the renewal of membrane are necessary leading to an increase in the operating cost (Kurniawan et al. 2006b). Another commonly used technique is the ion-exchange method. This method is costly and an appropriate pretreatment is necessary before passing the effluents through the ion-exchange resin. For example, the suspended solids in wastewater should be first removed (Ahluwalia and Goyal 2007). On the other hand, electrochemical treatment such as electrodialysis and membrane electrolysis requires a regular maintenance, clean wastewater and careful operation, all of these requirements will also increase the operating cost (Kurniawan et al. 2006b).

2.2 Biosorption

Sorption of dissolved metal ions through the chemical activity of biomasses is called biosorption (Volesky and Holan 1995). In the biosorption process, the dissolved metal ion is transferred from the bulk solution phase to the surface of a biomass and finally bound onto the biomass through physical and/or chemical

interactions (Kurniawan et al. 2006b). The functional groups of carboxyl, hydroxyl, amino and phosphate on the cell wall surface are found to be responsible for the biosorption of metal ions in certain types of algae, fungi and bacteria (Ahluwalia and Goyal 2007). Cell wall of biosorbent is the first component in contact with the metal ions in aqueous solution. Therefore, understandings of cell wall structure are important in biosorption process. The cell wall of fungi consists of 80-90% polysaccharide and the remaining 10-20% components are lipids, protein, polyphosphates and inorganic ions. In addition, chitin (consisting of N-acetylglucosamine residues) is commonly found in the cell wall of fungi. Bacteria can be classified as gram-negative bacteria and gram-positive bacteria. Gram-positive bacteria possess a thicker peptidoglycan layer than that of gram-negative bacteria. Peptidoglycan consists of N-acetylglucosamine and N-acetylmuramic acid. The cell wall of algae consists of cellulose fibrils, xylans, mannans, fucinic acid and alginic acids. Algae can be classified into three categories including green, red and brown algae. The cell wall of green algae is mainly composed of cellulose and glycoproteins. In the case of red algae, the cell wall is composed of cellulose and sulphated polysaccharides. Cellulose, alginic acid, mannuronic acid, guluronic acid and some corresponding salts of potassium, calcium or sodium are present in the cell

wall of brown algae (Wang and Chen 2009).

2.3 Comparison between traditional methods and biosorption for treating metal-laden wastewater

The potential biosorbents used for biosorption are usually available in large amounts which are naturally occurring, easy to grow, or obtained abundantly from the byproducts of some industries such as activated sludge wastewater treatment plant and fermentation industry. Moreover, the biosorption process usually takes place rapidly and attains equilibrium within an hour. Apart from swift adsorption, the metal-loaded biomass may also be regenerated by suitable desorbing agents (Ahluwalia and Goyal 2007; Gardea-Torresdey et al. 2004; Kapoor and Viraraghavan 1995). In relation to operating cost, biosorption is more economical than traditional treatments since it requires relatively simple instruments and less maintenance throughout the process and a wide variety of biosorbents can be inexpensively obtained. Some biomasses may also be able to adsorb trace amounts of metal ions down to the ppb levels, and thus very effective processes based on these biomasses can be developed for removal of metal ions out of dilute complex solutions (Gardea-Torresdey et al. 2004; Wong et al. 2001; Eccles 1999).

On the other hand, chemical and physical treatments such as chemical

precipitation and coagulation-flocculation for metal-laden wastewater are not fully efficient because they may not be very effective in removing heavy metals at low metal concentrations. Furthermore, quite a number of these treatment methods are expensive, as previously discussed in Section 2.1. Therefore, biosorption is a desirable low-cost and competitive alternative to conventional treatments for treating metal-laden wastewaters.

2.4 Mechanisms of metal biosorption

Metal biosorption can be achieved through various types of metal-binding mechanisms. Physical adsorption, ion-exchange, micro-precipitation and complexation are the binding mechanisms that commonly reported by literature. In addition, the reduction/oxidation process may also be involved in the biosorption mechanism (Gardea-Torresdey et al. 2004; Liu et al. 2002; Volesky 2001). Some alkali and alkaline earth metal ions are naturally present on the surface of certain types of biomass. The metal ions in aqueous solution can displace the alkali and alkaline earth metal ions through ion-exchange mechanism. Sulaymon et al. (2013) reported that sodium, potassium and calcium ions were present on the surface of green and blue algae. Ion-exchange occurred when the algae were in contact with the heavy metal ions. As a result, the heavy metal

ions were adsorbed, and release of light metal ions and increase of solution pH were observed. The metal ions can also be adsorbed onto the biomass surface through complexation in the form of unidentate and bidentate. Ashkenazy et al. (1996) studied the lead biosorption mechanism of acetone-washed yeast biomass. The XPS analysis demonstrated that the atomic concentration of nitrogen peak exhibited a significant change before and after biosorption. The results revealed that the nitrogen-containing groups might complex with the Pb(II) ions. In physical adsorption, van der Waals's force is present between the metal ions and the biomass surface. Apiratikul and Pavasant (2008) reported that the Pb(II), Cu(II) and Cd(II) removal by *Caulerpa lentillifera* were in a range of 4-6 kJ/mol. The result indicated that physisorption was the main mechanism in biosorption. Microprecipitation can also occur when the metal ions accumulate on the biomass surface. Vijavaraghavan and Balasubramanian (2010) studied the cerium(III) and europium(III) removal by crab shell particles. The crab shell material is mainly composed of calcium carbonate, chitin and protein. The authors found that calcium carbonate contributed significantly on the removal of cerium and europium ions. Microprecipitation occurred when carbonate ions were in contact with the cerium and europium ions and accumulated on the crab shell particle surface. In the reduction mechanism, heavy metal ions can be reduced to

a lower oxidation state through reduction. For example, chromium(VI) ions can be reduced to chromium(III) ions in the presence of biomass under acidic solution pHs (Veglio and Beolchini 1997). Park et al. (2005a) provided evidence that *Aspergillus niger* possessed the ability to reduce Cr(VI) to Cr(III) ions. The XPS spectra showed that the Cr species bound onto the fungal biomass surface was in trivalent form. The cell wall of the biosorbent consists of cellulose, hemicellulose, protein and polysaccharide. These molecules provide various types of functional groups such as amino, phosphate, hydroxyl and carboxyl for metal biosorption (Gardea-Torresdey et al. 2004). Due to the complexity of the biomass structure, more than one of the mentioned mechanisms may be involved in the biosorption mechanism. Solution pH and the type of biosorbent are important factors that govern the dominant mechanism of biosorption (Volesky 2001). The cell wall of fungi contains chitosan and chitin. Abundant hydroxyl and amino groups are present on the chitin and chitosan chains, which are responsible for metal biosorption through complexation (Kapoor and Viraraghavan 1995).

2.5 Spectroscopic techniques for the elucidation of metal binding mechanism

2.5.1 Fourier transform infrared spectroscopy (FTIR) and Diffuse reflectance

infrared fourier transform spectrometry (DRIFT)

As discussed in Section 2.4, the surface of biosorbent contains different functional groups such as carboxyl, hydroxyl, sulfate, phosphate and amine groups. These surface functional groups may involve in the metal-binding process. To characterize the surface functional groups of the biosorbent, FTIR has been widely used by many researchers. The changes in wavenumbers after biosorption may be useful for explaining the binding mechanism (Lin and Wang 2012; Sun et al. 2010; Zhang et al. 2010; Krishnani et al. 2008; Holman 1999). FTIR is a fast and non-destructive technique. Choi and Yun (2006) compared the FTIR spectra of sewage sludge and Cd-laden sludge (Fig. 2.1) and they observed that symmetrical stretching of the carboxyl group showed a higher intensity after adsorption, which might be attributed to a change in the counter ion associated with the carboxylate group. This result demonstrated that the carboxyl group contributed to the Cd(II) binding onto the sewage sludge.

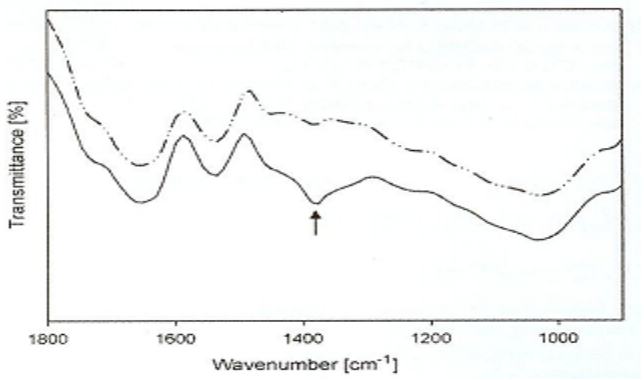

Figure 2.1 FTIR spectra of protonated sewage sludge (dotted line) and Cd-loaded

sewage sludge (solid line) (Choi and Yun 2006).

Similar to FTIR, DRIFT is another technique used for the characterization of surface functional groups on biosorbents (Saeed et al. 2009; Shin et al. 2007). The surface characteristics of juniper bark (JB) and juniper wood (JW) were examined using DRIFT (Shin et al. 2007). Preliminary studies showed that the Cd(II) uptake ability of JB was higher than that of JW. Moreover, the researchers found that the carboxylic groups were the major group involved in the Cd(II) biosorption by JB and JW. To explain the higher biosorption capacity of JB, DRIFT was employed to evaluate the surface concentrations of the carboxylic group on JB and JW (Fig. 2.2). The spectra were normalized so that the band intensities of carboxylic acid on the spectra were directly proportional to the surface densities of the acid. Fig. 2.2 shows that the band height at 1650 cm^{-1} were 8.6 and 3.4 for JB and JW, respectively, which indicated that a higher carboxylate concentration enhanced the Cd(II) binding ability of JB.

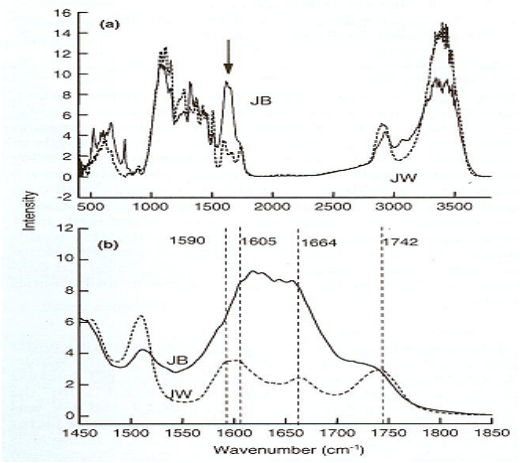

Figure 2.2 DRIFT spectra of JB and JW: (a) 400-3800 cm^{-1}; and (b) 1450-1850 cm^{-1} spectra (Shin et al. 2007).

2.5.2 Scanning electron microscopy/Energy dispersive X-ray analysis (SEM/EDX) and Transmission electron microscopy (TEM)

Scanning electron microscopy (SEM) has been commonly used to investigate the surface morphologies change of the biomass after the biosorption of heavy metal ions from an aqueous solution (Mata et al. 2008; Yin et al. 2008; Doshi et al. 2007; Deng and Ting 2005; Boddu et al. 2003; Wang et al. 2003b). The sample is scanned by a focused beam of high-energy electron. When the electron beams interact with the sample, various signals are produced. The signals are collected by a detector and a SEM image can be produced. Panda et al. (2006) investigated the performance of the husk of *Lathyrus sativus* for the removal of Cd(II) ions from the aqueous solution. The researchers recorded the SEM images of the biomass, before and after contact with Cd(II) (Fig. 2.3). From the images, they reported that some granules were found on the Cd-laden biomass surface, and posited that this observation might be due to the microprecipitation of Cd(II) after biosorption. Raize et al. (2004) also employed the SEM to investigate the surface morphology of a brown algae (*Sargassum vulgaris*) before

and after biosorption. They found that the cell wall matrix shrank and the cell wall layer was stuck after metal biosorption. The author proposed that these morphology changes might be attribute to the interaction between the Cd(II) ions and the negatively-charged functional groups on the algal cell wall.

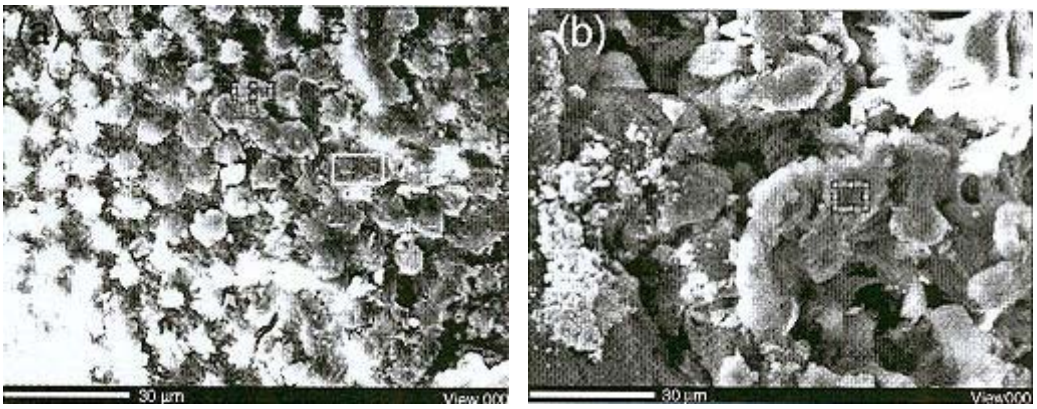

Figure 2.3 SEM images of (a) pristine biomass and (b) Cd-loaded biomass (Panda et al. 2006).

SEM is commonly combined with EDX which is useful for the surface characterization and elemental identification of a sample. In the instrument, a high-energy electron beam is applied to the sample, resulting in the emission of X-rays from the specimen. As the energies of the X-rays are unique to each element, the elemental compositions of the sample can be determined (Arief et al. 2008). The elemental compositions of a pristine husk of *Lathyrus sativus* biomass and Cd-loaded biomass were determined by Panda et al. (2006) (Fig. 2.4). The EDX spectra showed that Ca, N, O and P were present on the pristine

biomass surface. After biosorption, the Cd peak appeared, while the Ca peak disappeared in the EDX spectrum of the Cd-loaded biomass. The researchers discovered that ion-exchange occurred between the Cd ions and the Ca ions, which might be the Cd(II) binding mechanism of the biomass. Similar work was done by Kazy et al. (2009). Peaks of Na, P, S and K were found in the EDX spectrum of raw *Pseudomonas* sp.. After bisorption, the K peak disappeared, while peaks of U and Th appeared in the EDX spectra of metal-laden biomass. They also proposed that ion-exchange occurred between the K ions and the metal ions.

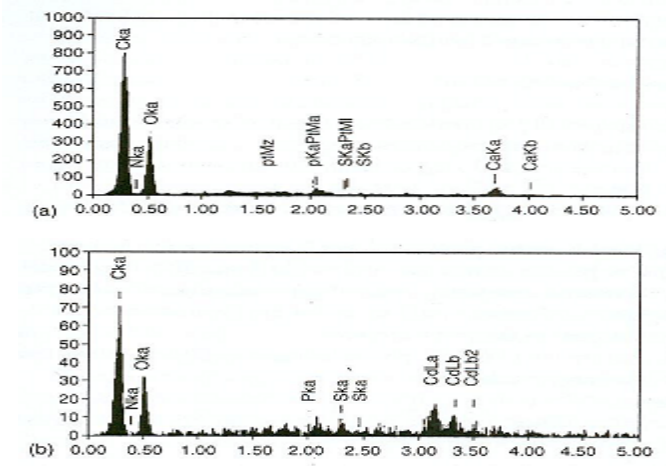

Figure 2.4 EDX spectra of (a) raw biomass and (b) Cd-loaded biomass (Panda et al. 2006).

The internal structure of a cell can be revealed by TEM (Bai et al. 2008; Liu et al. 2008; Kazy et al. 2006; Wang et al. 2003a). In this technique, a beam of electron is passed through the sample and an image is produced. This technique

is useful for determining whether the adsorption of metal ions occurs on the biomass surface or bioaccumulates inside the cell. Kazy et al. (2009) examined the internal structure of *Pseudomonas* sp., before and after uranium and thorium biosorption, by using the TEM technique. The pristine cell showed a distinct cell boundary and clear cytoplasm, while the metal-loaded cell showed some opaque regions, indicating the presence of microprecipitation of metal ions inside the cell.

2.5.3 Atomic force microscopy (AFM)

Similar to SEM, AFM is used for the characterization of cellular morphology (Kazy et al. 2009; Yin et al. 2008).

Kazy et al. (2009) utilized the tipping mode of AFM to investigate a bacterial surface before and after contact with uranium and thorium ions. In the tipping mode, the tip is oscillated near its resonance frequency, and thus intermittently contacts the bacterial surface. One of the advantages of using this mode is that the damage to the bacterial cell surface can be reduced significantly. The AFM images obtained by the researchers are shown in Fig. 2.5, and revealed that the cell length, width and height increased after biosorption. The degrees of enhancement in cell length and height in thorium-loaded biomass (length: 1.6 fold, height: 1.74 fold) were larger than those in the uranium-loaded biomass (length:

1.21 fold, height: 1.30 fold). Conversely, the degree of enhancement in cell width in the uranium-treated biomass (2.02 fold) was larger than that in the thorium-loaded biomass. These results demonstrated that the surface became more irregular after metal binding occurred.

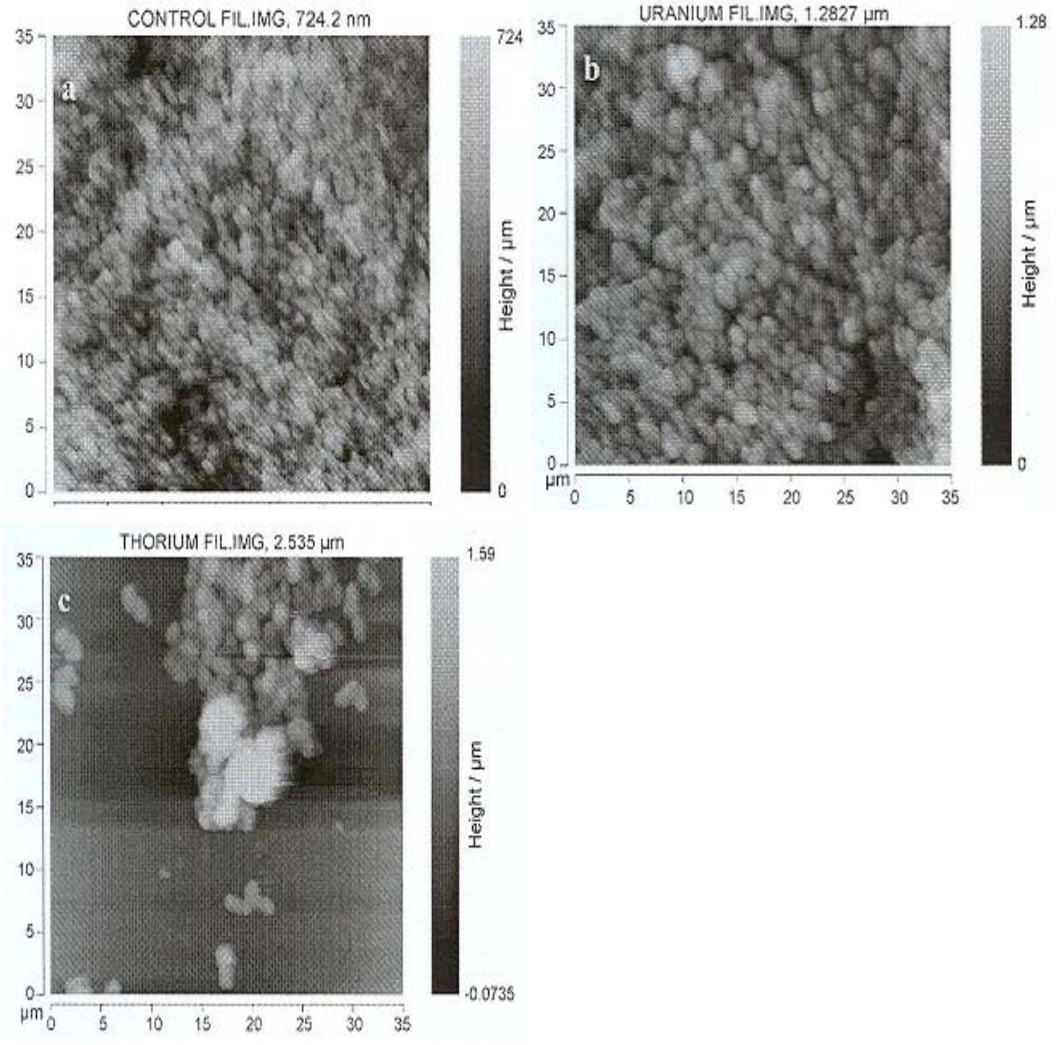

Figure 2.5 AFM micrographs of (a) pristine biomass, (b) uranium-loaded biomass and (c) thorium-loaded biomass (Kazy et al. 2009).

2.5.4 X-ray absorption study (XAS)

Extended X-ray absorption fine structure (EXAFS) is used for the

determination of short-range order in noncrystalline materials. Electrons are injected into an electron storage ring. In the ring, the electrons are accelerated to a very high speed and close to the speed of light, and synchrotron radiation is generated and emitted. Once the bound electron in the core shell absorbs the radiation, photoelectron emits. As a result, absorption edge is generated. Since elements possess unique shell energy, elements can be identified by using EXAFS (Smart and Moore 2012). X-ray absorption near edge structure (XANES) covers the range between the threshold and the point at which the EXAFS begins (Koningsberger and Prins 1988). The XANES spectrum includes the pre-edge, the position of the edge and the XANES fine structure after the edge (Smart and Moore 2012). EXAFS can only be obtained when atoms are in condensed state. An isolated atom does not produce EXAFS. The absorption edge is related to an X-ray photon which has enough energy to free an electron from an atom. When the electron is located in n = 1 shell, the edge is named K-edge. When n = 2, the edge is named L-edge (Koningsberger and Prins 1988). The XANES spectra can verify the oxidation state of the element; therefore, it is useful for determining whether the reduction of metal ion has taken place on the surface of biomass. EXAFS can display the coordination environment of an atom; hence, the functional groups involved in the metal removal process can be elucidated

(Parsons et al. 2002). Researchers frequently obtained the EXAFS and XANES spectra to further investigate the metal removal mechanism of biosorbents (Chen et al. 2007; Liu et al. 2006; Parsons et al. 2002).

Parsons et al. (2002) demonstrated the use of XAS for investigating the binding mode of Cu(II), Zn(II) and Cr(VI) onto hops biomass. The XANES spectra of metal-loaded hops biomass were obtained, and compared with those of several model compounds. The results showed that the edge energies of Cr(VI), Zn(II) and Cu(II) that bound to the biomass were similar to those of chromium acetate, zinc gluconate and copper acetate, respectively. These results revealed that the oxidation states of the metal ions did not change when they bound onto the hops biomass, except for one - Cr(VI), which was reduced to Cr(III).

The EXAFS spectra of metal-loaded hops biomass were also obtained, which were compared to those of the model compounds. The results demonstrated that the interatomic distances between the oxygen atoms and the metal ions in chromium acetate, zinc gluconate and copper acetate were almost the same as those in Cu(II), Zn(II) and Cr(VI)-loaded hops biomass, respectively. The researchers suggested that the metal ions bound onto the oxygen atom on the hops biomass surface, although the coordination numbers of the metal-loaded hops biomass were different from those of the model compounds.

2.5.5 X-ray photoelectron spectroscopy (XPS)

XPS is a form of photoemission that an electron ejects from a core level by an X-ray photon with energy hυ. The electron spectrometer analyzes the energy of the emitted photoelectrons. The number of electron and kinetic energy emitted from the sample are measured and analyzed. By plotting the intensity versus the binding energy of electron, a XPS spectrum is obtained. Each element has its own characteristic binding energy which is shown on the XPS spectra (Arief et al. 2008; Watts 2003). A number of researchers have probed the metal binding mechanism by examining the XPS spectra (Boddu et al. 2003; Park et al. 2004; Sun et al. 2010; Zheng et al. 2011).

The reduction of Ag(I) to Ag(0) by a *Lactobacillus* sp. strain A09 was confirmed by using XPS (Lin et al. 2005). Fig. 2.6 illustrates the XPS spectrum of the biomass exposed in Ag(I) solution. As shown in the figure, peaks with binding energies of 367.8 and 368.2 eV corresponded to Ag(I) and Ag(0), respectively. The results indicated that the biomass can reduce Ag(I) ions to Ag atoms.

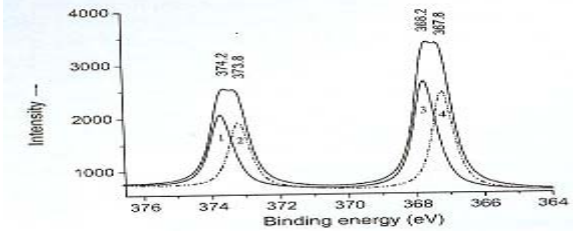

Figure 2.6 XPS spectrum of the biomass exposed in Ag(I) (Lin et al. 2005).

The valence states of Cr bound onto the dead fungal biomass of *Aspergillus niger* was investigated by Park et al. (2005a). The high-resolution XPS spectra of the biomass exposed in the Cr(VI) solution showed a peak at binding energy of 577.0-578.0 eV, which was similar to that of the Cr2p orbital in the $CrCl_3$ compound. This finding indicated the presence of Cr(III) on the biomass surface. Thus, the authors suggested that the removal of Cr(VI) by the dead fungal biomass was partly due to Cr(VI) reduction.

2.5.6 Electron spin resonance (ESR)

In ESR, the interaction between oscillating magnetic component of electromagnetic radiation and magnetic dipole moments is measured. Each electron contributes and possesses intrinsic molecular magnetic dipole moments. If electrons are in pairs, the net dipole moment is zero and cannot be measured by ESR (Bettina 2015). Some researchers employed ESR to provide evidence for the reduction of Cr(VI) to Cr(III) through an intermediate Cr(V) by biomasses (Suksabye et al. 2009; Nakajima and Baba 2004). Like XPS, ESR can also reveal the oxidation state of an element under examination. It is a physical method in which unpaired electron exhibits resonance adsorption of microwave

power in the presence of a magnetic field (Suksabye et al. 2009). Due to the unpaired electrons in Cr(III) and Cr(V) ions, both ions are ESR positive, while the Cr(VI) is ESR negative.

The oxidation states of Cr in coir pith after Cr(VI) biosorption from the aqueous solution were examined using ESR (Suksabye et al. 2009). The ESR spectra of coir pith exposed in the Cr(VI) solution at pH 1, 2 and 10 are illustrated in Fig. 2.7. Signals corresponding to Cr(III) (g= 1.971) and Cr(V) (g= 1.984) were observed on the ERS spectra of biomass exposed in Cr(VI) solution at pH 2 and 10. These results suggested that Cr(VI) was reduced to Cr(III) through the intermediate of Cr(V). On the other hand, no Cr(III) signal was observed at pH 1, and this observation might be due to the electrostatic repulsion of the bioreduced Cr(III) cations and the positively-charged coir pith surface.

The ESR spectra of the residual solution at pH values of 1, 2 and 10 were also taken (Fig. 2.8). The signals of Cr(V) and Cr(III) were not detected in the residual solution at pH 2 and 10, and these findings verified that the reduction of Cr(VI) to Cr(V)/Cr(III) was undertaken on the coir pith surface after Cr(VI) adsorption. This study demonstrated a reliable method for verifying the mechanism of Cr(VI) removal.

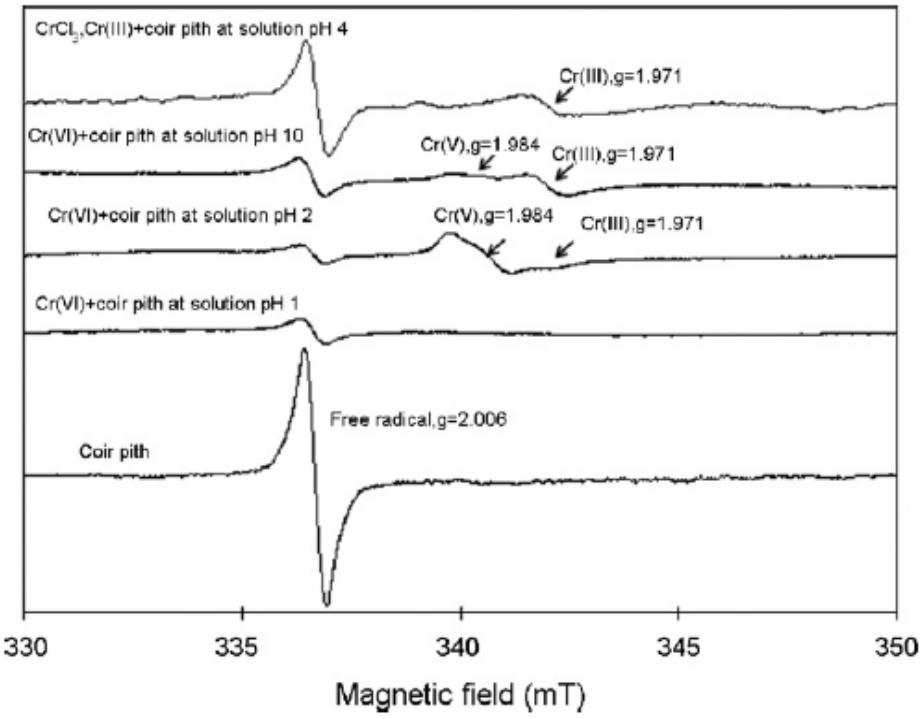

Figure 2.7 ESR spectra of coir pith exposed in the Cr(VI) solution at different solution pHs (Suksabye et al. 2009).

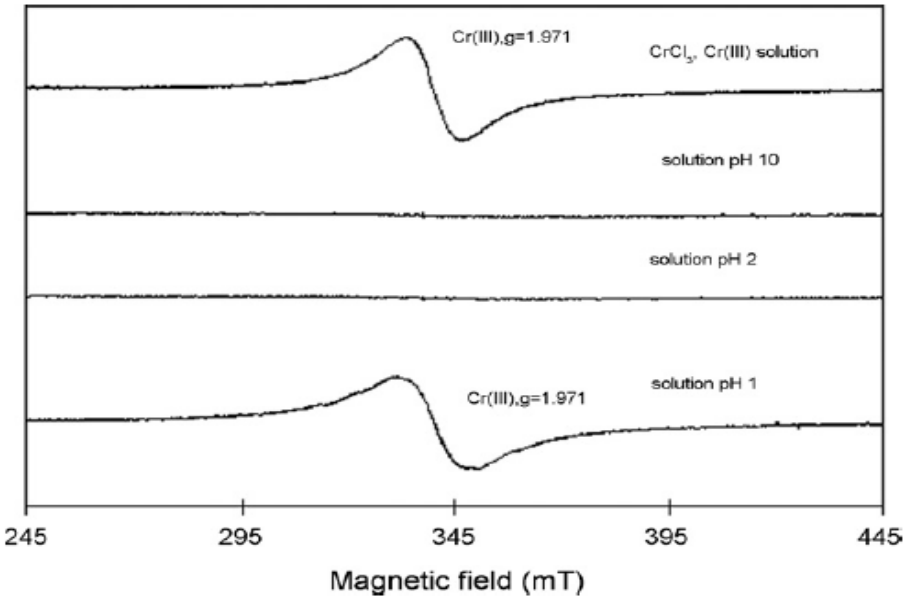

Figure 2.8 ESR spectra for residual solution after contact with the Cr(VI) solution (Suksabye et al. 2009).

2.6 Factors that affect the biosorption capacity of biomass

2.6.1 Culture age

The cell surface properties and morphology of biomass may change when the cell age increases. Therefore, the change in cell surface properties may affect the biosorption capacity of a biosorbent. The quantity of chitin and chitosan molecules in the cell wall of fungi can vary during the growth of fungal biomass. The quantity of chitin and chitosan molecules present on the fungal biomass surface may significantly influence the biosorption performance of the fungi (Kapoor and Viraraghavan 1995). Wong et al. (2001) studied the effect of culture age of *Micrococcus* sp. on Cu(II) biosorption. The Cu(II) biosorption capacities of the biomass obtained from the log phase and the stationary phase did not show any significant difference. The results suggested that the cell wall compositions did not change significantly from the log phase to the stationary phase. Merroun et al. (1997) utilized *Myxococcus xanthus* as biosorbent for the removal of Pb(II) ions in aqueous solution. They studied the effect of culture age of the biomass on the biosorption of lead. Culture ages of 24, 48, 66 and 72 h were used for lead removal and the results showed that culture age of 72 h exhibited the highest lead biosorption capacity. Wang et al. (2005) also studied

the culture age effect of biomass on heavy metal removal. In their study, *Pseudomonas putida* 5-X harvested from lag phase, log phase, stationary phase and death phase were used for the Cu(II) removal. They found that the Cu(II) biosorption capacity of biomass harvested from log phase decreased significantly when compared with that of biomass harvested from lag phase. The maximum Cu(II) biosorption was attained when biomass harvested from the early death phase was used. The results indicate that the cell age can significantly influence the biosorption performance of the biomass.

2.6.2 Biomass pretreatment

Biosorption is a process that mainly involves the interaction between metal ions and the surface functional groups of the cell wall. It implies that the functional groups/cell wall structure modification can greatly alter the metal-binding characteristics and capacity of the biomass. Both physical modification (e.g., heating, boiling, freezing or drying) and chemical modification (e.g., alkali treatment or cross-linking with organic solvent) can be performed to alter the chemistry of the functional groups/structure of the cell wall either by blocking some functional groups or by exposing more metal binding sites (Gupta et al. 2000). Aravindhan et al. (2004) showed that the percentage uptake of Cr

ions by MgCl-treated, $Ca(Cl)_2$-treated and H_2SO_4-treated biomass increased from 67% to 78%, 79% and 83%, respectively.

2.6.3 Initial heavy metal concentration

Usually, the higher the initial metal ion concentration, the larger the amount of metal ions will be adsorbed due to the increase in the chance of collision between the biomass and the metal ions. Leung et al. (2001) studied the adsorption of copper ions by *Pseudomonas pseudoalcaligenes* using different initial concentrations of Cu(II) solution. The results showed that the Cu(II) biosorption capacity of the biomass increased with increasing metal concentration.

2.6.4 Solution pH

Solution pH strongly influences the metal-binding performance of biomass. At high pH values, the biomass surfaces are deprotonated and therefore facilitate the adsorption of cations onto the negatively-charged biomass surfaces. Solution pH affects not only the availability of the functional groups on the biomass, but also the chemistry of metal ions in solution. For example, the precipitation of metal ions may occur at high solution pH. Sometimes, the solution pH can affect redox reactions. Thus, the optimum pH of the solution for biosorption of various types of biomass should be carefully determined and controlled.

2.6.5 Multimetal competition

Industrial wastewater contains many different types of heavy metal ions. These metal ions compete with each other for the limited binding sites on the biomass. If the biomass has a higher affinity with one type of the heavy metal ions or if one type of the heavy metal ions has a higher concentration, the ions are easier to be adsorbed by biomass than other competitive metal ions (Kratochvil and Volesky 1998b).

2.7 Immobilization of biomass

Use of freely-suspended biomass for biosorption has its inherent disadvantages. For instance, the separation of the biomass from the metal-biomass solution mixture is tedious; moreover, the freely-suspended biomass usually exhibits a low mechanical strength. The biomass may also aggregate at high biomass concentration. To solve this problem, immobilization of biomass can be employed by trapping the biomass into some polymers or adsorbing on inert materials such as silica, agar and cellulose (Gardea-Torresdey et al. 2004; Lei et al. 2000; Leung et al. 2000; Ting and Sun 2000; Wang et al. 2000).

Ting and Sun (2000) entrapped yeast cells (*Saccharomyces cerevisiae*) in

alginate and polyvinyl alcohol (PVA) and evaluated the copper removal performances of the alginate-yeast and PVA-yeast beads. The authors found that the PVA was a better material for the immobilization of the yeast cells than the alginate. They commented that PVA beads were durable and elastic. On the contrary, alginate beads were unstable and brittle. The study demonstrated that PVA was an alternative material for the cell immobilization.

Bayramoglu et al. (2003) used another material for the cell immobilization. In their study, a water-soluble derivative of natural polymer, carboxymethylcellulose (CMC), was used for entrapping a white-rot fungus *Trametes versicolor*. The authors commented that CMC was an environmental friendly material for cell immobilization since it is biodegradable. Moreover, CMC could provide carboxylic group as an active site for metal adsorption. The results showed that the immobilized living fungus and the immobilized heat inactivated fungus exhibited higher copper removal abilities than the plain CMC beads, suggesting the usability of CMC for cell entrapment.

2.8 Desorption

When the surface of the biomass is saturated with metal ions, it cannot further adsorb metal ions. To regenerate the biomass and recover the metal ions,

desorbing agents such as Na_2H_2EDTA, sulfide and strong acids may be used. This recovery process is called desorption, which may include precipitation, complexation or ion-exchange mechanisms between desorbing agents and adsorbed heavy metal ions (Gardea-Torresdey et al. 2004).

Deng et al. (2007) used 0.01 and 0.10 M HNO_3, EDTA and $CaCl_2$ to desorb Pb(II) ions from Pb-loaded green algae. Results showed that 0.1 M HNO_3 and 0.01 M EDTA could attain 85 and 82% Pb(II) recovery, respectively. The authors explained that the complexation of Pb(II) and EDTA might be attributed to the high value of the conditional formation constant at pH 5.0 ($K_F = 3.55 \times 10^{11}$).

The adsorbed Cd(II), Pb(II) and Hg(II) ions were eluted from microalgae using 0.1 M HCl (Tuzun et al. 2005). The results illustrated that the desorption efficiencies of the adsorbed metal ions were high (87-98%), implying the reusability of the biomass.

Chapter 3

Materials and Methods

3.1 Instrumentations

The YPG liquid medium and potato dextrose agar (PDA) were autoclaved by Hirayama HA-300 MIV at 121℃ for twenty minutes. The PDA plates were prepared in a biological safety cabinet. The plates inoculated with fungal biomass were incubated in a 25℃ warm room. The fungal biomass was cultivated inside YPG liquid medium on a Innova 2300 platform shaker (250 rpm). The fungi and YPG solution mixture were separated by a filter bag. The harvested fungi were oven dried at 60℃. Fungal suspension was prepared before each experiment. The fungal suspension was homogenized by Ultra-Turrax®T25 Basic IKA®-Werke homogenizer. Batch biosorption experiments were conducted in a Uniequip 400 shaker. The biosorbent and metal solution mixture were centrifuged by Beckman J-2M1, J-25I and J-E centrifuge machines (18,000 rpm, 25 min). The supernatants were analyzed for residual metal concentration by a flame atomic absorption spectrophotometer (Perkin Elmer Analyst 100 Spectrophotometer). For Cr(VI), a UV-visible spectrophotometer (Spectronic 20 Genesys UV-visible spectrophotometer) was used to analyze the residual metal concentration. Distilled and deionized (DDI) water was obtained by Fistreem Cyclon water deionization system. All glass

wares were washed by overnight acid soaking followed by overnight DDI water soaking.

3.2 Chemicals

PDA plate and YPG liquid medium were used to cultivate the fungi. The compositions of PDA and YPG are listed in Tables 3.1 and 3.2, respectively.

Table 3.1 Compositions of PDA

Composition	Concentration (g/L)
Potato extract	4.0
Glucose	20.0
Agar	15.0

Table 3.2 Compositions of YPG

Composition	Concentration (g/L)
D-glucose	4
Mycological peptone	3
Yeast extract	10

The metal stock solutions were prepared by dissolving metal salts in DDI water. Different metal ions with their corresponding metal salts are listed in Table 3.3.

Table 3.3 Sources of different metal ions

Metal ion	Metal salt
Cr(III)	$Cr(NO_3)_3 \cdot 9H_2O$
Cd(II)	$Cd(NO_3)_2 \cdot 4H_2O$
Cr(VI)	Na_2CrO_4

3.3 Procedures

3.3.1 Preparation of biosorbent

Mucor rouxii was maintained on a PDA (Oxoid CM 139) slant at 4 ℃. YPG medium (20 mL) containing 1% yeast extract, 0.3% mycological peptone and 0.4% D-glucose was used to incubate the fungal biomass. It was then shaken on an orbital shaker at 250 rpm in a condition of temperature 25℃ and pH 4.5. After 24 h of incubation, 20 mL of the fungal biomass was transferred to 400-mL YPG medium. The culture suspension was then incubated on an orbital shaker at 250 rpm for 3 days at temperature 30℃ and pH 4.5. The fungal biomass was harvested by filtration and washed several times with DDI water. The harvested biomass was oven-dried at 60℃ for 1 day and stored at 4℃ before use. To prepare the fungal biomass suspension for biosorption experiments, it was resuspended in DDI water and homogenized by the homogenizer at a speed

of 24000 rpm for 5 min.

3.3.2 Preparation of metal solution and analysis

The metal stock solutions were prepared by dissolving BDH A.R. grade metal salts in DDI water and diluted to desire concentrations in batch studies. The concentration of cadmium(II) and total chromium ions in aqueous solution were measured by a flame atomic absorption spectrophotometer. The metal concentrations of supernatant were diluted before the flame atomic absorption measurement. For the calibration of the atomic absorption spectrophotometer, spectral grade metal nitrate standards were used. A colorimetric method was employed to analyze the residual chromium(VI) concentration in the supernatant. Fifty milligrams of 1,5-diphenylcarbazide was dissolved in 20-mL acetone. Two hundred microliters of this solution was mixed with 660-μL of 0.2 M H_2SO_4 and 200-μL sample. A pink colored complex was formed from 1,5-diphenylcarbazide and Cr(VI) in acidic solution, which could be analyzed by the UV-visible spectrophotometer at 540 nm. The total chromium is the sum of chromium(VI) and chromium(III) ions in aqueous solution. The concentration of chromium(III) ions in aqueous solution could be calculated by subtracting chromium(VI) from total chromium.

3.3.3 Batch biosorption studies

Batch biosorption experiments were carried out to examine the effects of different parameters on the removal of metal ions by *Mucor rouxii*. In general, 10 mL metal ions were mixed with 5-mL biomass suspension in 50-mL Nalgene polypropylene tubes. The biomass-metal mixtures were shaken on an orbital shaker at 250 rpm and 25℃ for 24 h. Control experiments were carried out in which 10-mL metal ions were mixed with 5-mL DDI water in 50-mL Nalgene polypropylene tubes. All the reactor and control tubes were performed in duplicate. After mixing, solution pH was adjusted at the 3rd and 21st h by using NaOH and HNO_3. At designated time, the tubes were withdrawn from the shaker and the biomass was separated by centrifugation (18000 rpm for 25 min), and the metal ion concentration in the supernatant was measured by the flame atomic absorption spectrophotometer/UV-visible spectrophotometer. Additionally, the kinetics of metal ion biosorption by *Mucor rouxii* was determined in a 125 mL Nalgene polypropylene bottle containing 100 mg/L initial metal concentration and 5 mL biomass suspension. The isotherm study of *Mucor rouxii* was determined in a 50-mL Nalgene polypropylene bottle containing different initial metal concentrations and 1 g/L biomass concentration.

The biosorption capacity of the fungal biomass was calculated by the

following mass balance equation:

$$q = \frac{(C_0 - C_e)\ X\ V}{W} \qquad \text{(Equation 3.1)}$$

where q (mg-metal ion/g-biomass) is the biosorption capacity of the fungal biomass, C_0 (mg/L) is the initial metal concentration, C_e (mg/L) is the equilibrium metal concentration in the supernatant, V (L) is the volume of the metal-biomass solution and W (g) is the weight of the biomass.

3.3.4 Effect of incubation temperature on yield and biosorption capacities of *Mucor rouxii*

The preparation procedures of fungal biomass were the same as Section 3.3.1. However, the fungal biomass was cultivated in 400 mL YPG liquid medium on a platform shaker at temperatures 25, 30 and 37℃. The fungal biomass was then used for the biosorption experiment as described in Section 3.3.3.

3.3.5 Effect of incubation period on yield and biosorption capacities of *Mucor rouxii*

The preparation procedures of fungal biomass were the same as Section 3.3.1. However, 30℃ has been chosen for the cultivation of the fungal biomass in 400 mL YPG liquid medium on a platform shaker. The fungal biomass harvested at an incubation period ranging from two to seven days. The fungal biomass was

then used for the biosorption experiment as stated in Section 3.3.3.

3.3.6 Zeta potential measurement

The net surface charge and the isoelectric point of *Mucor rouxii* could be determined by a zetasizer. The fungal biomass (0.15 g/L) was suspended in potassium chloride solution (1 mM), adjusted to pH 2.0 to 8.0 and the zeta potential was measured by a Malvern 3000 HS_A Zetasizer.

3.3.7 Potentiometric titration of biomass suspension

The potentiometric titrations of biomass suspensions were conducted at 25℃ in which $NaNO_3$ (0.01 and 0.1 M) acted as a background electrolyte. The $NaNO_3$ solution was prepared by dissolving a known amount of $NaNO_3$ (Sigma-Aldrich, USA) using DDI water. The NaOH and HNO_3 solution were used in potentiometric titration. The 0.05 M NaOH and 0.1 M HNO_3 solution were prepared by dissolving NaOH (Sigma-Aldrich, Sweden) and diluting 2 M HNO_3 (Tedia, USA) using DDI water, respectively. The exact concentration of NaOH was standardized with potassium hydrogen phthalate (KHP) (Panreac, Spain) and the exact concentration of HNO_3 was determined by the standardized NaOH.

Five-milliliter biomass suspension and 100-mL $NaNO_3$ solution were added

to a 250 mL beaker to give desirable biomass concentration and ionic strength. Three milliliters of 0.0909 M HNO_3 were added to the suspension to protonate the biomass surface and to give a suspension pH value of less than 3. The suspension was purged of dissolved CO_2 by bubbling N_2 gas for 1 h before titration. The potentiometric titration was conducted using an autoburette (TIM 800 Titrator/ABU 901 Autoburette), with the addition of 0.0496 M NaOH in increments of 0.2 mL until the pH of the suspension reached approximately 11.0. During the titration process, N_2 was continuously bubbled. The pH of the biomass suspensions was recorded after each addition of titrant only when a stability of 0.1 mV/s had been attained. Four titrations were performed at each ionic strength (0.01 M and 0.1 M $NaNO_3$) and biomass concentration (1 g/L and 2 g/L). The titration curve was a plot of volume of 0.0496 M NaOH (mL) added versus the recorded pH and the titration data points were transferred to the input data of FITEQL 2.0 for the determination of deprotonation constants of the fungal biomass.

3.3.8 SEM/EDAX

The pristine and metal-laden *Mucor rouxii* biomass samples were mounted on a sample holder of a SEM instrument (JEOL Model JSM-6490 scanning

electron microscope) and a thin layer of gold was coated in the biomass surface with a BAL-TEC SCD 005 Sputter Coater at an argon pressure greater than 0.1 mbar for 120 s. Specimens were imaged at 20 kV accelerating voltage and 10 mm working distance and the image magnifications were 500, 5000 and 10000X. For EDAX, the biomass samples were simply spread onto an aluminum stub using double-side tape, not coated by gold, and mounted on the sample holder. The energy-dispersive X-ray spectra were obtained by an Oxford system energy-dispersive X-ray spectral system at 20 kV and 10 mm working distance.

3.3.9 FTIR spectroscopy

The FTIR spectra of pristine and metal-laden *Mucor rouxii* biomass were obtained by using a Bruker Vector 22 FTIR spectrometer in the region 4000 to 400 cm^{-1} to examine the molecular interactions between metal ions and the binding sites on the biomass surface. The samples were pulverized with spectral grade potassium bromide (KBr) with a sample/KBr ratio of about 1/8. The translucent discs were prepared by pressing the KBr-biomass mixture with the aid of an 8-ton pressure bench press.

3.3.10 XPS

XPS spectra of the biomass before and after exposure to metal solution were

obtained using a Kratos Axis Ultra DLD multi-technique system with monochromatized Al Kα radiation (250 W, 15 kV, 15 mA). Binding energy of C1s (285.0 eV) was used as an internal reference for all binding energies. The pressure inside the analysis chamber was around $4.6X10^{-8}$ Torr. The pass energy for survey scan and narrow scan were 160 eV and 40 eV, respectively. The software, Vision Processing, was employed to fit the peaks of XPS spectra.

3.3.11 Modeling of kinetic and isotherm data

Various kinetic and isotherm models were employed to simulate the kinetic and equilibrium data, respectively. A computer software, GraphPad Prism 3.0, was applied for the non-linear regression analysis.

3.3.12 Error analysis

Three error analyses, sum of squares error (SSE), root mean square error (RMSE) and standard error (SE), were used to evaluate the fitness of model curve. The calculations of the error values are expressed in Equations 3.2-3.4.

$$SSE = \sum_{i=1}^{m}(Q_i - q_i)^2 \qquad \text{(Equation 3.2)}$$

where m is the number of observation in the experimental isotherm, Q_i is the estimated value and q_i is the experimental value.

$$RMSE = \sqrt{\frac{1}{m}\sum_{i=1}^{m}(Q_i - q_i)^2} \qquad \text{(Equation 3.3)}$$

$$SE = \sqrt{\frac{1}{m-p}\sum_{i=1}^{m}(Q_i - q_i)^2} \qquad \text{(Equation 3.4)}$$

where p is the number of parameter in the regression model.

3.3.13 Biosorption edges of metal ions

Ten-milliliters of metal stock solution with different ionic strengths (0.01 M and 0.1 M $NaNO_3$) were mixed with 5 mL biomass stock suspension. Control experiments were also undertaken in the form of corresponding tests that did not contain any biomass. The pH values of all reactor tubes after mixing were adjusted to specified pH values. After pH adjustment, the tubes were shaken for three hours in an orbital shaker operating at 250 rpm and at 25°C. Then, the pH of each tube was recorded followed by centrifugation. The supernatants were analyzed for residual metal ion concentration.

Chapter 4

Optimization of Growth Conditions and Surface Characterization of *Mucor rouxii*

4. Optimization of Growth Conditions and Surface Characterization of *Mucor rouxii*

In this chapter, the biosorption capacities of *Mucor rouxii* towards Cd(II), Cr(VI) and Cr(III) were first investigated and compared with other studies. Then, the growth conditions of the fungal biomass for Cd(II) and Cr(VI) removal were optimized. Finally, the surface properties of the fungal biomass were characterized.

4.1 Biosorption of metal ions by *Mucor rouxii*

Mucor rouxii is a fungal species previously reported by our research group as an effective biosorbent for the removal of Pb(II) ions in aqueous solution. This fungal biomass exhibited great potential to be applied in developing effective and low-cost biosorbents for removing toxic heavy metal ions from contaminated waters. *Mucor rouxii* is non-pathogenic, low-cost and easily grown. The use of this fungal biomass for metal adsorption is an eco-friendly method for the removal of heavy metal ions from metal-laden wastewaters. The fungal biomass was therefore employed to investigate the biosorption capacities towards other metal ions, Cd(II), Cr(VI) and Cr(III), and the results are shown in Fig. 4.1. The metal removal abilities of the fungal biomass were 74.00±0.41 mg-Cd(II)/g-biomass,

43.32±0.64 mg-Cr(VI)/g-biomass and 35.48±0.49 mg-Cr(III)/g-biomass. In this study, the biosorption capacity towards Cr(VI) refers to the removal of Cr(VI) by biosorption, while the Cr(VI) removal ability means that Cr(VI) is removed by biosorption coupled with reduction. Mass balance equations are expressed as follows:

$$\text{Biosorption capacity of Cd} = \frac{(\text{Cd}_0 - \text{Cd}_e) \times V}{W} \quad \text{(Equation 4.1)}$$

where Cd_0 (mg/L) is the initial Cd(II) concentration, Cd_e (mg/L) is the equilibrium Cd(II) concentration in the supernatant, V (L) is the volume of the metal-biomass solution and W (g) is the weight of the biomass.

$$\text{Biosorption capacity of Cr} = \frac{(\text{Total Cr}_0 - \text{Total Cr}_e) \times V}{W} \quad \text{(Equation 4.2)}$$

where Total Cr_0 (mg/L) is the initial total Cr concentration, Total Cr_e (mg/L) is the equilibrium total Cr concentration in the supernatant, V (L) is the volume of the metal-biomass solution and W (g) is the weight of the biomass.

$$\text{Cr(VI) removal ability} = \frac{(\text{Cr(VI)}_0 - \text{Cr(VI)}_t) \times V}{W} \quad \text{(Equation 4.3)}$$

where $Cr(VI)_0$ (mg/L) is the initial Cr(VI) concentration, $Cr(VI)_t$ (mg/L) is the Cr(VI) concentration in the supernatant at time t, V (L) is the volume of the metal-biomass solution and W (g) is the weight of the biomass.

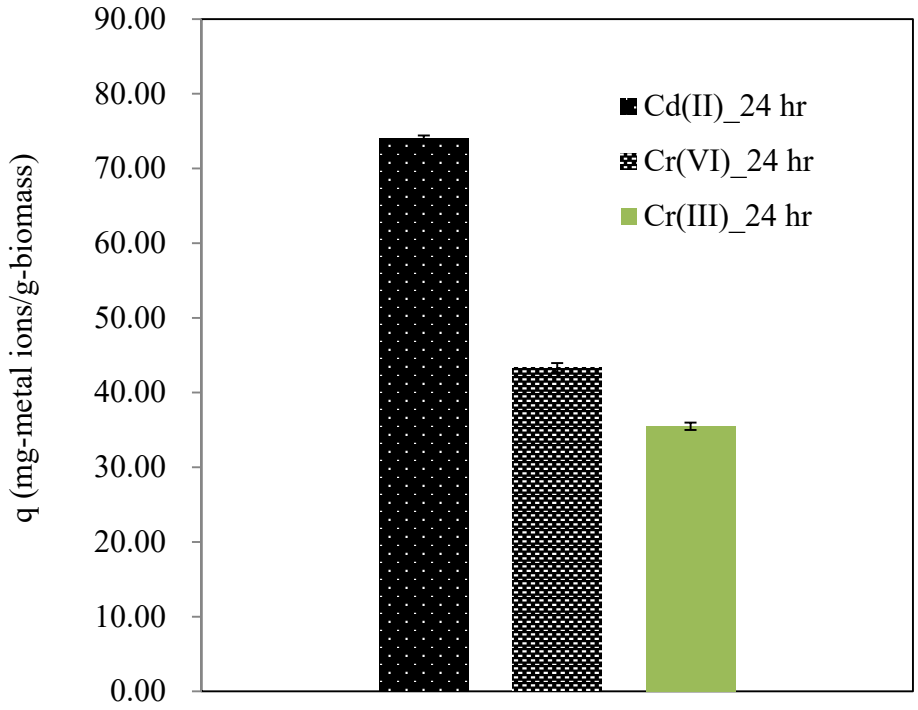

Figure 4.1 Biosorption capacities of *Mucor rouxii*.

(Growth conditions of *Mucor rouxii*: 25℃ liquid medium and 7 incubation days

Experimental conditions: Cd(II) - 100 ppm; 1 g/L and pH 7.5

Cr(VI) - 100 ppm; 1 g/L and pH 2.0

Cr(III) - 100 ppm; 1 g/L and pH 5.5)

4.2 Comparison of biosorption capacities between *Mucor rouxii* and other biosorbents

In order to evaluate the metal removal performances of *Mucor rouxii*, the results in Section 4.1 were compared with the biosorption capacities that have been reported in previous studies.

Fig. 4.2 compares the Cd(II) biosorption capacity of *Mucor rouxii* to those of bacteria and fruit wastes (previous results obtained by other researchers in my supervisor's research group). The results showed that the fungal biomass, *Mucor rouxii*, exhibited the highest Cd(II) removal ability of 74.00 mg-Cd(II)/g-biomass, followed by watermelon peel (fruit waste) and *Kytococcus sedentarius* (bacterium). The Cd(II) removal ability of the fungal biomass was also compared with other sorbents that are reported in other studies (Table 4.1). Table 4.1 shows that the biosorption performance of *Mucor rouxii* was superior to the other types of biosorbents.

The Cr(VI) removal abilities of different fungi were compared in Fig. 4.3 (previous results obtained by other researchers in my supervisor's research group), and the results showed that *Mucor rouxii* exhibited an outstanding ability in Cr(VI) removal. The Cr(VI) removal ability of *Mucor rouxii* was also compared with

other sorbents reported in other literature, as shown in Table 4.2. As can be seen, the biosorption capacity of Cr(VI) by the fungal biomass was higher than most of the other types of biosorbents.

Table 4.3 shows the comparison of the Cr(III) biosorption capacities among various sorbents. *Mucor rouxii* did not exhibit an outstanding Cr(III) biosorption capacity compared with other sorbents. Therefore, *Mucor rouxii* might not be a superior biosorbent for the biosorption of Cr(III) ions.

From the above comparisons, we noted that *Mucor rouxii* exhibits relatively high biosorption capacities towards Cd(II) and Cr(VI). Hence, *Mucor rouxii* was chosen for the removal of Cd(II) and Cr(VI) in further studies. Biosorption of metal ions from aqueous solution mainly depends on the physico/chemical interaction between the metal ions and the biomass. The morphological differences among different biomasses significantly affect the metal removal ability of the biomass. The cell wall of *Mucor rouxii* contains chitin and chitosan, which provide superior metal removal ability.

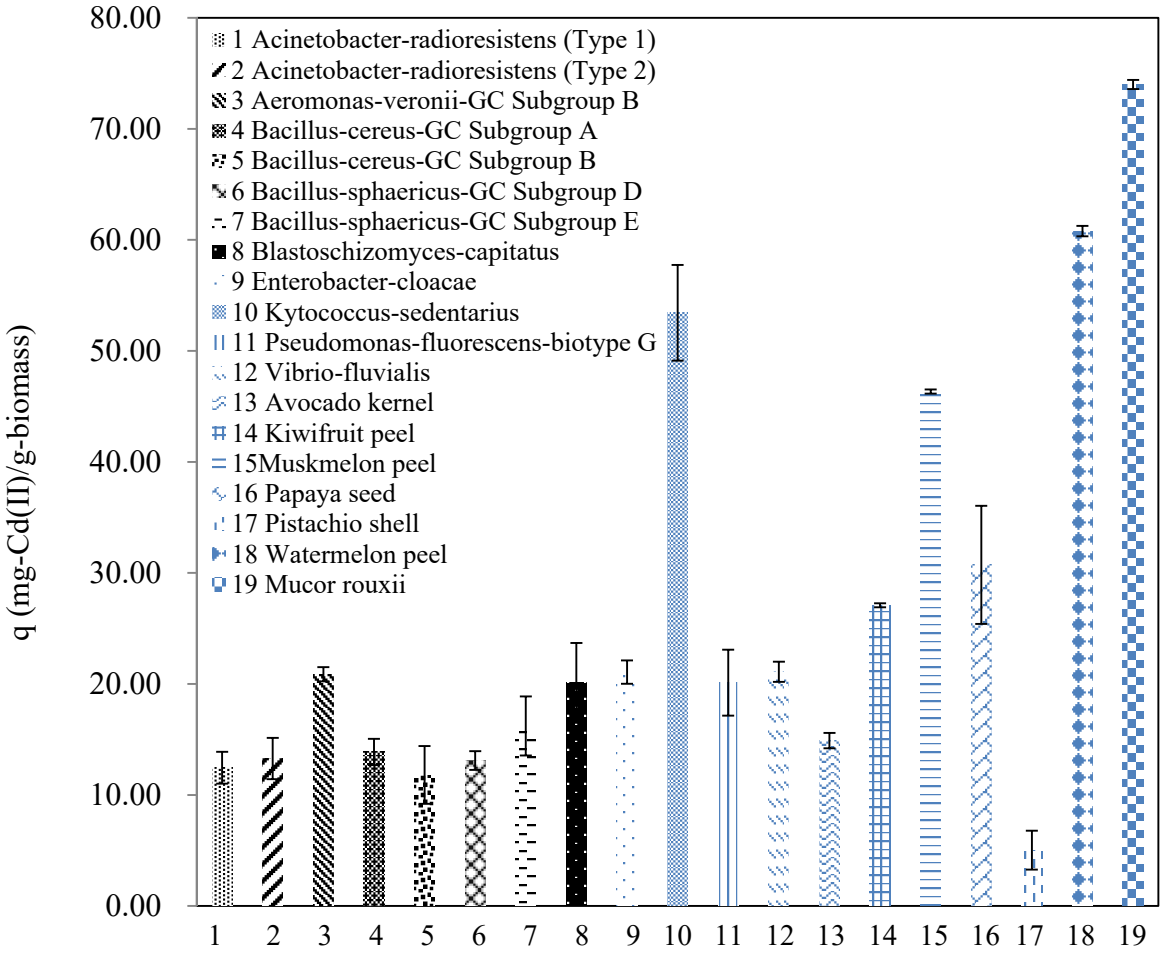

Figure 4.2 Comparison of Cd(II) removal by different biomasses.

Table 4.1 Cd(II) biosorption capacity of *Mucor rouxii* in comparison with other types of sorbents.

Type of sorbent	Name	Initial metal concentrations (ppm)	Biomass dose (g/L)	pH	q_{max} (mg/g)	References
Fungi	*Rhizopus cohnii*	20-100	1.0-15.0	1.5-6.5	40.50	Luo et al. (2010)
	Mucor heimalis	10-50	1.0-2.5	1.0-8.0	85.47	Srivastava and Hasan (2011)
	Phanerochaete chrysosporium	5-500	0.2 g	2.0-7.0	27.79	Say et al. (2001)
	Cladosporium cladosporioides 1	NA	NA	NA	5.02	Pethkar et al. (2001)
	Cladosporium cladosporioides 2	NA	NA	NA	48.60	Pethkar et al. (2001)
	Pleurotus florida	10	0.1 g	5.0	9.76	N. Das et al. (2007)
	Paecilomyces lilacinus	100	1.0 g	NA	24.23	Zeng et al. (2010)
	Aspergillus niger	10	0.01-0.2 g	5.0-6.0	3.98	Kapoor et al. (1999)
	Mucor rouxii	**40-300**	**0.2-5.0**	**2.0-8.0**	**100.70**	**This study**
Mushrooms	*Pleurotus platypus*	10-100	0.5-6.0	2.0-8.0	34.96	Vimala and Das (2009)
	Agaricus bisporus	10-100	0.5-6.0	2.0-8.0	29.67	Vimala and Das (2009)
	Calocybe indica	10-100	0.5-6.0	2.0-8.0	24.09	Vimala and Das (2009)
Bacteria	*Bacillus jeotgali*	35	0.5	4.0-7.0	57.90	Green-Ruiz et al. (2008)
	Geobacillus toebii sub.sp. *decanicus*	10-300	0.25-10	2.0-8.0	29.20	Ozdemir et al. (2009)

	Geobacillus thermoleovorans sub.sp. *stromboliensis*	10-300	0.25-10	2.0-8.0	38.80	Ozdemir et al. (2009)
Industrial wastes	Coffee ground	10-700	2.5-25.0 g	2.5-7.5	15.65	Azouaou et al. (2010)
	Wheat stem	1-225	2.5	2.0-6.0	25.26	Tan et al. (2011)
	Corncob	1-225	2.5	2.0-6.0	20.82	Tan et al. (2011)
	Rice husk	1-225	2.5	2.0-6.0	28.75	Tan et al. (2011)
Algae	*Gymnogongrus torulosus*	25-500	1.0	2.0-5.5	74.19	Areco and Afonso (2010)
	Chondracanthus chamissoi	5-200	0.06-0.24	2.0-7.0	85.43	Yipmantin et al. (2011)
	Sargassum sinicola	NA	0.5 g	4.5	62.42	Patron-Prado et al. (2011)
	Sargassum lapazeanum	NA	0.5 g	4.5	71.20	Patron-Prado et al. (2011)

NA: Not available.

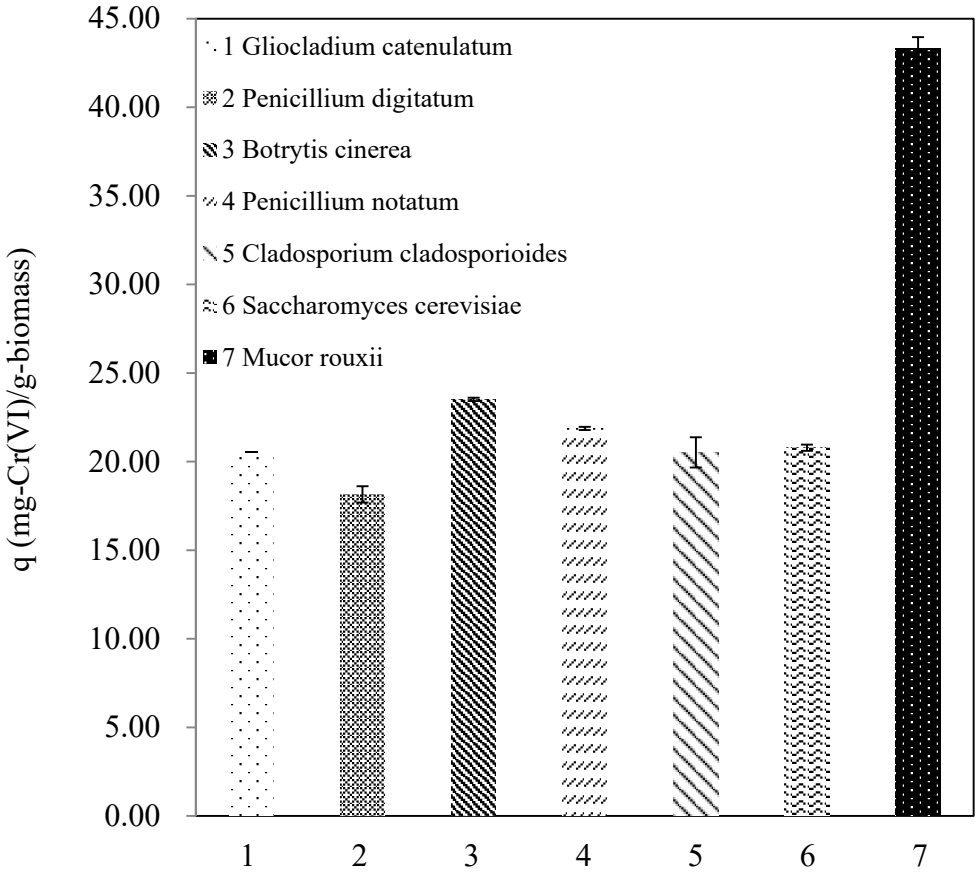

Figure 4.3 Comparison of Cr(VI) removal by different biomasses.

Table 4.2 Cr(VI) removal by *Mucor rouxii* in comparison with other types of sorbents.

Type of biosorbent	Name	Initial metal concentrations (ppm)	Biomass dose (g/L)	pH	q (mg/g)	References
Fungi	*Aspergillus sydoni*	10-60	4.0-24.0	1.0-10.0	9.07	Kumar et al. (2008)
	Aspergillus niger	10-60	4.0-24.0	1.0-10.0	17.61	Kumar et al. (2008)
	Agaricus bisporus	5-125	3.0-15.0	1.0-7.0	8.00	Ertugay and Bayhan (2008)
	Lentinus sajor-caju	20-400	1.7-13.3	2.0-7.0	23.32	Arica and Bayramoglu (2005)
	Penicillium janthinellum	10-60	4.0-24.0	1.0-10.0	9.35	Kumar et al. (2008)
	Penecillium purpurogenum	10-750	2.0	2.0-7.0	40.00	Say et al. (2004)
	Rhizopus arrhizus	50-200	5.0	1.3	23.92	Preetha and Viruthagiri (2007)
	Saccharomyces cerevisiae	10-200	1.0	1.0-6.0	32.60	Ozer and Ozer (2003)
	Mucor rouxii	20-300	0.2-5.0	2.0-7.0	**43.32**	**This study**
Bacteria	*Bacillus circulans*	50-200	NA	2.5-4	34.50	Srinath et al. (2002)
	Nostoc muscrum	0-150	NA	2-7	22.92	Gabr et al. (2009)
	Phormidium sp.	10-100	1.0	1-5	24.30	Aksu et al. (2009)
Algae	*Chlorella vulgaris*	25-150	1.0	2	27.77	Aksu et al. (1999)

	Odeogonium hatei	10-100	0.1-1.0	1-4	31.00	Gupta and Rastogi (2009)
Agricultural products	Almond shell	10	2.0	4.0-9.0	22.22	Agarwal et al. (2006)
	Coffee dust	0-500	0.5-5.0	1.0-6.0	39.00	Prabhakaran et al. (2009)
	Larch bark	10-300	2.0	2.0-6.0	31.30	Aoyama and Tsuda (2001)

NA: Not available.

Table 4.3 Cr(III) removal by *Mucor rouxii* in comparison with other types of sorbents.

Type of sorbent	Name	Initial metal concentrations (ppm)	Biomass dose (g/L)	pH	q (mg/g)	References
Algae	*Spirulina platensis*	100-300	0.4-1.5	NA	125.00	Shashirekha et al. (2008)
	Chlorella miniata	20-400	5.0	3.0-4.5	41.12	Han et al. (2006)
Fungi	*Termitomyces clypeatus*	10-1000	2.0	2.0-7.0	54.05	Das and Guha (2007)
	Mucor rouxii	**100**	**1.0**	**5.5**	**35.48**	**This study**
Agro-wastes	Agave bagasse	5-100	0.25	4.0	28.72	Garcia-Reyes and Rangel-Mendez (2010)
	Carrot residues	20-1350	10.0	2.0-5.0	45.10	Mohan and Pittman (2006)
Biological sludge	Waste-activated sludge	2-8	5.0	2.0-7.0	25.64	Iddou and Ouali (2008)
Resins	Amberlite IR-120 resin	750	5.0	NA	67.70	Mohan and Pittman (2006)
	SKN1 resin	50-150	0.5-10.0	2.0-8.0	46.30	Mohan and Pittman (2006)

NA: Not available

4.3 Optimization of growth conditions of *Mucor rouxii* for biosorption

Before using *Mucor rouxii* as a biosorbent for a series of experiments, an optimization of growth conditions was conducted. The effects of incubation temperature and incubation period on the yield and biosorption capacities of the biomass were investigated.

4.3.1 Effect of incubation temperature on the yield and biosorption capacities of *Mucor rouxii*

The fungal biomass was cultivated in a 400 mL YPG liquid medium on a platform shaker at different temperatures, 25℃, 30℃ and 37℃, for seven days. Fig. 4.4 illustrates the effect of incubation temperature on the yield of the biomass. The yield was almost the same at incubation temperatures of 25℃ and 30℃; however, the yield of the biomass cultivated at 37℃ was only about half of that obtained at 25℃ or 30℃. The results indicated that a high temperature might inhibit the growth of *Mucor rouxii*. One-way analysis of variance followed by unpaired Student's t test were performed to analyze if there are significant differences between the experimental condition groups. The result showed that the yield of the biomass cultivated at 37℃ is significantly lower than that obtained at 25℃ (Appendix 1A).

The fungal biomass cultivated was then used to study the biosorption capacities towards Cd(II) and Cr(VI) (Fig. 4.5). The fungal biomass cultivated at different temperatures demonstrated similar biosorption capacities towards Cr(VI) (no significant differences), while a significant decrease was observed in the Cd(II) uptake ability of the biomass incubated at 37℃ (Appendix 1B). Therefore, 30℃ was chosen as the incubation temperature of *Mucor rouxii*.

4.3.2 Effect of incubation duration on the yields and biosorption capacities of *Mucor rouxii*

Fig. 4.6 displays the yields of the biomass harvested in different incubation periods (2-7 days). The results illustrated that the yield of the fungal biomass was 40% higher for a growth duration of three days, compared to seven days, and gradually decreased due to a depletion of nutrient and oxygen in the liquid medium. The yield of the fungal biomass obtained from a growth duration of three days was significantly higher than that obtained from seven days and the average yield of the biomass reached a maximum at Day 3. Therefore, a growth duration of three days was the optimum harvest day of the biomass.

Biomasses with different incubation durations were employed to investigate their Cd(II) and Cr(VI) removal abilities and the results are depicted in Fig. 4.7.

The biomasses harvested after two to six days exhibited significantly higher biosorption capacities towards Cd(II) when compared with the biomass harvested after seven days. In the case of Cr(VI) biosorption, the biomasses harvested after incubation for two days exhibited significantly lower biosorption capacities towards Cr(VI) than the biomass harvested after incubation for seven days. Synowiecki and Al-Khateeb (1997) reported that the main components (chitin and chitosan) of *Mucor rouxii* varied with growth time, which might be one of the reasons for the differences in metal removal among the biomasses that were harvested on different days. A period of three days was chosen as the incubation duration for the fungal biomass since the maximum yield of the fungal biomass was attained on Day 3 and the biomass exhibited good Cd(II) and Cr(VI) removal abilities.

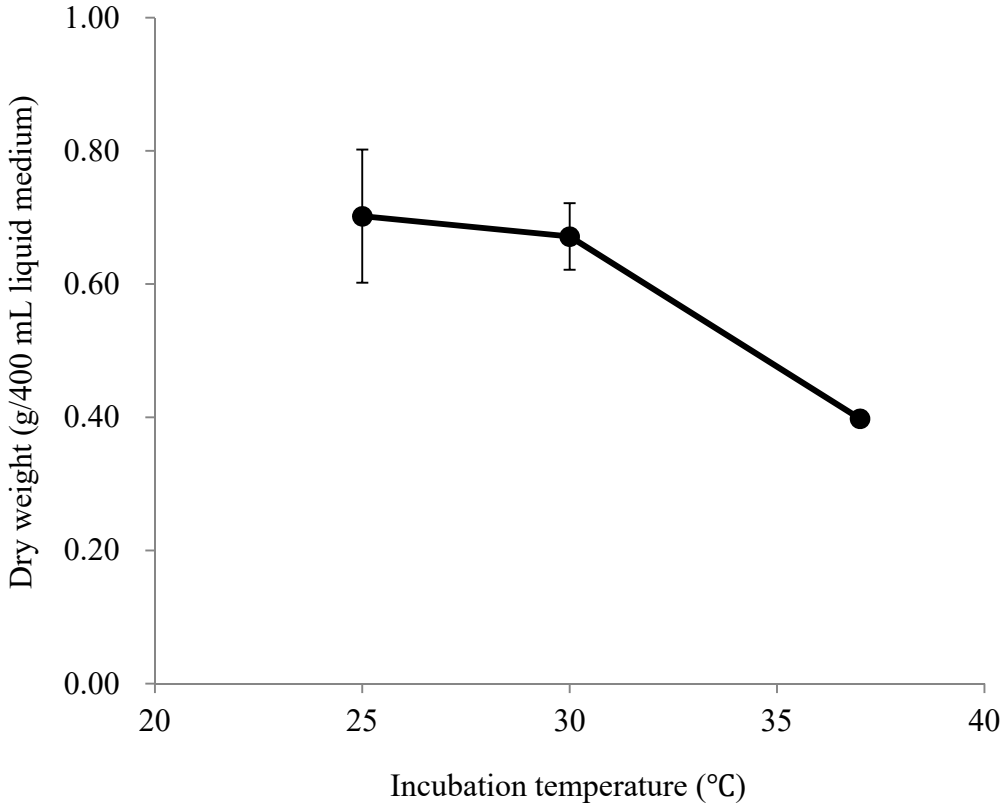

Figure 4.4 Effect of incubation temperature on the yield of *Mucor rouxii*.

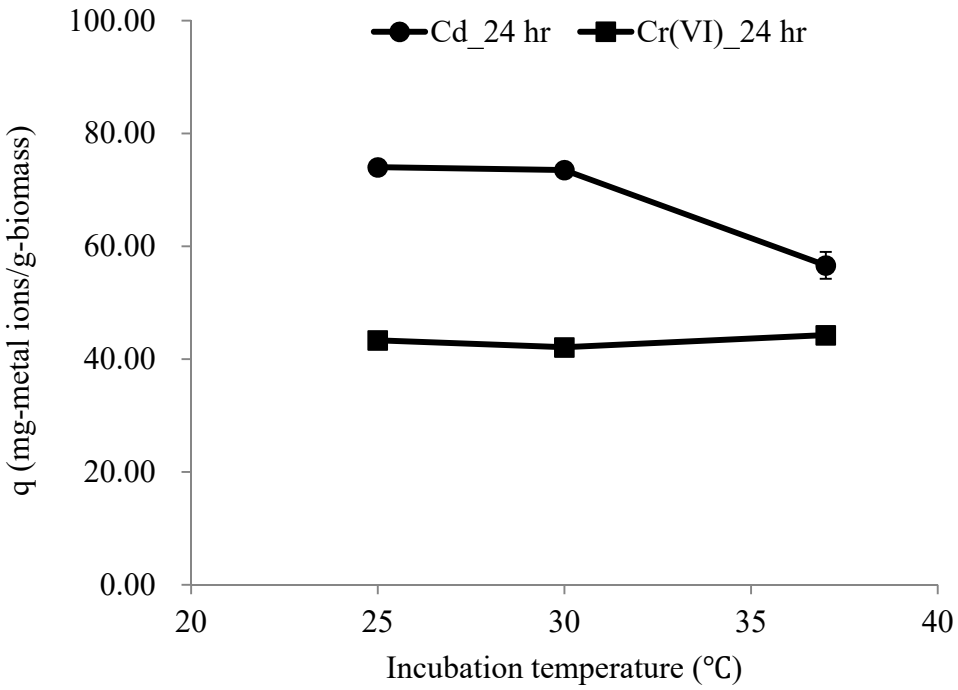

Figure 4.5 Effect of incubation temperature on biosorption capacities of *Mucor rouxii*.

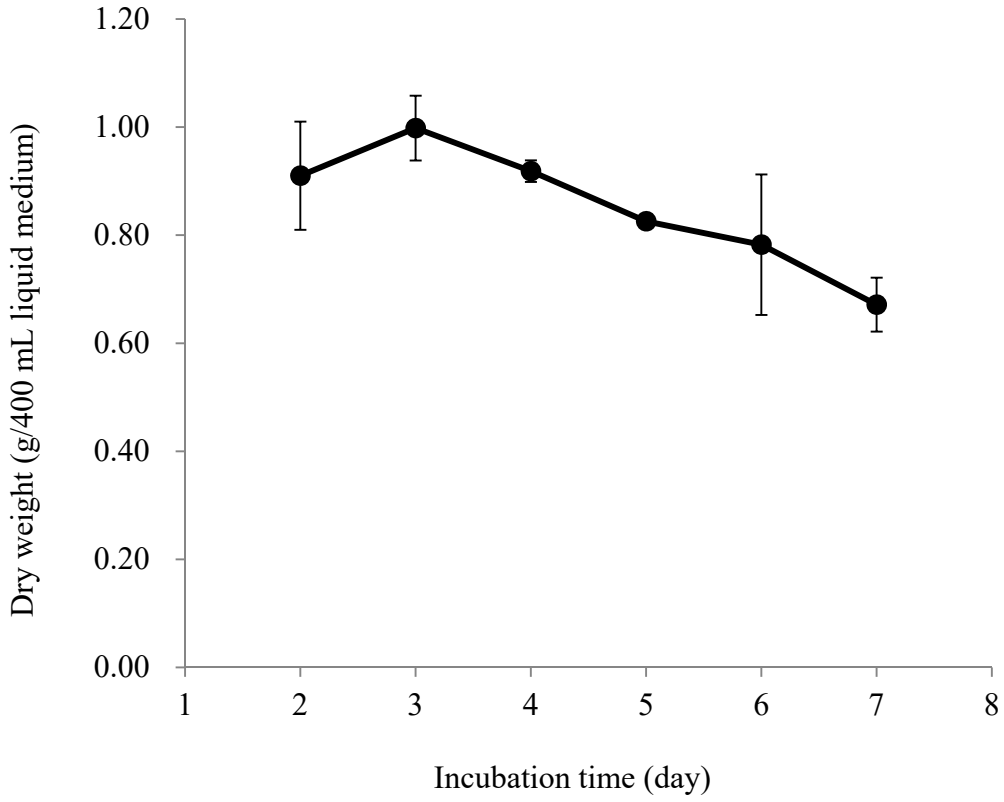

Figure 4.6 Effect of incubation time on the yield of *Mucor rouxii*.

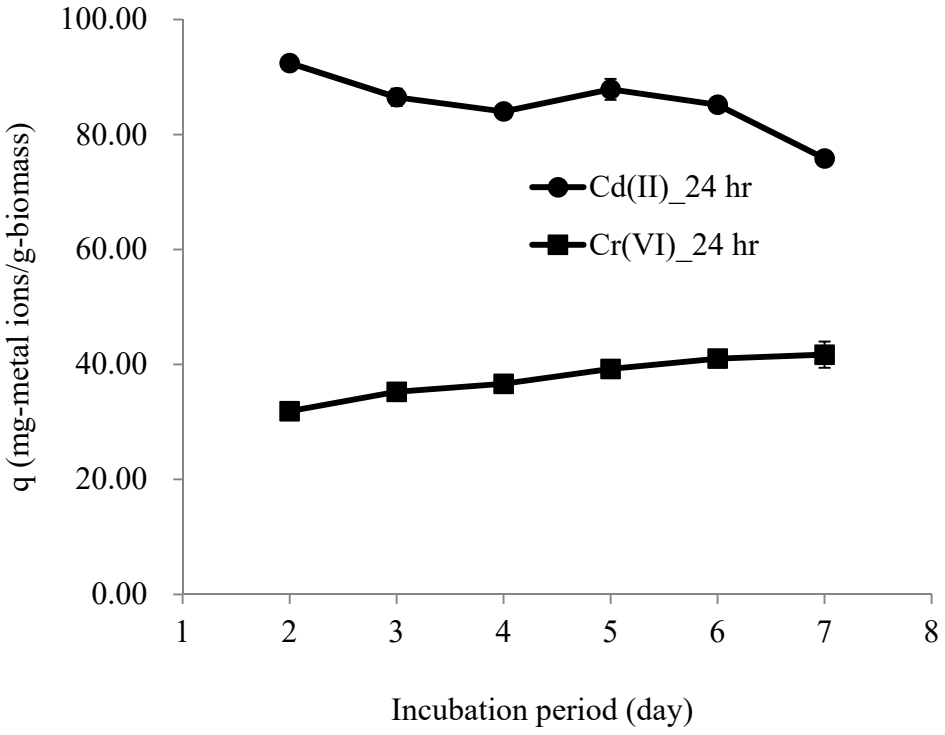

Figure 4.7 Effect of incubation time on the biosorption capacities of *Mucor rouxii*.

4.4 Surface characterizations of *Mucor rouxii*

The biosorption capacity of a biosorbent is significantly affected by the surface properties of the biomass. For a comprehensive understanding of the surface characteristics of *Mucor rouxii*, zeta potential measurements, potentiometric titrations, and spectroscopic studies using SEM/EDAX, FTIR and XPS were carried out. The fungal biomass employed for characterization studies was cultivated at 30℃ for three days.

4.4.1 Zeta potential measurement

Zeta potential measurements were conducted to examine the surface charges of *Mucor rouxii* at different solution pHs. Fig. 4.8 shows the zeta potential of the fungal biomass in a pH range from 2.0 to 8.0. The zeta potential of the pristine biomass decreased from +25 to -15 mV when the pH increased from 2.0 to 4.0. The value of the zeta potential became negative when the pH was further increased to 8.0. The net positive charge (pH 2.0-3.5) might be attributed to the protonation of the surface sites, while the net negative charge (pH 3.5-8.0) might be ascribed to the subsequent deprotonation of the functional groups. The zero point charge (ZPC) was found to be approximately 3.5, which was similar to the isoelectric point of other fungi reported by other researchers (Das et al. 2007;

Deng and Ting 2005).

In our batch biosorption studies, the pH values of 7.5 and 2.0 were selected for the removal of Cd(II) and Cr(VI), respectively. As seen in Fig. 4.8, the biomass surface carries a net negative charge at pH 7.5, which facilitated the biosorption of cationic Cd(II) ions. On the other hand, the biosorption of anionic Cr(VI) was favorable at pH 2.0 as the biomass possessed a net positive surface charge.

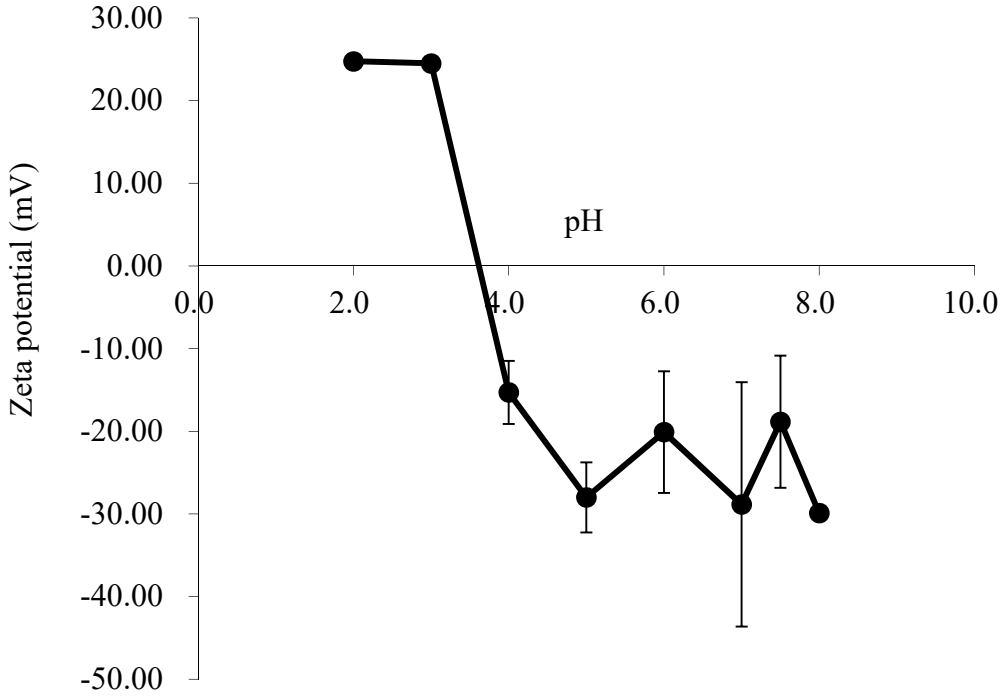

Figure 4.8 Zeta potentials of *Mucor rouxii* at different solution pHs.

4.4.2 Surface sites determination

The surface acidity of the biomass was determined using the surface complexation model (SCM). The results of potentiometric titrations were used as the input data for the surface equilibrium program FITEQL 2.0 to obtain the protonation/deprotonation constants of surface functional groups. Based on the constants, we could deduce the types of functional groups that were present on the biomass surface.

4.4.2.1 Surface complexation model (SCM)

SCM assumes the presence of discrete functional groups on the adsorption surface in which interactions between sorption sites and protons occur. The biosorption process can therefore be treated as a chemical reaction with a quantifiable deprotonation constant (Ngwenya et al. 2009; Yee and Fein 2003).

The cell wall of several types of fungi, including *Allomyces*, *Aspergillus*, *Fusarium* and *Mucor*, contains chitin and chitosan, which are responsible for the maintenance of the shape and strength of cell. Chitin is a polysaccharide composed of N-acetyl-D-glucosamine units and chitosan is a derivative of chitin. The structures of chitin and chitosan are shown in Figs. 4.9 and 4.10, which illustrate that hydroxyl and amide/amine groups are present on the chitin and

chitosan chains (Sarkar and Majumdar 2011; Synowiecki and Al-Khateeb 2003; Lo et al. 1999). Bartnicki-García (1963) reported that the cell wall of the filamentous *Mucor rouxii* was composed of three main components: chitosan, phosphate and chitin. The findings indicate that at least four discrete functional groups (hydroxyl, amide, amine and phosphate groups) contribute to the acid-base characteristics of *Mucor rouxii*. SCM was employed to model the surface acidity of the fungal biomass using the following generic acid-base equilibrium equation:

$$R\text{-}S\text{-}H^0 \leftrightarrows R\text{-}S^- + H^+ \qquad \text{(Equation 4.4)}$$

where *R* represents the fungal cell wall and S represents a type of functional group.

The corresponding mass-action equation of Equation 4.4 can be expressed as:

$$K_1 = \frac{\{R-S^-\}\, a_{H+}}{\{R-S-H^0\}} \qquad \text{(Equation 4.5)}$$

where K_1 represents the deprotonation constant of Equation 4.5, a represents the activity of the proton in the solution and the curly brackets represent the activities of surface sites.

Similar to mineral surfaces, fungal surfaces are charged and electric fields are formed around the surfaces. The interaction between the electric field and the solution ions should be considered when using Equation 4.5 to describe an

equilibrium equation that involves surface sites (Fein et al. 1997). The effect of the fungal surface electric field on the equilibrium reaction is formulated by the following equation:

$$K = K_{Intrinsic}\ \exp(\frac{-\Psi F}{R T}) \qquad \text{(Equation 4.6)}$$

where K is the conditional stability, $K_{intrinsic}$ is the equilibrium constant referenced to zero surface charge and zero surface coverage, Ψ (V) is the electric field potential of the fungal surface, F (C mol^{-1}) is the Faraday constant, R (J mol^{-1} K^{-1}) is the gas constant, and T (K) is the temperature.

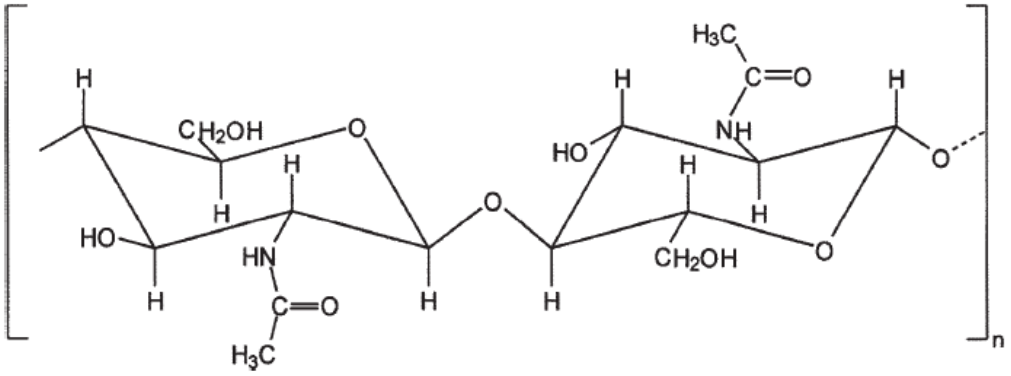

Figure 4.9 Structure of chitin (Synowiecki and Al-Khateeb 2003).

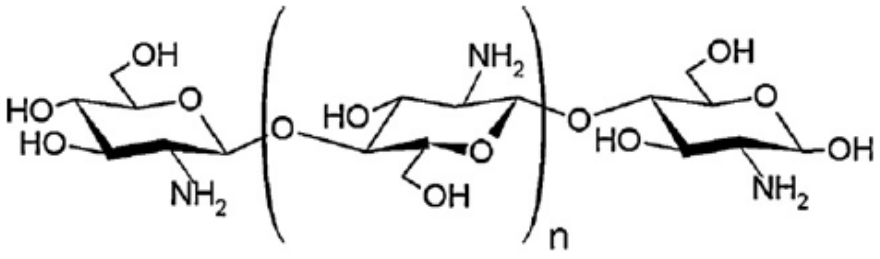

Figure 4.10 Structure of chitosan (Sarkar and Majumdar 2011).

4.4.2.2 Potentiometric titration

Sodium hydroxide solution was used as a titrant for potentiometric titration while nitric acid was used for the acidification of cell suspension. To determine the exact concentrations of NaOH and HNO_3, the former was standardized by potassium hydrogen phalate (KHP), and the latter was titrated by standardized NaOH. Figs. 4.11 and 4.12 demonstrate the standardization curves of NaOH and HNO_3, respectively. The concentrations of NaOH and HNO_3 were found to be 0.0496 M and 0.0909 M, respectively.

For the potentiometric titrations of cell suspensions, biomass concentrations of 1.0 and 2.0 g/L were suspended at different ionic strengths (0.1 M and 0.01 M $NaNO_3$) and titrated with standardized NaOH at a pH range of 2.0-11.0. The titration experiments were not performed at solution pH below 2.0 or above 11.0 to avoid cell lysis. Therefore, under the current pH range, it might appear that some functional groups had not been titrated. It is important to note that additional functional groups might be found if a wider pH range was used.

Figs. 4.13 and 4.14 illustrate the titration curves of biomass suspensions at the background electrolytes of 0.1 M and 0.01 M $NaNO_3$, respectively. The overlappings of duplicates indicated that the titration experiments were

reproducible. The two figures show that higher initial pHs were observed at higher biomass concentrations due to acidification of the biomass suspensions by the standardized HNO_3 before each titration; therefore, more surface functional groups underwent protonation at a higher biomass concentration, resulting in a higher initial pH. The two figures also illustrate that the slopes of the curves of 1 g/L biomass were steeper than those of the 2 g/L biomass. At a higher biomass concentration, a larger amount of sodium hydroxide was required to react with the protonated functional group on the biomass surface; therefore, the volume of NaOH added was larger and hence the titration curves were flattened. These results revealed that a higher biomass concentration exhibited a higher buffering capacity.

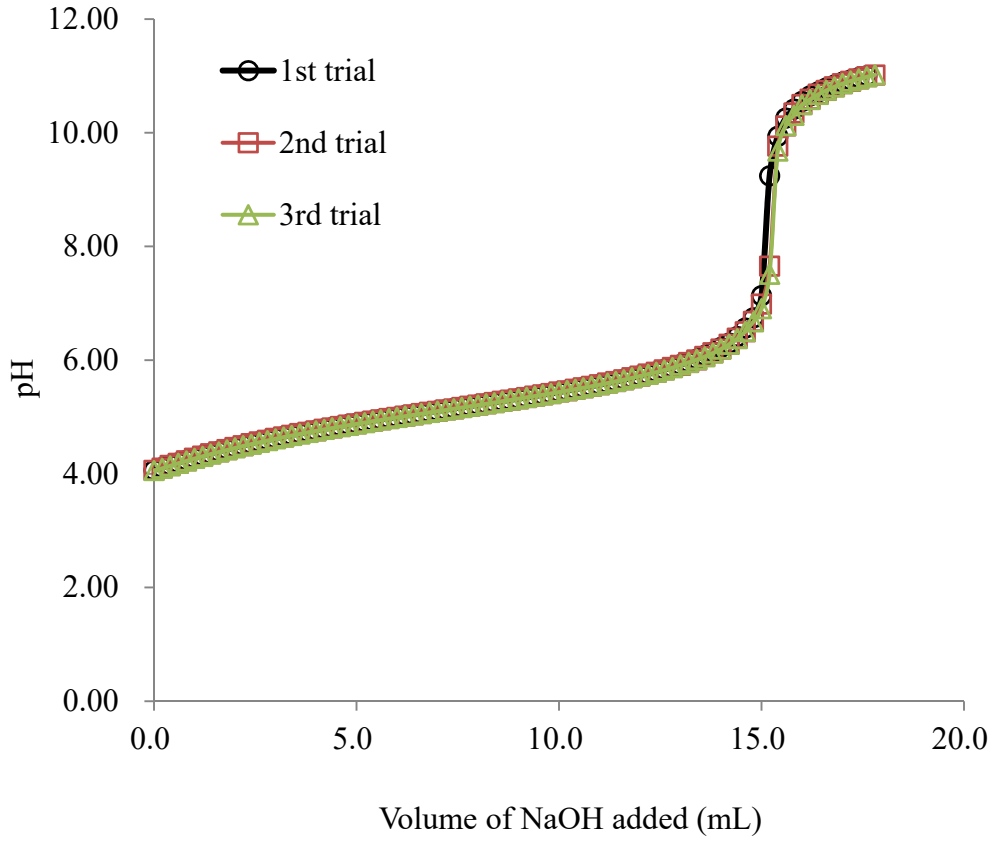

Figure 4.11 Standardization curves of NaOH.

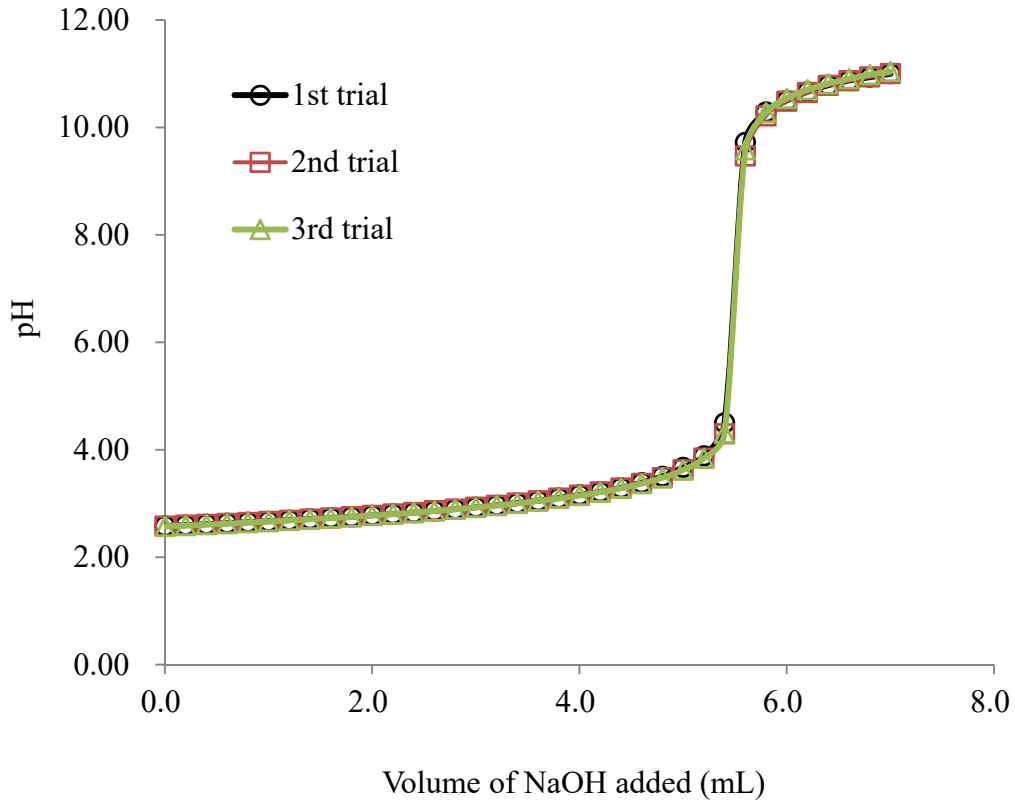

Figure 4.12 Standardization curves of HNO_3.

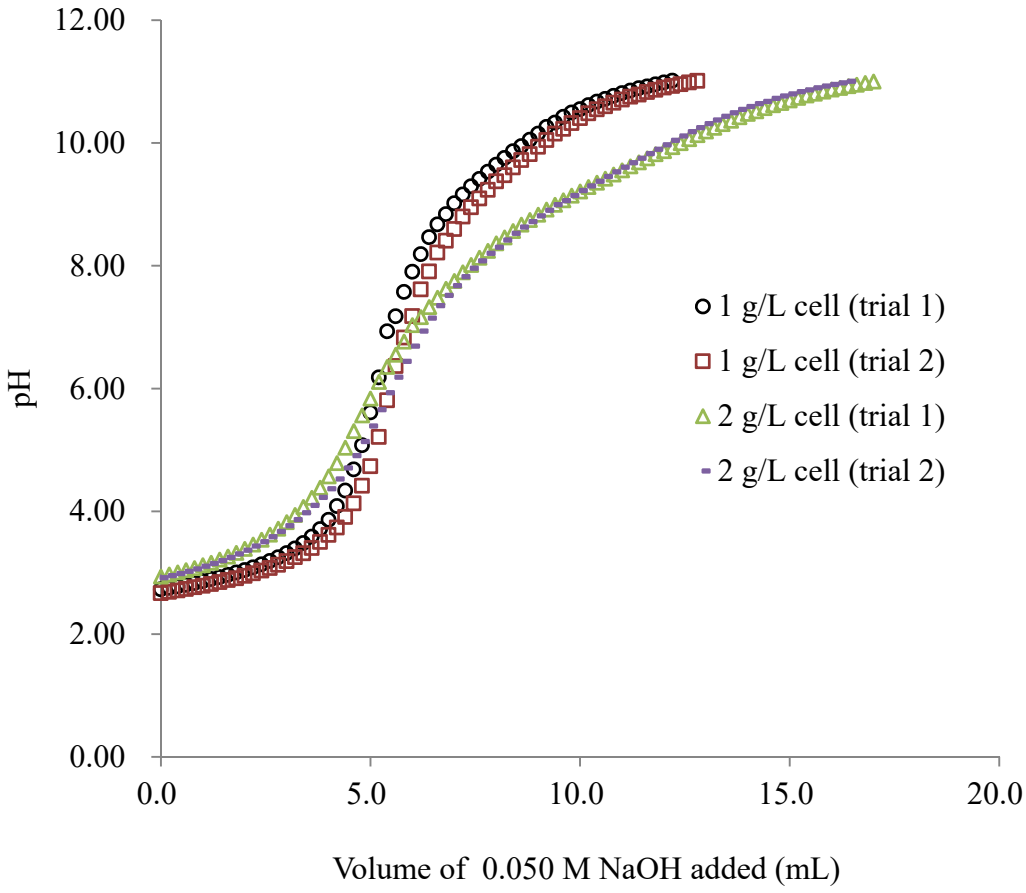

Figure 4.13 Titration curves of *Mucor rouxii* (0.1 M $NaNO_3$).

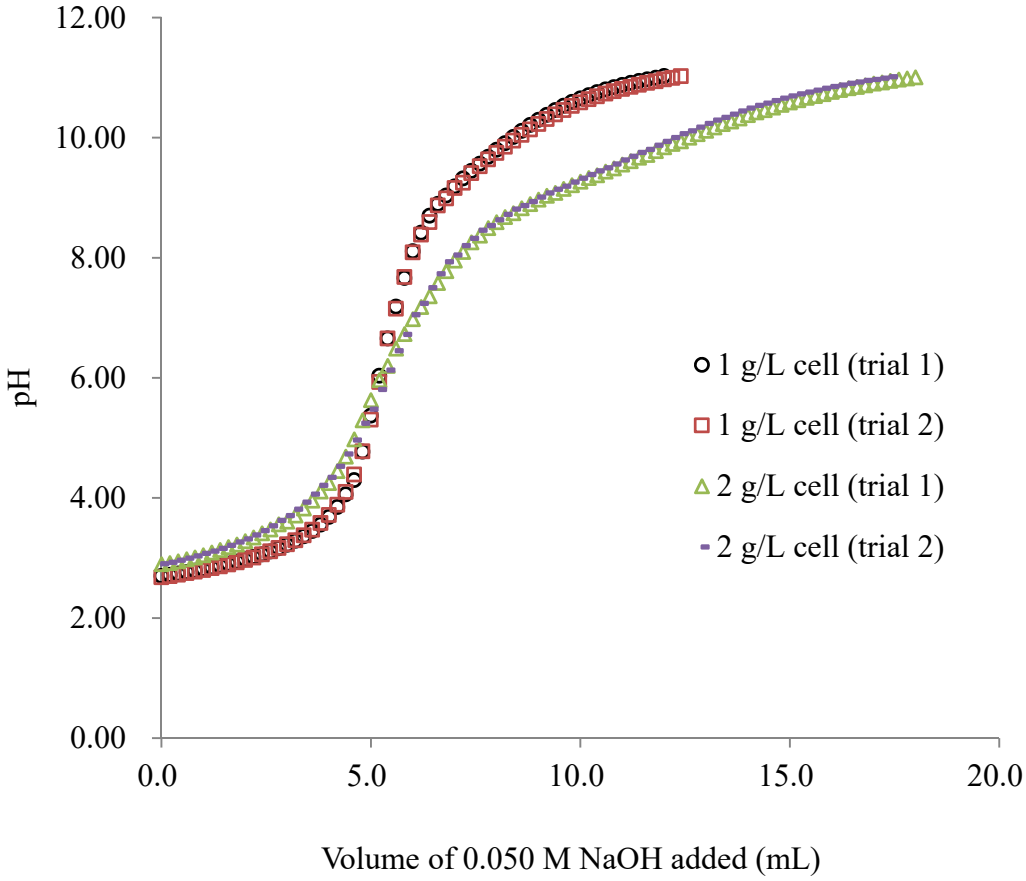

Figure 4.14 Titration curves of *Mucor rouxii* (0.01 M $NaNO_3$).

4.4.2.3 Data treatment

Gran developed a mathematical technique to determine the end point of an S-shaped titration curve, in which the curve was converted into two intersecting straight lines. Gran's method is suitable for applying to heterogeneous surface. A precise equivalence point and surface site concentrations can be obtained from Gran's method. In the case of heterogeneous surface, the sorption surface is considered as a continuous distribution of sorption sites. Gran's method has many advantages: (i) the determination of equivalence point is more precise when compared with inflection point; (ii) the statistical reliability of the analysis increases since two independent Gran functions are involved; and, (iii) sorption sites can be classified as strong, weak and very weak acid (Naja et al. 2005). The data points of potentiometric titration were transformed into a Gran plot which was obtained by plotting the Gran function (G) versus the volume of added NaOH (V_b) (Pan et al. 2007).

Gran function is given by the following equations:

Acidic side: $G = (V_0 + V_{at} + V_b) \times 10^{E/59.175}$ (Equation 4.7)

Alkaline side: $G = (V_0 + V_{at} + V_b) \times 10^{-E/59.175}$ (Equation 4.8)

where V_0 (mL) is the initial volume of suspension, V_{at} (mL) is the total volume of

HNO_3 added, V_b (mL) is the volume of NaOH added and E (mV) is the measured electrode potential.

The value of E is calculated as follows:

$$pH = pH_{iso} + \frac{P_{25} \times 0.5916\,(pH^0 - pH_{iso}) - E}{P_{25} \times 0.5916} \times \frac{T_{25}}{T} \qquad \text{(Equation 4.9)}$$

where pH is the measured pH, pH_{iso} is the isothermal pH (default value = pH 7), P_{25} (%) is the sensitivity at 25℃, pH^o is the zero pH, T_{25} is 298.16K and T (K) is the calibration temperature actually measured by means of a temperature sensor. From the potentiometric titration data, “sensitivity”, “calibration temperature” and “zero pH” were recorded.

Figs. 4.15-4.18 show the comparison of the Gran plots of cell titrations. From the Gran plots, V_{e1} and V_{e2}, which were the intersection points on the X-axis, were obtained.

The Gran plots obtained at different cell concentrations are compared in Figs. 4.15 and 4.16. The differences between V_{e1} and V_{e2} increased with increasing cell concentrations. Since the number of surface functional groups is directly proportional to the cell concentration, a larger amount of NaOH was required to react with the protonated functional groups as a higher cell concentration was used.

The Gran plots obtained at different ionic strengths are compared in Figs.

4.17 and 4.18. The two figures showed that there were no significant differences between V_{e1} and V_{e2} at ionic strengths of 0.1 M and 0.01 M $NaNO_3$.

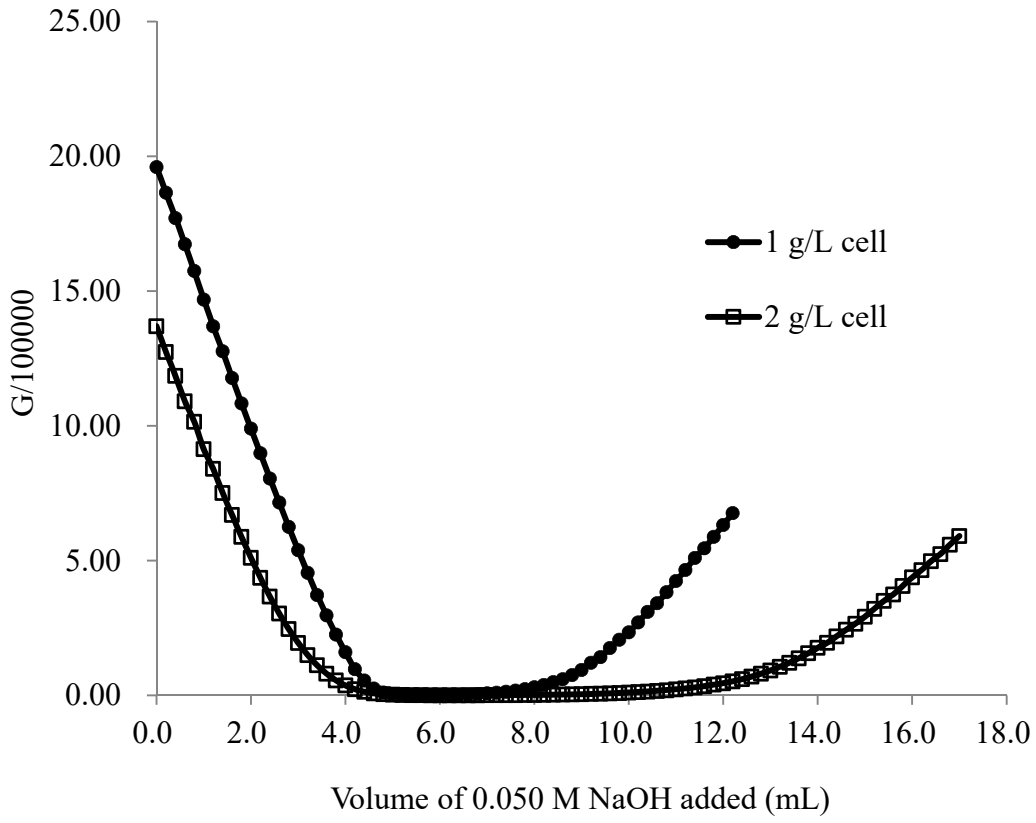

Figure 4.15 Comparison of Gran plots under different biomass concentrations (0.1 M $NaNO_3$).

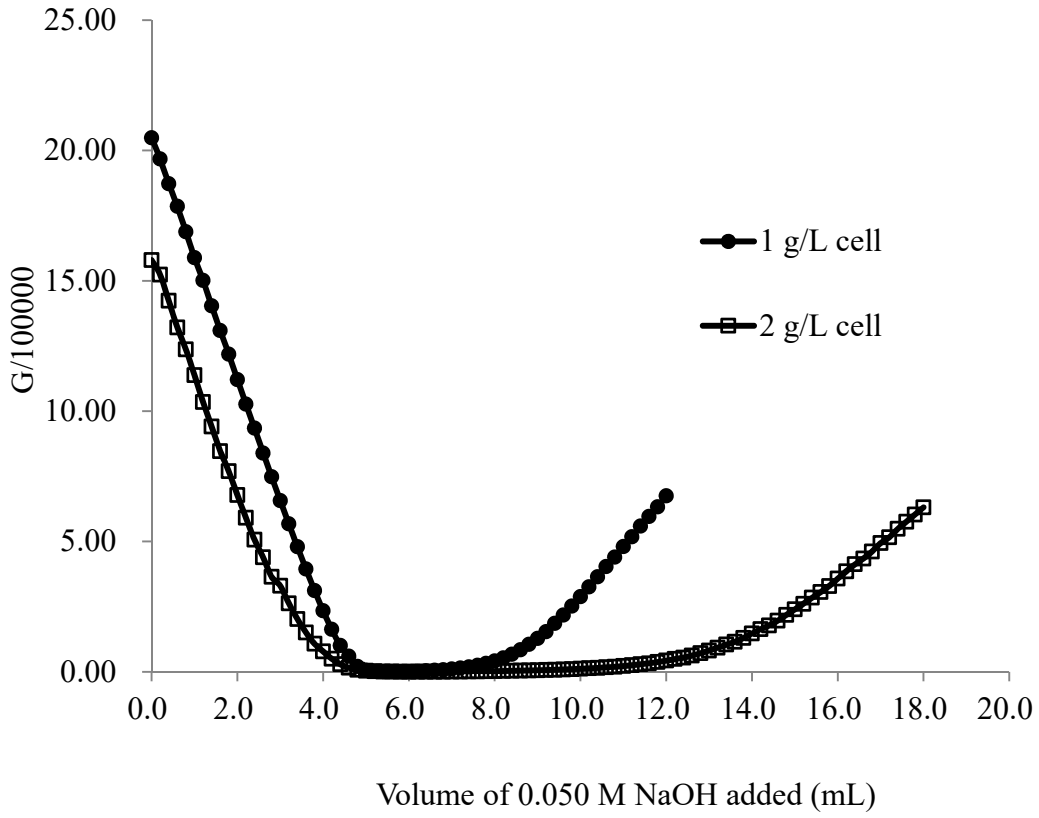

Figure 4.16 Comparison of Gran plots under different biomass concentrations (0.01 M $NaNO_3$).

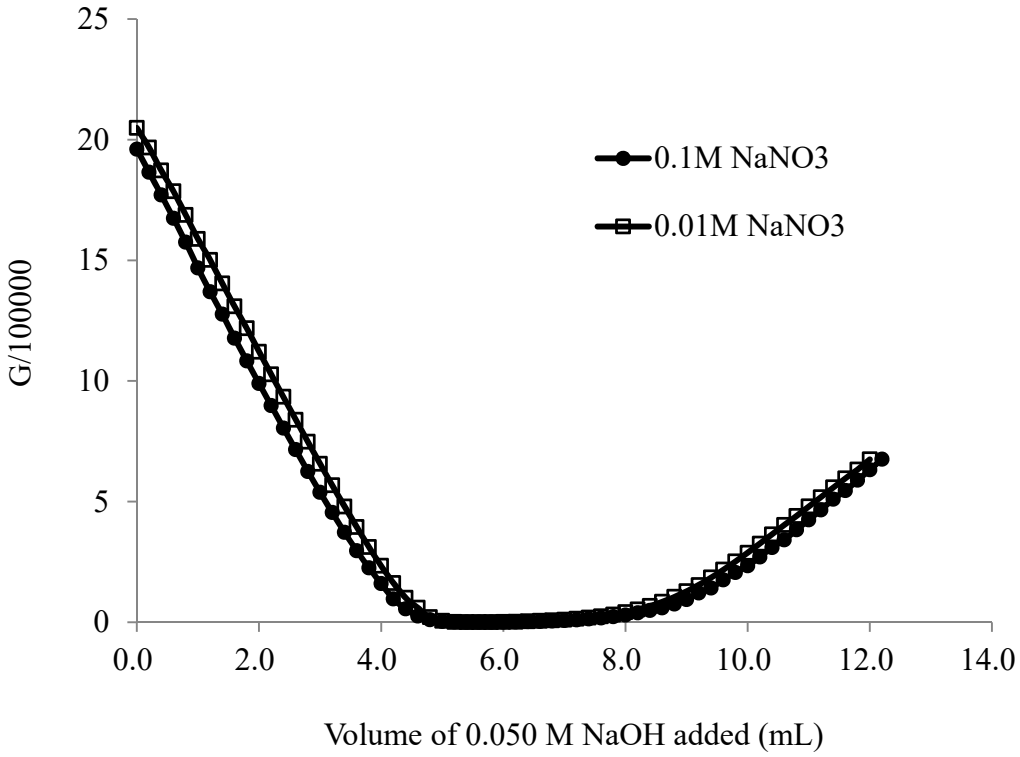

Figure 4.17 Comparison of Gran plots under different ionic strengths (1 g/L).

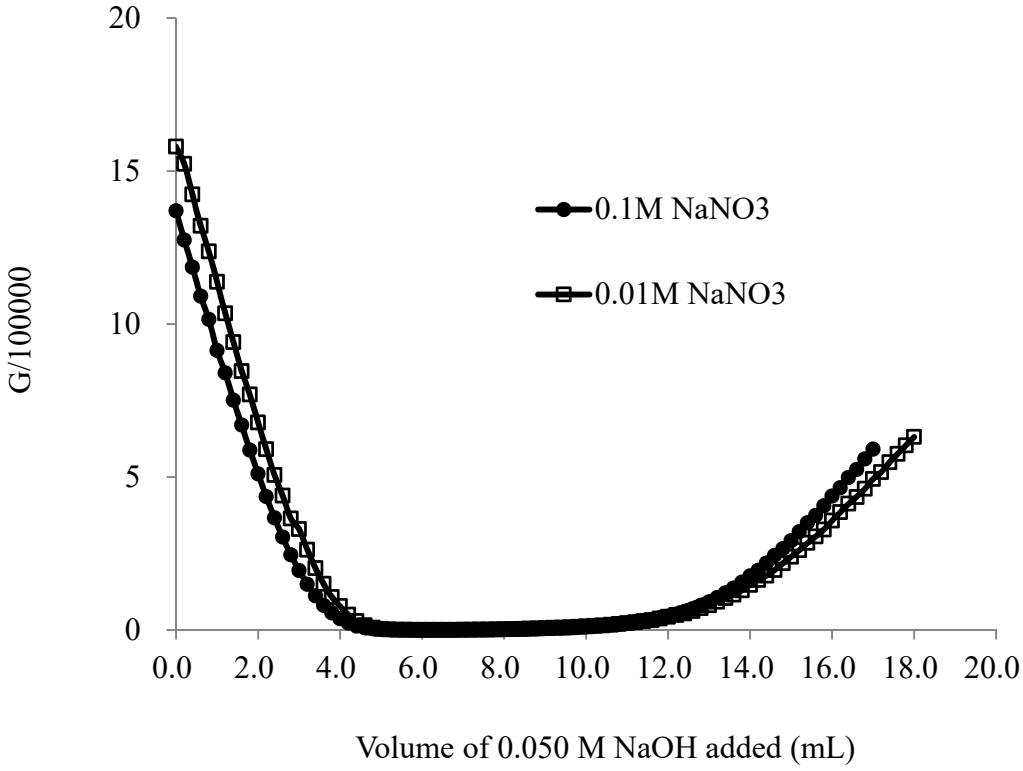

Figure 4.18 Comparison of Gran plots under different ionic strengths (2 g/L).

Since we obtained the V_{e1} and V_{e2} from the Gran plots, the total concentration of consumed protons (TOTH) for each titration point can be estimated using the following equation:

$$TOTH = -(V_b - V_{e1}) \times C_b / (V_0 + V_{at} + V_b) \quad \text{(Equation 4.10)}$$

where V_b (mL) is the volume of NaOH added, V_{e1} (mL) is the value obtained from the Gran plot, C_b (M) is the concentration of NaOH, V_0 (mL) is the initial volume of the suspension and V_{at} (mL) is the total volume of HNO_3 added.

4.4.2.4 Data modeling

SCM is the model used for the simulation of adsorption of metal ions onto metal oxide surfaces. The metal oxide surfaces are treated as infinite plane and hydroxyl groups contribute to the acid-base properties of metal oxide. Metal ions in aqueous solution interact with metal oxide surfaces by forming inner-sphere complex and/or outer-sphere complex. Electric double layer (EDL) is considered after complexation since the surface charge changes. Constance capacitance model (CCM) represents the adsorbed ions on a plane that is parallel to the surface. The surface potential is not affected by the ionic strength in aqueous solution since only the adsorbed ions will be considered in CCM (Warren and Haack 2001). CCM is closely related to diffuse-layer model (DLM) and it

can be applied to high ionic strength and low potential system (Dzombak and Morel 1990). The diffused layer of the diffused layer model (DLM) represents the interfacial region with an inner layer. The region includes the adsorbed ions and a second outer layer of counter-ions. (Warren and Haack 2001). The adsorbed ions are on one surface layer, the non-adsorbed ions are in the diffuse layer (Dzombak and Morel 1990). Stern model (SM) is a combination of CCM and DLM. CCM does not consider the change of ionic strength but DLM accounts for the change. The outer-sphere complex can be adsorbed onto the plane with a single specific capacitance (Gao and Mucci 2001). Although there are different models, all models oberve the following rules: (i) sorption occurs on specific sorption sites; (ii) sorption reactions can be expressed quantitatively by mass law equations; (iii) surface charge is governed by the sorption reactions; and, (iv) the correction factor derived from the EDL theory can be applied to mass law constants to evaluate the effect of surface charge (Dzombak and Morel 1990). The experimental data did not converge when DLM and SM were used for this simulation.

The TOTH values obtained from Section 4.4.2.3 were used as the input data for the computer program FITEQL 2.0 to calculate the protonation/deprotonation constants and the concentration of the cell surface functional groups. The

optimum value of equilibrium constant and the total surface site concentrations in a chemical equilibrium equation can be determined by FITEQL 2.0 (Dzombak and Morel 1990). According to Dzombak and Morel (1990), to operate FITEQL, several steps should be involved: (i) input the chemical equilibrium equation; (ii) input the total component concentrations and the known K values; if K values are unknown, input a guess value; (iii) input the experimental data (free concentrations and total concentrations); (iv) compute the equilibrium concentrations; (v) compute the components which both free concentration and total concentration are known; and, (vi) test the convergence.

The constant capacitance model (CCM) was employed to model the potentiometric titration data. This model is based on the following assumptions: (i) the surface equilibrium constants of CCM are valid only for a particular ionic strength; (ii) the adsorbed ions only occupy one surface plane, all surface complexes are inner-sphere complexes and the background electrolyte are considered to be inert with respect to the surface; and, (iii) the surface-charge potential relationship is described as:

$$\sigma_0 = \sigma_H + \sigma_{is} = C\,\Psi_0 \qquad \text{(Equation 4.11)}$$

where σ_0 is the surface charge, σ_H is the net proton charge, σ_{is} is the charge of the inner-sphere surface complexes, C is the capacitance of the solid-water interface

and Ψ_0 (V) is the surface potential (Du et al. 1997).

CCM is one type of SCM. SCM offers several advantages compared with commonly used isotherm models such as Langmuir and Freundlich models. SCM not only considers the metal ion speciation in aqueous solution, but is also capable of simulating experimental data when changing sorbent to sorbate ratio or pH (Fein et al. 2001). In my CCM calculations, the numbers of surface functional groups that contributed to the buffering and the value of surface capacitance (C) were varied in order to best fit to each titration data set. Five models, namely one-site-one-pK_a, two-site-two-pK_a, three-site-three-pK_a, four-site-four-pK_a and five-site-five-pK_a, were used to simulate the potentiometric titration data of *Mucor rouxii*.

The variance, V(Y), is the difference between the experimental data and the model, and is calculated as:

$$V(Y) = \frac{\sum \left(\frac{Y_{cal} - Y_{exp}}{S_{exp}}\right)^2}{n_p\, n_{II} - n_a} \qquad \text{(Equation 4.12)}$$

where Y_{cal} is the calculated value, Y_{exp} is the experimental value, S_{exp} is the error that corresponds to the experimental data, n_p is the number of data points, n_{II} is the number of group II components and n_a is the number of adjustable parameters.

The value of a variance between 0.1 and 20 is considered to be a good fit with the experimental data (Ngwenya et al. 2009). The surface area of the fungal

biomass was estimated to be 395 m^2/g. A change in surface area from 150 to 500 m^2/g caused a less than 5% change in the surface site concentrations and the deprotonation constants. Therefore, the modeling error caused by the uncertainty of the surface area was negligible.

4.4.2.4.1 One-site-one-pK_a model

In this model, only one type of functional group was assumed to be a dominant group on the fungal biomass surface. The surface functional group was considered to undergo deprotonation which is described by the following equilibrium:

$$R\text{-}A\text{-}H^0 \leftrightarrows R\text{-}A^- + H^+ \qquad K_1 \qquad \text{(Equation 4.13)}$$

where R represents the fungal cell wall and A represents a type of functional group.

$$K_1 = [RA^-]\,[H^+]\,P / [RAH]$$

where $P = \exp(-\Psi_0 F / R T)$

4.4.2.4.2 Two-site-two-pK_a model

Compared with the one-site-one pK_a model, one more type of surface functional group was considered in the two-site-two-pK_a model. The deprotonation equations of functional groups A and B are expressed as follows:

$R\text{-}A\text{-}H^0 \leftrightharpoons R\text{-}A^- + H^+$ K_1 (Equation 4.14)

$R\text{-}B\text{-}H^0 \leftrightharpoons R\text{-}B^- + H^+$ K_2 (Equation 4.15)

$K_1 = [RA^-] [H^+] P / [RAH]$

$K_2 = [RB^-] [H^+] P / [RBH]$

where $P = \exp (- \Psi_0 F / R T)$

4.4.2.4.3 Three-site-three-pK_a model

In the model, three active sites, A, B and C, were assumed to be present on the biomass surface, in which the deprotonation reactions of the three groups are expressed as:

$R\text{-}A\text{-}H^0 \leftrightharpoons R\text{-}A^- + H^+$ K_1 (Equation 4.16)

$R\text{-}B\text{-}H^0 \leftrightharpoons R\text{-}B^- + H^+$ K_2 (Equation 4.17)

$R\text{-}C\text{-}H^0 \leftrightharpoons R\text{-}C^- + H^+$ K_3 (Equation 4.18)

$K_1 = [RA^-] [H^+] P / [RAH]$

$K_2 = [RB^-] [H^+] P / [RBH]$

$K_3 = [RC^-] [H^+] P / [RCH]$

where $P = \exp (- \Psi_0 F / R T)$

4.4.2.4.4 Four-site-four-pK_a model

Based on the zeta potential results in Section 4.4.1, net positive charges were

recorded at low solution pHs, which might be due to the protonation of surface functional group. Thus, compared with three-site-three-pK_a model, an additional protonation reaction (Equation 4.19) is added to the four-site-four-pK_a model, and the equilibrium reactions are described below:

$R\text{-}A\text{-}H^0 \leftrightarrows R\text{-}A^- + H^+$ K_1 (Equation 4.19)

$R\text{-}B\text{-}H^0 \leftrightarrows R\text{-}B^- + H^+$ K_2 (Equation 4.20)

$R\text{-}C\text{-}H^0 \leftrightarrows R\text{-}C^- + H^+$ K_3 (Equation 4.21)

$R\text{-}D + H^+ \leftrightarrows R\text{-}D\text{-}H^+$ K_4 (Equation 4.22)

$K_1 = [RA^-]\,[H^+]\,P / [RAH]$

$K_2 = [RB^-]\,[H^+]\,P / [RBH]$

$K_3 = [RC^-]\,[H^+]\,P / [RCH]$

$K_4 = [R\text{-}D\text{-}H^+]\,P / [RD]\,[H^+]$

where $P = \exp(-\Psi_0 F / R T)$

4.4.2.4.5 Five-site-five-pK_a model

There might be more than four active sites could interact with protons in aqueous solution; therefore, one more deprotonation reaction (Equation 4.24) was considered in five-site-five-pK_a when compared with four-site-four-pK_a model. The equilibrium reactions are shown below:

$R\text{-}A\text{-}H^0 \leftrightarrows R\text{-}A^- + H^+$ K_1 (Equation 4.23)

$R\text{-}B\text{-}H^0 \leftrightarrows R\text{-}B^- + H^+$ K_2 (Equation 4.24)

$R\text{-}C\text{-}H^0 \leftrightarrows R\text{-}C^- + H^+$ K_3 (Equation 4.25)

$R\text{-}D + H^+ \leftrightarrows R\text{-}D\text{-}H^+$ K_4 (Equation 4.26)

$R\text{-}E\text{-}H^0 \leftrightarrows R\text{-}E^- + H^+$ K_5 (Equation 4.27)

$K_1 = [RA^-] [H^+] P / [RAH]$

$K_2 = [RB^-] [H^+] P / [RBH]$

$K_3 = [RC^-] [H^+] P / [RCH]$

$K_4 = [RDH^+] P / [RD] [H^+]$

$K_5 = [R\text{-}E^-] [H^+] P / [REH]$

where $P = \exp (- \Psi_0 F / R T)$

4.4.2.5 Interpretation of the modeling results

Table 4.4 summarizes the average variances obtained by fitting the data of the different titration systems to the one-, two-, three- and four-site models (the 5-site model did not converge). The results showed that the experimental data of all titration systems could be best simulated by the four-site-four-pK_a model with the smallest variances. The variances decreased significantly with each additional site and were reduced to the minimum when the four-site-four-pK_a models were employed. The plots of TOTH versus pH at different titration conditions show that the experimental titration curves could be best simulated by

the four-site-four-pK_a model curves (Appendices 3A-D).

Tables 4.5-4.8 compile the proton binding constants and site concentrations of *Mucor rouxii*. Based on the results in Table 4.8, the mean pK_a values obtained from the four-site-four-pK_a model were 3.22±0.52, 4.92±0.43, 6.79±0.21 and 8.77 ±0.31. The most acidic sites with pK_a= 3.22 could be assigned to phosphodiester groups (the pK_a value of the phosphodiester varies from 3.2 to 3.5) (Zhang et al. 2010; Ngwenya et al. 2009). Sites with pK_a= 4.92 could be ascribed to carboxyl groups (the pK_a value of the carboxyl group varies from 2.0 to 6.0) (Zhang et al. 2010; Cox et al. 1999). Sites with pK_a= 8.77 were ascribed to hydroxyl groups (the pK_a value of the hydroxyl group varies from 8.0 to 12.0) (Zhang et al. 2010; Cox et al. 1999). Sites with pK_a= 6.79 were assigned to amine groups (the pK_a value of the amine group usually varies from 9.0 to 11.0). It should be noted that the pK_a value of the amine group was lower than that described in some studies (Zhang et al. 2010; Ngwenya et al. 2009; Cox et al. 1999); however, the exact pK_a of a functional group depends on the molecular structure as well. In addition, lower pK_a values (from 6.1 to 9.0) were also reported by some researchers (Kushwaha et al. 2010; Gonzalez et al. 2008; Leone et al. 2007; Yun et al. 2001; vanderVegte and Hadziioannou 1997). The zero point charge of 3.5 was found in zeta potential measurement, indicating that a net positive charge was developed

on the fungal surface at low pHs. Protonation of various functional groups including the phosphodiester, carboxyl, amine groups contributed to the net positive charge.

The mean surface site concentrations of *Mucor rouxii* obtained from the four-site-four-pK_a model were 0.55±0.09 (phosphodiester), 0.30±0.09 (carboxyl), 1.44 ± 0.20 (hydroxyl) and 0.37 ± 0.05 (amine) mmol/g-biomass. The concentration of the hydroxyl group was the highest; this might be because the fungal cell wall contained considerable amounts of chitin and other polysaccharides. Moreover, a larger standard deviation was also observed in the surface concentration of the hydroxyl group; this might be due to the presence of more than one functional group (Ojeda et al. 2008). By comparing our modeling results with those of other literature which studied bacterial species (Ojeda et al. 2008; Yee et al. 2004; Daughney et al. 2001; Fein et al. 1997), we found that the surface site concentrations of the bacterial species were generally lower than those of the *Mucor rouxii*. The total site concentration of *Mucor rouxii* was 2.66 mmol/g-biomass, while those of *Aquabacterium commune*, *Bacillus subtilis* and *Calothrix* were 1.54, 0.23 and 1.46 mmol/g-biomass, respectively. The lower total site concentrations might be one of the reasons why bacterial species exhibited a lower biosorption capacities towards Cd(II) ions, as shown in Fig. 4.2.

From the figure, bacterial species (numbered 1-12) exhibited lower Cd(II) biosorption capacities compared with *Mucor rouxii*.

Table 4.4 Average variances of one-, two-, three- and four-site models in different titration systems.

One-site-one-pK$_a$ model				Three-site-three-pK$_a$ model			
System	Variance	Avg. Variance	S.D.	System	Variance	Avg. Variance	S.D.
1 g/L cell (0.1 M $NaNO_3$)	329.90	321.65	11.67	1 g/L cell (0.1 M $NaNO_3$)	7.20	4.39	3.97
	313.40				1.58		
1 g/L cell (0.01 M $NaNO_3$)	205.60	229.45	33.73	1 g/L cell (0.01 M $NaNO_3$)	13.20	8.81	6.21
	253.30				4.42		
2 g/L cell (0.1 M $NaNO_3$)	152.00	164.25	17.32	2 g/L cell (0.1 M $NaNO_3$)	78.30	65.29	18.40
	176.50				52.28		
2 g/L cell (0.01 M $NaNO_3$)	246.10	239.05	9.97	2 g/L cell (0.01 M $NaNO_3$)	49.08	52.83	5.30
	232.00				56.58		
Two-site-two-pK$_a$ model				Four-site-four-pK$_a$ model			
System	Variance	Avg. Variance	S.D.	System	Variance	Avg. Variance	S.D.
1 g/L cell (0.1 M $NaNO_3$)	11.60	8.70	4.10	1 g/L cell (0.1 M $NaNO_3$)	1.31	1.10	0.30
	5.80				0.88		
1 g/L cell (0.01 M $NaNO_3$)	20.20	14.69	7.80	1 g/L cell (0.01 M $NaNO_3$)	1.66	1.43	0.33
	9.17				1.20		
2 g/L cell (0.1 M $NaNO_3$)	81.86	69.52	17.46	2 g/L cell (0.1 M $NaNO_3$)	0.56	0.45	0.17
	57.17				0.33		
2 g/L cell (0.01 M $NaNO_3$)	57.45	59.39	2.74	2 g/L cell (0.01 M $NaNO_3$)	0.39	0.40	0.02
	61.32				0.42		

Table 4.5 Proton binding constants and surface site concentrations of *Mucor rouxii* in different titration systems (One-site-one-pK_a model).

	One-site-one-pK_a model					
				Concentration of group A		
System	pK_{a_A}	Avg.	S.D.	(mol/L)	Avg.	S.D.
1 g/L cell,	5.748	5.72	0.04	1.604E-03	1.642E-03	5.37E-05
0.1 M $NaNO_3$	5.694			1.680E-03		
1 g/L cell,	6.200	6.16	0.06	2.215E-03	2.202E-03	1.84E-05
0.01 M $NaNO_3$	6.117			2.189E-03		
2 g/L cell,	5.741	5.53	0.31	3.030E-03	2.530E-03	7.08E-04
0.1 M $NaNO_3$	5.309			2.029E-03		
2 g/L cell,	5.837	5.73	0.15	2.562E-03	2.512E-03	7.07E-05
0.01 M $NaNO_3$	5.626			2.462E-03		

Table 4.6 Proton binding constants and surface site concentrations of *Mucor rouxii* in different titration systems (Two-site-two-pK_a model).

	Two-site-two-pK_a model											
							Concentration of group A			Concentration of group B		
System	pK_{aA}	Avg.	S.D.	pK_{aB}	Avg.	S.D.	(mol/L)	Avg.	S.D.	(mol/L)	Avg.	S.D.
1 g/L cell,	4.361	4.30	0.09	7.669	7.62	0.07	5.551E-04	5.59E-04	4.88E-06	1.618E-03	1.64E-03	2.83E-05
0.1 M $NaNO_3$	4.239			7.565			5.620E-04			1.658E-03		
1 g/L cell,	4.642	4.59	0.07	7.919	7.96	0.06	5.853E-04	6.01E-04	2.26E-05	2.123E-03	2.16E-03	5.02E-05
0.01 M $NaNO_3$	4.540			8.006			6.172E-04			2.194E-03		
2 g/L cell,	4.896	4.77	0.17	7.711	7.72	0.01	6.038E-04	6.28E-04	3.46E-05	1.913E-03	1.72E-03	2.73E-04
0.1 M $NaNO_3$	4.651			7.729			6.527E-04			1.527E-03		
2 g/L cell,	4.690	4.71	0.03	8.051	8.04	0.01	5.257E-04	5.66E-04	5.70E-05	2.123E-03	2.10E-03	3.32E-05
0.01 M $NaNO_3$	4.728			8.034			6.063E-04			2.076E-03		

Table 4.7 Proton binding constants and surface site concentrations of *Mucor rouxii* in different titration systems (Three-site-three-pK_a model).

	Three-site-three-pK_a model								
System	pK_{aA}	Avg.	S.D.	pK_{aB}	Avg.	S.D.	pK_{aC}	Avg.	S.D.
1 g/L cell, 0.1 M $NaNO_3$	4.363 4.167	4.27	0.14	6.942 6.474	6.71	0.33	8.970 8.597	8.78	0.26
1 g/L cell, 0.01 M $NaNO_3$	4.541 4.482	4.51	0.04	6.813 6.821	6.82	0.00	9.179 9.087	9.13	0.07
2 g/L cell, 0.1 M $NaNO_3$	4.868 4.667	4.77	0.14	7.243 7.253	7.25	0.00	9.108 9.158	9.13	0.04
2 g/L cell, 0.01 M $NaNO_3$	4.587 4.731	4.66	0.10	6.850 7.118	6.98	0.19	9.024 9.116	9.07	0.07

System	Concentration of group A			Concentration of group B			Concentration of group C		
	(mol/L)	Avg.	S.D.	(mol/L)	Avg.	S.D.	(mol/L)	Avg.	S.D.
1 g/L cell, 0.1 M $NaNO_3$	4.650E-04 4.497E-04	4.57E-04	1.08E-05	4.633E-04 3.910E-04	4.27E-05	5.11E-05	1.197E-03 1.305E-03	1.25E-03	7.64E-05
1 g/L cell, 0.01 M $NaNO_3$	4.424E-04 4.937E-04	4.68E-04	3.63E-05	4.637E-04 4.142E-04	4.39E-04	3.50E-05	1.575E-03 1.631E-03	1.60E-03	3.96E-05
2 g/L cell, 0.1 M $NaNO_3$	5.014E-04 5.531E-04	5.27E-04	3.66E-05	6.087E-04 5.001E-04	5.54E-04	7.68E-05	1.322E-03 1.082E-03	1.20E-03	1.70E-04
2 g/L cell, 0.01 M $NaNO_3$	4.130E-04 5.200E-04	4.67E-04	7.57E-05	4.117E-04 3.719E-04	3.92E-04	2.81E-05	1.607E-03 1.527E-03	1.57E-03	5.66E-05

Table 4.8 Proton binding constants and surface site concentrations of *Mucor rouxii* in different titration systems (Four-site-four-pK_a model).

	Four-site-four-pK_a model										
System	pK_{aA}	Avg.	S.D.	pK_{aB}	Avg.	S.D.	pK_{aC}	Avg.	S.D.	pK_{aD}	Avg.	S.D.
1 g/L cell,	2.970	2.66	0.44	4.826	4.53	0.42	7.177	6.83	0.49	9.123	8.86	0.37
0.1 M $NaNO_3$	2.350			4.237			6.483			8.597		
1 g/L cell,	3.601	3.08	0.73	5.547	4.97	0.82	6.951	6.82	0.18	8.978	9.01	0.04
0.01 M $NaNO_3$	2.564			4.393			6.695			9.032		
2 g/L cell,	3.503	3.60	0.13	5.067	5.11	0.06	6.723	6.71	0.02	8.395	8.33	0.09
0.1 M $NaNO_3$	3.687			5.153			6.690			8.268		
2 g/L cell,	3.442	3.54	0.14	5.094	5.07	0.03	6.740	6.79	0.07	8.890	8.88	0.02
0.01 M $NaNO_3$	3.647			5.055			6.833			8.861		

System	Concentration of group A			Concentration of group B			Concentration of group C			Concentration of group D		
	(mol/L)	Avg.	S.D.	(mol/L)	Avg.	S.D.	(mol/L)	Avg.	S.D.	(mol/L)	Avg.	S.D.
1 g/L cell,	6.14E-04	5.40E-04	1.04E-04	3.73E-04	4.06E-04	4.70E-05	4.42E-04	4.30E-04	1.70E-05	1.25E-03	1.32E-03	1.12E-04
0.1 M $NaNO_3$	4.67E-04			4.40E-04			4.18E-04			1.40E-03		
1 g/L cell,	4.53E-04	4.00E-04	7.48E-05	2.23E-04	3.04E-04	1.14E-04	2.41E-04	2.92E-04	7.19E-05	1.25E-03	1.30E-03	8.41E-05
0.01 M $NaNO_3$	3.47E-04			3.85E-04			3.42E-04			1.36E-03		
2 g/L cell,	1.20E-03	1.25E-03	7.57E-05	5.20E-04	5.01E-04	2.62E-05	8.32E-04	7.39E-04	1.32E-04	2.82E-03	2.67E-03	2.16E-04
0.1 M $NaNO_3$	1.31E-03			4.83E-04			6.45E-04			2.52E-03		
2 g/L cell,	1.15E-03	1.10E-03	7.57E-05	3.81E-04	4.29E-04	6.83E-05	7.31E-04	6.63E-04	9.62E-05	3.19E-03	3.07E-03	1.63E-04
0.01 M $NaNO_3$	1.05E-03			4.78E-04			5.94E-04			2.96E-03		

4.4.3 SEM images and EDAX spectra

The surface morphologies and the elemental analyses of the virgin fungal biomass were examined by scanning electron microscopy (SEM) and energy dispersive analysis of X-rays (EDAX), respectively. The SEM images of pristine biomass (Fig. 4.19) show that the biomass surface is smooth and the biomass is filamentous. The width of the filament was approximately 5 μm. EDAX spectrum (Fig. 4.20) gives information that the biomass surface mainly consists of carbon, nitrogen, oxygen and phosphorus, which are the main compositions of the cell wall. Unlike the results reported by some studies (cations such as K^+, Ca^{2+}, Mg^{2+} and Al^{3+} were found on biomass surface) (Allouche et al. 2011; Akar et al. 2007), we observed that no cations were present on the fungal biomass surface. This result suggested that the metal removal might not be due to ion exchange between heavy metal ions and surface cations such as alkali and alkaline earth metal cations.

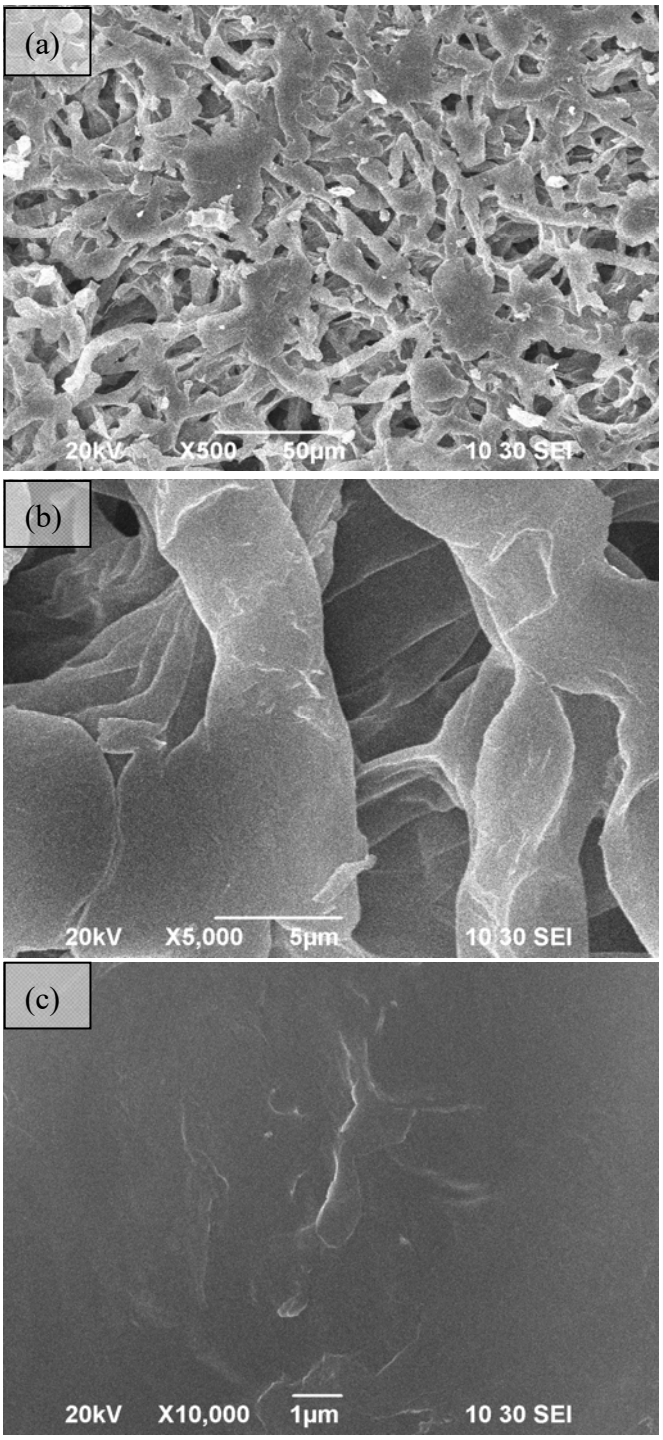

Figure 4.19 SEM images of (a) pristine biomass (500X), (b) pristine biomass (5000X) and (c) pristine biomass (10000X).

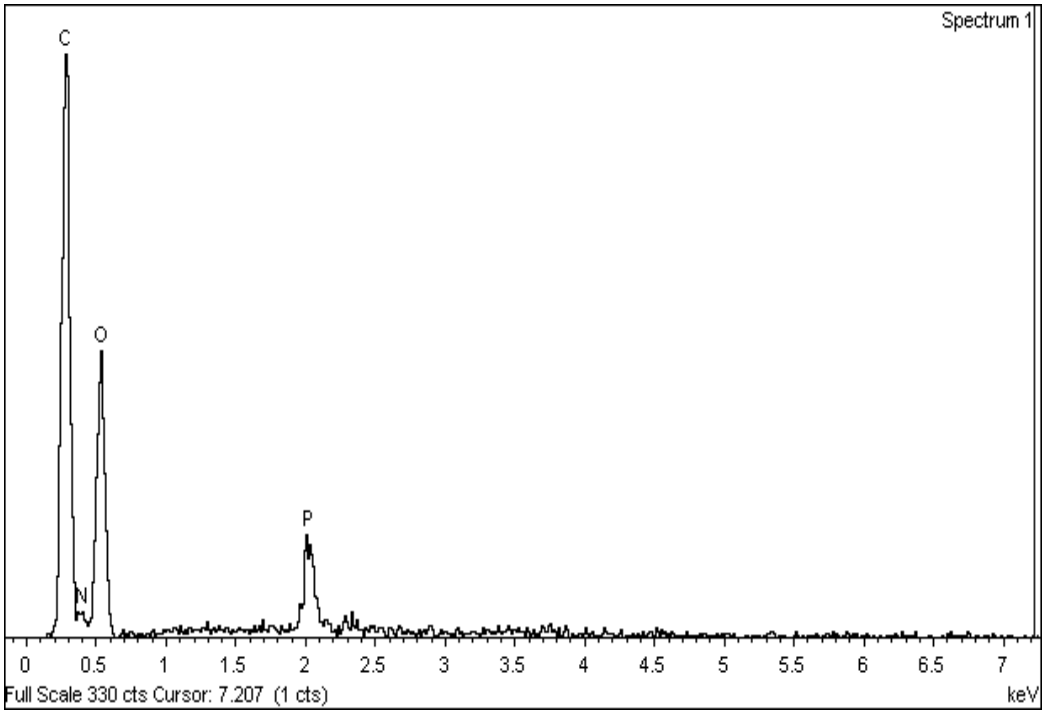

Figure 4.20 EDAX spectrum of pristine biomass.

4.4.4 FTIR analysis

FTIR was employed to characterize the surface functional groups of the fungal biomass. The FTIR spectrum of the pristine biomass (Fig. 4.21) shows the peaks at 3443.4, 2924.3, 1636.0, 1541.0, 1507.7, 1384.7, 1264.6 and 1072.8 cm^{-1}. The O-H stretching was located in the region of 3500-3200 cm^{-1} while the wavenumber of symmetric NH_2 stretching was in between 3310-3280 cm^{-1}. The broad and strong band at 3443.4 cm^{-1} was a combination of stretching vibration in O-H and N-H. The peak at 2924.3 cm^{-1} was attributed to the C-H stretching in alkyl chains (Das et al. 2007; Smith 1999). Assignment for the peak at 1636.0 cm^{-1} might be complicated as there are several functional groups (C=O stretching in amide I (1680-1630 cm^{-1}), NH_2 scissoring in the amines (1650-1580 cm^{-1}) and asymmetric stretching in the carboxylate ions (1650-1540 cm^{-1}) that lie around this wavenumber. Bands at 1541.0 cm^{-1} might correspond to the N-H bending and C-N stretching in amides II or might attribute to the NH and NH_2 bending in amines. Another peak at 1507.7 cm^{-1} might be due to the C-$N(CH_3)_2$ stretching in the amide III, while the peak at 1384.7 cm^{-1} could be assigned to the symmetric stretching of the carboxylate ion. The stretching vibration of C-O in carboxylic acids was observed at 1264.6 cm^{-1}. The strong and broad band at 1072.8 cm^{-1}

represented the P=O stretching of the phosphodiester, phosphorylated proteins or polyphosphate products (Ojeda et al. 2008; Smith 1999). From the results of FTIR analysis, we could conclude that the main functional groups present on the biomass surface were amine/amide, carboxyl, hydroxyl and phosphodiester groups, which were consonant with the potentiometric titration results.

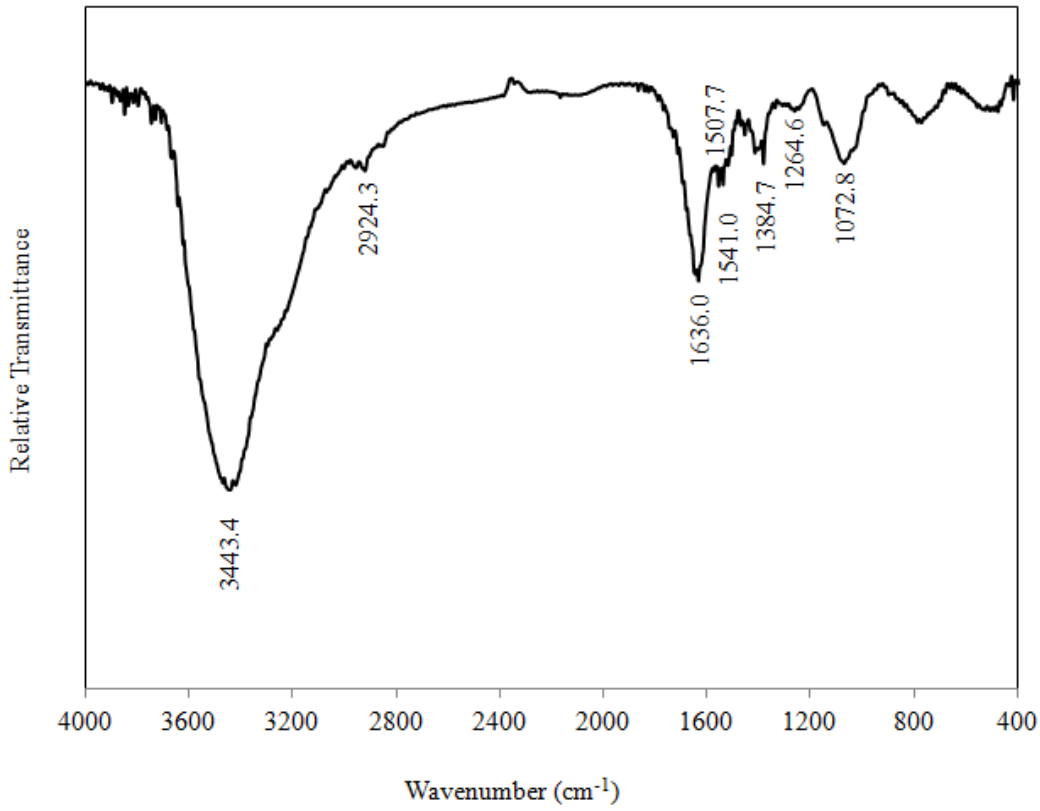

Figure 4.21 FTIR spectrum of pristine biomass.

4.4.5 XPS analysis

XPS has been widely used to investigate the oxidation state and elemental composition on the biomass surface. A characteristic binding energy will be displayed on the XPS spectra for each element (Arief et al. 2008). Fig. 4.22 shows the wide scan XPS spectrum of the pristine biomass, which revealed that the cell surface was mainly composed of C, N, O and P, and these results are comparable to those of the EDAX spectrum. The atomic concentrations of the elements displayed in Table 4.9 show that the percentage of carbon was the highest (73.29%), followed by oxygen (20.40%), nitrogen (5.77%) and phosphorus (0.54%). In order to obtain more information about the fungal biomass surface, the peaks of C, N and O were deconvoluted using a computer program called Vision Processing.

The high resolution XPS spectrum of C1s is shown in Fig. 4.23. The C1s spectrum was composed of four individual peaks in which the binding energies of 285.00, 286.54, 288.27 and 289.31 eV could be assigned to the C atom in the forms of C-(C,H), C-(O,N), C=O and O=C-O, respectively (Table 4.10). The atomic concentration of the four components followed this sequence: C-(C,H) > C-(O,N) > C=O > O=C-O, which revealed that the concentration of the ether/

hydroxyl/ amine was the highest, followed by the amide and carboxylate groups. These results were consonant with the potentiometric titration results ([OH] > [COOH]).

The deconvoluted N1s spectrum showed that N1s comprised two peaks (Fig. 4.24). The binding energies of 400.08 and 401.98 eV could be assigned to the N atom in the forms of NH_2 and NH_3^+, respectively.

The deconvolution of O1s spectrum is shown in Fig. 4.25. The O1s spectrum was formed by two individual component peaks with binding energies of 531.30 and 532.79 eV, which could be assigned to the oxygen atom in the form of O=C and O-C, respectively.

The P2p peak at binding energy of 133.8 eV could be assigned to the phosphorus atom in the form of P-O.

From the results of high resolutions spectra of C, N and O, it could be concluded that the functional groups of hydroxyl, carboxyl, amide/amine and phosphodiester were present on the biomass surface.

The results of potentiometric titration, EDAX, FTIR and XPS were consonant with each other. The integrated results revealed the presence of phosphodiester (pK_a = 3.22±0.52), carboxyl (pK_a = 4.92±0.43), amino groups (pK_a = 6.79±0.21) and hydroxyl (pK_a = 8.77±0.31) on the fungal biomass surface with

the corresponding site concentrations of 0.55±0.09, 0.30 ±0.09, 0.37±0.05 and 1.44±0.20 mmol/g-biomass, respectively.

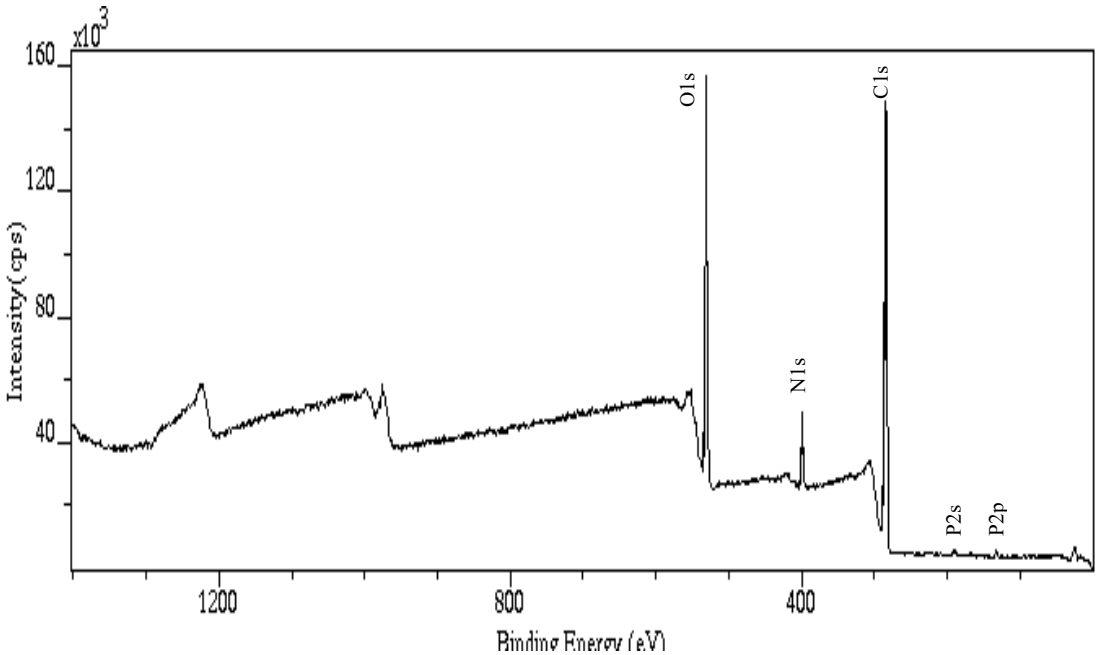

Figure 4.22 Wide scan XPS spectrum of pristine biomass.

Table 4.9 Binding energies and atomic concentrations of different elements on pristine biomass.

	Pristine biomass	
Peak	Binding energy (eV)	Atomic concentration (%)
C1s	285.00	73.29
N1s	400.10	5.77
O1s	532.70	20.40
P2p	133.80	0.54
Cd3d	415.40	0.00

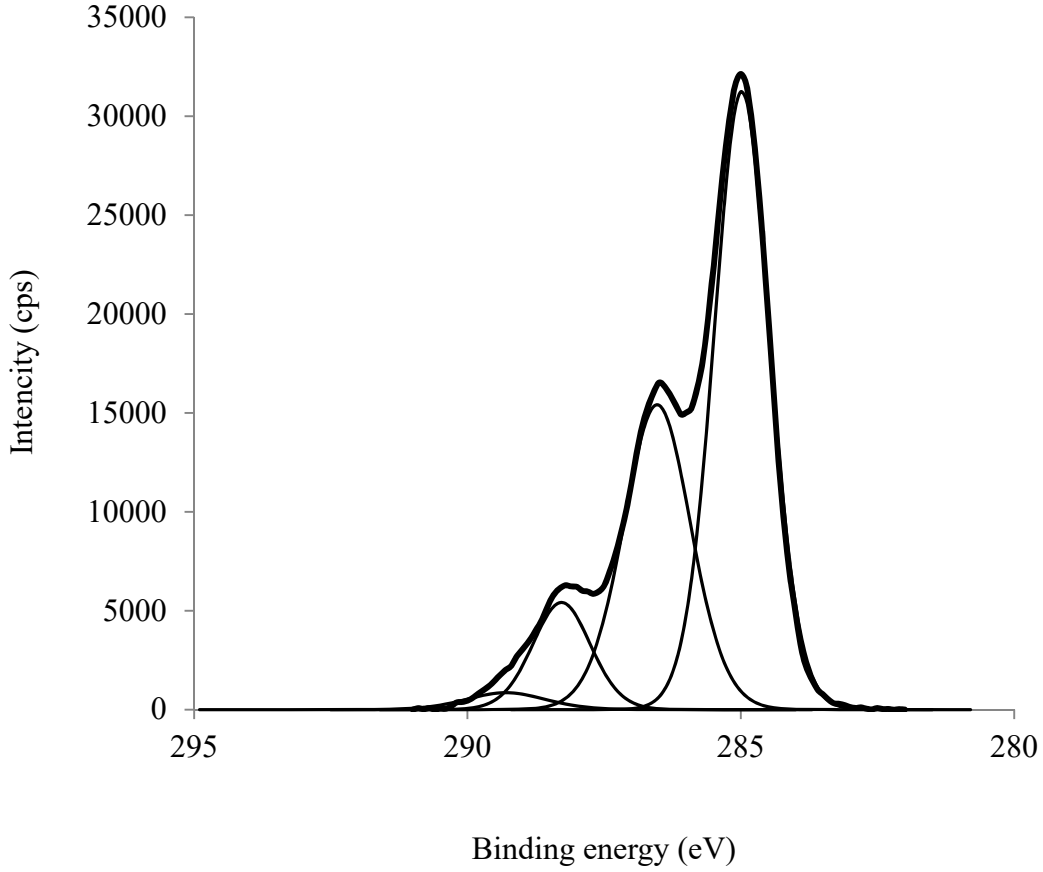

Figure 4.23 High resolution XPS (C1s) spectrum of pristine biomass.

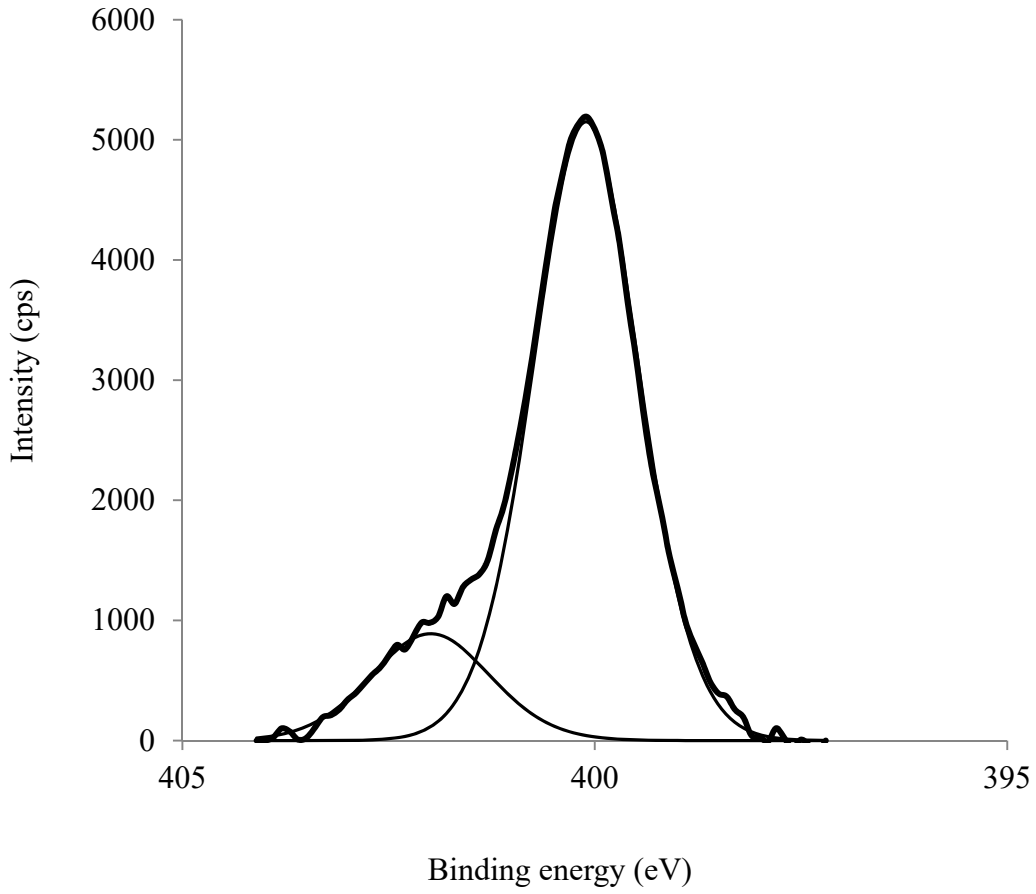

Figure 4.24 High resolution XPS (N1s) spectrum of pristine biomass.

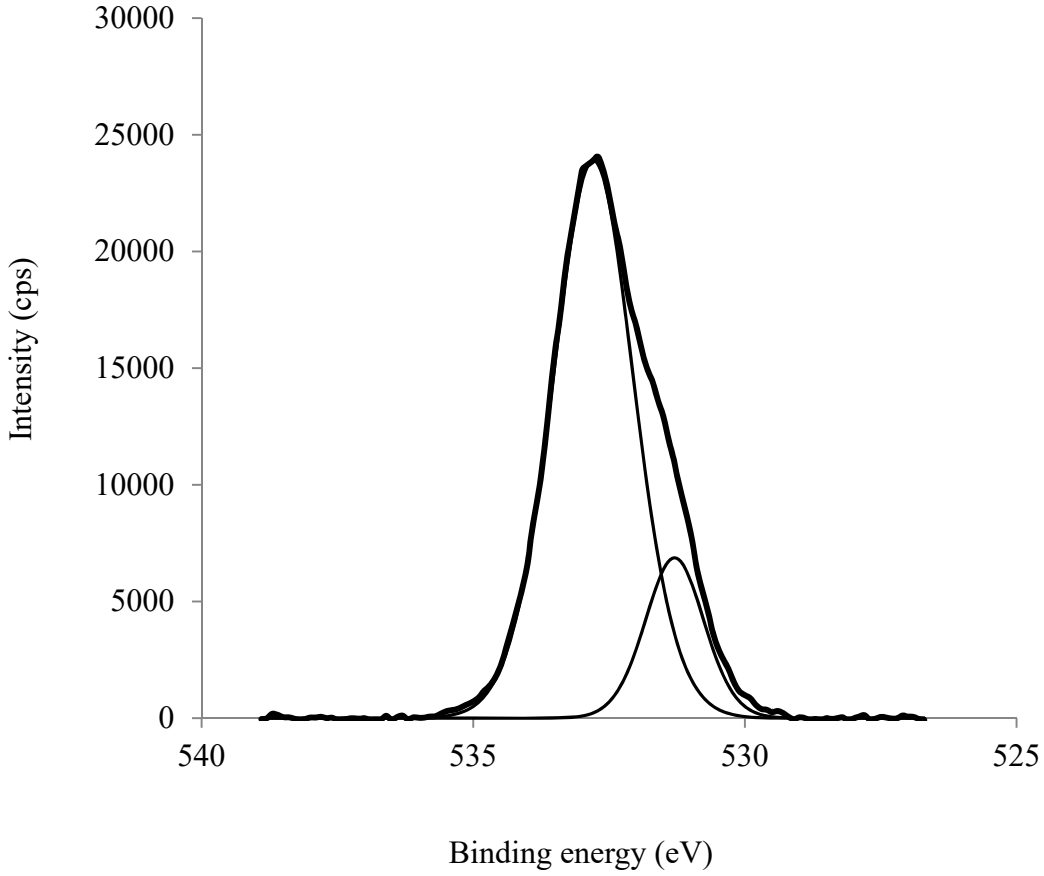

Figure 4.25 High resolution XPS (O1s) spectrum of pristine biomass.

Table 4.10 Binding energies and atomic concentrations of high resolutions XPS spectra of *Mucor rouxii*.

		Pristine biomass	
Element	Assignment	Binding energy (eV)	Atomic concentration (%)
C1s	C-(C, H)	285.00	55.02
C1s	C-(O, N)	286.54	32.87
C1s	C=O	288.27	9.96
C1s	O=C-O	289.31	2.15
N1s	NH_2	400.08	83.66
N1s	NH_3^+	401.98	16.34
O1s	O-C	532.79	82.73
O1s	O=C	531.30	17.27
P2p	P-O	133.80	100.00

Chapter 5

Biosorption of Cd(II) by *Mucor rouxii*

5. Biosorption of Cd(II) by *Mucor rouxii*

This chapter reports the effects of pH, biomass concentration, initial metal concentration, contact time, temperature and agitation speed on the Cd(II) biosorption by *Mucor rouxii*. Different isotherm and kinetic models were employed to simulate the equilibrium and kinetic data of Cd(II) biosorption by the fungal biomass. Thermodynamic studies were then conducted to determine the adsorption characteristics of Cd(II) by the fungal biomass. The Cd(II) binding mechanism of the fungal biomass is studied. Further, the applicability of surface complexation model for biosorption of Cd(II) is also discussed.

5.1 Effect of pH

Solution pH strongly influences the metal-binding performance of biomass since pH governs the speciation of metal ions and the protonation/deprotonation of functional groups on the biomass surface. Speciation diagram of cadmium complexes in solution pHs ranging from 0.0 to 14.0 was plotted by a software called MINEQL^{+} 3.01. The speciation simulation conditions are 100 ppm Cd; temperature 25℃ and open system. The speciation diagram of cadmium complexes in aqueous solution is shown in Fig. 5.1. As illustrated in the figure, Cd^{2+} is the dominant species at a pH below 7.5. When pH further increases, the

percentages of $Cd(OH)^+$, $Cd(OH)_2$ and $Cd(OH)_3^-$ increase. Formation of insoluble $Cd(OH)_2$ occurs when the pH is above 8.0.

To examine the effect of the solution pH on Cd(II) removal, pH values ranging from 2.0 to 8.0 were studied. The results, as shown in Fig. 5.2, indicated that the biosorption capacity generally increased as the solution pH increased. Negligible biosorption was observed at low pH (pH 2, 3 and 4). Since most of the protons were associated with the adsorption sites, repulsion between the protonated sites and the Cd^{2+} ions occurred. When the pH was further increased, the biosorption capacities increased as the Cd^{2+} and $Cd(OH)^+$ ions could be rapidly attracted to the deprotonated sites. A maximum biosorption capacity (71.68 mg-Cd(II)/g-biomass) was obtained at pH 7.5. At pH 8.0, a 10% decrease in cadmium concentration was observed in the control experiment; this might be attributed to the formation of insoluble $Cd(OH)_2$.

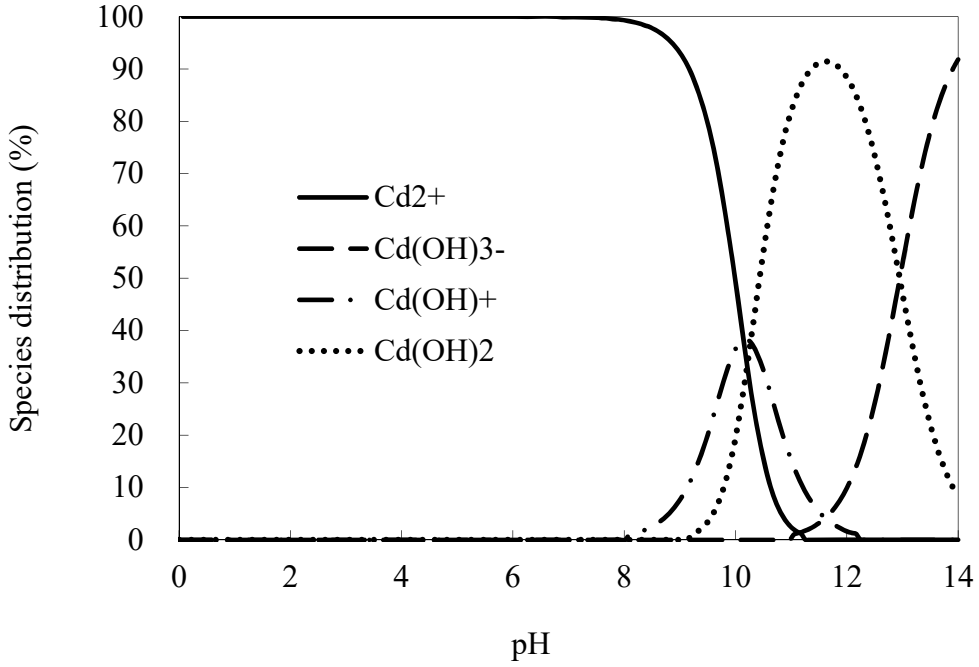

Figure 5.1 Speciation diagram of Cd(II) in aqueous solution (100 ppm).

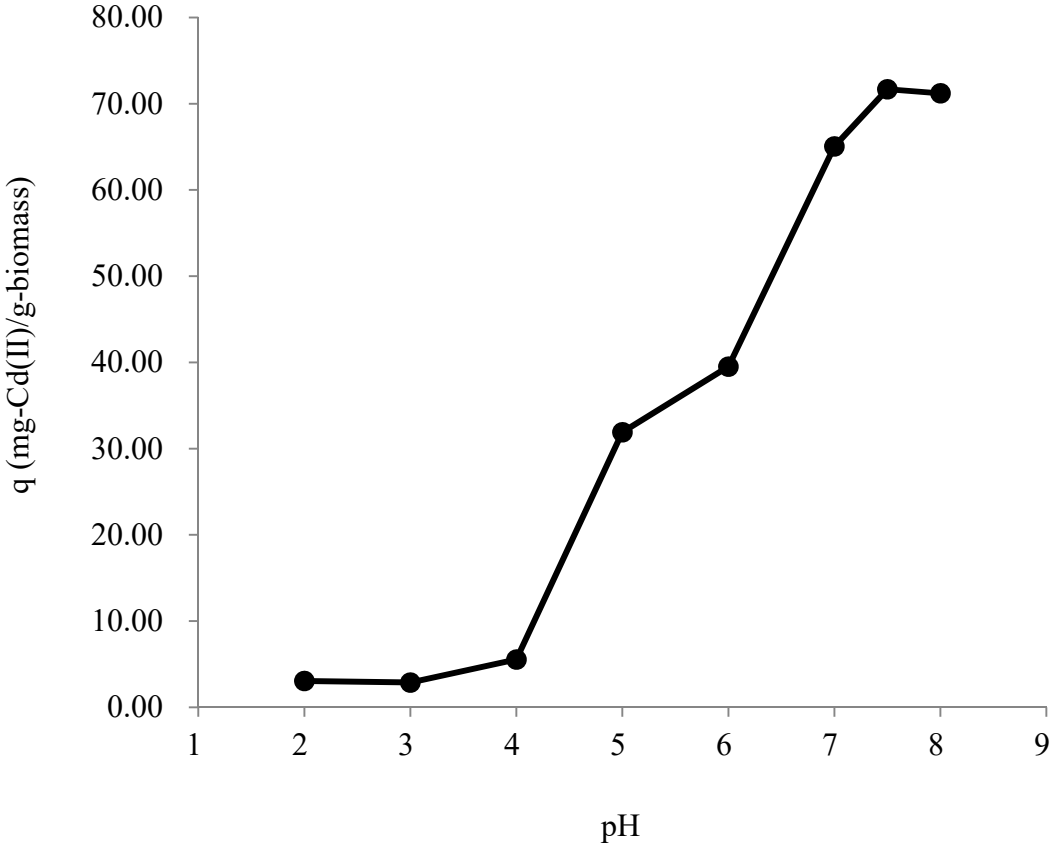

Figure 5.2 Effect of pH on Cd(II) biosorption by *Mucor rouxii*.

5.2 Effect of biomass concentration

The biomass concentration may affect the Cd(II) removal efficiency of *Mucor rouxii*. To study the effect of biomass concentration on Cd(II) biosorption, biomass concentrations ranging from 0.2 to 5 g/L were investigated. Fig. 5.3 illustrates that the percentage removal of Cd(II) increased as the biomass concentration increased, until reaching a plateau. This could be attributed to the fact that more biomass resulted in more sorption sites for metal ions biosorption. The percentage removal of cadmium ions almost reached a maximum at a biomass concentration of 2 g/L and did not significantly increase when the concentration was increased further. The maximum removal of Cd(II) ions (95.98%) was attained at a biomass concentration of 4 g/L. On the other hand, an increase in biomass concentration would decrease the biosorption capacity. At a high biomass concentration, numerous binding sites were still vacant and therefore a low biosorption capacity was resulted.

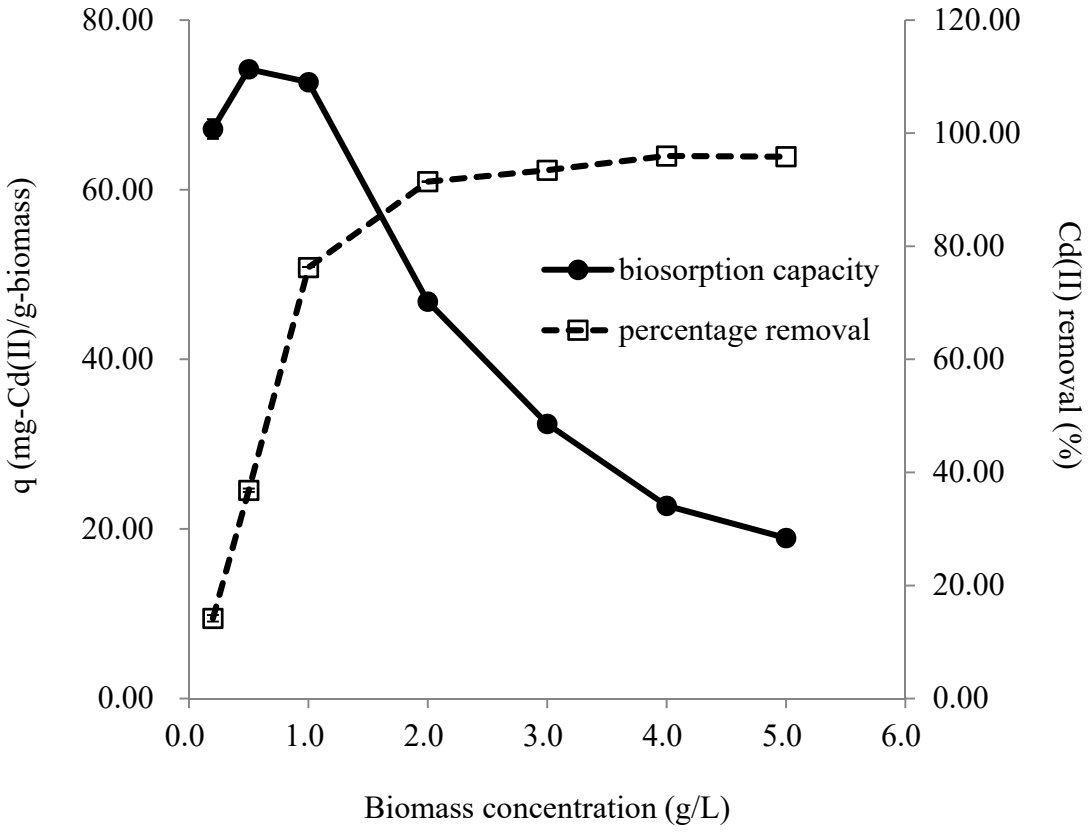

Figure 5.3 Effect of biomass concentration on Cd(II) biosorption and percentage removal by *Mucor rouxii*.

5.3 Sorption isotherms

Initial metal concentration is another factor that may affect the Cd(II) removal performance of *Mucor rouxii*. Therefore, the effect of initial metal concentration on the Cd(II) removal by the fungal biomass was examined in this section. Fig. 5.4 shows the plot of Cd(II) biosorption capacity, q (in mg Cd(II) per gram biomass), versus residual Cd(II) equilibrium concentration remaining in aqueous solution, C_e (ppm). The figure illustrated that the biosorption capacity increased with increasing initial metal concentration until the capacity became saturated at 61 mg/L. Under low metal concentrations, sharp increases in q values were observed, showing that the fungal biomass exhibited a high affinity towards Cd(II) ions.

In order to obtain more information about the biosorption properties of the fungal biomass, two-parameter (Langmuir, Freundlich and Temkin) and three-parameter (Sips and Redlich-Peterson) isotherm models were employed to simulate the experimental data by using linear and non-linear regression analysis. A computer software, GraphPad Prism 3.0, was applied for the non-linear regression analysis. The fitness of the isotherm model was evaluated by the correlation coefficient (r^2) and error analyses (SSE, RMSE and SE).

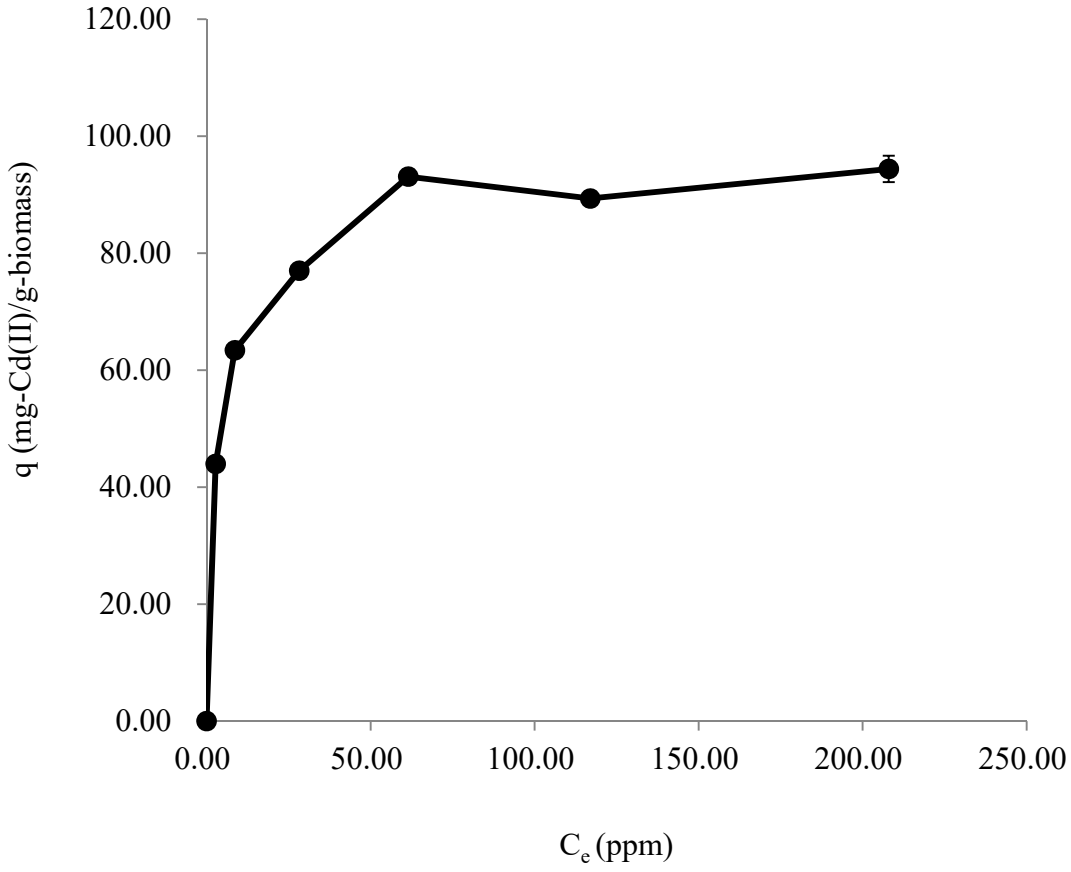

Figure 5.4 Cd(II) biosorption isotherm of *Mucor rouxii*.

5.3.1 Two-parameter models

5.3.1.1 Langmuir isotherm model

The Langmuir equation is widely employed to quantify and compare the sorption performance of different biosorbents. Originally, this model was developed to describe the gas adsorption of solid activated carbon surface. The model has three assumptions. First, the adsorption layer is a monolayer. Second, the surface is uniform and all the adsorption sites are equivalent. Third, there are no interactions between adsorbed adsorbates (Atkins 2002). The Langmuir isotherm is given as:

$$q_e = \frac{b_L\ q_{max}\ C_e}{1 + b_L\ C_e} \qquad \text{(Equation 5.1)}$$

The linear form of the Langmuir equation can be expressed as:

$$\frac{C_e}{q_e} = \frac{1}{q_{max}}\ C_e + \frac{1}{b_L\ q_{max}} \qquad \text{(Equation 5.2)}$$

where q_e (mg/g) is the amount of the metal ions adsorbed per unit weight of the biomass at equilibrium, b_L (L/mg) is the Langmuir isotherm constant, q_{max} (mg/g) is the maximum biosorption capacity and C_e (mg/L) is the equilibrium metal concentration (Cesur and Balkaya 2007).

The parameters q_{max} and b_L were calculated from the slope and the intercept of the plot of C_e/q_e versus C_e, respectively (Fig. 5.5). These two values are the

important parameters in evaluating the biosorption performance of biomass since a high value of q_{max} represents a high adsorption capacity, while a high value of b_L indicates a strong binding between heavy metal ions and the biomass (Kratochvil and Volesky 1998b). The predicted values of q_{max} and b_L were 95.24 mg-Cd(II)/g-biomass and 0.29 L/mg, respectively.

5.3.1.2 Freundlich isotherm model

The Freundlich equation is another model commonly used for simulating isotherm data. This model describes the sorption of heterogeneous surfaces or the sorption of surface sorbing sites with different affinities. The stronger binding sites are assumed to be occupied first and the ability of a sorbate to adsorb on a given sites decreases as the degree of occupation of neighboring sites increases (Davis et al. 2003). The Freundlich is presented as:

$$q_e = k_F C_e^{1/n_F} \qquad \text{(Equation 5.3)}$$

The linearized form of the Freundlich equation is described as follows:

$$\ln q_e = \frac{1}{n_F} \ln C_e + \ln k_F \qquad \text{(Equation 5.4)}$$

where k_F and n_F are Freundlich constants, and represent adsorption capacity and adsorption intensity, respectively (Cesur and Balkaya 2007; Lo et al. 2003b).

The values of k_F and n_F could be obtained from non-linearized Freundlich equation by plotting ln q_e versus ln C_e (Fig. 5.6). The value of k_F and n_F were

found to be 40.75 L/g and 5.75, respectively. A high value of n_F (greater than 1) suggesting that the removal of metal ions by an adsorbent is a favorable physical process (Safa and Bhatti 2011). However, the linearized Freundlich model was not suitable for describing the experimental data due to a low correlation coefficient ($r^2 = 0.9112$) and high error values (SE = 7.76) (Table 5.1).

In addition to the linearized Langmuir and Freundlich isotherm models, non-linear forms of the two models were also employed to describe the experimental data, as illustrated in Fig. 5.7. The isotherm parameters, correlation coefficients and error analyses of the Langmuir and Freundlich models (linearized and non-linearized) are listed in Table 5.1. As shown in the table, the experimental data were better simulated by both the linearized and non-linearized Langmuir isotherms with higher correlation coefficients and lower error values when compared with those obtained from the Freundlich isotherms. In the Freundlich model, the equation is exponential, indicating that biosorption capacity (q_e) increases with the equilibrium metal concentration (C_e). Theoretically, an infinite amount of biosorption can occur based on this equation. However, a plateau could be observed from the adsorption isotherm of Cd(II), as shown in Fig. 5.4. Therefore, the experimental data could be better simulated by the Langmuir model than the Freundlich model, revealing that the adsorption properties of the

fungal biomass might be close to the assumptions of the Langmuir isotherm model, i.e. the homogeneous and monolayer biosorption of Cd(II) (Marin et al. 2009; Perez-Marin et al. 2007). The maximum biosorption capacity (q_{max}) and isotherm constant (b_L) obtained from the non-linearized Langmuir isotherm model are 93.59 mg-Cd(II)/g-biomass and 0.28 L/mg, respectively.

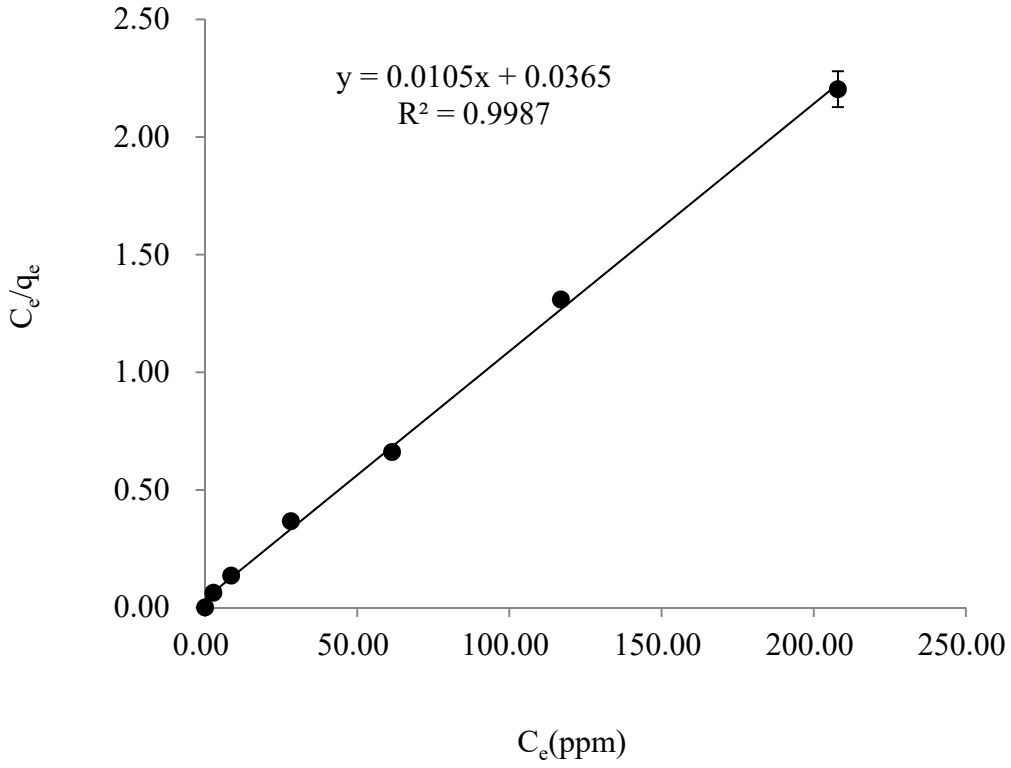

Figure 5.5 Linearized Langmuir isotherm model for Cd(II) biosorption by *Mucor rouxii*.

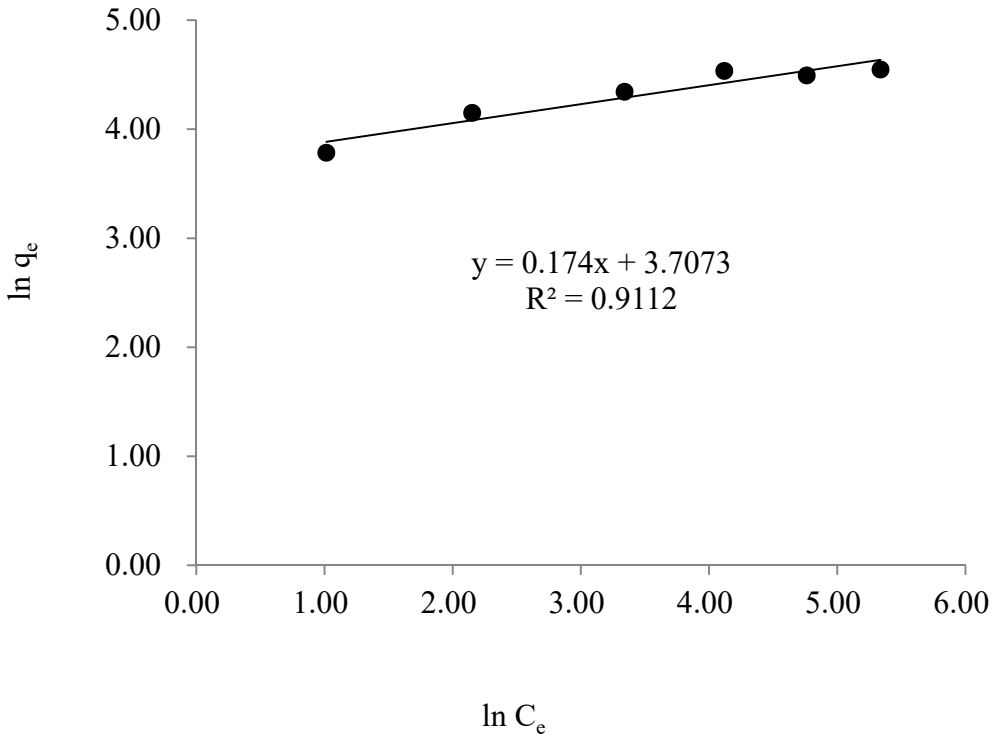

Figure 5.6 Linearized Freundlich isotherm model for Cd(II) biosorption by *Mucor rouxii*.

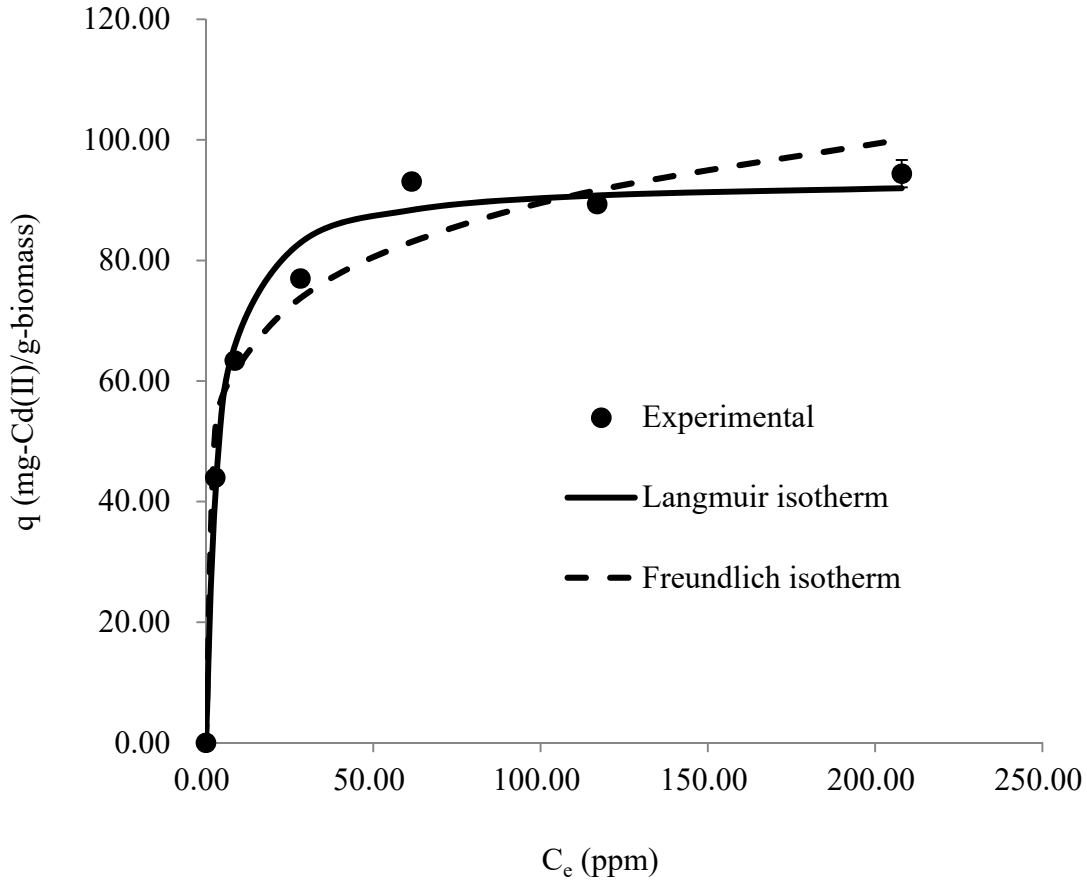

Figure 5.7 Non-linearized Langmuir and Freundlich isotherm models for Cd(II) biosorption by *Mucor rouxii*.

Table 5.1 Comparison of parameters obtained from the linearized and non-linearized Langmuir and Freundlich isotherm models for Cd(II) biosorption by *Mucor rouxii*.

	Langmuir					
	q (mg-Cd(II)/g-biomass)	b_L (L/mg)	r^2	SSE	RMSE	SE
Linearized	95.24 ± 1.94	0.29 ± 0.02	0.9987 ± 0.0006	102.83	4.14	5.07
Non-linearized	93.59 ± 1.01	0.28 ± 0.01	0.9883 ± 0.0028	83.20	3.72	4.56
	Freundlich					
	k_F (L/g)	n_F	r^2	SSE	RMSE	SE
Linearized	40.75 ± 0.56	5.75 ± 0.01	0.9112 ± 0.0066	241.16	6.34	7.76
Non-linearized	44.27 ± 0.40	6.54 ± 0.06	0.9699 ± 0.0018	211.85	5.94	7.28

5.3.1.3 Temkin isotherm model

Temkin and Pyzhev developed this model based on the assumption that the heat of adsorption of all the adsorbates on the surface would decrease linearly with increasing surface coverage of adsorbent due to adsorbate-adsorbent interactions. The adsorption is characterized by a uniform distribution of binding energies. Similar to the Freundlich model, the Temkin isotherm was employed to describe adsorption on a heterogeneous surface (Elkady et al. 2011; Liu 2008; Gunay et al. 2007). The Temkin isotherm is represented by the following equation:

$$q_e = \frac{R\,T}{b_T} \ln\,(a_T\,C_e) \qquad \text{(Equation 5.5)}$$

where R (8.314 J/mol-K) is the gas constant, T (K) is the absolute temperature, b_T is the heat adsorption constant and a_T is the Temkin isotherm constant.

The value of b_T calculated from the Temkin model was low (0.21 kJ/mol), indicating a weak ionic interaction between Cd(II) ions and the fungal biomass surface. Therefore, physical biosorption should be a dominant process in Cd(II) binding onto the fungal biomass (Aytas et al. 2011).

5.3.2 Three-parameter models

5.3.2.1 Sips isotherm model

The Sips model is a combination of the Langmuir and Freundlich isotherm models. It reduces to the Freundlich isotherm at low metal ion concentrations and exhibits the monolayer adsorption characteristic of the Langmuir isotherm at high sorbate concentrations (Liu 2008; Gunay et al. 2007; Perez-Marin et al. 2007). The Sips isotherm can be expressed as:

$$q_e = \frac{q_{max}\, b\, C_e^{1/n}}{1 + b\, C_e^{1/n}} \qquad \text{(Equation 5.6)}$$

where b and n are constants.

The value of n obtained from the Sips model was found to be 1.435.

5.3.2.2 Redlich-Peterson isotherm model

Similar to the Sips isotherm model, the Redlich-Peterson equation also incorporates the characteristics of the Langmuir and Freundlich isotherms. The Redlich-Peterson model can be written as follows:

$$q_e = \frac{k_R\, C_e}{1 + \alpha\, C_e^{\beta}} \qquad \text{(Equation 5.7)}$$

where k_R, α and β are Redlich-Peterson constants. The value of β generally lies between zero and one. As β equals 1, the equation becomes the same as the Langmuir model (Liu 2008; Perez-Marin et al. 2007; Vijayaraghavan et al. 2006).

The value of β was found to be close to 1 (β = 0.949), which indicated that

the Redlich-Peterson equation was very similar to the Langmuir equation. Hence, the results further indicate that the biosorption of Cd(II) by the fungal biomass could be homogenous and could involve monolayer biosorption.

Fig. 5.8 shows the five non-linearized isotherm models and Table 5.2 summarizes the isotherm constants, correlation coefficients and error values of the five models. As listed in Table 5.2, the Sips model (r^2 = 0.9935, SE = 3.93) provided the best fit to the experimental data with the highest correlation coefficient and the lowest error value, followed by the Redlich-Peterson model (r^2 = 0.9923, SE = 4.25) and the Langmuir isotherm equation (r^2 = 0.9883, SE = 4.56), while the Freundlich model showed the highest error value (r^2 = 0.9699, SE = 7.28). In other words, the Sips, Redlich-Peterson and Langmuir models were capable of describing the relationship between the equilibrium uptake and the final concentration of Cd(II) ions in the residue aqueous solution. The simulation results further suggested that monolayer surface adsorption could be the main biosorption process under the examined conditions. The simulation results showed that the simulation of isotherm data by three parameters models (the Sips and Redlich-Peterson isotherms) were slightly better than those of the two parameters models (the Langmuir, Freundlich and Temkin isotherms).

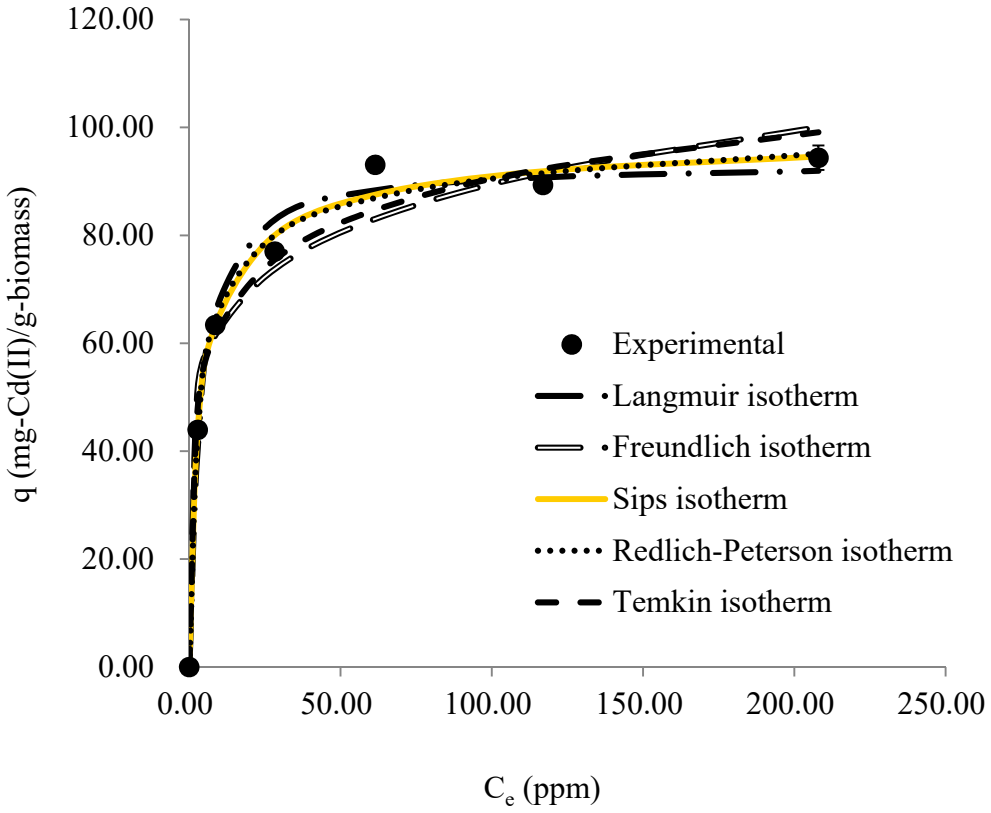

Figure 5.8 Non-linearized isotherm models for Cd(II) biosorption by *Mucor rouxii*.

Table 5.2 Comparison of parameters obtained from the non-linearized isotherm models for Cd(II) biosorption by *Mucor rouxii*.

Models		
Non-linearized Langmuir	q_{max} (mg/g)	93.59 ± 1.01
	b_L (L/mg)	0.2753 ± 0.01
	r^2	0.9883 ± 0.0028
	SSE	83.20
	RMSE	3.72
	SE	4.56
Non-linearized Freundlich	k_F (L/g)	44.27 ± 0.40
	n_F	6.543 ± 0.06
	r^2	0.9699 ± 0.0018
	SSE	211.85
	RMSE	5.94
	SE	7.28
Sips	q_{max} (mg/g)	100.7 ± 2.76
	n	1.435 ± 0.09
	b (L/mg)	0.3772 ± 0.02
	r^2	0.9935 ± 0.0011
	SSE	46.26
	RMSE	2.78
	SE	3.93
Redlich-Peterson	k_R (L/g)	35.06 ± 4.50
	α (L/mg)	0.4774 ± 0.08
	β	0.9490 ± 0.01
	r^2	0.9923 ± 0.0009
	SSE	54.14
	RMSE	3.00
	SE	4.25
Temkin	a_T (L/mg)	20.98 ± 0.23
	b_T (J/mol)	209.5 ± 2.76
	r^2	0.9824 ± 0.0011
	SSE	123.72
	RMSE	4.54
	SE	5.56

5.3.3 Dubinin Radushkevich (D-R) isotherm model

The D-R isotherm was applied to estimate the mean biosorption energy (E) of the Cd(II) binding by the fungal biomass (Aytas et al. 2011; Uluozlu et al. 2008). The mean biosorption energy is defined as the free energy when one mole of ions migrates from infinity in solution to the biomass surface, which yields information about the mechanism of biosorption (Gunay et al. 2007; Malkoc 2006). The D-R model is more general than the Langmuir isotherm since this model does not assume the homogeneous surface or constant adsorption potential (Aytas et al. 2011; Safa and Bhatti 2011). The D-R equation is given by the following equation:

$$q_e = q_D\, e^{-\beta\varepsilon^2} \qquad \text{(Equation 5.8)}$$

$$\varepsilon = R\,T \ln\left(1 + \frac{1}{C_e}\right) \qquad \text{(Equation 5.9)}$$

where q_D (mg/g) is the maximum biosorption capacity, β (mol^2/kJ^2) is the activity coefficient related to the mean biosorption energy, ε is the Polanyi potential, R (0.008314 kJ/mol-K) is the gas constant, T (K) is the temperature and C_e (mg/ L) is the equilibrium concentration of the metal ions in aqueous solution.

The linear form of the D-R isotherm equation is expressed as:

$$\ln q_e = \ln q_D - \beta\,\varepsilon^2 \qquad \text{(Equation 5.10)}$$

The parameters q_D and β were calculated from the intercept and slope of the plot of ln q_e versus ε^2, respectively, as shown in Fig. 5.9. The D-R isotherm parameters and error analyses are tabulated in Table 5.3. The predicted values of q_D and β were found to be 84.61 mg-Cd(II)/g-biomass and 1.16 mol^2/kJ^2, respectively.

The value of β could be used to calculate the mean biosorption energy (E). The value of E is calculated by the following equation:

$$E = \frac{1}{\sqrt{2\beta}} \qquad \text{(Equation 5.11)}$$

According to the literature (Aytas et al. 2011; Argun et al. 2007; Gunay et al. 2007; Malkoc 2006; Vijayaraghavan et al. 2006), if E<8 kJ/mol, physical adsorption is the dominant mechanism in the Cd(II) biosorption process, whereas if the magnitude of E is in the range of 8-16 kJ/mol, ion exchange or chemical adsorption is likely to be the dominant mechanism. The mean biosorption energy was estimated to be 0.6564 kJ/mol for the Cd(II) biosorption, indicating that physisorption was involved in cadmium removal. However, the correlation coefficient obtained from the D-R isotherm is a bit low (r^2 = 0.83), suggesting that the isotherm model might not be a very reliable model for describing the experimental data.

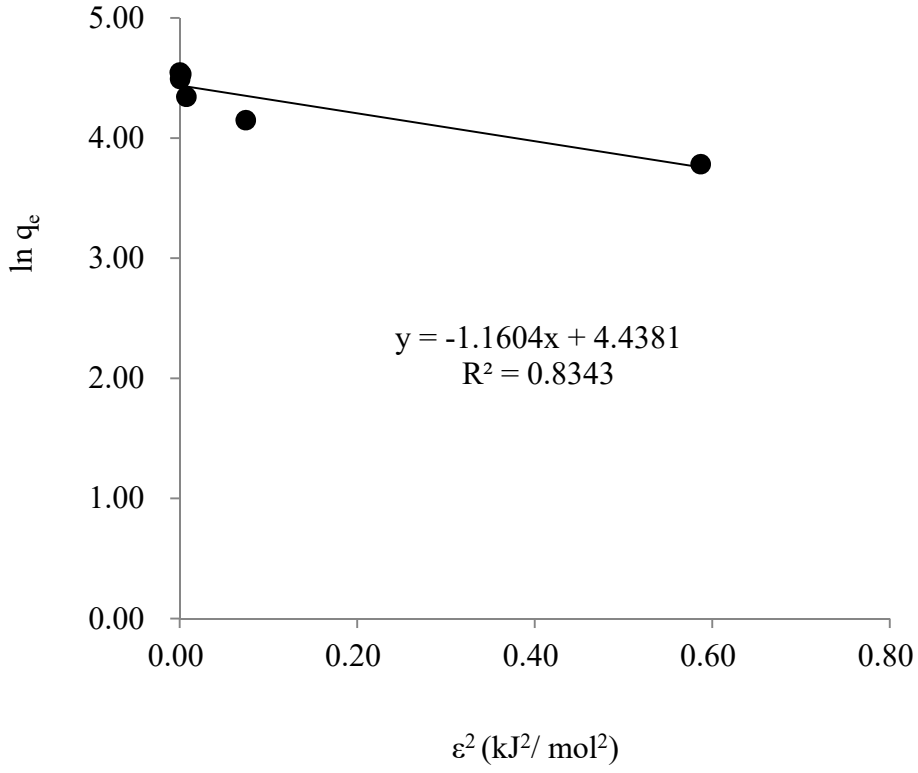

Figure 5.9 Linearized D-R isotherm plot for Cd(II) biosorption onto *Mucor rouxii*.

Table 5.3 D-R isotherm parameters and error analyses for Cd(II) biosorption by *Mucor rouxii*.

Model		
Dubinin-Radushkevich	q_D (mg/g)	84.61 ± 0.89
	β (mol^2/kJ^2)	1.1604 ± 0.13
	r^2	0.8343 ± 0.0075
	SSE	449.25
	RMSE	8.65
	SE	10.60

5.4 Adsorption kinetics

To obtain the kinetic profile of Cd(II) biosorption by *Mucor rouxii* in aqueous solution, the amount of Cd(II) sorbed onto the biomass surface was studied as a function of time. In the study, the biosorption capacities were evaluated at predetermined time intervals. Fig. 5.10 shows that the biosorption process could be divided into two phases. During the first 15 minutes, the biosorption towards Cd(II) ions was very rapid and approximately 62% of Cd(II) removal was attained within this period, indicating that the fungal biomass was an efficient biosorbent for Cd(II) biosorption. The adsorption rate in the second phase was slower and eventually reached the equilibrium after three hours.

In order to obtain more information from the kinetic profiles (e.g. the adsorption rate constant), four kinetic models were employed to describe the experimental data, namely the pseudo-first order, the pseudo-second order, the Elovich and the fractional power equation. Similar to the isotherm models, the non-linear regression analysis was interpreted by the computer software GraphPad Prism 3.0 and the applicability of the kinetic models was evaluated by the correlation coefficient (r^2) and error analyses (SSE, RMSE and SE).

5.4.1 Pseudo-first order equation

The pseudo-first order equation, also called the Lagergren model, is commonly used to describe experimental kinetic data. This model is formulated based on the assumption that the adsorption rate is proportional to the number of vacant sorption sites on the adsorbents (Safa and Bhatti 2011; Schiewer and Patil 2008). The pseudo-first order equation is written as:

$$\frac{dq_t}{dt} = k_1 (q_e - q_t) \quad \text{(Equation 5.12)}$$

where q_t (mg/g) is the amount of metal ions adsorbed at time t (min), k_1 (min^{-1}) is the rate constant of pseudo-first order equation and q_e (mg/g) is the amount of metal ions adsorbed per unit weight of the biomass at equilibrium.

By integrating Equation 5.12 and applying boundary conditions (i.e. t ranges from 0 to t and q ranges from 0 to q), the equation becomes:

$$q_t = q_e (1 - e^{-k_1 t}) \quad \text{(Equation 5.13)}$$

The linearized form of Equation 5.13 is formulated as:

$$\ln (q_e - q_t) = -k_1 t + \ln q_e \quad \text{(Equation 5.14)}$$

By plotting ln (q_e - q_t) against t, the parameters k_1 and q_e could be obtained from the slope and intercept of the linear plot, respectively (Fig. 5.11). The values of k_1 and q_e were found to be 20.78 mg-Cd(II)/g-biomass and 0.0227 min^{-1}, respectively (Table 5.4). The predicted q_e was much lower than the experimental q_e (71.41 mg-Cd(II)/g-biomass) and the correlation coefficient was low (r^2 =

0.8160), indicating that the kinetic data could not be described by the pseudo-first order model.

5.4.2 Pseudo-second order equation

The pseudo-second order equation is also widely applied to model experimental kinetic data. Unlike the pseudo-first order model, the pseudo-second order equation is constructed based on the assumption that the adsorption rate is proportional to the square of the vacant sorption sites (Liu 2008; Schiewer and Patil 2008). The pseudo-second order equation is formulated as:

$$\frac{dq_t}{dt} = k_2 (q_e - q_t)^2 \qquad \text{(Equation 5.15)}$$

where k_2 (g/mg-min)is the rate constant of pseudo-second order equation.

Integrating Equation 5.15 gives:

$$q_t = \frac{q_e^2 k_2 t}{1 + q_e k_2 t} \qquad \text{(Equation 5.16)}$$

The linearized form of Equation 5.16 is rearranged as:

$$\frac{t}{q_t} = \frac{1}{q_e} t + \frac{1}{k_2 q_e^2} \qquad \text{(Equation 5.17)}$$

The slope and intercept of the straight line were used to calculate the values of q_e and k_2, respectively (Fig. 5.12). The linearized pseudo-second order model provided high correlation for the experimental kinetic data, as reflected by the high correlation coefficient (r^2 = 0.9999) and the low error value (SE = 4.52), as shown in Table 5.4. The calculated q_e and k_2 were determined to be 71.94

mg-Cd(II)/g-biomass and 0.003450 g/mg-min, respectively. The q_e obtained from the linearized pseudo-second order equation was in agreement with the experimental q_e (71.41 mg-Cd(II)/g-biomass); therefore, it is very clear from the results that the kinetic data were well described by the pseudo-second order kinetic model.

In addition to the linearized pseudo-first and pseudo-second order kinetic models, the non-linear forms of the two models were also used to describe the kinetic data as demonstrated in Fig. 5.13. Comparisons of the kinetic parameters, correlation coefficients and error analyses for the pseudo-first and pseudo-second order models (linearized and non-linearized) are given in Table 5.4. As listed in the table, the experimental data were better explained by both of the linearized and non-linearized pseudo-second order models with high correlation coefficients and low error values when compared with those obtained from the pseudo-first order kinetic model. It is worth noting that the difference between the predicted q_e (20.78 mg/g) and the experimental q_e (71.41 mg/g) was the largest in the case of the linearized pseudo-first order model. This difference might be due to the fact that the q_e is calculated from the y-intercept of the plot of ln (q_e - q_t) versus t. The intercept is mainly influenced by the initial metal uptake, which is expected to be much lower than the experimental q_e (Schiewer and Patil 2008). Therefore,

the experimental data could not be well simulated by the linearized pseudo-first order model and the lowest correlation coefficient was resulted ($r^2 = 0.8160$). In this study, the non-linearized pseudo-second order exhibits the lowest error value (SE = 2.25) and the model q_e and k_2 were found to be 69.49 ± 0.78 mg-Cd(II)/g-biomass and 0.0064±0.0020 g/mg-min, respectively.

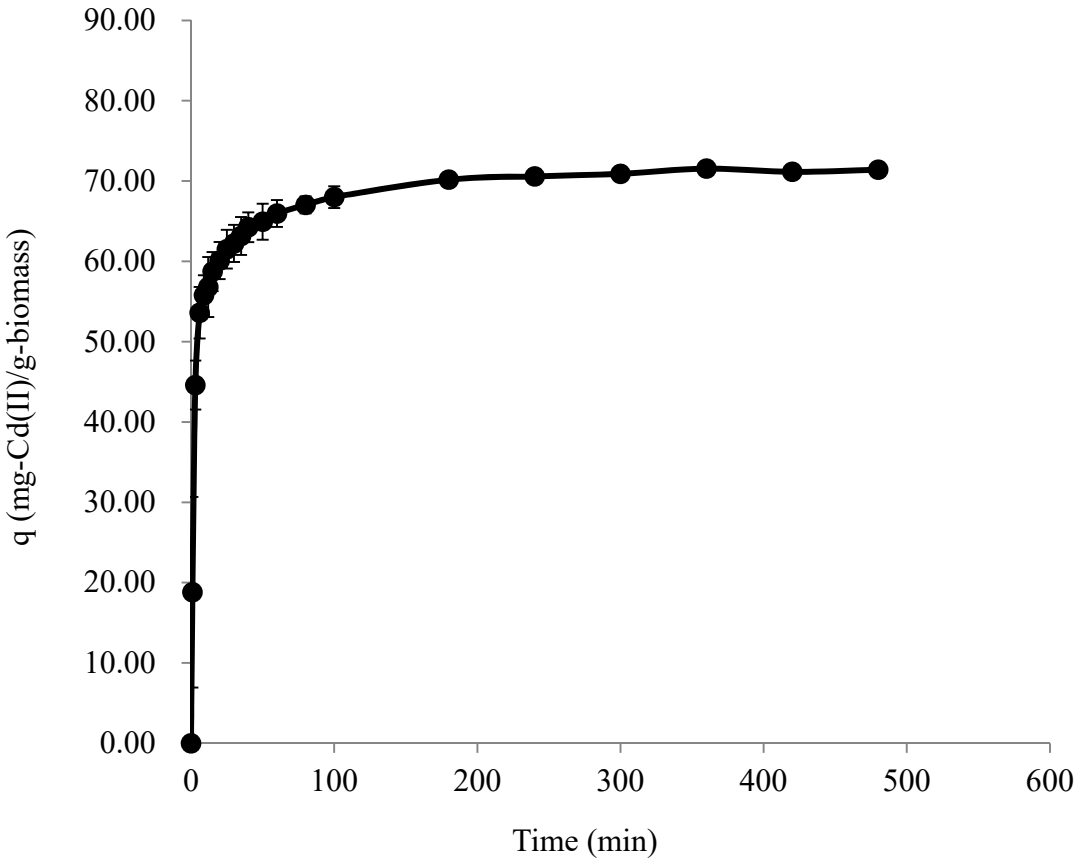

Figure 5.10 Kinetics on Cd(II) biosorption by *Mucor rouxii* (25℃).

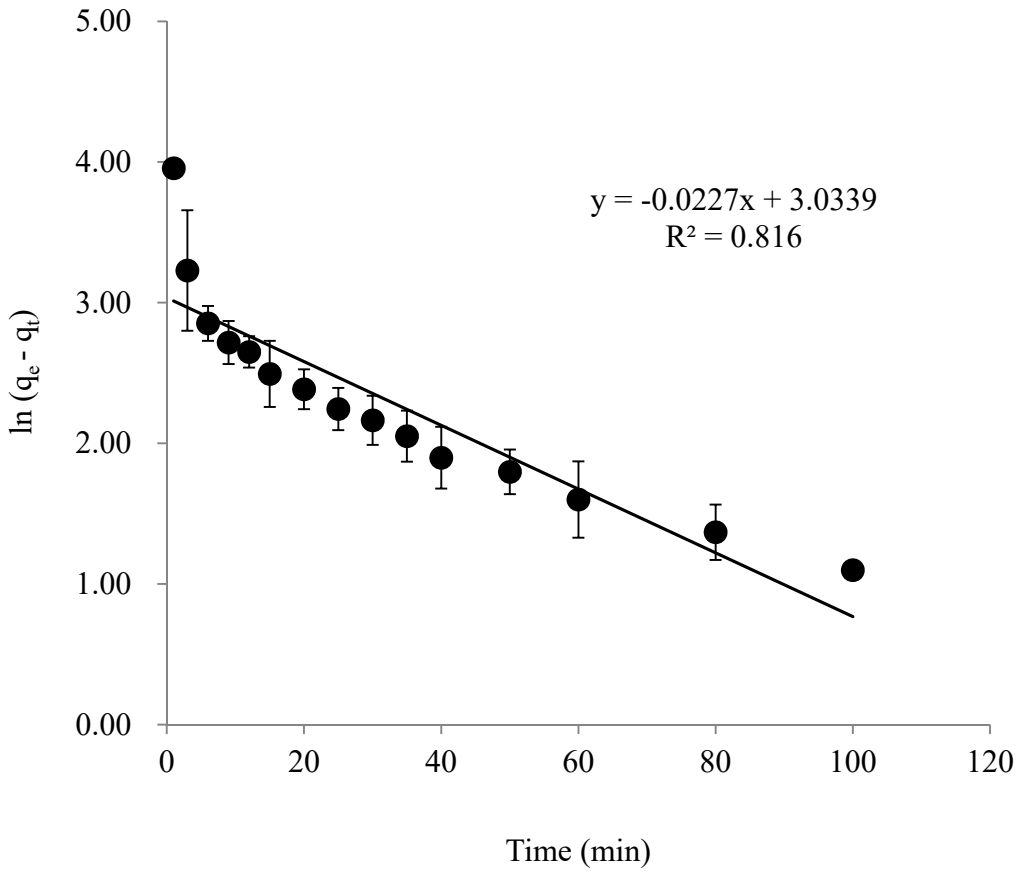

Figure 5.11 Linearized pseudo-first order plot of Cd(II) biosorption by *Mucor rouxii* (25℃).

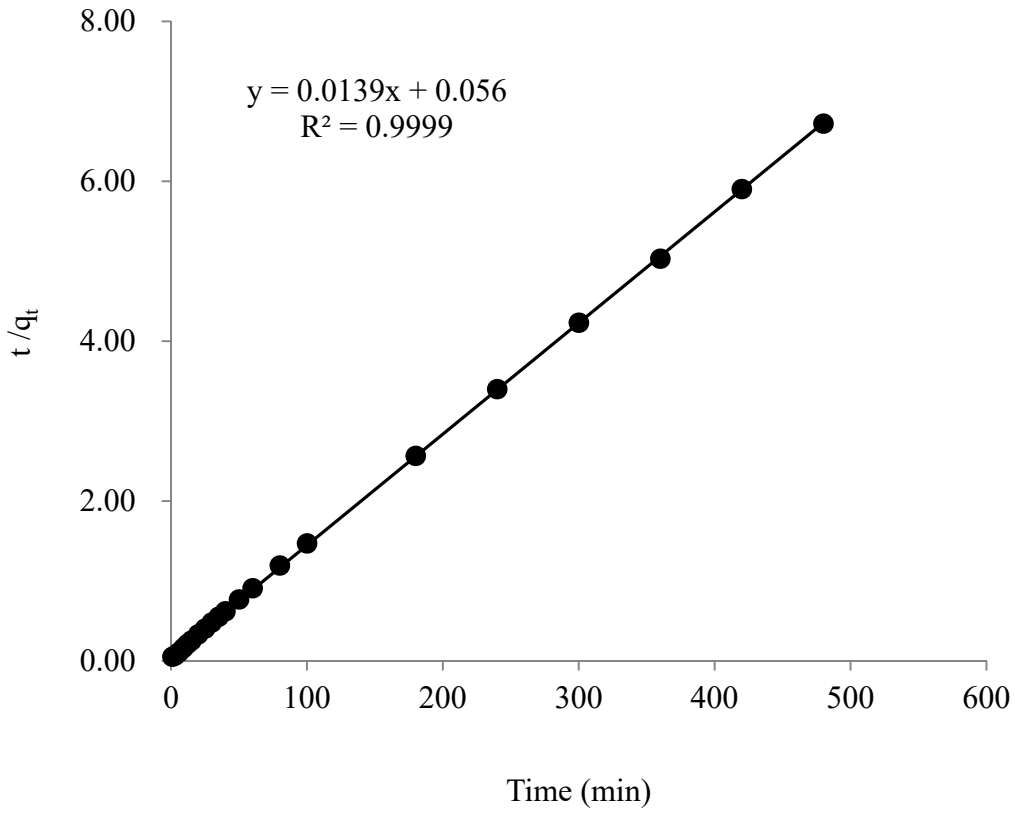

Figure 5.12 Linearized pseudo-second order plot of Cd(II) biosorption by *Mucor rouxii* (25℃).

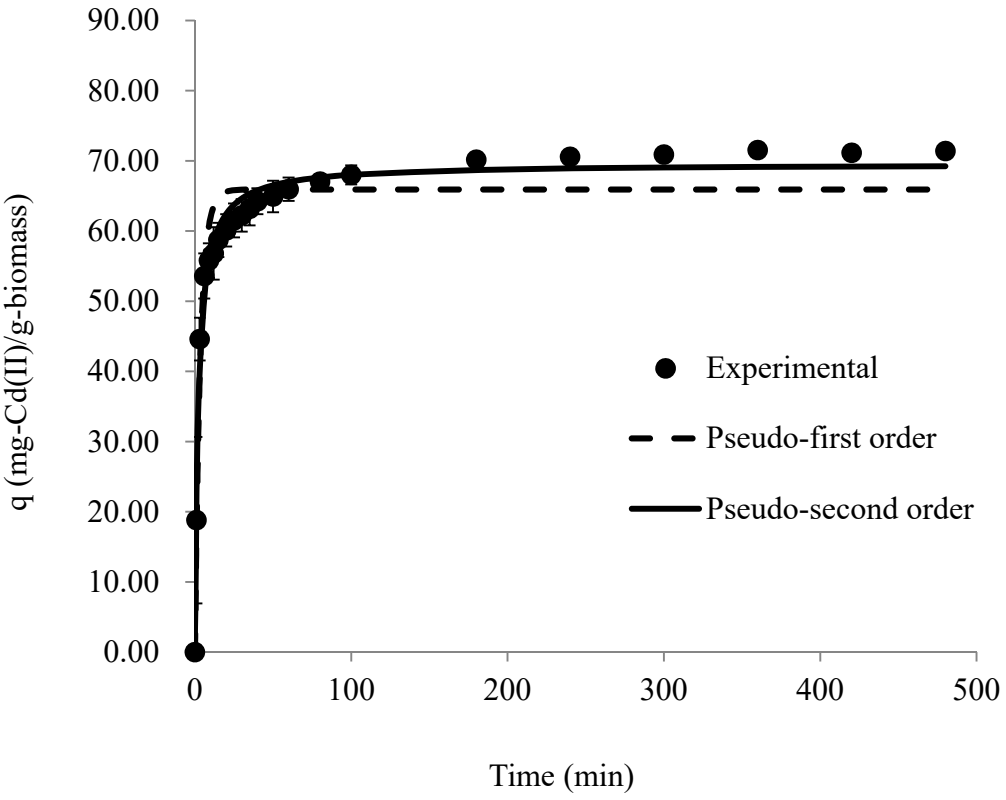

Figure 5.13 Non-linearized pseudo-first and pseudo-second order kinetic plots of Cd(II) biosorption by *Mucor rouxii* (25℃).

Table 5.4 Comparison of parameters obtained from the linearized and non-linearized pseudo-first and pseudo-second order models for Cd(II) biosorption by *Mucor rouxii* (25℃).

	Pseudo-first order					
	q_e (mg-Cd(II)/g-biomass)	k_1 (min^{-1})	r^2	SSE	RMSE	SE
Linearized	20.78 ± 3.81	0.0227 ± 0.0004	0.8160 ± 0.0347	51745.80	49.64	52.19
Non-linearized	65.85 ± 1.15	0.2969 ± 0.1080	0.9388 ± 0.0009	372.75	4.21	4.43
	Pseudo-second order					
	q_e (mg-Cd(II)/g-biomass)	k_2 (g/mg-min)	r^2	SSE	RMSE	SE
Linearized	71.94 ± 0.73	0.003450 ± 0.0008	0.9999 ± 0.000	387.89	4.30	4.52
Non-linearized	69.49 ± 0.78	0.006439 ± 0.0020	0.9850 ± 0.0101	96.29	2.14	2.25

5.4.3 Elovich equation

The Elovich equation was employed to describe the chemisorptions kinetics in which the adsorption rate decreased with increasing surface coverage (Gunay et al. 2007; Perez-Marin et al. 2007). This model is based on the assumption that the surface sites of adsorbent are heterogeneous and the sites show distinct activation energies during the chemisorption processes (Marin et al. 2009). The equation is expressed as:

$$\frac{dq_t}{dt} = \alpha\, e^{-\beta q_t} \qquad \text{(Equation 5.18)}$$

where α (mg/g-min) is the initial adsorption rate and β (g/mg) is related to the extent of surface coverage.

Given that $q_t = 0$ when $t = 0$, the integrated form of Equation 5.18 is written as:

$$q_t = \frac{1}{\beta} \ln\left(t + \frac{1}{\alpha\,\beta}\right) - \frac{1}{\beta} \ln\frac{1}{\alpha\,\beta} \qquad \text{(Equation 5.19)}$$

When t is much larger than 1/ (α β), Equation 5.19 is simplified to:

$$q_t = \frac{1}{\beta} \ln\,(\alpha\,\beta) + \frac{1}{\beta} \ln t \qquad \text{(Equation 5.20)}$$

The constants α and β were found to be 2276 mg/g-min and 0.16 g/mg, respectively. The correlation coefficients were not satisfactory (r^2 = 0.9132) when the experimental data were simulated by the Elovich equation, implying that

chemisorption might not be involved in the biosorption process in this study.

5.4.4 Fractional power equation

The fractional power equation is shown below:

$$q_t = k\, t^{\nu} \qquad \text{(Equation 5.21)}$$

where k (mg/g-$h^{-\nu}$) and ν are the constants of fractional power equation.

The values of k and ν were found to be 42.30 mg/g-h^{ν} and 0.097, respectively.

The four non-linearized kinetic models are displayed in Fig. 5.14, and the kinetic constants, correlation coefficients and error values of the four models are presented in Table 5.5. It is found that the biosorption of Cd(II) onto the fungal biomass correlated well with the pseudo-second order model (r^2 = 0.9850, SE = 2.25) as compared with the pseudo-first order (r^2 = 0.9388, SE = 4.43), Elovich (r^2 = 0.9132, SE = 5.45) and Fractional power model (r^2 = 0.8815, SE = 6.37). It is very clear from the table that only the pseudo-second order model exhibits an adequate description for the experimental kinetic data. According to Schiewer and Patil (2008), the adsorption of a divalent metal cation onto a deprotonated biomass surface can be expressed by the following equation:

$$2B^- + M^{2+} \leftrightarrows B_2M \qquad \text{(Equation 5.22)}$$

where B^- represents the biomass surface that carries negative charge and M^{2+}

represents the divalent metal cation. The metal ion adsorption rate based on Equation 5.22 is written as:

Adsorption rate = $k [M] [B]^2$ (Equation 5.23)

where k is the kinetic constant.

The $[B]^2$ (Equation 5.23) is similar to the term $(q_e-q_t)^2$ (Equation 5.15) in the pseudo-second order equation. In our Cd(II) biosorption kinetics, the high correlation between the experimental data and the pseudo-second order model might imply that one Cd(II) ion was bound to two monovalent surface active sites on the fungal biomass (e.g. carboxyl group). Nevertheless, the pseudo-second order equation does not consider the effect of metal concentration on the reaction rate.

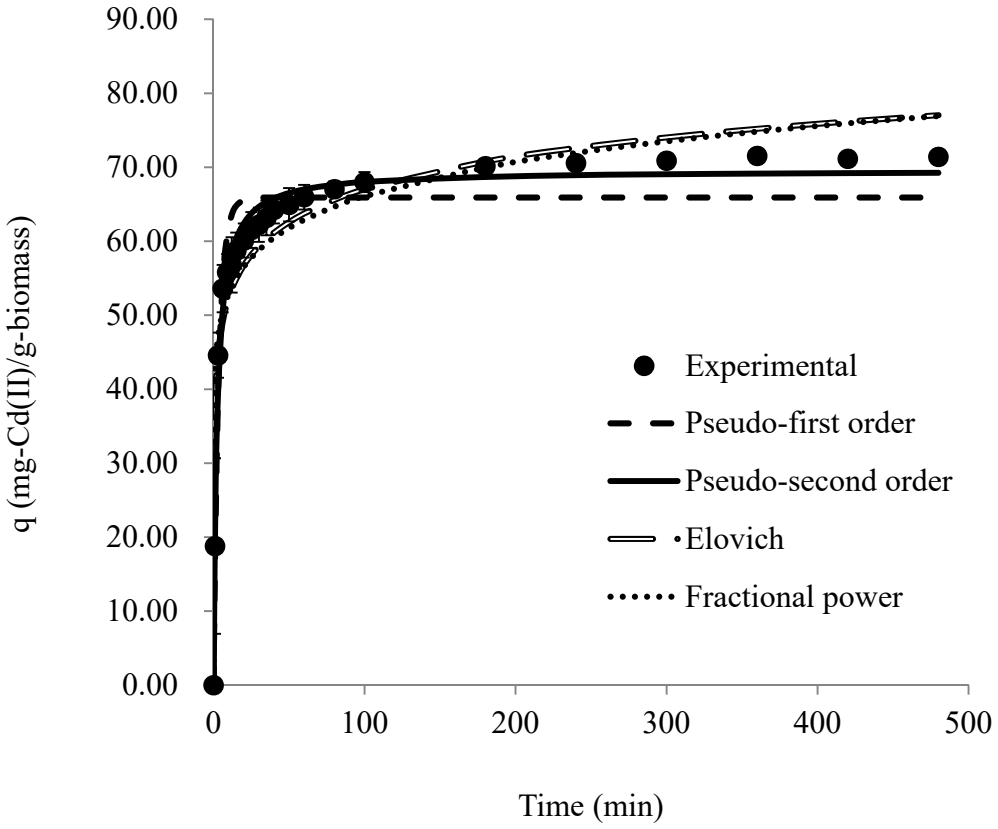

Figure 5.14 Non-linearized kinetic models for Cd(II) biosorption by *Mucor rouxii* (25℃).

Table 5.5 Comparison of parameters obtained from the non-linearized kinetic models for Cd(II) biosorption by *Mucor rouxii* (25℃).

Models		
Non-linearized Pseudo-first order	q_e (mg/g)	65.85 ± 1.15
	k_1 (min^{-1})	0.2969 ± 0.1080
	r^2	0.9388 ± 0.0009
	SSE	372.75
	RMSE	4.21
	SE	4.43
Non-linearized Pseudo-second order	q_e (mg/g)	69.49 ± 0.78
	k_2 (g/mg-min)	0.006439 ± 0.0020
	r^2	0.9850 ± 0.0101
	SSE	96.29
	RMSE	2.14
	SE	2.25
Elovich	α (mg/g-min)	2276 ± 4122.36
	β (g/mg)	0.1564 ± 0.0190
	r^2	0.9132 ± 0.0242
	SSE	563.97
	RMSE	5.18
	SE	5.45
Fractional power	k (mg/g-h^{-v})	42.30 ± 4.17
	v	0.09691 ± 0.0153
	r^2	0.8815 ± 0.0165
	SSE	769.86
	RMSE	6.05
	SE	6.37

5.5 Effect of temperature

Changes in temperature may affect the kinetics of the Cd(II) biosorption process. Fig. 5.15 shows the effect of temperature on Cd(II) biosorption at temperatures 25, 40 and 60℃, and indicates that the biosorption capacity increased with increasing temperature. The biosorption capacity of the fungal biomass increased by 11.07 and 57.74% as the temperature increased from 25℃ to 40 and to 60℃, respectively. This trend might be attributed to the increase in the chance of collision between the sorbent and sorbate, or due to the decrease in the thickness of the boundary layer around the fungal biomass (Malkoc 2006). The results implied that the biosorption was an endothermic process. The experimental data obtained at 40 and 60 ℃ were simulated by different kinetic models and the results are compiled in Table 5.6, which show that the experimental data matched well with the non-linearized pseudo-second order model and the kinetic constant (k_2) increased with increasing temperature. The predicted q_e, obtained from the non-linearized pseudo-second order model, was calculated to be 80.00 and 112.30 mg-Cd(II)/g-biomass at 40 and 60 ℃, respectively. These predictions were very close to the experimental q_e (79.08 mg/g at 40℃ and 112.31 mg/g at 60 ℃).

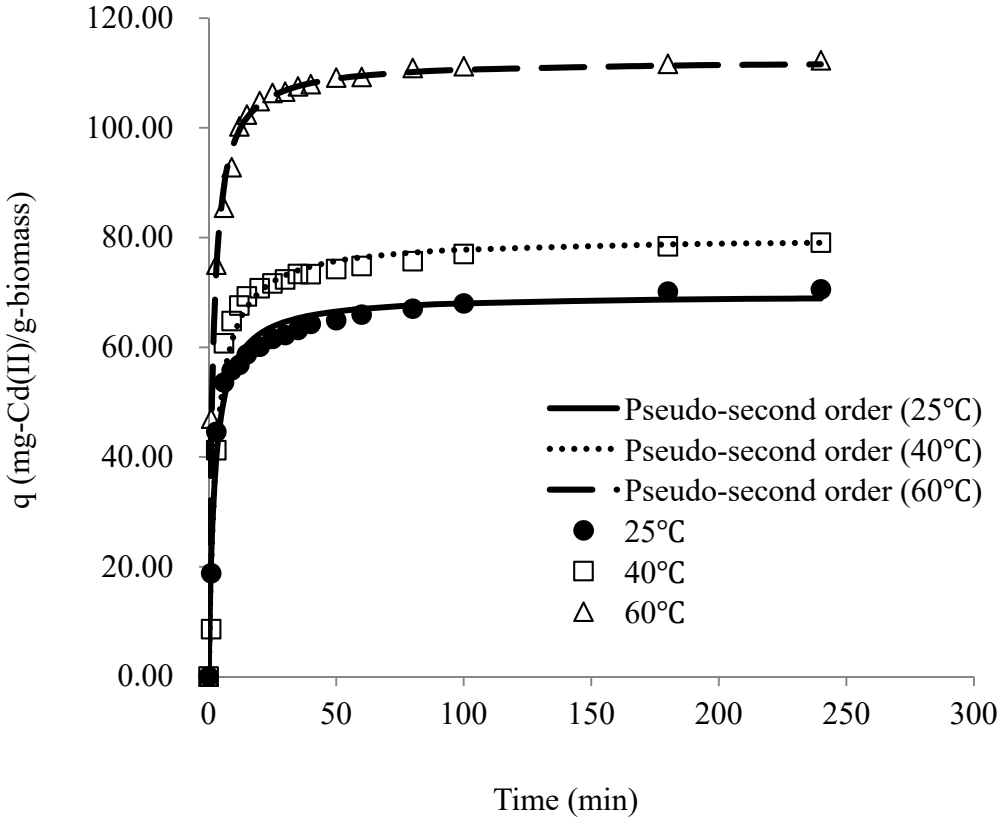

Figure 5.15 Effect of temperature on Cd(II) biosorption by *Mucor rouxii*.

Table 5.6 Comparison of parameters obtained from the linearized and non-linearized kinetic models for Cd(II) biosorption by *Mucor rouxii* (25, 40 and 60℃).

Models		Non- linearized			Linearized		
		25 ℃	40 ℃	60 ℃	25 ℃	40 ℃	60 ℃
Pseudo-first order	q_e (mg/g)	65.85	74.42	106.70	20.78	17.96	17.32
	k_1 (min^{-1})	0.2969	0.2390	0.3888	0.0227	0.0209	0.0240
	r^2	0.9388	0.9819	0.9608	0.8160	0.7931	0.7635
	SSE	372.75	163.75	552.46	51745.80	60336.22	144079.37
	RMSE	4.21	3.10	5.70	49.64	59.58	92.06
	SE	4.43	3.30	6.07	52.19	63.42	98.01
Pseudo-second order	q_e (mg/g)	69.49	80.00	112.30	71.94	80.00	112.36
	k_2 (g/mg-min)	0.006439	0.004439	0.005796	0.003450	0.003676	0.005316
	r^2	0.9850	0.9845	0.9974	0.9999	0.9995	1.000
	SSE	96.29	229.86	36.42	387.89	298.97	51.98
	RMSE	2.14	3.68	1.46	4.30	4.19	1.75
	SE	2.25	3.91	1.56	4.52	4.46	1.86

Elovich	α (mg/g-min)	2276	239.30	4846
	β (g/mg)	0.1564	0.09529	0.09334
	r^2	0.9132	0.8639	0.9376
	SSE	563.97	1228.04	879.60
	RMSE	5.18	8.50	7.19
	SE	5.45	9.05	7.66
Fractional power	k (mg/g-h^{ν})	42.30	41.91	71.85
	ν	0.09691	0.1393	0.1001
	r^2	0.8815	0.8059	0.9134
	SSE	769.86	1751.44	1220.26
	RMSE	6.05	10.15	8.47
	SE	6.37	10.81	9.02

5.6 Biosorption thermodynamics

Thermodynamic parameters, including the change in free entropy (ΔS°), enthalpy (ΔH°) and energy (ΔG°), can provide a degree of information about the adsorption mechanism. Therefore, in this section, these parameters were evaluated to determine the sorption characteristics of Cd(II) by the fungal biomass. The values of ΔS° and ΔH° can be calculated from Equation 5.24 (Ozcan et al. 2006).

$$\ln K_d = \frac{\Delta S^\circ}{R} - \frac{\Delta H^\circ}{R T} \qquad \text{(Equation 5.24)}$$

where K_d (ml/g) = q_e/C_e, R (8.314 J/mol-K) is the universal gas constant and T (K) is the absolute temperature. By plotting ln K_d against 1/T (Fig. 5.16), the values of ΔS° and ΔH° were determined from the intercept and slope of the plot, respectively. The change in free energy (ΔG°) is given as follows:

$$\Delta G^\circ = \Delta H^\circ - T \Delta S^\circ \qquad \text{(Equation 5.25)}$$

The Arrhenius relationship was used for the evaluation of activation energy of adsorption (E_a), which represents the minimum energy required for the reaction to occur. Based on the rate constants (k_2) determined in Section 5.5, E_a can be calculated by the following equation (Ozcan et al. 2006):

$$\ln k_2 = \ln A - \frac{E_a}{R T} \qquad \text{(Equation 5.26)}$$

where k_2 (g/mg-min) is the kinetic constant of the pseudo-second order model and A is the Arrhenius factor. When plotting ln k_2 versus 1/T, the value of E_a is obtained from the slope of the plot (Fig. 5.17).

The thermodynamic parameters of Cd(II) biosorption are summarized in Table 5.7. The negative values of ΔG° revealed that the biosorption process for Cd(II) was thermodynamically feasible and spontaneous. Moreover, the values of ΔG° decreased with increasing temperature, indicating that biosorption was more favorable at higher temperature. The positive value of ΔH° indicated that the Cd(II) sorption process was of an endothermic nature. In aqueous solutions, some water molecules were attached to the biomass surface, which should be first detached from the surface before the Cd(II) ions could be bound onto the biomass. Therefore, some energy was required for the displacement of water molecules before biosorption, leading to the absorption of heat from the surrounding. The positive value of ΔS° suggested that there was an increase in the randomness at the solid/solution interface during biosorption (Sari and Tuzen 2008). This is because the displaced water molecules gained more translational entropy than was lost by the Cd(II) ions (Anirudhan and Radhakrishnan, 2008). The range of 0.96-9.65 kJ/mol of activation energies represents a physisorption process, whereas 96.49-964.85 kJ/mol of activation energies suggests a chemisorption

mechanism (Oura et al. 2003). The value of E_a was calculated to be 10.38 kJ/ mol, revealing that Cd(II) biosorption by *Mucor rouxii* was mainly through physisorption.

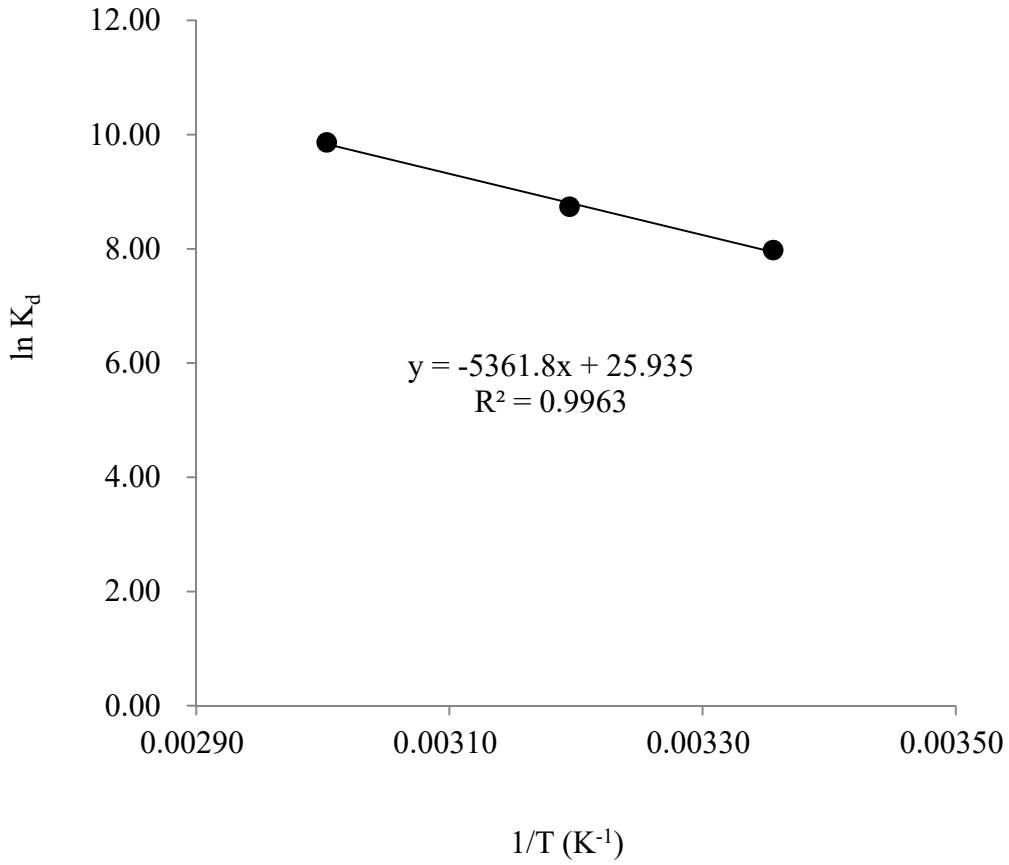

Figure 5.16 Plot of ln K_d vs. 1/T for the biosorption of Cd(II) by *Mucor rouxii*.

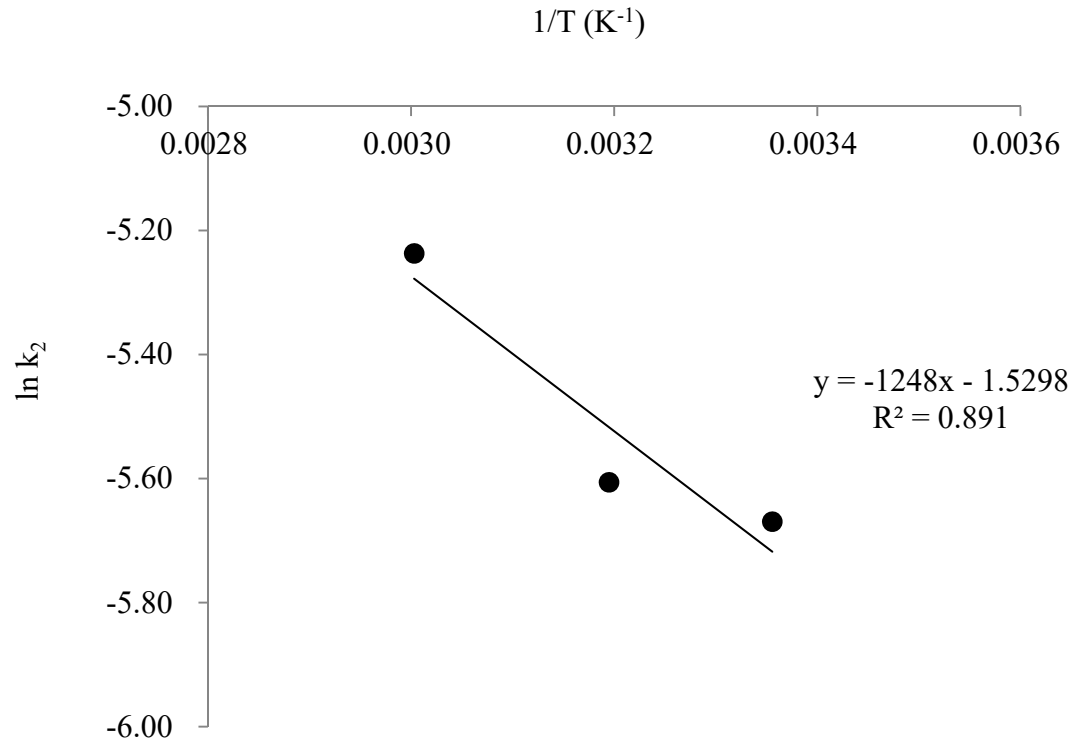

Figure 5.17 Plot of ln k_2 vs. 1/T for the biosorption of Cd(II) by *Mucor rouxii*.

Table 5.7 Thermodynamic parameters of Cd(II) biosorption by *Mucor rouxii*.

T (℃)	k_2 (g/mg-min)	K_d (ml/g)	E_a (kJ/mol)	ΔG° (kJ/mol)	ΔH° (kJ/mol)	ΔS° (kJ/mol-K)
25	0.003450	2917.75		-19.67		
40	0.003676	6231.68	10.38	-22.90	44.58	0.22
60	0.005316	19221.29		-27.22		

5.7 Intraparticle diffusion

The adsorption of metal ions onto the biomass surface is controlled by either external mass transfer or intraparticle diffusion, or by both. The adsorption process mainly consists of three steps: (1) mass transfer of metal ions from bulk solution to the surface of the biomass particle; (2) pore diffusion of metal ions to the adsorption sites; (3) adsorption of metal ions onto the active sites. Among the three steps, the third step should be the fastest. Therefore, the adsorption of metal ions onto the biomass surface is controlled by either boundary layer diffusion (step 1) or intraparticle diffusion (step 2), or by both steps (Hameed and EI-Khaiary 2008; Cheung et al. 2007). If the adsorption process is carried out under the conditions of poor mixing, dilute adsorbate concentration and small size adsorbent, external mass transfer may be the rate determining step in the adsorption process. On the other hand, if the adsorption process is carried out under the conditions of well mixing, high adsorbate concentration and large size adsorbent, intraparticle diffusion may be the rate limiting step in the adsorption process (Hameed and EI-Khaiary 2008).

Weber-Morris established the intraparticle diffusion equation in which the sorbate uptake is directly proportional to the square root of t. The intraparticle

diffusion is formulated as (Hameed and EI-Khaiary 2008):

$$q_t = k_{diff}\, t^{1/2} + c \qquad \text{(Equation 5.27)}$$

where k_{diff} (mg/g-min$^{1/2}$) is the intraparticle diffusion rate constant and c is the intercept.

Fig. 5.18 illustrates the intraparticle diffusion plots of Cd(II) biosorption at different temperatures. If the intraparticle diffusion was the only rate-limiting step, the plot should pass through the origin; if not, the external mass transfer controlled the biosorption to some extent. Three linear regions were observed in Fig. 5.18. It could be deduced that there were three processes that controlled the Cd(II) biosorption rate but only one was rate determining in any particular time range (Cheung et al. 2007). The first region represented the stage that the biosorption rate was controlled by the diffusion of the sorbate from the bulk solution to the external surface of the sorbent. The second region corresponded to the stage that the biosorption rate was limited by the intraparticle diffusion, while the third region represented the attainment of the equilibrium. The rate constants were obtained from the slopes of the three linear regions, which represent the Cd(II) adsorption rates and they are tabulated in Table 5.8. From the table, it could be observed that the values of k_{diff1} are the largest followed by k_{diff2} and k_{diff3}, indicating that the diffusion of metal ions from the bulk solution to

the biomass surface was rapid. The rate constants increased with increasing temperature, revealing that a higher temperature facilitated the removal of Cd(II) by the fungal biomass.

The fractional uptake of adsorbate molecule, F, at time t is expressed as:

$$F = \frac{q_t}{q_e} = \frac{C_0 - C_t}{C_0 - C_\infty} \quad \text{(Equation 5.28)}$$

According to Do (1998), F at short time (when t is relatively small) can be expressed as:

$$F = \frac{4}{\pi^{1/2}} \frac{{D_{app}}^{1/2}}{R} t^{1/2} \quad \text{(Equation 5.29)}$$

where R is the half length of diffusion path, and D_{app} is the apparent intraparticle diffusion coefficient.

According to Choy et al. (2004), if the linear plot of F versus $t^{1/2}$ passes through the origin, intraparticle diffusion may be the predominant rate-determining step of the adsorption process. If the plot illustrates considerable deviation from the origin, external mass transfer may also control the adsorption process to some degree. As shown in Fig. 5.19, the plot did not pass through the origin, suggesting that besides intraparticle diffusion external mass transfer might control the adsorption process to some degree. The apparent intraparticle diffusion coefficient (D_{app}) of Cd(II) in the biomass could be calculated from the slope of the linear plot. The values of the D_{app} increased

from 1.26×10^{-15} to 1.50×10^{-14} m^2/s when the temperature increased from 25 to 60℃ (Table 5.9). The results implied that temperature may have a considerable effect in intraparticle diffusion. The molecular diffusion coefficient of Cd(II) ions is 7.19×10^{-10} m^2/s (Yang and Volesky 1999). The apparent intraparticle diffusion coefficient of Cd(II) is much smaller than the molecular diffusion coefficient of Cd(II) in aqueous solution.

The value of D_{app} can also be used for determining the activation energy for diffusion. The Arrhenius equation is expressed as (EI-Naggar et al. 2008):

$$\ln D_{app} = \ln D_o - \frac{E_a}{RT} \quad \text{(Equation 5.30)}$$

where D_o (m^2/s) is the pre-exponential constant analogous to Arrhenius frequency factor and E_a (kJ/mol) is the activation energy for diffusion. By plotting the ln D_{app} versus 1/T, the value of E_a could be obtained from the slope of the plot. The Arrhenius plot is illustrated in Fig. 5.20 and the value of activation energy for diffusion was 17277 kJ/mol (Table 5.10).

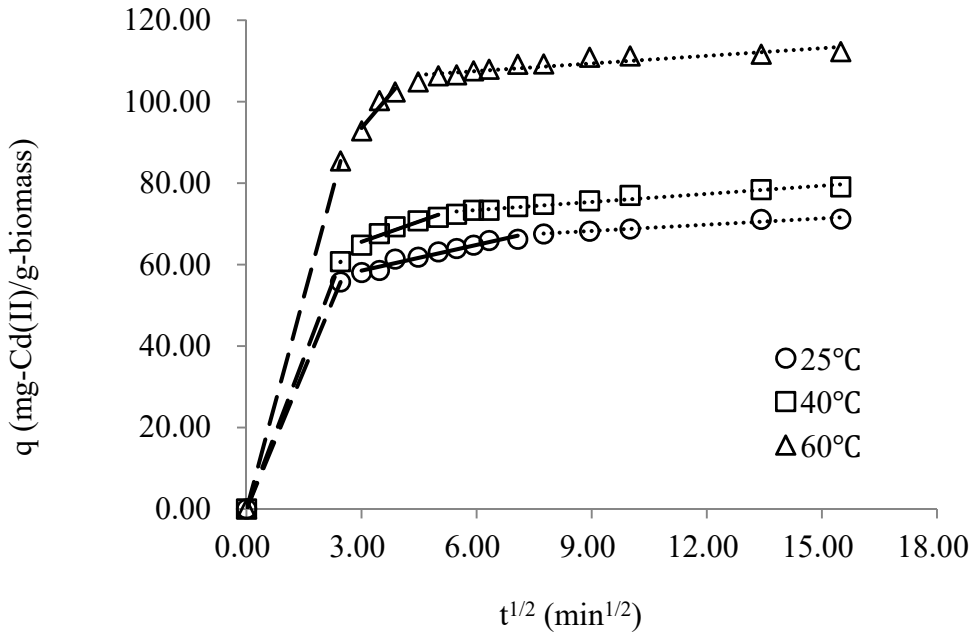

Figure 5.18 Intraparticle diffusion model for Cd(II) biosorption by *Mucor rouxii* at different temperatures.

Table 5.8 Parameters obtained from the intraparticle diffusion model for Cd(II) biosorption by *Mucor rouxii* at different temperatures.

	Temperature (℃)		
	25	40	60
k_{p1} (mg/g-min$^{1/2}$)	22.76	24.80	34.89
r^2	1.000	1.000	1.000
k_{p2} (mg/g-min$^{1/2}$)	2.11	3.32	11.09
r^2	0.9531	0.9340	0.9282
k_{p3} (mg/g-min$^{1/2}$)	0.51	0.66	0.63
r^2	0.9556	0.9537	0.8261

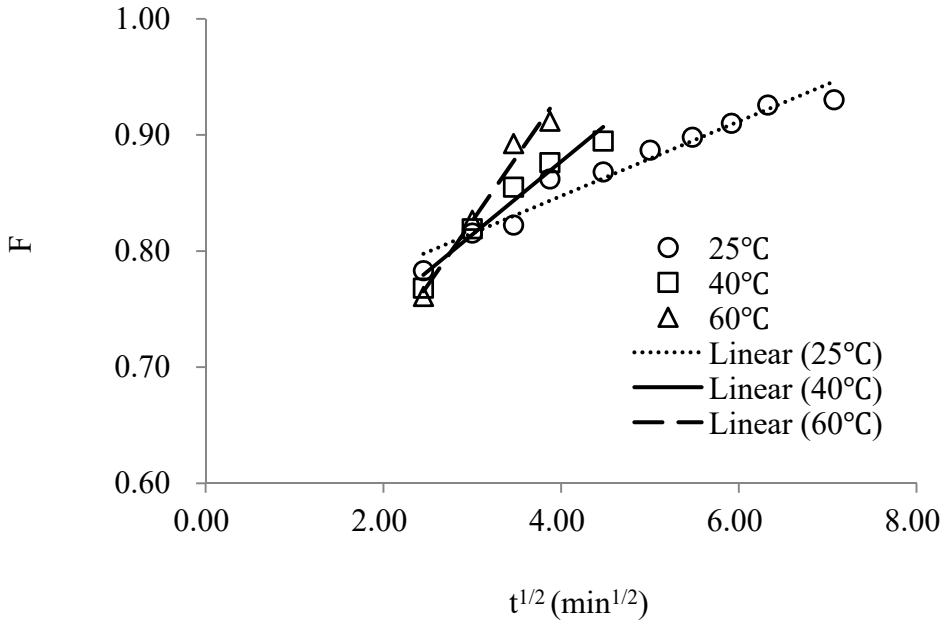

Figure 5.19 The F vs $t^{1/2}$ plot of Cd(II) biosorption by *Mucor rouxii* at different temperatures.

Table 5.9 Intraparticle diffusion coefficients of Cd(II) biosorption by *Mucor rouxii* at different temperatures.

Temperature	D_{app} (m^2/s)	r^2
25℃	1.26×10^{-15}	0.9660
40℃	4.86×10^{-15}	0.9520
60℃	1.50×10^{-14}	0.9740

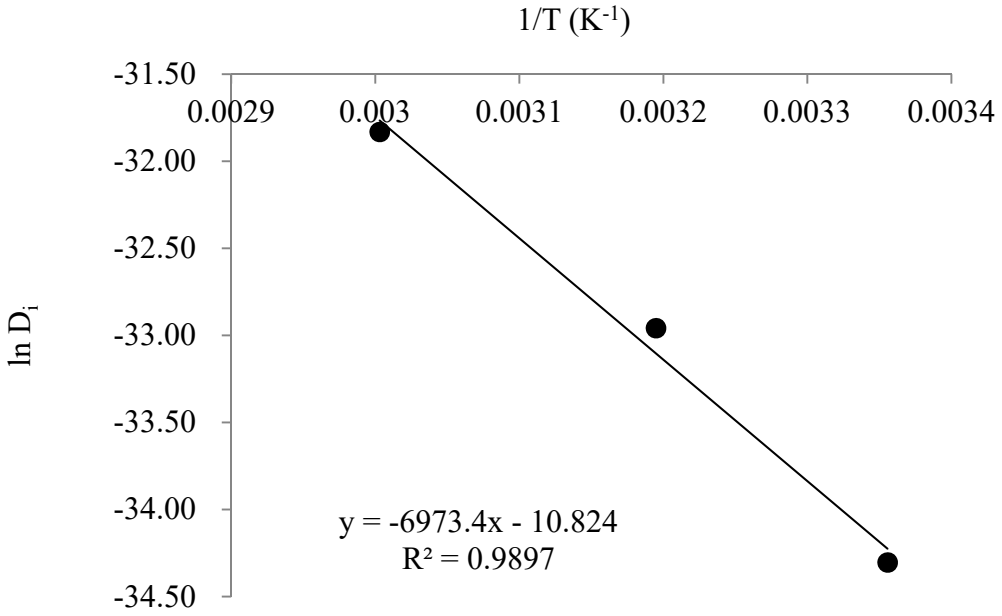

Figure 5.20 Arrhenius plot for the diffusion coefficients of Cd(II) in *Mucor rouxii*.

Table 5.10 Arrhenius parameters for the diffusion of Cd(II) in *Mucor rouxii*.

Temperature	D_{app} (m^2/s)	D_0 (m^2/s)	Ea (kJ/mol)	r^2
25℃	1.26×10^{-15}			
40℃	4.86×10^{-15}	1.99×10^{-5}	17277	0.9897
60℃	1.50×10^{-14}			

5.8 Effect of agitation speed

Changes in agitation speed may affect the kinetics of Cd(II) adsorption process. Fig. 5.21 shows the effect of agitation speed (50-500 rpm) on Cd(II) biosorption. The maximum biosorption (83.22 mg-Cd(II)/g-biomass) was attained at 150 rpm. At low agitation speeds (50-150 rpm), the biosorption capacity increased with increasing speed. This result indicated that higher agitation speeds could enhance the transport of Cd(II) ions from the aqueous solution to the biomass surface since the thickness of the external mass transfer boundary layer around the biomass particles was reduced. However, the biosorption capacity decreased at 200 and 500 rpm, which might be caused by an improper contact between Cd(II) ions in solution and the biomass at vigorous agitation speeds. The observation in this study was similar to the findings reported by other researchers. They found that the maximum biosorption capacities were attained at moderate agitation speed (Shroff and Vaidya 2011; Benguella and Benaissa 2002). The intraparticle diffusion plot is shown in Fig. 5.22 and the parameters are summarized in Table 5.11. If the intraparticle diffusion was the only rate-determining step, the plot should pass through the origin; if not, the external mass transfer controlled the biosorption to some degree.

The intraparticle diffusion plots were not linear over the whole contact time. Multilinear regions were observed in Fig. 5.22. The steepest region corresponded to the stage that the biosorption rate was limited by the boundary layer diffusion of Cd(II) ions. The second region represented that the kinetics was controlled by the intraparticle diffusion of the metal ions, while the third region indicated that the biosorption was close to attain equilibrium. The three linear regions suggested that there were three processes controlling the Cd(II) biosorption rate but only one was rate determining in any particular contact time range (Cheung et al. 2007). The values of k_{diff1}, k_{diff2} and k_{diff3} at agitation speed of 150 rpm were found to be large, indicating that the optimum agitation speed for the biosorption of Cd(II) onto the fungal biomass was 150 rpm.

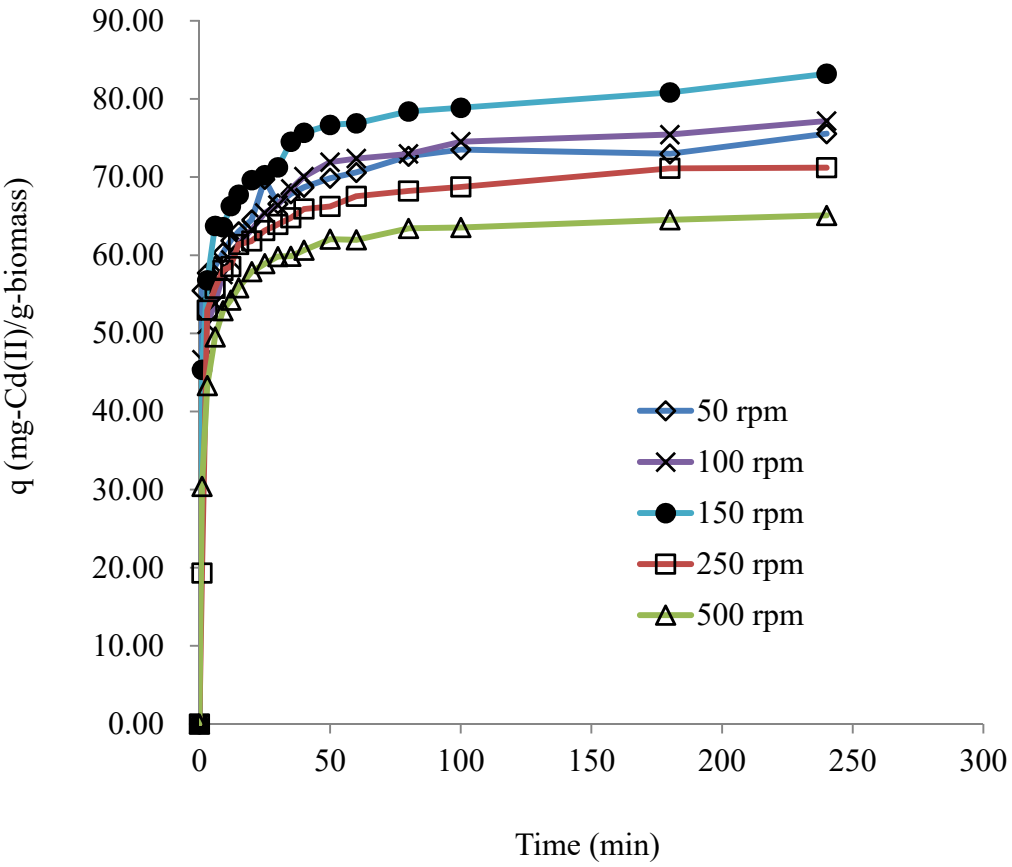

Figure 5.21 Effect of agitation speed on Cd(II) biosorption by *Mucor rouxii*.

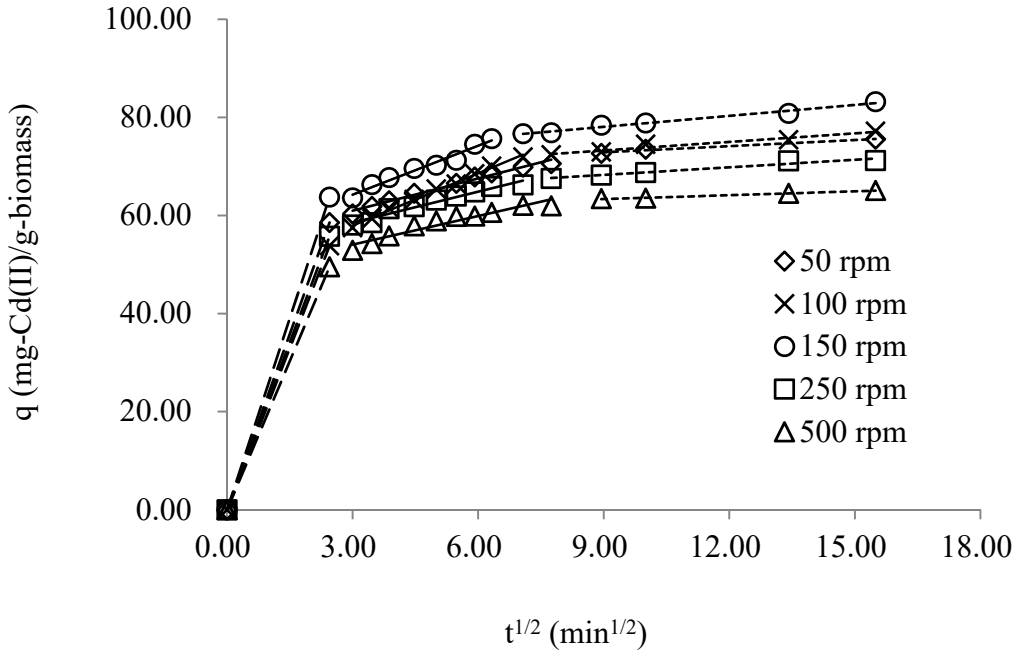

Figure 5.22 Intraparticle diffusion model for Cd(II) biosorption by *Mucor rouxii* at different agitation speeds.

Table 5.11 Parameters obtained from the intraparticle diffusion model for Cd(II) biosorption by *Mucor rouxii* at different agitation speeds.

	Agitation speed (rpm)				
	50	100	150	250	500
k_{p1} (mg/g-min$^{1/2}$)	23.91	21.98	26.02	22.76	20.22
r^2	1.000	1.000	1.000	1.000	1.000
k_{p2} (mg/g-min$^{1/2}$)	2.19	3.55	3.33	2.11	1.95
r^2	0.9846	0.9945	0.9680	0.9531	0.9283
k_{p3} (mg/g-min$^{1/2}$)	0.42	0.58	0.74	0.51	0.26
r^2	0.9819	0.9511	0.9812	0.9556	0.9935

5.9 SEM images and EDAX spectra

The changes in surface morphology and the elemental analyses of the Cd-loaded fungal biomass were examined by the technique of SCM coupled with EDAX. The SEM images of Cd-loaded biomass (Figs. 5.23d-f) were different from those of the pristine biomass (Figs. 5.23a-c). After biosorption, some fine granules were observed on the biomass surface. The surface of the Cd-loaded biomass appeared to be much rougher than that of the pristine biomass, revealing that Cd(II) ions were bound onto the surface of the fungus. The surface of the Cd-loaded biomass was corrugated and became more irregular and uneven, possibly due to the interaction between the Cd(II) ions and the functional groups of the cell wall. Compared with the EDAX spectrum of pristine biomass (Fig. 4.20), additional peaks of Cd were observed after biosorption (Fig. 5.24), indicating the presence of Cd(II) ions on the biomass surface.

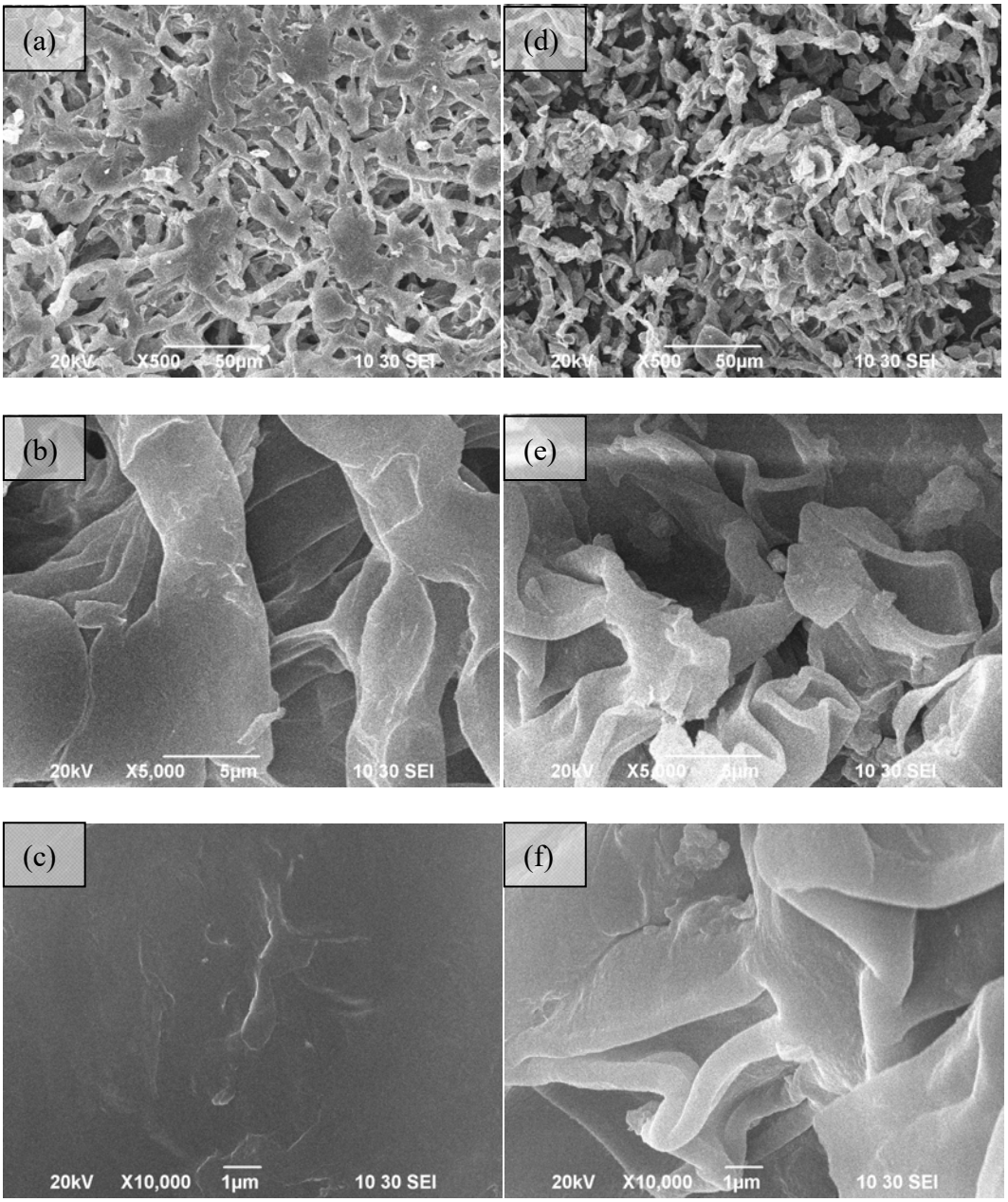

Figure 5.23 SEM images of (a) pristine (500X), (b) pristine (5000X), (c) pristine (10000X), (d) Cd-loaded biomass (500X), (e) Cd-loaded biomass (5000X) and (f) Cd-loaded biomass (10000X).

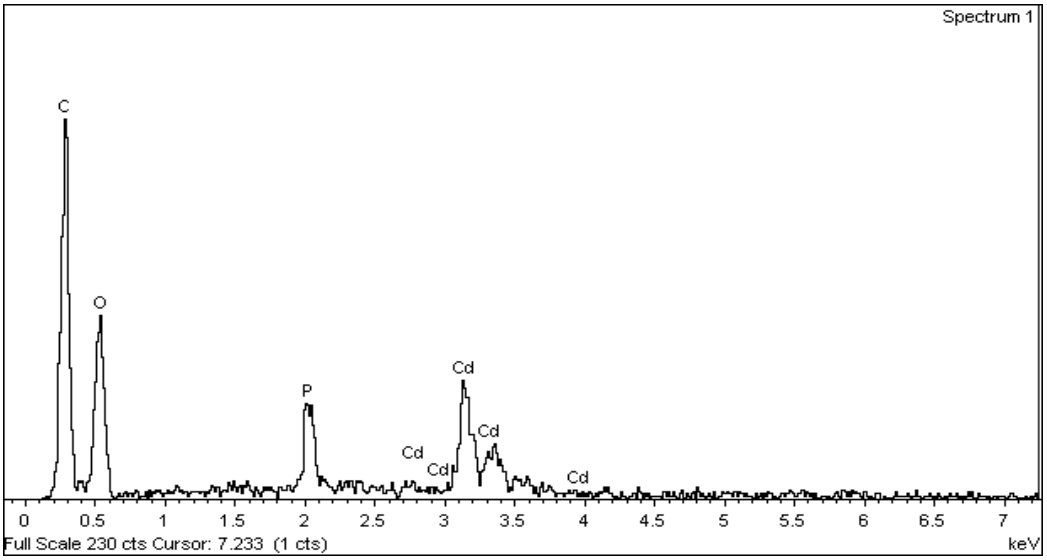

Figure 5.24 EDAX spectrum of Cd-loaded biomass.

5.10 FTIR analysis

The FTIR spectrum of Cd-loaded biomass was compared with that of the pristine biomass, and the changes in wavenumbers of the surface functional groups of the biomass might be useful for explaining the binding mechanism. After biosorption, several significant changes were observed in the FTIR spectrum of the biomass (Fig. 5.25). Two new bands were formed at 3417.8 and 3278.8 cm^{-1}, which might result from the asymmetric stretching of NH_2 in amines and NH stretching in amide, respectively (Yan and Viraraghavan 2008; Smith 1999). Hence, the amine or amide groups might contribute to the metal removal. Significant shifting of a strong band from 1636.0 cm^{-1} to 1652.4 cm^{-1} was observed, suggesting the involvement of amide/ amine/ carboxyl groups in the cadmium removal. The peak assigned to the stretching vibration of C-O in carboxylic acids shifted from 1264.6 cm^{-1} to 1240.7 cm^{-1}, which indicated that carboxyl groups might be involved in the cadmium biosorption. The frequency differences ($\Delta = \nu_{C=O} - \nu_{C-O}$) between C=O and C-O of the pristine and Cd-loaded biomass were calculated. The difference is related to the relative symmetry of the two carbon-oxygen bonds and suggests the binding status of the carboxyl group. The Δ values of the pristine and Cd-loaded biomass were found to be

374.1 and 411.7 cm^{-1}, respectively. The higher value of frequency difference in the presence of cadmium ions may indicate the involvement of carboxylate group in the Cd(II) biosorption process (Chen and Yang, 2006). The Cd(II) ions could bind to the carboxyl groups in the forms of unidentate, bidentate and bridging. According to Nakamoto (2009), the Δ value of the complexes is in the following order: unidentate (Δ = 312-455) > Ionic/bridging (Δ = 138-201) > bidentate (Δ = 42-165). The Δ value of the Cd-loaded biomass was 411.7 cm^{-1}, suggesting that the complexation between the Cd(II) ions and the carboxyl group was in the form of unidentate. The P=O stretching band at 1072.8 cm^{-1} shifted to 1074.2 cm^{-1}. This observation might be due to the formation of metal complexes between the P=O group and the Cd(II) ions. In summary, carboxyl, phosphodiester and amine/amide groups were involved in Cd(II) binding process. The result of FTIR analysis after Cd(II) biosorption by the fungal biomass was compared with those by chitin and chitosan. Researchers reported that the Cd(II) biosorption capacities of chitosan and chitin were 10 and 12 mg/g, respectively (Benguella and Benaissa, 2002; Hydari et. al, 2012). It could be noted that those biosorption capacities were much lower than that of *M. rouxii* (q_{max} = 100.70 mg/g). This could be attributed to the fact that *M. rouxii* contains other types of functional groups (e.g. carboxyl and phosphodiester groups) for Cd(II) biosorption, leading

to a higher biosorption capacity. In addition, chitosan crystallinity might occur in raw chitosan due to the involvement of amine groups in hydrogen intramolecular or intermolecular bonds. Cd(II) ions therefore has difficulty to access the amine groups of the chitosan (Zawisza and Sitko, 2013).

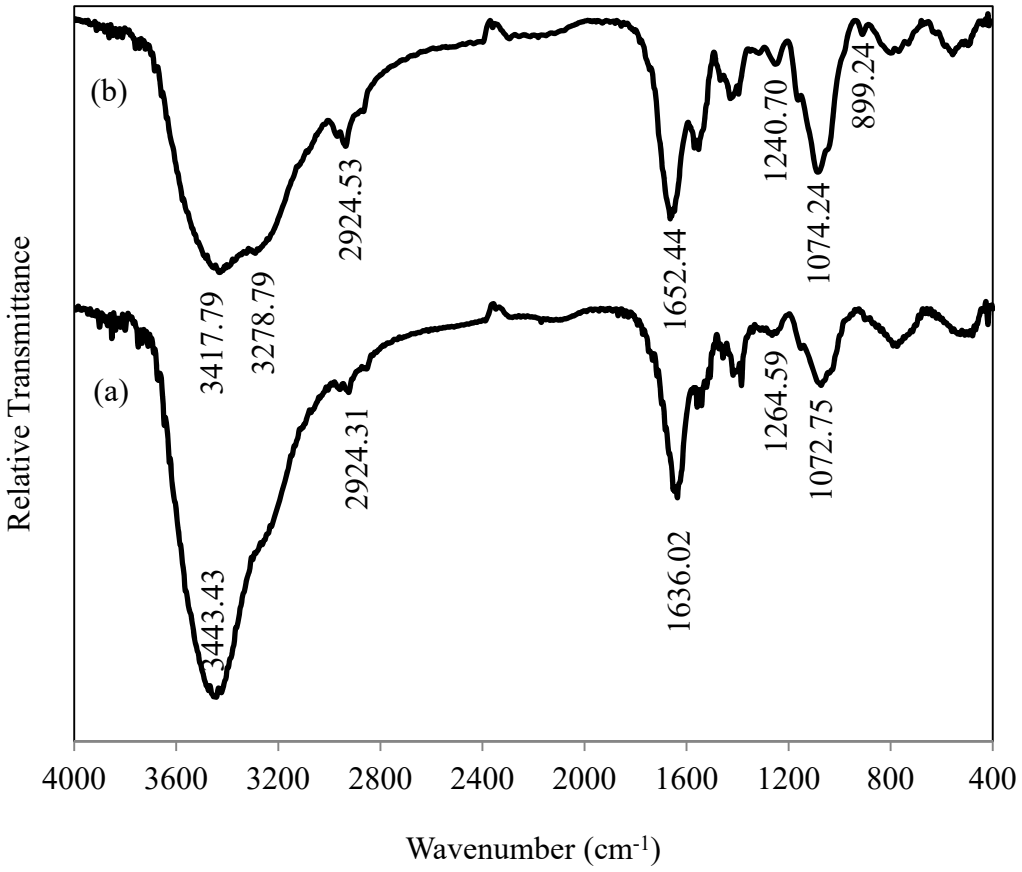

Figure 5.25 FTIR spectra of (a) pristine and (b) Cd-loaded biomass.

5.11 XPS analysis

Fig. 5.26 shows the wide scan XPS spectrum of the Cd-loaded biomass. After biosorption, an additional peak at the binding energy of 405.6 eV for Cd3d appeared when compared with that of the pristine biomass (Fig. 4.22), indicating the presence of cadmium on biomass. The binding energies and atomic concentrations of C, N, O, P and Cd are summarized in Table 5.12.

Determining the changes in binding energies or atomic concentrations after biosorption may be helpful for elucidating the Cd(II) binding mechanism onto the biomass. Therefore, the peaks of C, N and O were deconvoluted and compared with those of the virgin biomass, and the results are listed in Table 5.13. The high resolution XPS spectrum of C1s is shown in Fig. 5.27. After biosorption, the shifts in binding energies of the C atom in the form of C-(O, N) (0.14 eV) and C=O (0.13 eV) were relatively small, while the binding energy of carboxylate carbon exhibited a significant shift (0.37 eV). These results suggested that the carboxylate group might be the main functional group involved in the interaction between Cd(II) ion and the biomass.

The deconvoluted N1s spectrum of the Cd-loaded biomass is illustrated in Fig. 5.28. After the cadmium biosorption, the atomic concentrations of the N

atom in the two forms exhibited significant changes. The results suggested that the amine groups might be one of the binding sites involved in the cadmium removal.

The deconvolution of the O1s spectrum is shown in Fig. 5.29. After biosorption, obvious changes were also observed in the atomic concentrations of O=C and O-C, which could be due to the electrostatic interaction between the Cd(II) ion and the carboxylate group.

A shift of 0.3 eV in the binding energy of P2p was observed after Cd(II) biosorption, indicating the involvement of P-O group in the Cd(II) binding process.

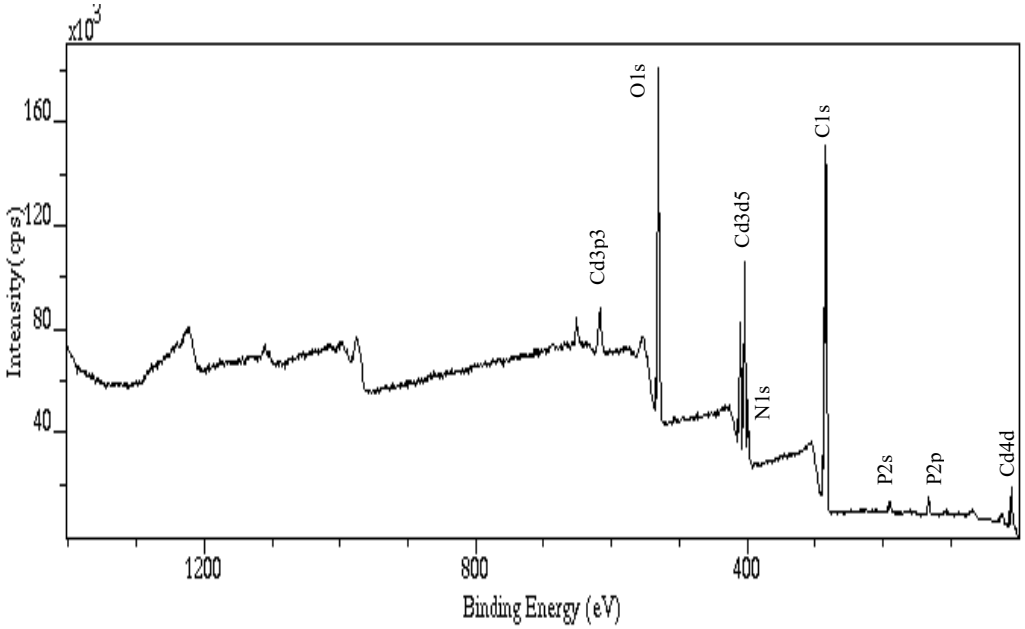

Figure 5.26 Wide scan XPS spectrum of Cd-loaded biomass.

Table 5.12 Binding energies and atomic concentrations of different elements on Cd-loaded biomass.

	Cd-loaded biomass	
Peak	Binding energy (eV)	Atomic concentration (%)
C1s	285.00	69.40
N1s	400.20	5.21
O1s	532.70	22.32
P2p	133.50	1.33
Cd3d	405.60	1.74

Table 5.13 Comparison of binding energies and atomic concentrations of elements before and after Cd(II) biosorption.

Element	Assignment	Pristine biomass		Cd-loaded biomass		Change in binding energy (eV)
		Binding energy (eV)	Atomic conc. (%)	Binding energy (eV)	Atomic conc. (%)	
C1s	C-(C, H)	285.00	55.02	285.08	61.20	0.08
C1s	C-(O, N)	286.54	32.87	286.68	25.35	0.14
C1s	C=O	288.27	9.96	288.14	10.23	0.13
C1s	O=C-O	289.31	2.15	288.94	3.23	0.37
N1s	NH_2	400.08	83.66	400.09	96.55	0.00
N1s	NH_3^+	401.98	16.34	402.11	3.45	0.13
O1s	O-C	532.79	82.73	532.87	67.76	0.08
O1s	O=C	531.30	17.27	531.43	32.24	0.13
P2p	P-O	133.80	100.00	133.50	100.00	0.30

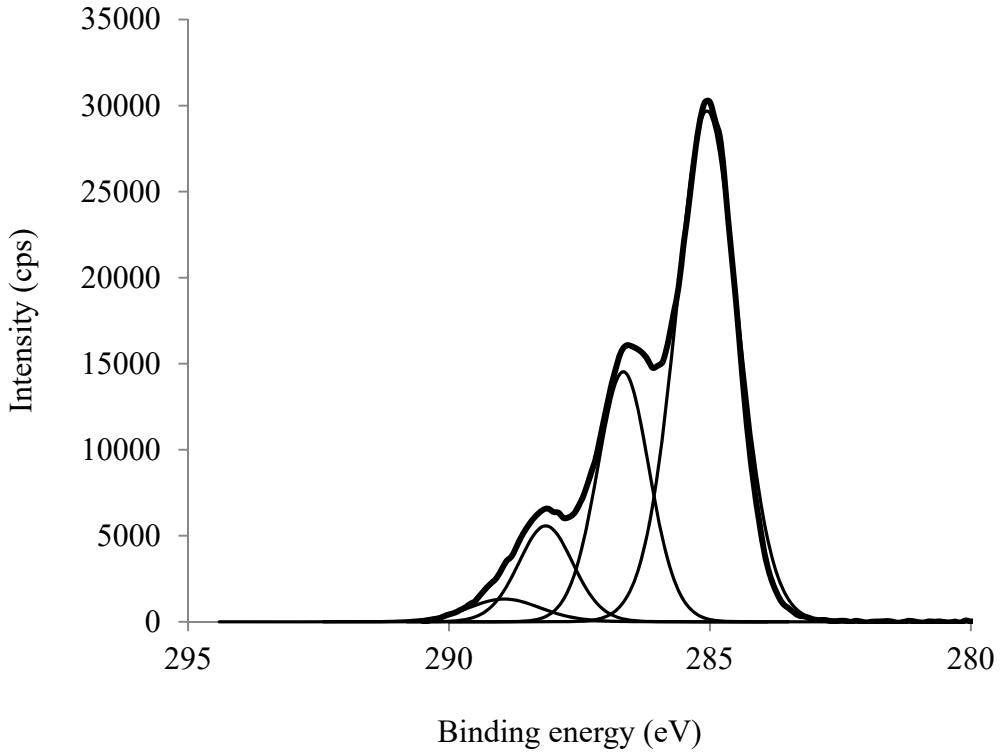

Figure 5.27 High resolution XPS (C1s) spectrum of Cd-loaded biomass.

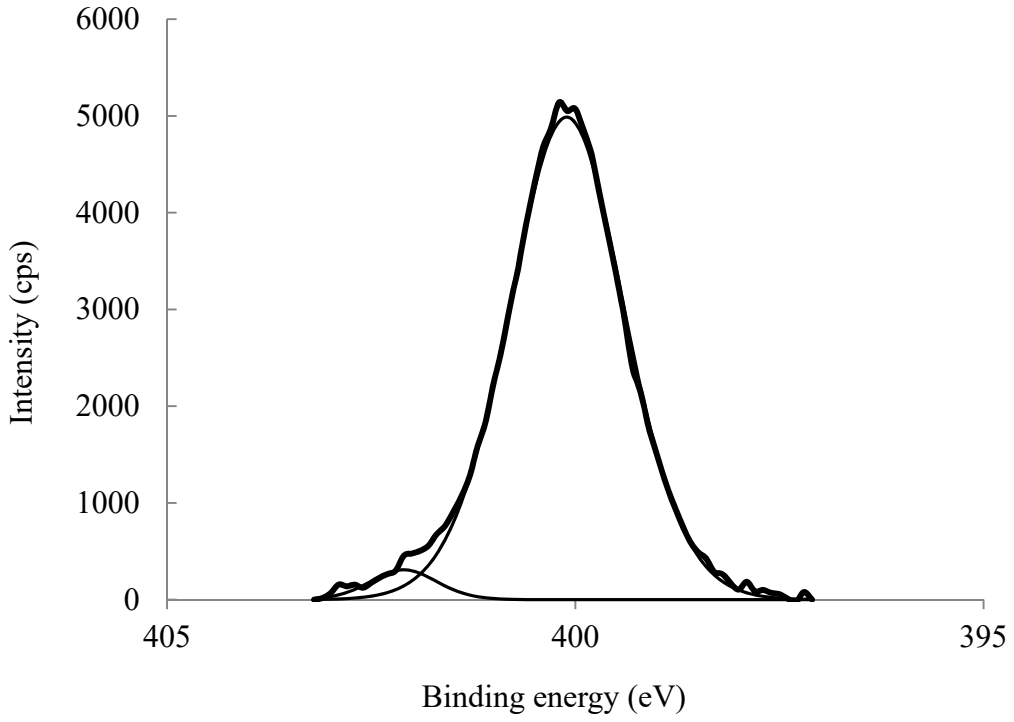

Figure 5.28 High resolution XPS (N1s) spectrum of Cd-loaded biomass.

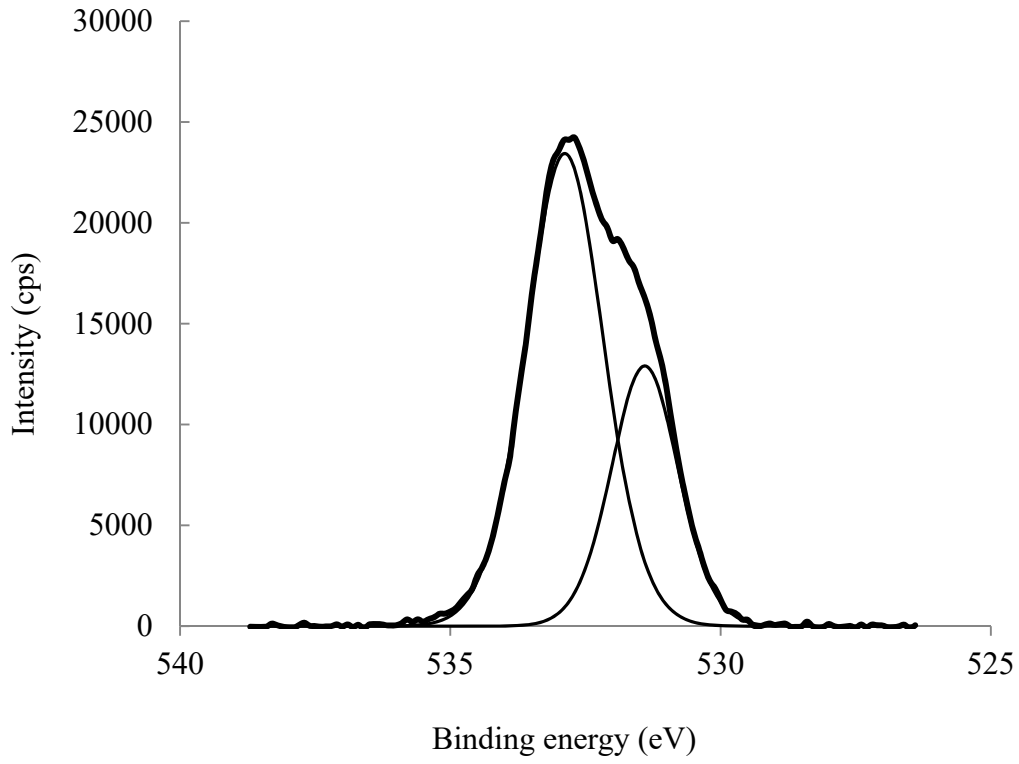

Figure 5.29 High resolution XPS (O1s) spectrum of Cd-loaded biomass.

5.12 Biosorption mechanisms of Cd(II) by *Mucor rouxii*

As mentioned in Section 4.4.2.1, the cell wall of *Mucor rouxii* was reported to consist mainly of chitosan, phosphate and chitin. The functional groups of hydroxyl, phosphate and the amine/amide groups were therefore abundant on the cell wall. Based on the combined results of potentiometric titration, cell wall biochemistry, FTIR and XPS studies, we proposed that phosphodiester (pK_a= 3.22 ±0.52), carboxyl (pK_a= 4.92±0.43), hydroxyl (pK_a= 8.77±0.31) and the amine groups (pK_a= 6.79±0.21) were present on the fungal biomass surface that was cultivated in this study. High concentrations of hydroxyl groups (2.09±0.85 mmol/g) might be attributed to the plentiful chitin and other polysaccharides. The equilibrium reactions of the four types of functional groups are shown below:

$$R\text{-}O\text{-}PO_2H\text{-}O\text{-}R \leftrightarrows R\text{-}O\text{-}PO_2^-\text{-}O\text{-}R + H^+ \quad \text{(Equation 5.31)}$$

$$RCOOH \leftrightarrows RCOO^- + H^+ \quad \text{(Equation 5.32)}$$

$$RNH_3^+ \leftrightarrows RNH_2 + H^+ \quad \text{(Equation 5.33)}$$

$$ROH \leftrightarrows RO^- + H^+ \quad \text{(Equation 5.34)}$$

These four types of functional groups (i.e. the phosphodiester, carboxyl, amine and hydroxyl groups) contributed to the surface charge of the biomass. It was observed that when the pH value was beyond 3.0, the zeta potential started to

decrease, revealing the deprotonation of phosphodiester groups (pK_a = 3.22±0.52) as shown in Equation 5.31. Furthermore, the value of zeta potential generally decreased as the pH increased due to the subsequent deprotonation of carboxyl (pK_a = 4.92±0.43) and the amine groups (pK_a = 6.79±0.21) as illustrated in Equations 5.39 and 5.40, respectively. In Fig. 5.2, we could notice that the q values increased gradually when the pH values increased from 3.0 to 7.0. The enhancement of biosorption capacity might be related to the formation of a metal complex between the deprotonated phosphodiester/ carboxyl group and Cd(II) ion. The involvements of the phosphodiester and carboxyl groups in the Cd(II) removal process are shown in Equations 5.35 and 5.36, respectively.

$$R\text{-}O\text{-}PO_2^-\text{-}O\text{-}R + Cd(II) \leftrightarrows R\text{-}O\text{-}PO_2^-\text{-}O\text{-}R\text{-}Cd(II) \quad \text{(Equation 5.35)}$$

$$RCOO^- + Cd(II) \leftrightarrows RCOO^-\text{-}Cd(II) \quad \text{(Equation 5.36)}$$

The result of potentiometric titration suggested that the pK_a of the hydroxyl group was 8.77±0.31. In this study, the Cd(II) batch experiment studies were performed at pH 7.5; therefore the hydroxyl groups might not form any metal complexes with Cd(II) ions.

The lone pair of electrons of nitrogen or oxygen containing groups could be donated to the metal ion to form a coordination complex, in which the electronegativity of oxygen atom is higher than that of the nitrogen atom;

therefore, the donation of the lone pair of electrons from nitrogen is easier than from oxygen. Some possible binding mechanisms of Cd(II) ions by the amine group are illustrated as follows:

$RNH_2 + Cd(II) \leftrightarrows RNH_2\text{-}Cd(II)$ (Equation 5.37)

$RNH_2 + H^+ \leftrightarrows RNH_3^+$ (Equation 5.38)

$RNH_3^+ + Cd(II) \leftrightarrows RNH_2\text{-}Cd(II) + H^+$ (Equation 5.39)

Both RNH_2 (Equation 5.37) and RNH_3^+ (Equation 5.39) were capable of binding cadmium ions from an aqueous solution. As shown in Equation 5.38, the lone pair of electrons of nitrogen could be donated to the Cd(II) ions to form a coordination complex. At low pH, the RNH_2 group could easily undergo protonation and formed RNH_3^+ (Equation 5.38). The Cd(II) ions in the aqueous solution might displace the proton and coordinate with the nitrogen atom of RNH_2.

By comparing the FTIR spectra of the pristine biomass and the Cd-loaded biomass, we suggested that the phosphodiester, carboxyl and amine groups were involved in cadmium biosorption. In the XPS analysis, the changes in the binding energies of C1s (O=C-O) and P2p (P-O) were 0.37 and 0.30 eV, respectively, and we deduced that the carboxyl and phosphodiester groups were involved in the Cd(II) removal. The significant changes in atomic

concentrations of N1s (NH_3^+) also suggested the involvement of the amine groups in Cd(II) binding. The results of the FTIR were consistent with XPS studies in which phosphodiester, carboxyl and amine groups played an important role in Cd(II) removal.

Results of EDAX and XPS analyses showed that the fungal biomass surface mainly consists of C, N, O and P. Peaks of alkali and alkaline earth metal ions (e.g. sodium, potassium, magnesium and calcium ions) commonly found on the surface of algal or other fruit wastes did not appear. Hence, the removal of cadmium ions by the fungal biomass might not be due to an ion exchange between the Cd(II) and the cell surface cations, e.g., alkali and alkaline earth metal ions. However, the Cd(II) cation could still be adsorbed on the carboxylate groups through ion exchange with protons from carboxyl groups. When the solution pH was beyond 3, the net surface charge of the fungal biomass decreased because of the deprotonation of the phosphodiester group ($pK_a = 3.22 \pm 0.52$); at the same time, the cadmium biosorption capacity was enhanced. This phenomenon might be attributed to the electrostatic interaction between the cadmium ions and deprotonated phosphodiester groups. The interaction between the carboxylate group and the cadmium ion might also be caused by electrostatic attraction. From the deconvoluted N1s spectra, it was noticed that the peak of N1s exhibited

a significant change in atomic concentration and binding energy, indicating that the nitrogen containing groups like amine might have interacted with the Cd(II) ions.

5.13 Biosorption edges of Cd(II) ions

According to Martinez and Ferris (2001), high-resolution biosorption data can be obtained when experiments are conducted at low initial metal concentration with a small change in solution pH. In this section, the adsorption edges of Cd(II) were studied using different biomass-metal ratios and ionic strengths, and the percentage adsorption of Cd(II) ions was plotted against a equilibrium solution pH as shown in Figs. 5.30-5.32.

5.13.1 Biomass concentration effect

Fig. 5.30 depicts the sorption performance of Cd(II) at different biomass concentrations. It was observed that the percentage removal of Cd(II) ions increased with increasing biomass concentration. Approximately 64% and 86% Cd(II) removal were attained at an equilibrium pH of 6.60 under the biomass concentrations of 1.00 and 2.00 g/L, respectively. These results could be attributed to the fact that more active sites were available for Cd(II) biosorption under high biomass concentration, resulting in high percentage removal of metal ions.

5.13.2 Ionic strength effect

Fig. 5.31 illustrates the ionic strength effect on the Cd(II) biosorption

capacity. The results showed that the Cd(II) removal efficiency decreased as the ionic strength increased. At a high ionic strength, Cd(II) ion competed with Na^+ ions for the surface biosorption sites on the fungal biomass surface. Therefore, the Cd(II) removal efficiency decreased as the ionic strength increased. It could also be observed that the curves deviated as the pH increased. At low pH, excess protons were present in the aqueous solution. Therefore, the excess protons play an important role in affecting the Cd(II) removal efficiency. When pH further increased, ionic strength would play a more significant role than the protons.

5.13.3 Initial metal concentration effect

The biosorption performance was better at the lower initial metal concentration as shown in Fig. 5.32. The results demonstrated that the percentage of Cd(II) ions removal decreased with increasing initial metal concentration. At a high initial metal concentration, most of the surface functional groups became saturated. As a result, a large amount of free metal ions were still present in the aqueous solution. Thus, a lower removal percentage was observed when using a higher initial metal concentration.

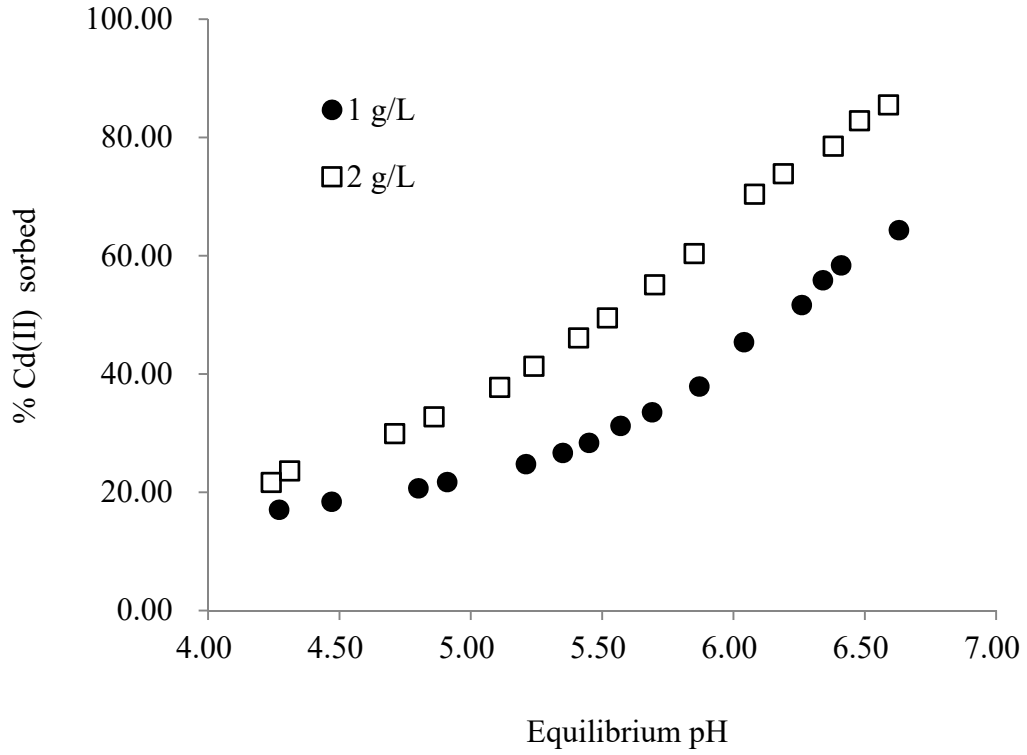

Figure 5.30 Biomass concentration effect on Cd(II) biosorption edge of *Mucor rouxii*.

([Cd(II)] = 50 ppm; [$NaNO_3$] = 0.01 M)

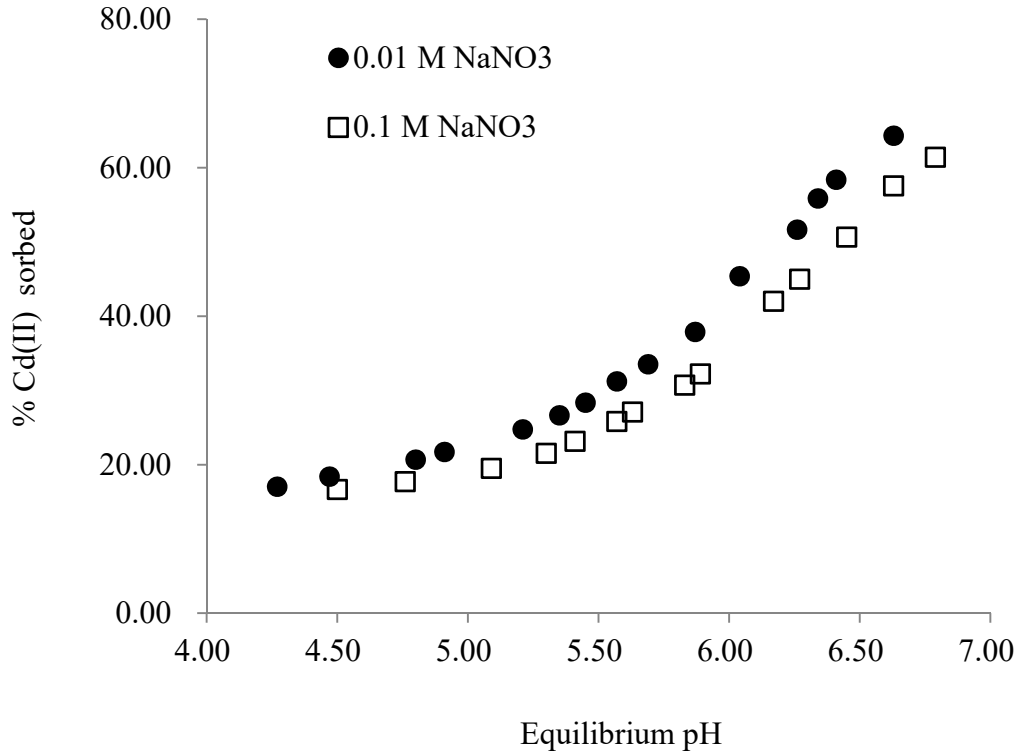

Figure 5.31 Ionic strength effect on Cd(II) biosorption edge of *Mucor rouxii*.

([Cd(II)] = 50 ppm; [Biomass] = 1 g/L)

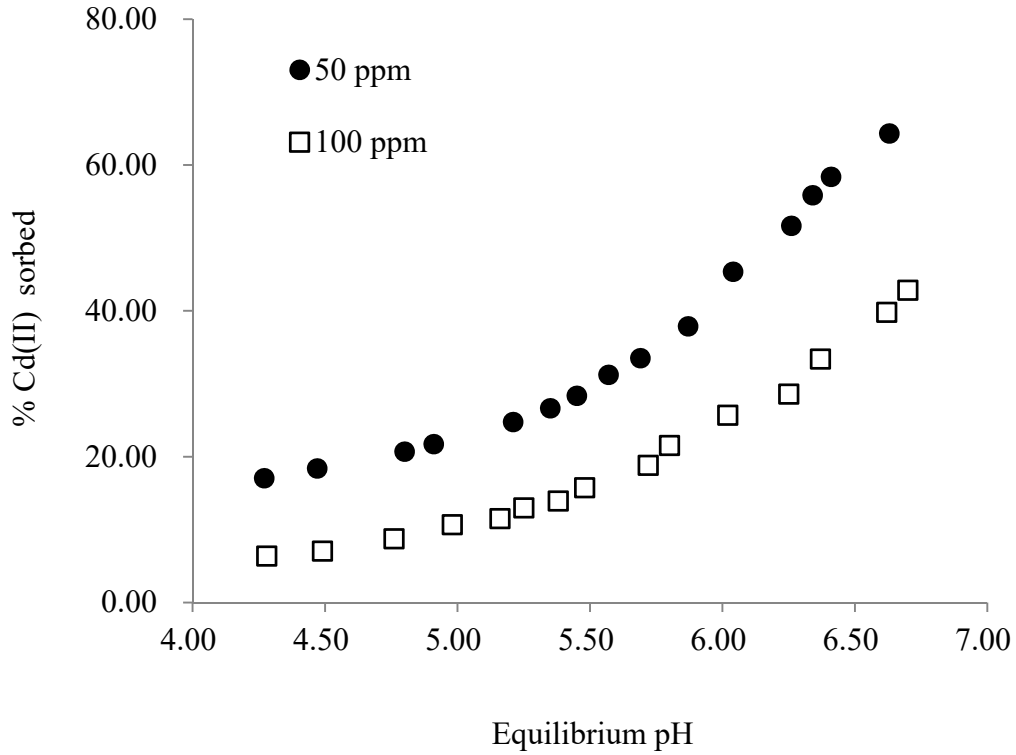

Figure 5.32 Initial metal concentration effect on Cd(II) biosorption edge of *Mucor rouxii*.

([Biomass] = 1 g/L; [$NaNO_3$] = 0.01 M)

5.14 Chemical equilibrium model for Cd(II) biosorption

In this section, the FITEQL 2.0 with constant capacitance model was employed to interpret the Cd(II) sorption edge data. DLM and SM did not converge. FITEQL is a general nonlinear least squares optimization program. The parameters in the chemical equilibrium model can be adjusted to obtain the best fit model to the experimental data. For example, the equilibrium constants of solution, the types of surface complex, the solubility products or the total concentrations of functional groups can be adjusted (Dzombak and Morel 1990). The deprotonation constants and the site concentrations of the surface functional groups that were determined from the potentiometric titration of biomass suspension (Section 4.4.2) were utilized as input data for the chemical equilibrium equation to simulate the Cd(II) biosorption data. Based on the Cd(II) binding mechanisms proposed in Section 5.12, phosphodiester ($pK_a = 3.22$), carboxyl ($pK_a = 4.92$) and amine groups ($pK_a = 6.79$) were involved in Cd(II) biosorption. For each set of data, one-site-one-pK_a (carboxyl group) and two-site-two-pK_a (carboxyl and phosphodiester groups) models were used for the determination of stability constants and site concentrations of the metal-biomass complexes. The amine group was not considered in this section since it was observed that the

equilibrium solution pH of all sorption edge systems was below 6.79; therefore the amine group should be in the form of NH_3^+ leading to a repulsion between the protonated amine groups and the Cd(II) cations. The two models are described in the following sections.

One-site-one-pK_a metal adsorption model

The results of the pH effect on Cd(II) biosorption (Fig. 5.2) indicated that the Cd(II) binding increased rapidly in the pH range of 4.0-7.0, suggesting that the carboxyl groups might play a major role in the removal of Cd(II) ions from an aqueous solution. Hence, the carboxyl groups were considered in the one-site-one-pK_a model. The equilibrium equation is expressed as:

$RCOO^- + M^{n+} \leftrightharpoons RCOO^-M^{n+}$ K_1 (Equation 5.40)

Two-site-two-pK_a metal adsorption model

In this model, one more surface active site - the phosphodiester group - was added to the one-site-one-pK_a model. The equilibrium equations are formulated as:

$RCOO^- + M^{n+} \leftrightharpoons RCOO^-M^{n+}$ K_1 (Equation 5.41)

$R\text{-}O\text{-}PO_2^-\text{-}O\text{-}R + M^{n+} \leftrightharpoons R\text{-}O\text{-}PO_2^-\text{-}O\text{-}R\ M^{n+}$ K_2 (Equation 5.42)

The curves of the one-site-one-pK_a and two-site-two-pK_a models for each set of data are depicted in Figs. 5.33-5.36. The V(Y), stability constants and site

concentrations of the Cd-biomass complexes calculated from each set of data are compiled in Table 5.14. As shown in the figures, the sorption data of all biosorption systems could not be well simulated by the one-site model (carboxyl group) when compared with those of the two-site model (carboxyl and phosphodiester group). Additionally, we could observe that the one-site model underestimated the percentage of Cd(II) ions sorption by the fungal biomass at low pH values (pH 4.2-5.0). The underestimation indicated that the adsorption data could not be solely explained by the carboxyl group; there should be another type of surface site responsible for the adsorption of Cd(II) at low pH. Hence, an additional functional group (phosphodiester; $pK_a = 3.22$) was considered and the two-site model was employed to simulate the data. As listed in Table 5.14, the variances of one-site models are larger than those of two-site models, suggesting that two-site models provided an excellent match with the experimental data. The average Cd-carboxyl and Cd-phosphodiester log stability constants were 1.19 ±0.23 and 6.87±0.51, respectively. The Cd-carboxyl stability constant was comparable to that of the Cd-acetate complex (log stability constant = 1.90) while the Cd-phosphodiester stability constant was comparable to that of the Cd-tripolyphosphate complex (log stability constant = 6.58). The results indicated that the Cd complexes on the cell wall exhibited relatively high

thermodynamic stabilities which were similar to or higher than those of the Cd-acetate or Cd-tripolyphosphate complexes (Fein et al. 1997; Andersen 1984). The CCM model seemed to be capable of simulating the Cd(II) sorption edge data if only V(Y) was considered. The site concentrations were slightly over-predicted using CCM model.

Table 5.14 Comparison of parameters estimated by one-site and two-site models of Cd(II) biosorption by *Mucor rouxii*.

Metal conc. (ppm)	Biomass dose (g/L)	$NaNO_3$ conc. (M)	Model	V(Y)	Capacitance F/m^2	Log K_1	Log K_2	Site 1 concentration (mol/g)	Site 2 concentration (mol/g)
50	1.00	0.01	one-site-one-pK_a	22.76	50	1.877	-	0.0331	-
			two-sites-two-pK_a	0.2288	50	1.286	7.119	0.2109	1.22E-04
50	1.00	0.1	one-site-one-pK_a	18.21	23	1.984	-	0.0290	-
			two-sites-two-pK_a	0.1338	46	1.127	7.150	0.2331	9.79E-05
100	1.00	0.01	one-site-one-pK_a	4.44	50	1.450	-	0.0355	-
			two-sites-two-pK_a	0.3788	47	0.9105	6.105	0.1769	1.08E-04
50	2.00	0.01	one-site-one-pK_a	54.29	30	2.168	-	0.0318	-
			two-sites-two-pK_a	1.382	44	1.444	7.094	0.2633	9.97E-05

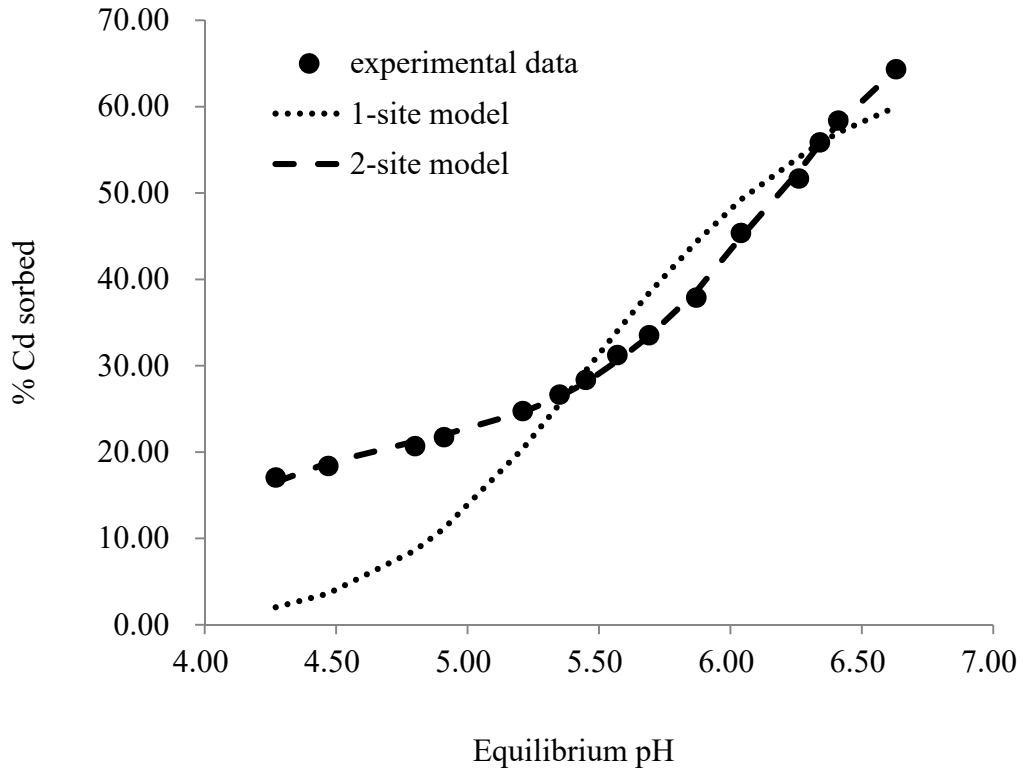

Figure 5.33 Simulation of Cd(II) biosorption edge of *Mucor rouxii* by one-site-one pK_a and two-site-two-pK_a model.

([Cd(II)] = 50 ppm; [Biomass] = 1 g/L; [$NaNO_3$] = 0.01 M)

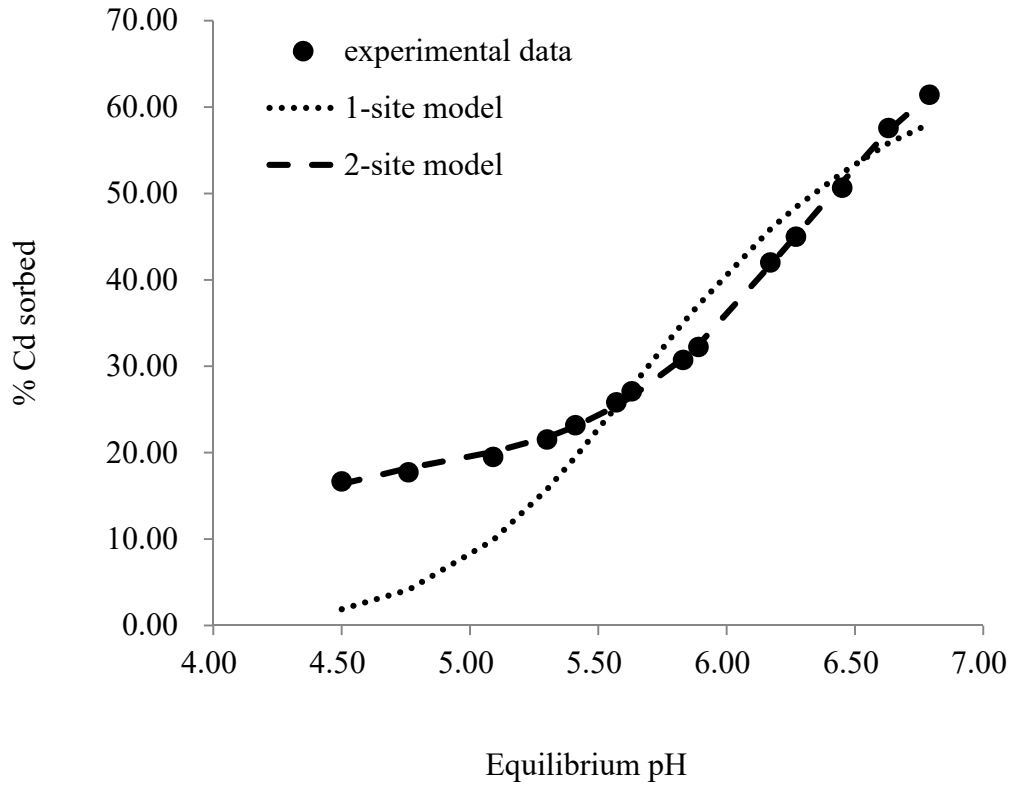

Figure 5.34 Simulation of Cd(II) biosorption edge of *Mucor rouxii* by one-site-one pK_a and two-site-two-pK_a model.

([Cd(II)] = 50 ppm; [Biomass] = 1 g/L; [$NaNO_3$] = 0.1 M)

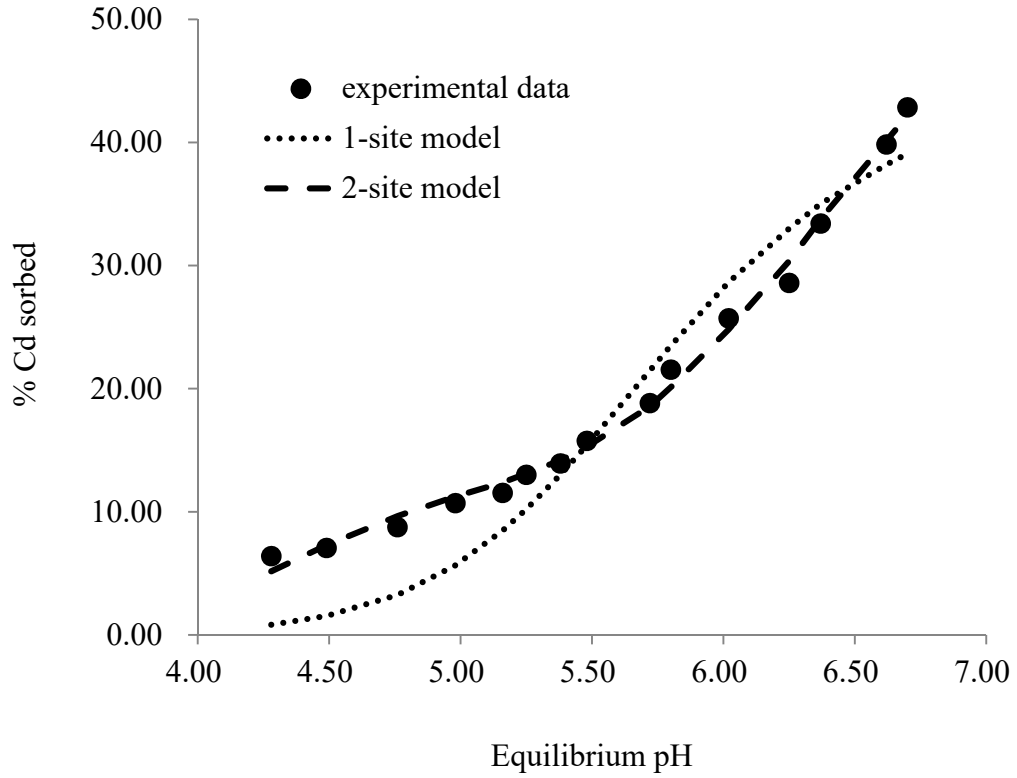

Figure 5.35 Simulation of Cd(II) biosorption edge of *Mucor rouxii* by one-site-one pK_a and two-site-two-pK_a model.

([Cd(II)] = 100 ppm; [Biomass] = 1 g/L; [$NaNO_3$] = 0.01 M)

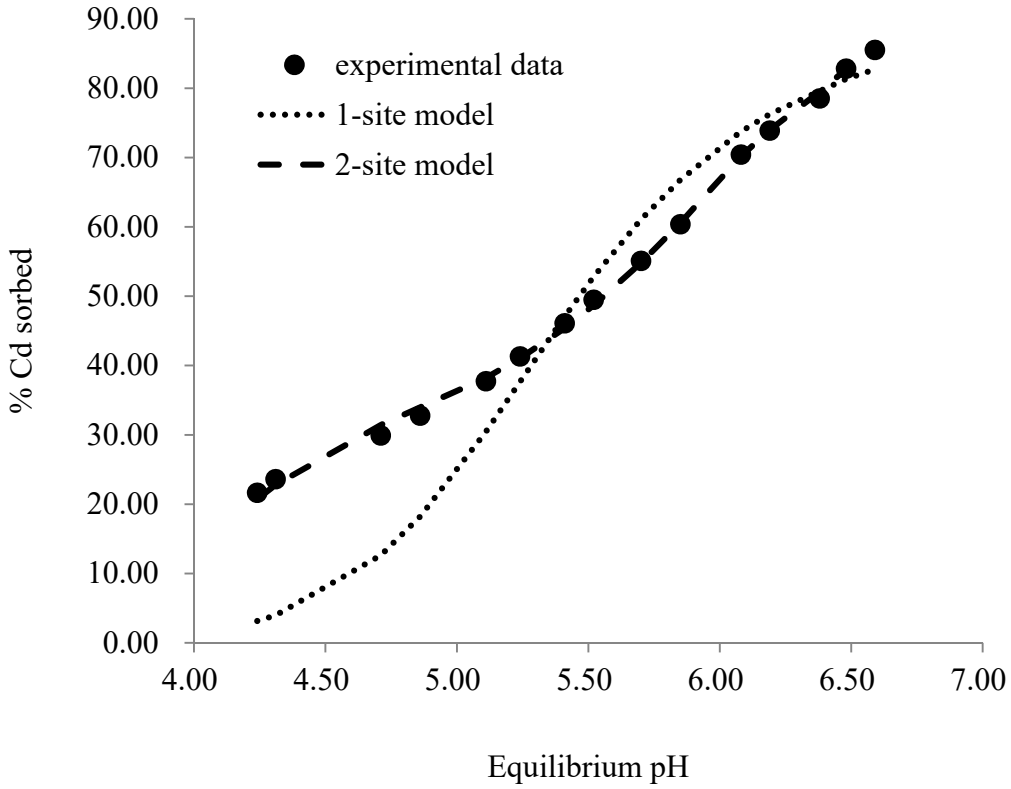

Figure 5.36 Simulation of Cd(II) biosorption edge of *Mucor rouxii* by one-site-one pK_a and two-site-two-pK_a model.

([Cd(II)] = 50 ppm; [Biomass] = 2 g/L; [$NaNO_3$] = 0.01 M)

Chapter 6

Removal of Cr(VI) by *Mucor rouxii*

6. Removal of Cr(VI) by *Mucor rouxii*

This section first presents the effects of pH, biomass concentration, initial metal concentration, contact time, temperature and agitation speed on Cr(VI) removal by *Mucor rouxii*. The mathematical modeling of equilibrium and kinetic data of Cr(VI) removal by different isotherm and kinetic models is then reported. Finally, the Cr(VI) removal mechanisms of the fungal biomass are discussed.

6.1 Effect of pH

Solution pH strongly influences the metal-binding performance of biomass. Solution pH affects not only the availability of the functional groups on the biomass, but also the chemistry of Cr(VI) ions in solution. Speciation diagram of Cr(VI) complexes in solution pHs ranging from 0.0 to 14.0 was plotted by MINEQL^{+} 3.01. The speciation simulation conditions are 100 ppm Cr(VI); temperature 25℃ and open system. The speciation diagram of Cr(VI) complexes in aqueous solution is illustrated in Fig. 6.1. At pH ranges between 0.0 and 5.0, approximately 90% of the Cr(VI) species are in the form of $HCrO_4^-$ and 10% of the species present as $Cr_2O_7^{2-}$ in aqueous solution. When the solution pH further increases, the fractions of $HCrO_4^-$ and $Cr_2O_7^{2-}$ reduce, whereas

the percentage of CrO_4^{2-} increases and becomes completely dominant at pH 8.0.

To examine the effect of the solution pH on Cr(VI) removal, pH values ranging from 2.0 to 7.0 were studied. Fig. 6.2 depicts the effect of pH on Cr removal. The concentration of total Cr represents the total concentrations of Cr(III) and Cr(VI) in the aqueous solution. As shown in the figure, the solution concentrations of Cr(VI) and total Cr decreased with decreasing solution pH. At pHs 2.0 and 3.0, the biomass (PZC= 3.5) possessed a net positive surface charge, thus, the adsorption of Cr(VI) was favorable due to the electrostatic attraction between the anionic Cr(VI) and the positively-charged biomass surface. On the other hand, the concentration of Cr(III), which was formed mainly from the reduction of Cr(VI), increased with decreasing pH. At low pH values, $HCrO_4^-$ and $Cr_2O_7^{2-}$ are the main species present in the aqueous solution and the reduction equations are shown below:

$$HCrO_4^- + 7H^+ + 3e^- \leftrightharpoons Cr^{3+} + 4H_2O \qquad E^0 = +1.35V \qquad \text{(Equation 6.1)}$$

$$Cr_2O_7^{2-} + 14H^+ + 6e^- \leftrightharpoons 2Cr^{3+} + 7H_2O \qquad E^0 = +1.33V \qquad \text{(Equation 6.2)}$$

Based on the above equations, it could be noticed that the reduction of Cr(VI) is favorable in acidic conditions, hence, more Cr(III) ions were formed at a lower pH.

Fig. 6.3 depicts the effect of pH on the biosorption capacity of the total Cr

and percentage removal of Cr(VI). Both the biosorption capacity and the percentage removal increased with decreasing pH. At low pH values, the Cr(VI) anions were facilely attracted to the protonated surface sites and reduced to Cr(III), resulting in the high biosorption capacity and percentage removal of Cr(VI). The maximum biosorption capacity and the percentage removal of Cr(VI) were 30.73 mg-total Cr/g-biomass and 41.00 % at pH 2, respectively.

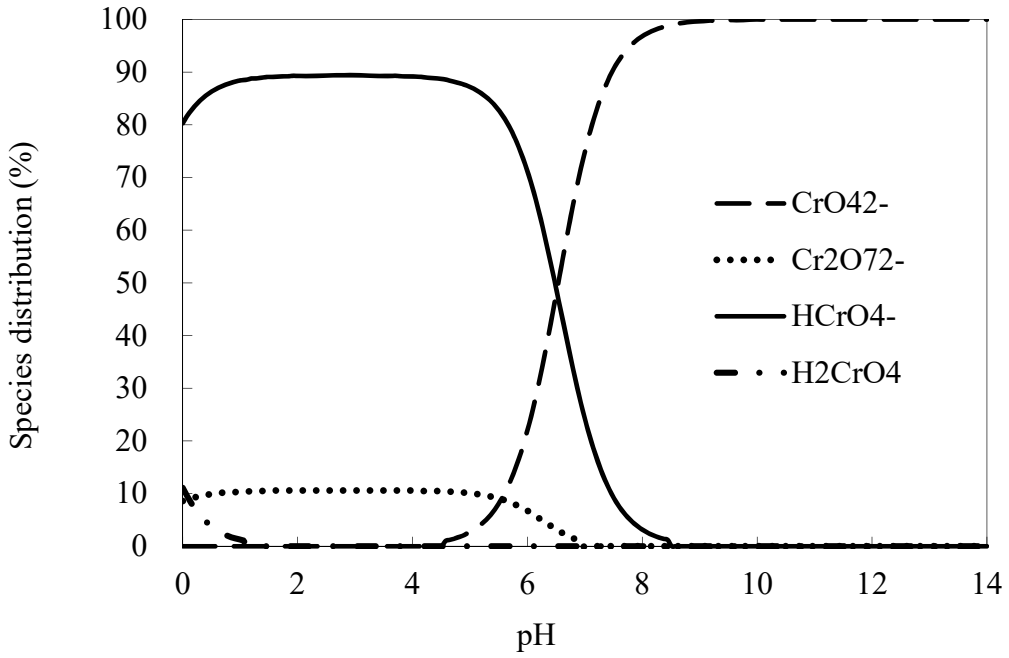

Figure 6.1 Speciation diagram of Cr(VI) in aqueous solution (100 ppm).

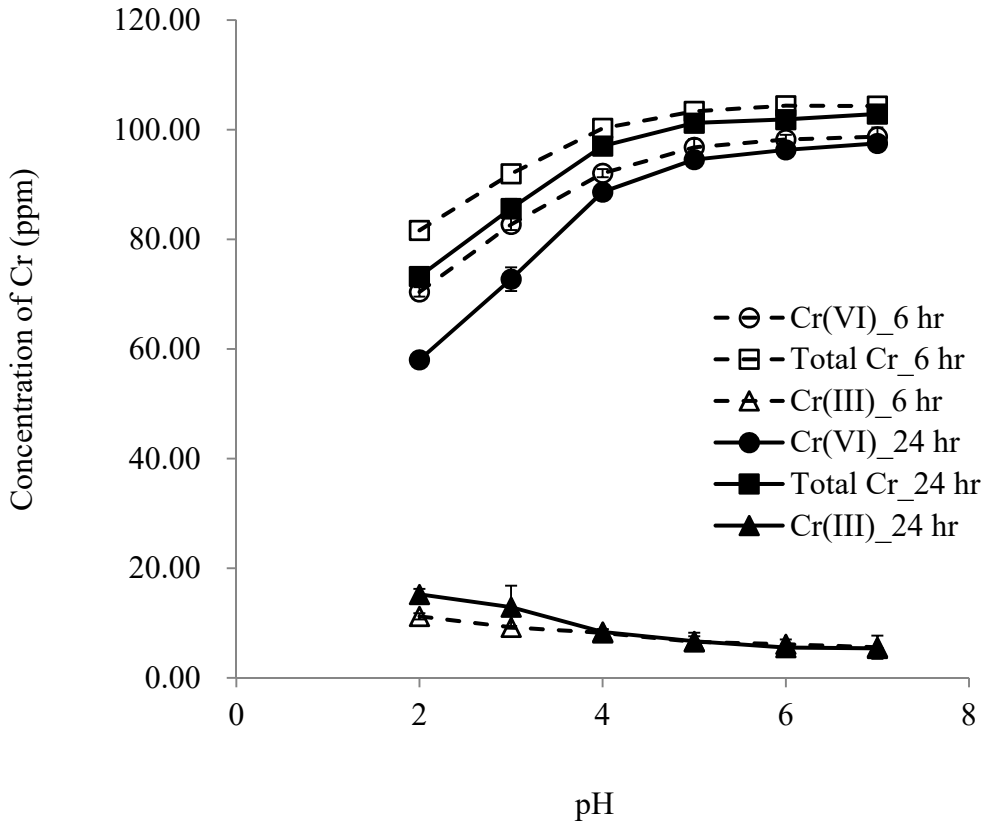

Figure 6.2 Cr concentration profiles in the solution at different pH.

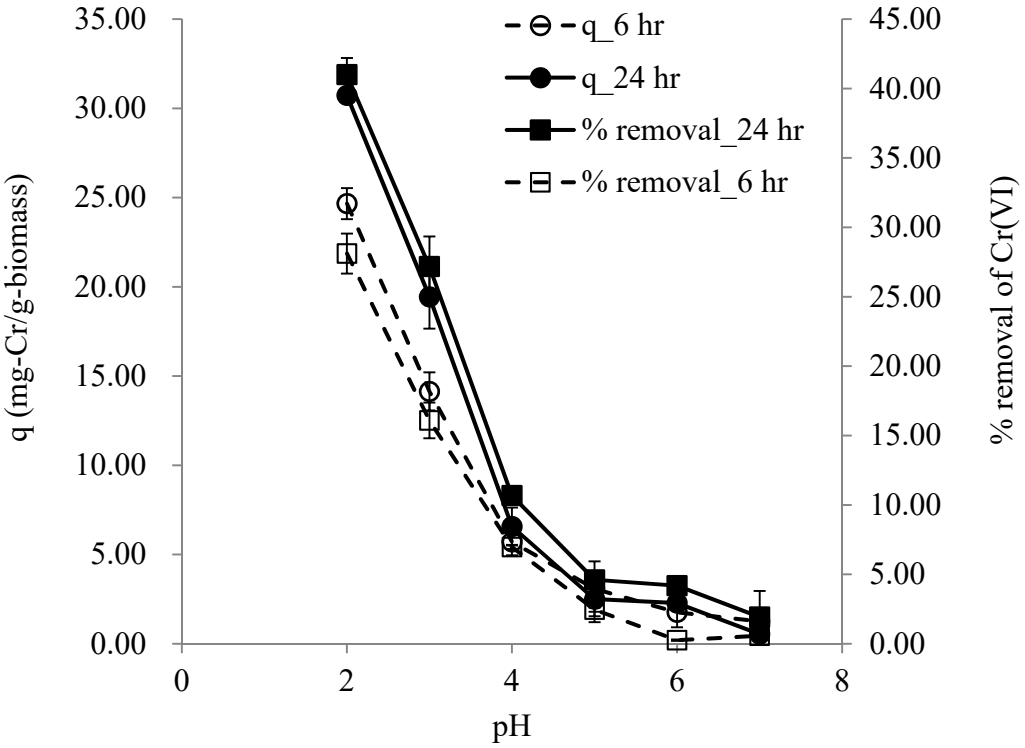

Figure 6.3 Effect of pH on total Cr biosorption and percentage removal of Cr(VI) by *Mucor rouxii*.

6.2 Effect of biomass concentration

The biomass concentration may affect the Cr(VI) removal efficiency of *Mucor rouxii*. To study the effect of biomass concentration on Cr(VI) removal, biomass concentrations ranging from 0.2 to 5.0 g/L were investigated. Fig. 6.4 displays the Cr concentration profiles in aqueous solution at different biomass concentrations. The concentrations of Cr(VI) and total Cr decreased with increasing biomass concentration since more surface functional groups were available for adsorption of Cr(VI) at high biomass doses. As the contact time increased, the concentration of Cr(VI) further decreased due to the reduction of Cr(VI) to Cr(III). The Cr(III) concentration generally increased with increasing biomass concentration because abundant electron donating groups on the biomass surface were available for the reduction of Cr(VI) to Cr(III). As the contact time increased from 6 h to 24 h, more Cr(III) ions were formed due to the reduction reaction.

The effect of the biomass concentration on the biosorption capacity of the total Cr and percentage removal of Cr(VI) is illustrated in Fig. 6.5. As can be seen in the figure, the biosorption capacity of the total Cr decreased with increasing biomass concentration since abundant surface sites were still available

for Cr adsorption under high biomass doses. On the other hand, the percentage removal of Cr(VI) increased with increasing biomass concentration. At a higher biomass concentration, more surface functional groups were available for the adsorption and reduction of Cr(VI), and thus, the Cr(VI) removal was enhanced under high biomass concentration. Approximately 80% Cr(VI) removal was attained within 24 h at the biomass concentration of 5.0 g/L. The results indicated that a high biomass concentration provided a larger amount of surface functional groups for the Cr(VI) removal or adsorption of Cr.

The Cr(VI) removal kinetics at different biomass concentrations (1, 5 and 10 g/L) were investigated (Appendix 4). The concentrations of Cr(VI) and total Cr decreased with increasing biomass concentration since more surface functional groups were available for biosorption of Cr(VI) at high biomass concentrations. The concentration of Cr(VI) further decreased as the contact time increased. It is due to the reduction of Cr(VI) to Cr(III) ions. The Cr(III) concentration generally increased with increasing biomass concentration because abundant electron donating groups on the fungal biomass surface were available for the reduction of Cr(VI) to Cr(III). Approximately 41, 78 and 91% Cr(VI) removal were attained within 24 h at the biomass dosages of 1, 5 and 10 g/L, respectively. A complete removal of Cr(VI) ions was attained at a contact time of 72 h when a

biomass concentration of 10 g/L was used. The results revealed that a complete removal of Cr(VI) is possible if a sufficiently high biomass dosage was applied.

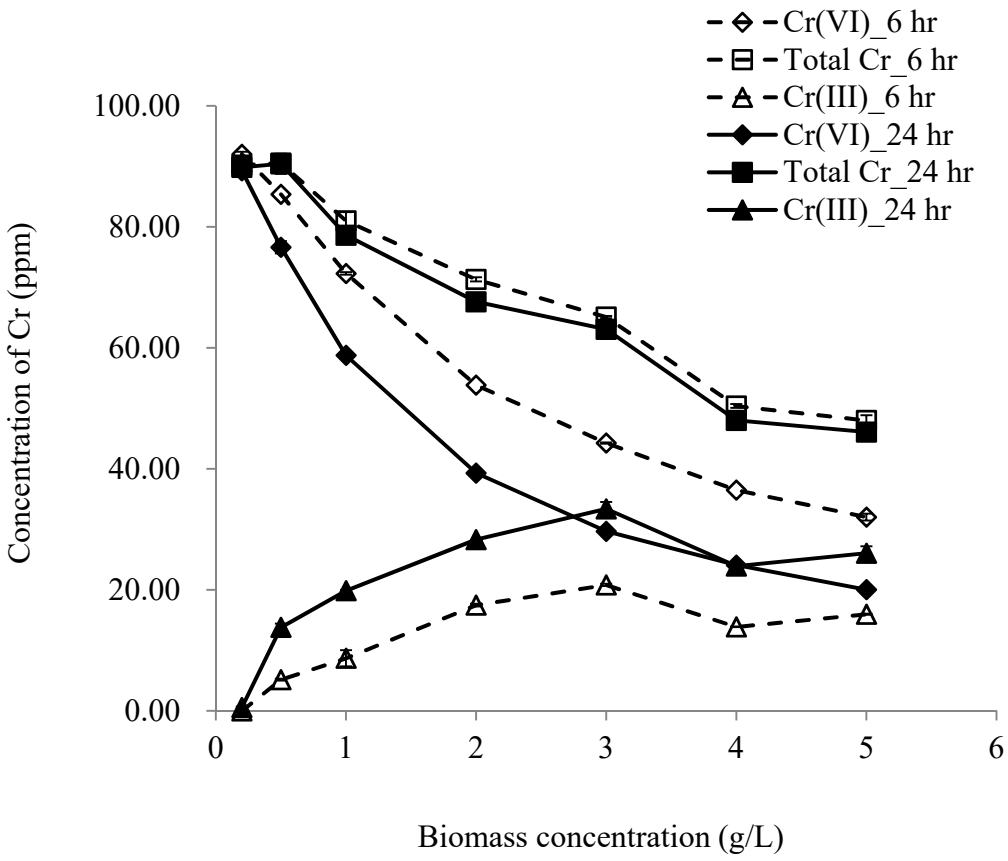

Figure 6.4 Cr concentration profiles in the solution at different biomass concentrations.

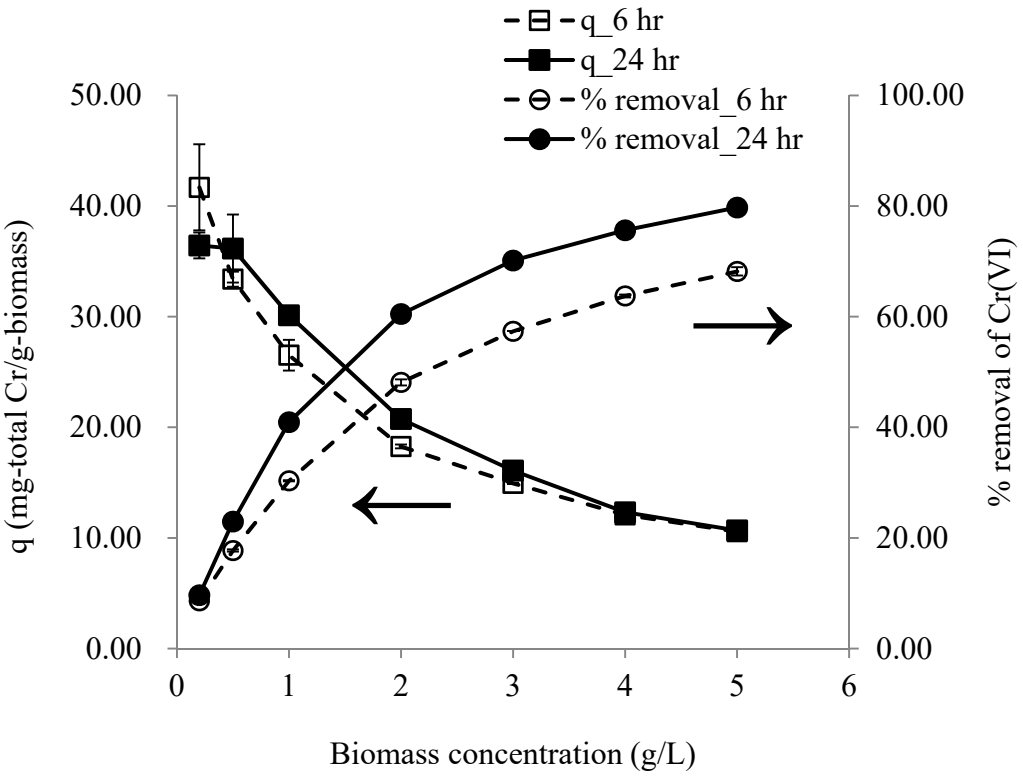

Figure 6.5 Effect of biomass concentration on total Cr biosorption and percentage removal of Cr(VI) by *Mucor rouxii*.

6.3 Sorption isotherms

Initial metal concentration is another factor that may affect the Cr(VI) removal performance of *Mucor rouxii*. Therefore, the effect of initial metal concentration on the Cr(VI) removal by the fungal biomass was studied. Fig. 6.6 shows the Cr concentration profiles in the aqueous solution at different initial metal concentrations. The concentrations of Cr(VI) and total Cr in the aqueous solution increased with the increasing initial metal concentration. As the metal concentration increased, a lesser fraction of Cr(VI) ions could be adsorbed onto the biomass surface since the surface adsorption sites were fully occupied by Cr(VI) ions. It could also be observed that the concentration of Cr(VI) decreased as the contact time increased. The further removal of Cr(VI) might be due to the reduction of Cr(VI) to Cr(III). The concentration of Cr(III) in the aqueous solution was not significantly affected by the initial metal concentration but affected by the contact time. As the contact time increased, more Cr(III) ions were found in the aqueous solution. The appearance of Cr(III) ions was due to the reduction of Cr(VI) to Cr(III) in acidic condition.

The isotherm plots of Cr(VI) and total Cr at different contact times of 6 and 24 h are shown in Figs. 6.7a and 6.7b, respectively. The q_e represents the

amount of Cr(VI) ions removed by the fungal biomass. The Cr(VI) ions could be removed by biosorption and/or reduction. From the figures, the Cr(VI) and total Cr removal increased with the increasing initial metal concentration and contact time, and eventually reached a plateau. The isotherm data of Cr(VI) and total Cr at different contact times were simulated by the linearized Langmuir (Fig. 6.8) and the linearized Freundlich models (Fig. 6.9), while the non-linearized plots of the two models are depicted in Fig. 6.10. The isotherm parameters, correlation coefficients and error analyses obtained from the simulation of the plots are summarized in Table 6.1.

The experimental data of Cr(VI) at a contact time of 6 h could be better simulated by the linearized Langmuir isotherm models with higher r^2 and lower error values when compared with those obtained from the linearized Freundlich model. Both the linearized Langmuir and Freundlich models could satisfactorily simulate the experimental data of Cr(VI) at a contact time of 24 h and total Cr at contact times of 6 and 24 h. The values of r^2 obtained from the linearized Langmuir model were lower than those obtained from the linearized Freundlich model. On the other hand, the error values obtained from linearized Freundlich model were much higher than those obtained from the linearized Langmuir model.

The non-linearized Langmuir isotherm model could better simulate the

experimental data of Cr(VI) and total Cr at different contact times than non-linearized Freundlich model since higher correlation coefficients and lower error values were obtained when compared with the non-linearized Freundlich model. The value of r^2 decreased as the contact time increased in the case of Cr(VI) isotherm plot, while the value of r^2 increased as the contact time increased in the case of the total Cr isotherm plot. In addition, the non-linearized Langmuir isotherm model could better simulate the experimental data of Cr(VI) and total Cr at different contact times than the linearized Langmuir isotherm model with better correlation coefficients and lower error values.

The Sips, Redlich-Peterson and Temkin isotherm models were also employed to simulate the isotherm data of Cr(VI) and total Cr at different contact times (Fig. 6.11) and the corresponding parameters together with those of non-linearized Langmuir and Freundlich isotherm models are tabulated in Table 6.2. The Redlich-Peterson model ($r^2 = 0.9798$, SE = 3.24) provided the best match with the isotherm data of Cr(VI) at a contact time of 6 h and total Cr at a contact time of 24 h, while the Sips model provided the best simulation for the isotherm data of Cr(VI) at a contact time of 24 h and total Cr at a contact time of 6 h. As the contact time increased, the values of r^2 decreased in the case of the Cr(VI) isotherm plot. In the case of the total Cr isotherm plot, the values of r^2 generally

increased as the contact time increased. In general, the performances of Sips and Redlich-Peterson models were comparable to that of non-linearized Langmuir isotherm model. The simulation results shows that it is possible to apply isotherm models to simulate the removal of total Cr and Cr(VI) and to evaluate the total Cr biosorption capacity of a biomass at different contact times even though the Cr biosorption is coupled with a redox reaction.

The linearized D-R isotherm model was further used to simulate the isotherm data of Cr(VI) and total Cr at different contact times and the results showed that the model could not satisfactorily simulate the experimental data since the correlation coefficients (r^2 = 0.70-0.81) were low and the error values (SE = 9.03-16.19) were high (Table 6.2).

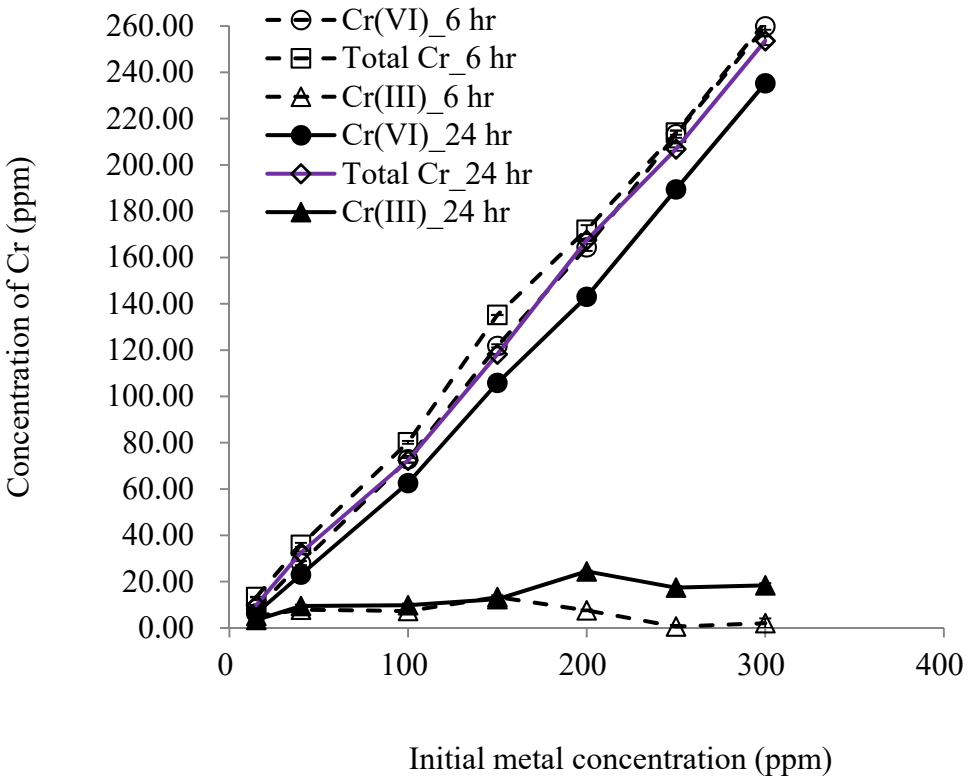

Figure 6.6 Cr concentration profiles in the solution at different initial metal concentrations.

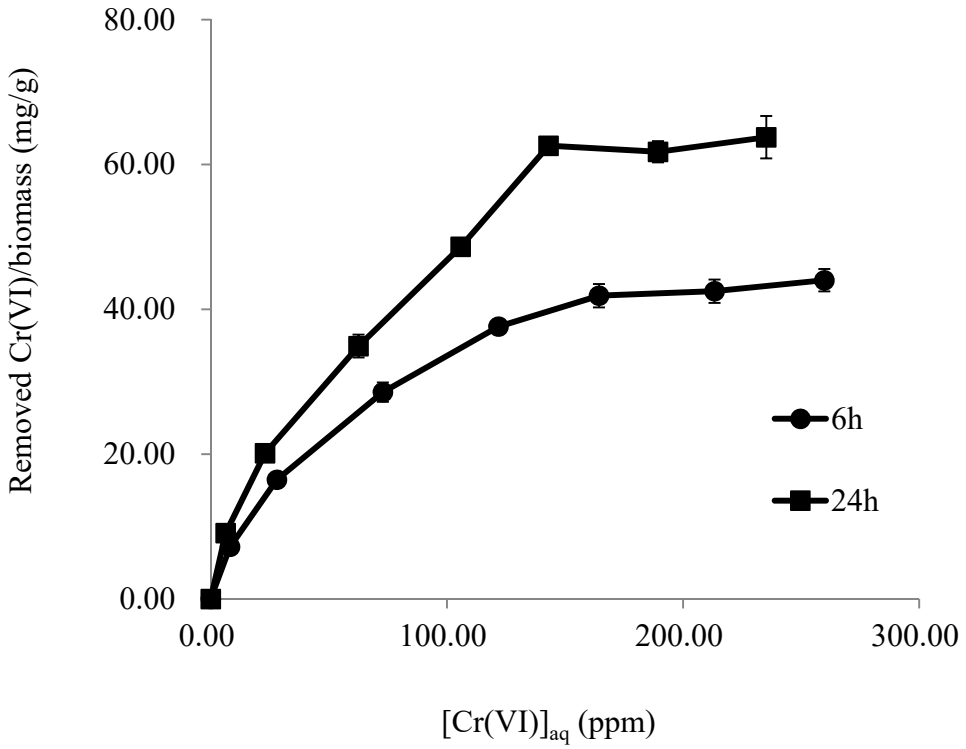

Figure 6.7a Cr(VI) biosorption isotherm of *Mucor rouxii* at different times.

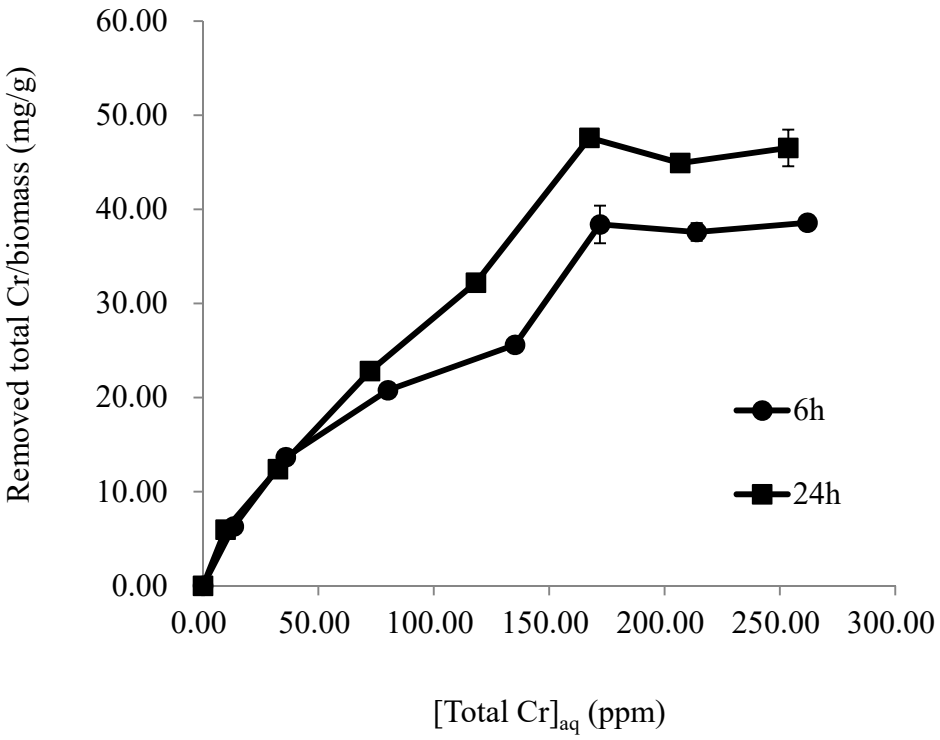

Figure 6.7b Total Cr biosorption isotherm of *Mucor rouxii* at different times.

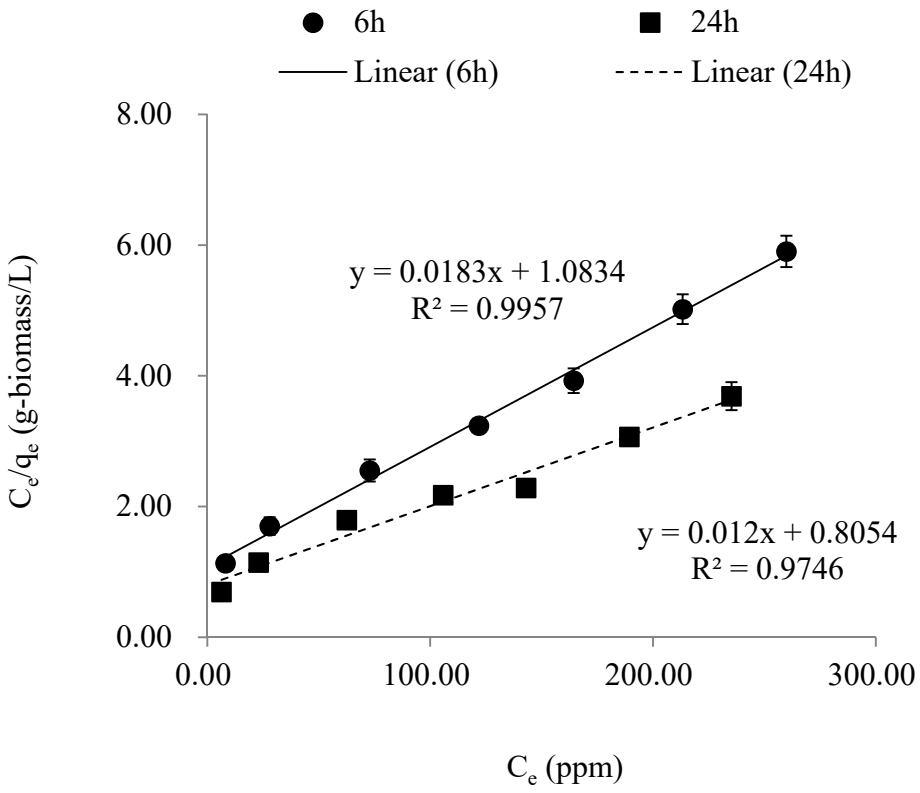

Figure 6.8a Linearized Langmuir isotherm model for Cr(VI) biosorption by *Mucor rouxii* at different times.

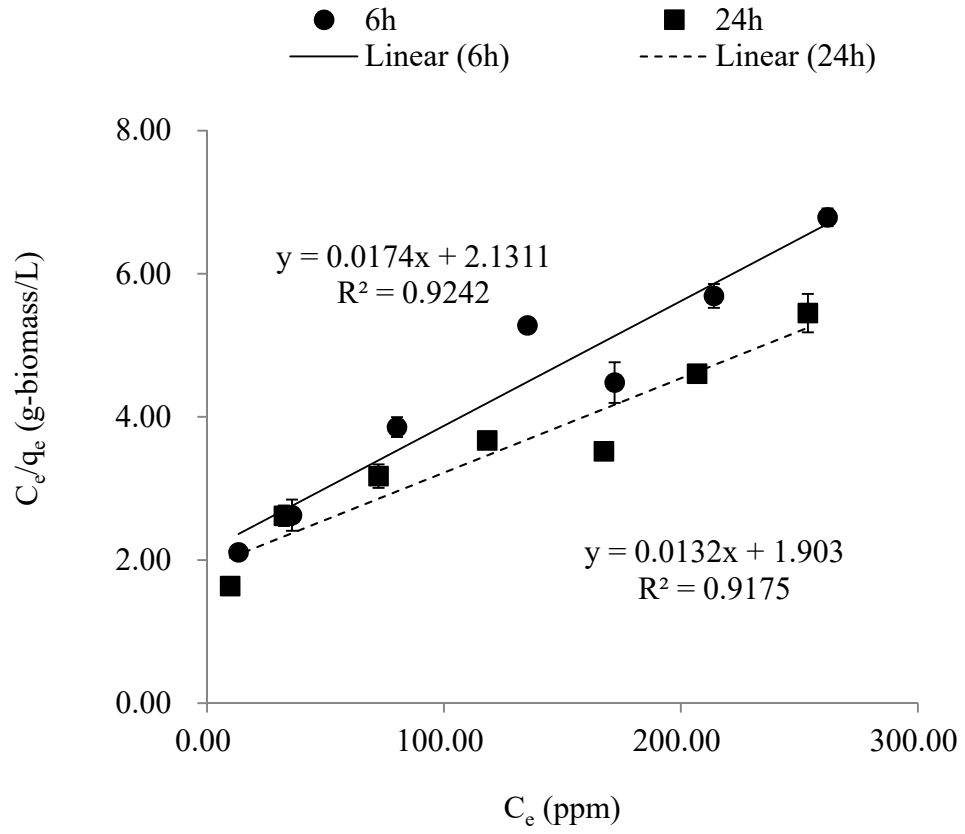

Figure 6.8b Linearized Langmuir isotherm model for total Cr biosorption by *Mucor rouxii* at different times.

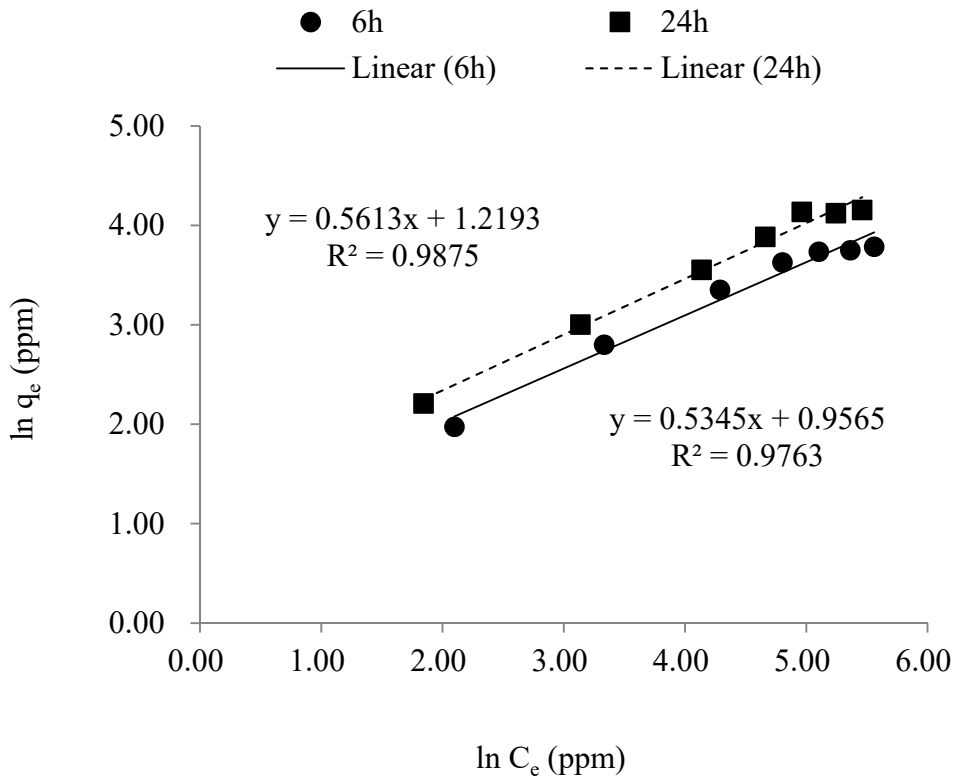

Figure 6.9a Linearized Freundlich isotherm model for Cr(VI) biosorption by *Mucor rouxii* at different times.

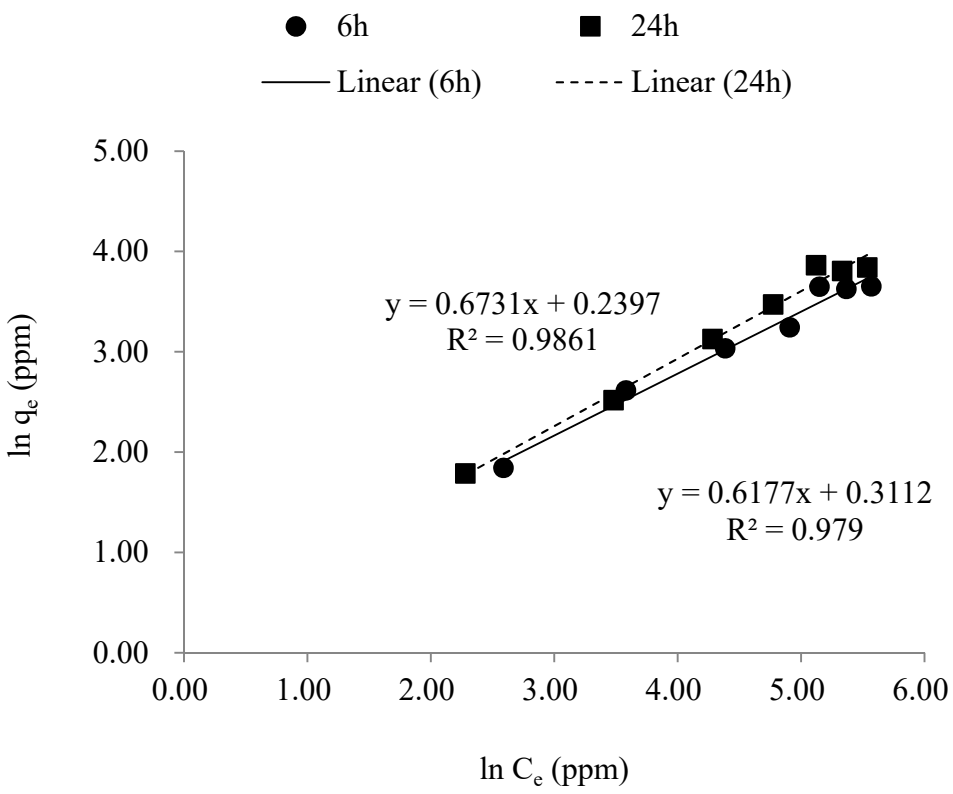

Figure 6.9b Linearized Freundlich isotherm model for total Cr biosorption by *Mucor rouxii* at different times.

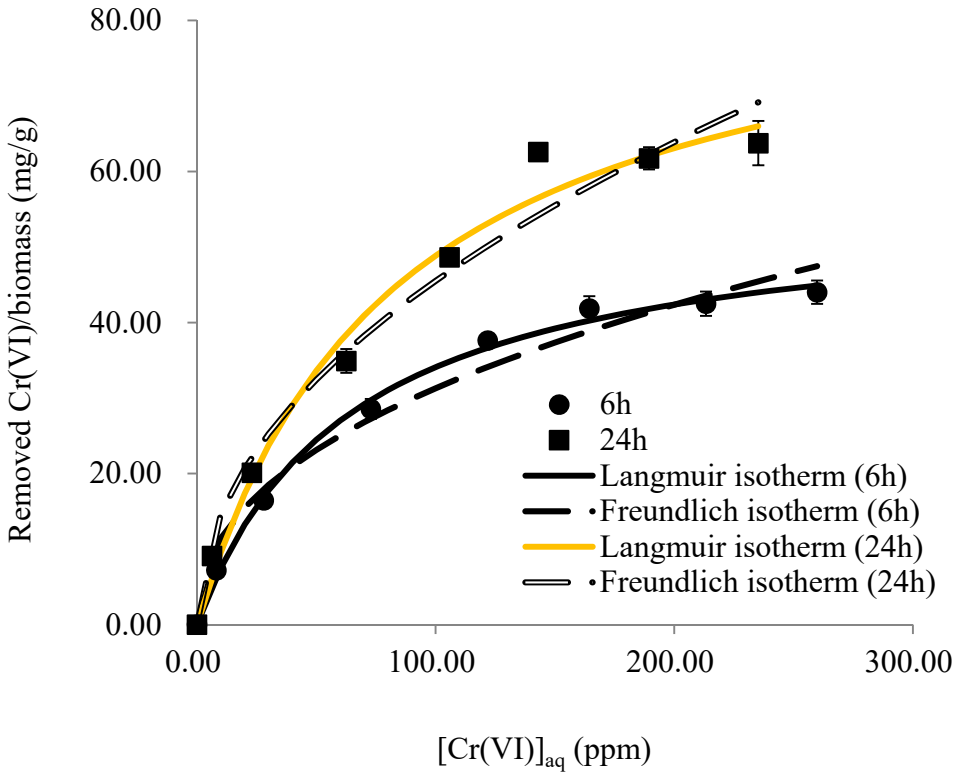

Figure 6.10a Non-linearized Langmuir and Freundlich isotherm models for Cr(VI) biosorption by *Mucor rouxii* at different times.

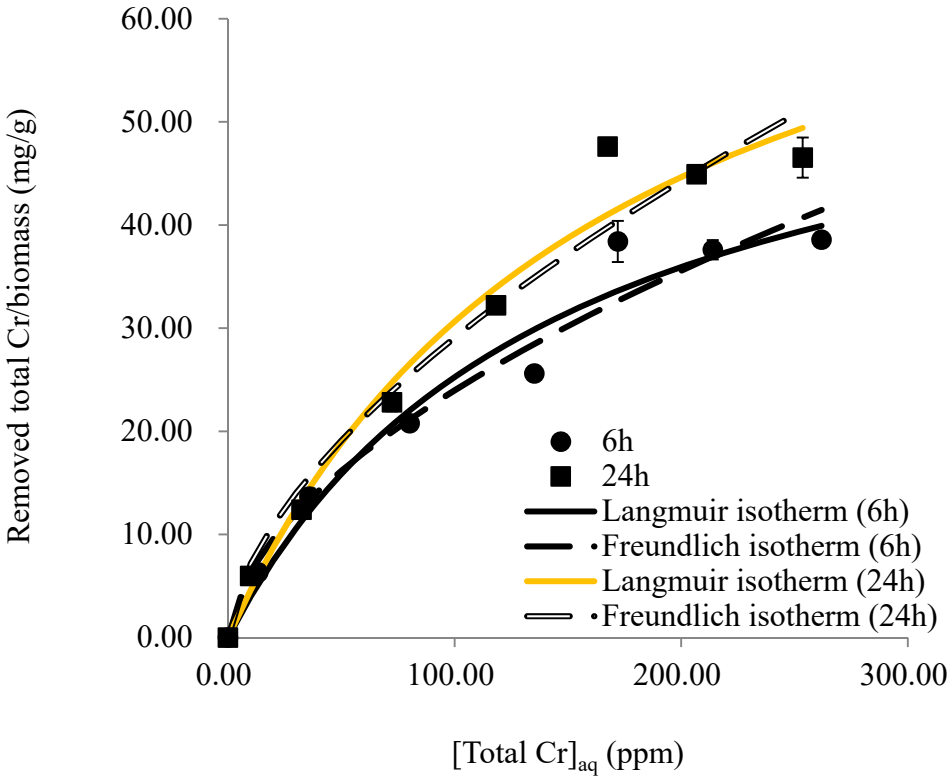

Figure 6.10b Non-linearized Langmuir and Freundlich isotherm models for total Cr biosorption by *Mucor rouxii* at different times.

Table 6.1 Comparison of parameters obtained from the linearized and non-linearized Langmuir and Freundlich isotherm models for Cr biosorption by *Mucor rouxii*.

		Cr(VI) (6h)	Cr(VI) (24h)	Total Cr (6h)	Total Cr (24h)
Linearized Langmuir	q_{max} (mg/g)	54.64 ± 2.73	83.33 ± 5.37	57.47 ± 0.23	75.76 ± 5.33
	b_L (L/mg)	0.0169 ± 0.0020	0.0149 ± 0.0019	0.0082 ± 0.0000	0.0069 ± 0.0007
	r^2	0.9957 ± 0.0050	0.9746 ± 0.0016	0.9242 ± 0.0189	0.9175 ± 0.0035
	SSE	7.97	74.35	50.14	64.39
	RMSE	1.07	3.26	2.68	3.03
	SE	1.26	3.86	3.17	3.59
Linearized Freundlich	k_F (L/g)	2.60 ± 0.22	3.38 ± 0.27	1.37 ± 0.01	1.27 ± 0.07
	n_F	1.87 ± 0.1	1.78 ± 0.07	1.62 ± 0.00	1.49 ± 0.03
	r^2	0.9763 ± 0.0043	0.9875 ± 0.0052	0.9790 ± 0.0106	0.9861 ± 0.0013
	SSE	84.42	148.89	55.79	100.37
	RMSE	3.47	4.61	2.82	3.79
	SE	4.11	5.46	3.34	4.48

Non-linearized Langmuir	q_{max} (mg/g)	56.04 ± 2.35	89.18 ± 6.31	62.23 ± 0.01	82.16 ± 5.48
	b_L (L/mg)	0.0155 ± 0.0013	0.0120 ± 0.0016	0.0068 ± 0.0002	0.0059 ± 0.0005
	r^2	0.9966 ± 0.0059	0.9858 ± 0.0055	0.9698 ± 0.0124	0.9759 ± 0.0054
	SSE	7.10	64.53	48.11	61.56
	RMSE	1.00	3.04	2.62	2.97
	SE	1.19	3.59	3.10	3.51
Non-linearized Freundlich	k_F (L/g)	4.20 ± 0.29	4.79 ± 0.50	1.75 ± 0.06	1.78 ± 0.14
	n_F	2.29 ± 0.09	2.05 ± 0.11	1.76 ± 0.01	1.65 ± 0.05
	r^2	0.9766 ± 0.0069	0.9745 ± 0.0072	0.9675 ± 0.0122	0.9645 ± 0.0071
	SSE	49.04	115.92	51.97	90.57
	RMSE	2.65	4.07	2.72	3.60
	SE	3.13	4.81	3.22	4.26

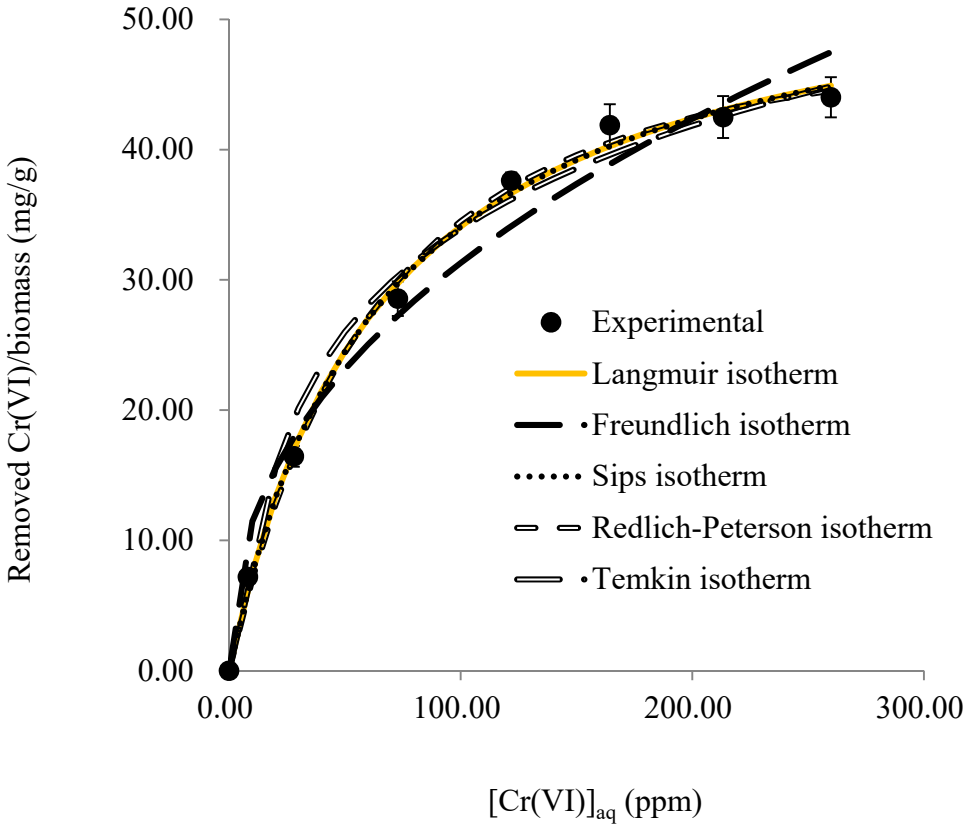

Figure 6.11a Non-linearized isotherm models for Cr(VI) biosorption by *Mucor rouxii* (6 h).

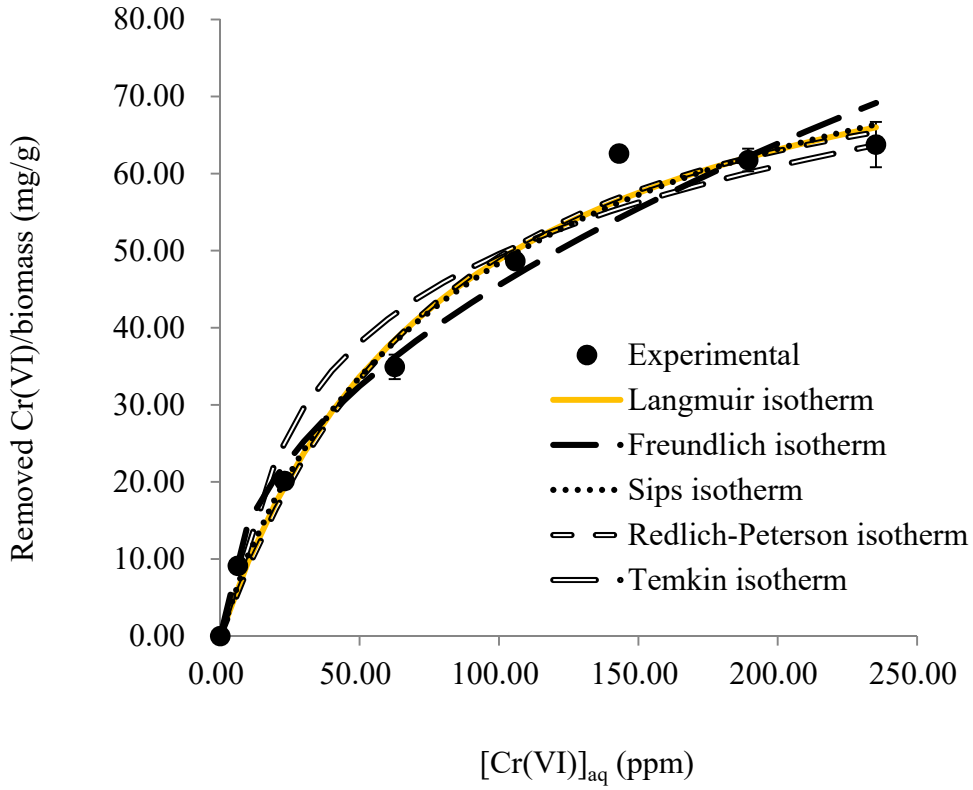

Figure 6.11b Non-linearized isotherm models for Cr(VI) biosorption by *Mucor rouxii* (24 h).

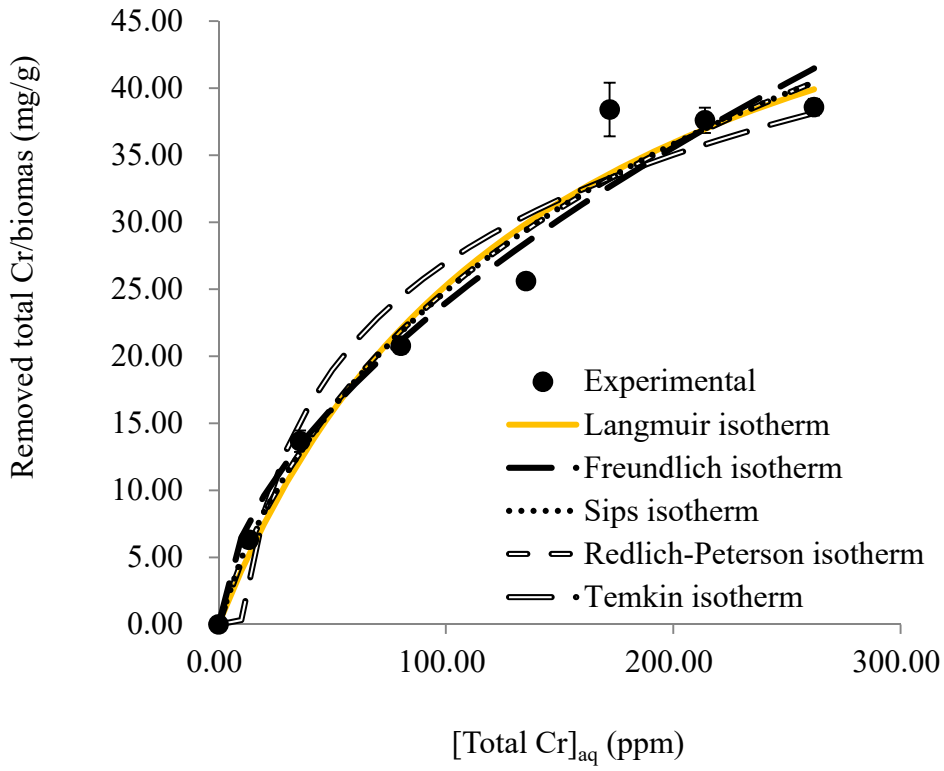

Figure 6.11c Non-linearized isotherm models for total Cr biosorption by *Mucor rouxii* (6 h).

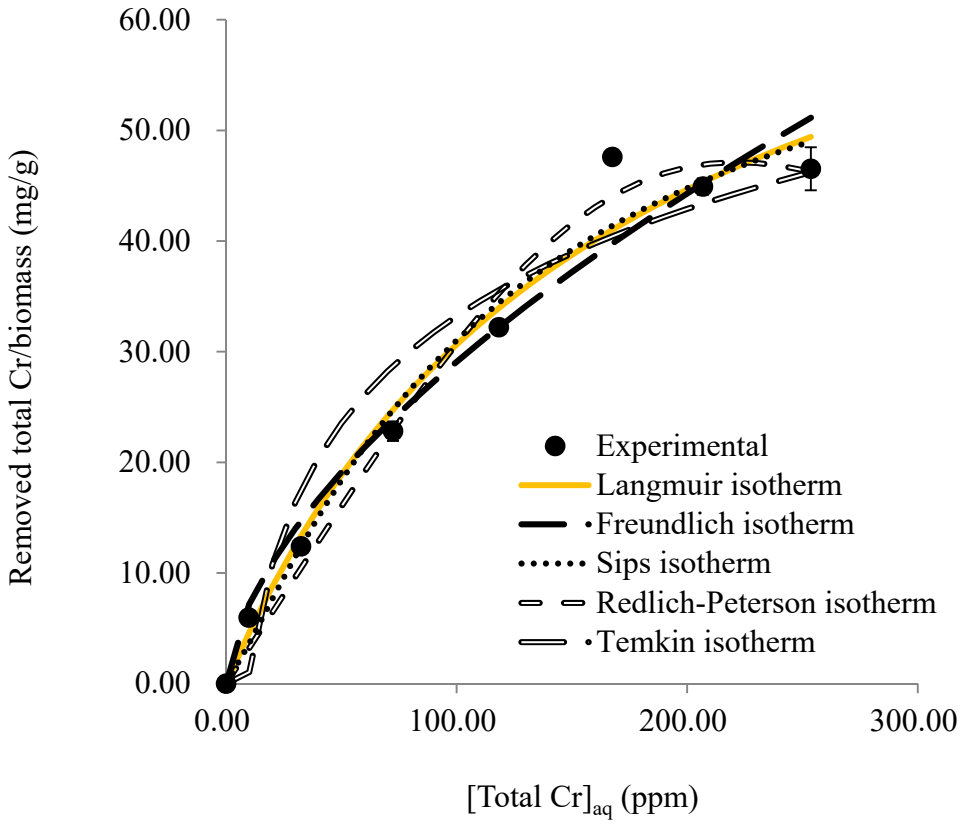

Figure 6.11d Non-linearized isotherm models for total Cr biosorption by *Mucor rouxii* (24 h).

Table 6.2 Comparison of parameters obtained from the non-linearized isotherm models for Cr biosorption by *Mucor rouxii*.

		Cr(VI) 6h	Cr(VI) 24h	Total Cr 6h	Total Cr 24h
Langmuir	q_{max} (mg/g)	56.04 ± 2.35	89.18 ± 6.31	62.23 ± 0.01	82.16 ± 5.48
	b_L (L/mg)	0.0155 ± 0.0013	0.0120 ± 0.0016	0.0068 ± 0.0002	0.0059 ± 0.0005
	r^2	0.9966 ± 0.0059	0.9858 ± 0.0055	0.9698 ± 0.0124	0.9759 ± 0.0054
	SSE	7.10	64.53	48.11	61.56
	RMSE	1.00	3.04	2.62	2.97
	SE	1.19	3.59	3.10	3.51
Freundlich	k_F (L/g)	4.20 ± 0.29	4.79 ± 0.50	1.75 ± 0.06	1.78 ± 0.14
	n_F	2.29 ± 0.09	2.05 ± 0.11	1.76 ± 0.01	1.65 ± 0.05
	r^2	0.9766 ± 0.0069	0.9745 ± 0.0072	0.9675 ± 0.0122	0.9645 ± 0.0071
	SSE	49.04	115.92	51.97	90.57
	RMSE	2.65	4.07	2.72	3.60
	SE	3.13	4.81	3.22	4.26

Sips	q_{max} (mg/g)	55.98 ± 1.12	96.70 ± 6.13	82.95 ± 0.92	69.66 ± 3.57
	n	0.9985 ± 0.0333	1.10 ± 0.02	1.21 ± 0.01	0.8593 ± 0.0016
	b (L/mg)	0.0155 ± 0.0027	0.0150 ± 0.0026	0.0094 ± 0.0003	0.0038 ± 0.0003
	r^2	0.9966 ± 0.0059	0.9862 ± 0.0052	0.9712 ± 0.0122	0.9767 ± 0.0054
	SSE	7.10	62.90	46.06	59.51
	RMSE	1.00	3.00	2.56	2.92
	SE	1.33	3.97	3.39	3.86
Redlich-Peterson	k_R (L/g)	0.7750 ± 0.0296	0.9578 ± 0.0279	0.5678 ± 0.0315	0.3225 ± 0.0105
	α (L/mg)	0.0083 ± 0.0008	0.0056 ± 0.0000	0.0373 ± 0.0052	6.42E-08 ± 2.20E-07
	β	1.0880 ± 0.0021	1.11 ± 0.02	0.7674 ± 0.0138	2.94 ± 0.40
	r^2	0.9969 ± 0.0059	0.9860 ± 0.0054	0.9706 ± 0.0122	0.9852 ± 0.0016
	SSE	6.42	63.78	46.97	37.87
	RMSE	0.96	3.02	2.59	2.33
	SE	1.27	3.99	3.43	3.08
Temkin	a_T (L/mg)	0.1947 ± 0.0164	0.2006 ± 0.0172	0.1029 ± 0.0008	0.1078 ± 0.0041
	b_T (J/mol)	216.80 ± 9.05	149.90 ± 7.28	213.90 ± 1.70	177.30 ± 6.15

	r^2	0.9890 ± 0.0047	0.9653 ± 0.0003	0.9523 ± 0.0102	0.9399 ± 0.0018
	SSE	23.19	157.86	76.10	153.53
	RMSE	1.82	4.75	3.30	4.68
	SE	2.15	5.62	3.90	5.54
Linearized D-R	q_D (mg/g)	34.78 ± 0.31	46.93 ± 0.43	29.07 ± 0.46	32.80 ± 0.37
	β (mol^2/kJ^2)	19.84 ± 1.03	12.84 ± 0.39	49.93 ± 1.69	30.61 ± 0.37
	r^2	0.8057 ± 0.0130	0.7428 ± 0.0202	0.7755 ± 0.0169	0.7010 ± 0.0128
	SSE	421.33	1390.96	407.59	876.57
	RMSE	7.76	13.68	7.63	11.19
	SE	9.18	16.19	9.03	13.24

6.4 Adsorption kinetics

To obtain the kinetic profiles of Cr(VI) removal by *Mucor rouxii* in aqueous solution, the concentrations of Cr were examined as a function of time. Fig. 6.12 illustrates the Cr concentration profiles during the removal of Cr(VI) from aqueous solution at a contact time of 72 h. The Cr(VI) concentration decreased rapidly within six hours due to the electrostatic attraction between the anionic Cr(VI) and the positively-charged biomass surface, while the concentration of Cr(III), which was not initially present in aqueous solution, increased with increasing contact time. The results showed that the fungal biomass was able to reduce Cr(VI) to Cr(III). It is important to note that the concentration of total Cr decreased sharply within the first few hours and reached equilibrium after 24 h. On the other hand, the contact time for Cr(VI) and Cr(III) to reach equilibrium were much longer than that for the total Cr. The adsorption of anionic Cr(VI) onto the positively-charged biomass surface (PZC = 3.5) should be very rapid, therefore, the reduction of Cr(VI) to Cr(III) might be the rate determining step in the removal of Cr(VI) from the aqueous solution by *Mucor rouxii* .

The Cr(VI) removal kinetics of the fungal biomass is illustrated in Fig. 6.13. The kinetic data were simulated by four kinetic models (pseudo-first order, pseudo-second order, Elovich and fractional power equations), and the computer

software GraphPad Prism 3.0 was used for the interpretation of the non-linear regression analysis. The correlation coefficient and error analyses of each model acted as indicators for evaluating the goodness of fit.

Figs. 6.14 and 6.15 illustrate the linearized pseudo-first and pseudo-second order kinetic plots, respectively. The kinetic parameters and error analyses obtained from the two linearized models are listed in Table 6.3. The results showed that the kinetic data of Cr(VI) could not be satisfactorily simulated by either the linearized pseudo-first or pseudo-second order kinetic models since the correlation coefficient obtained from the linearized pseudo-first order model was low (r^2 = 0.9028) and the error value calculated from the linearized pseudo-second order equation was high (SE = 9.78). The non-linearized forms of the two models are depicted in Fig. 6.16 and the results showed that both the non-linearized pseudo-first (r^2 = 0.6083, SE = 10.77) and pseudo-second order models (r^2 = 0.7069, SE = 9.31) could not provide a good correlation with the kinetic data because the correlation coefficients were low and the error values were high.

The Elovich and fractional power equations were also employed to describe the kinetic data of Cr(VI) (Fig. 6.17). The results indicated that the fractional power model showed the best correlation among all the models with the highest

correlation coefficient (r^2 = 0.9479) and the lowest error value (SE = 3.93), followed by the Elovich (r^2 = 0.8148, SE = 7.41), the non-linearized pseudo-second order (r^2 = 0.7069, SE = 9.32) and the non-linearized pseudo-first order equations (r^2 = 0.6083, SE = 10.77) (Table 6.4).

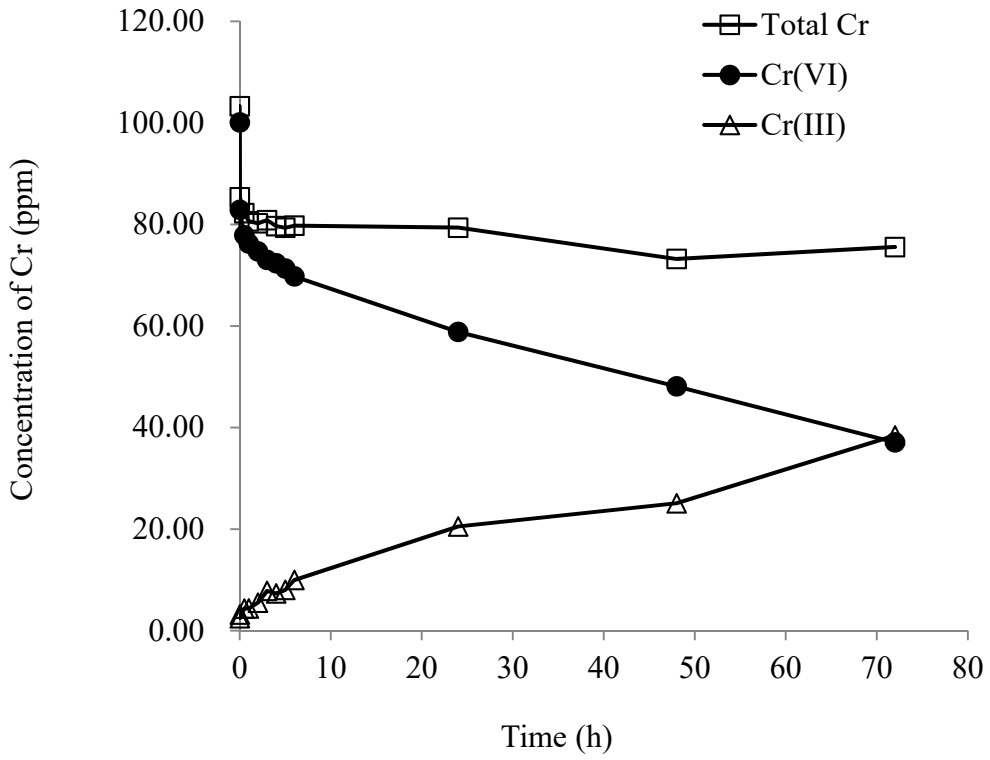

Figure 6.12 Cr concentration profiles during the removal of Cr(VI) from aqueous solution by *Mucor rouxii* (25℃).

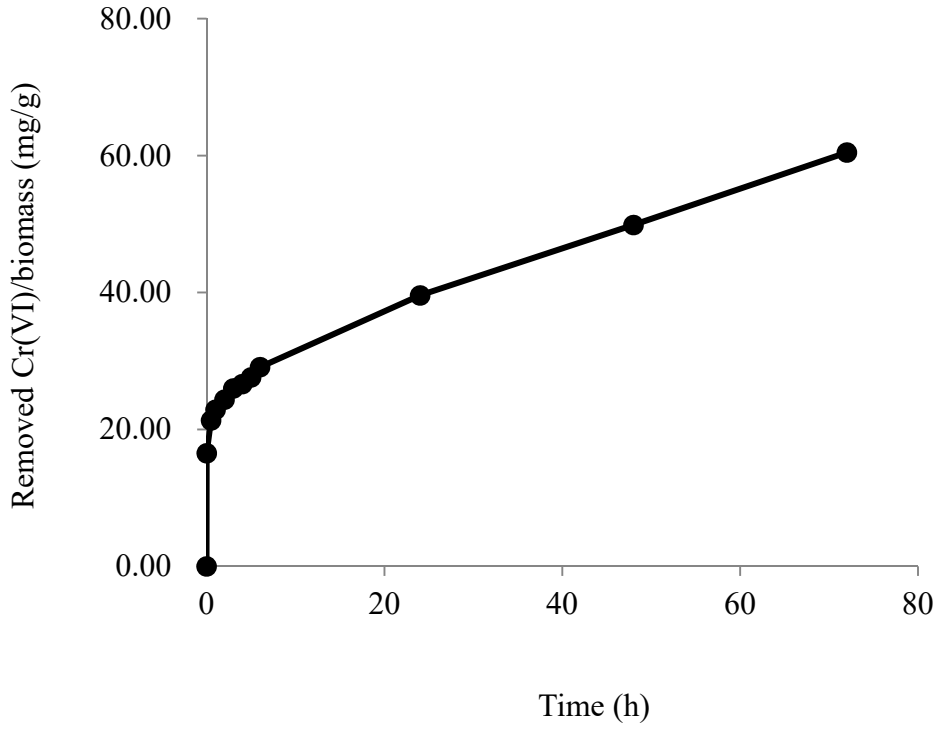

Figure 6.13 Kinetics on Cr(VI) removal by *Mucor rouxii* (25℃).

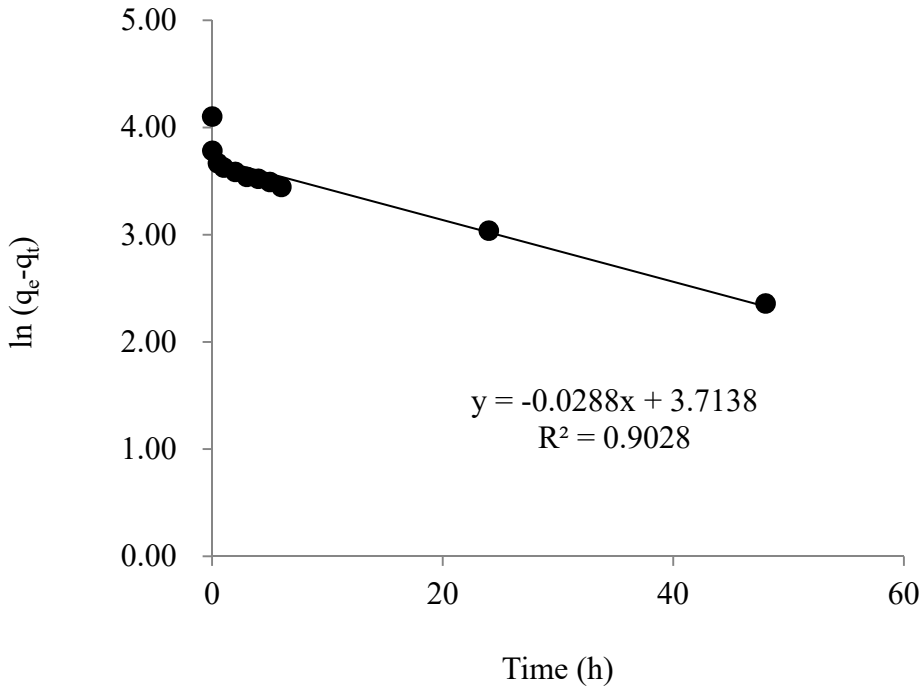

Figure 6.14 Linearized pseudo-first order plot of Cr(VI) removal by *Mucor rouxii* (25℃).

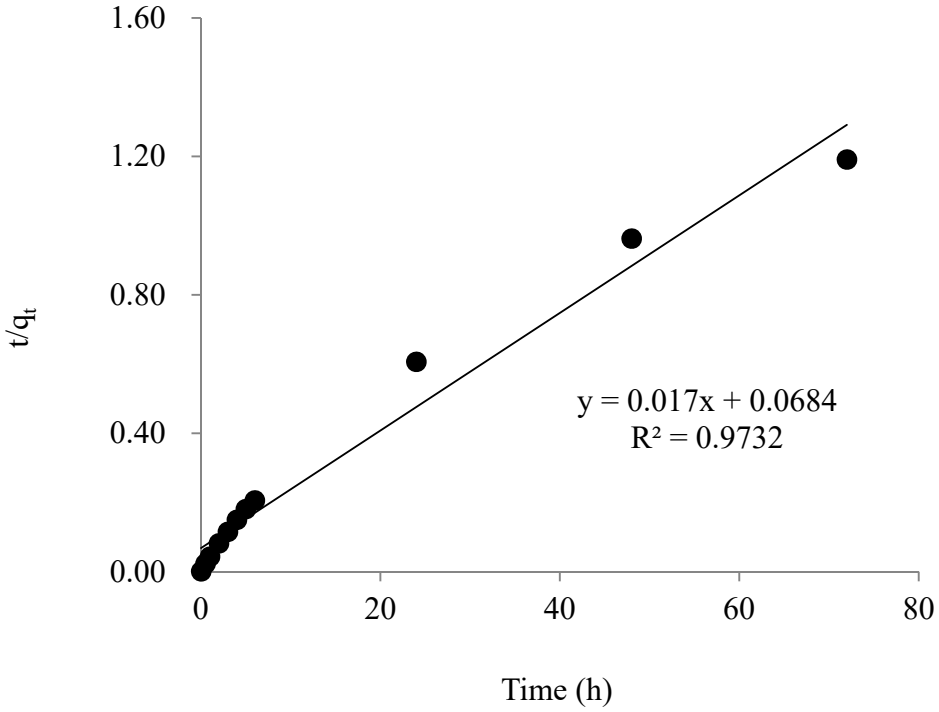

Figure 6.15 Linearized pseudo-second order plot of Cr(VI) removal by *Mucor rouxii* (25℃).

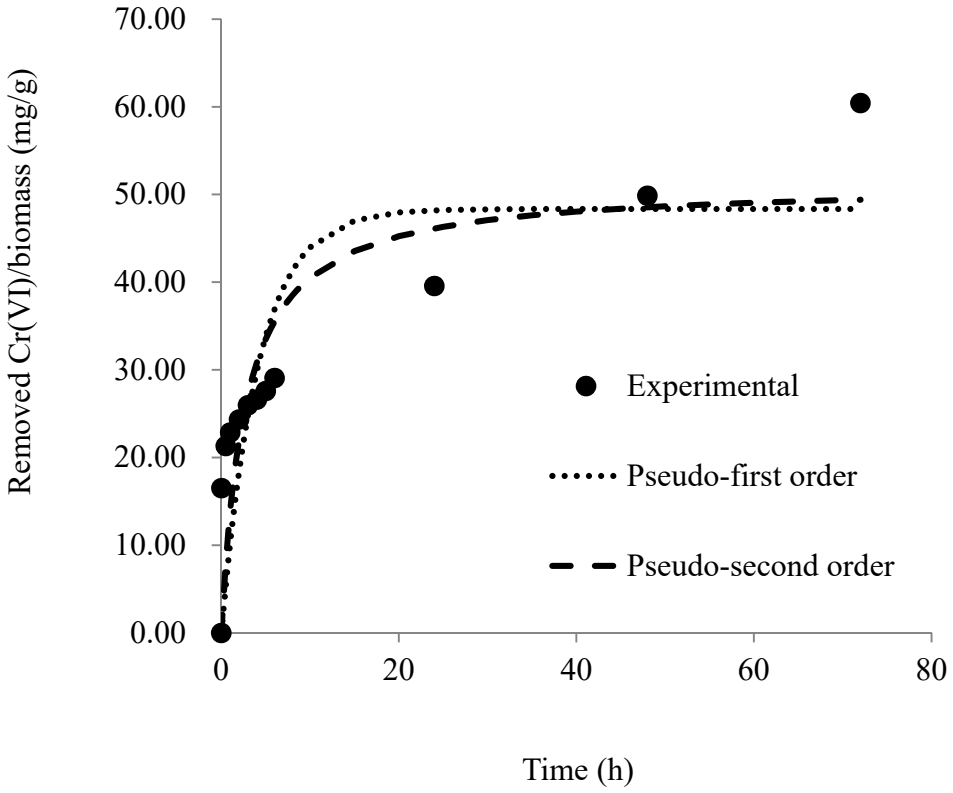

Figure 6.16 Non-linearized pseudo-first and pseudo-second order kinetic plots of Cr(VI) removal by *Mucor rouxii* (25℃).

Table 6.3 Comparison of parameters obtained from the linearized and non-linearized pseudo-first and pseudo-second order models for Cr(VI) removal by *Mucor rouxii* (25℃).

	Pseudo-first order					
	q_e (mg/g)	k_1 (h^{-1})	r^2	SSE	RMSE	SE
Linearized	41.01	0.0288	0.9028	4996.69	21.31	23.56
Non-linearized	48.35	0.2406	0.6083	1044.48	9.74	10.77
	Pseudo-second order					
	q_e (mg/g)	k_2 (g/mg-h)	r^2	SSE	RMSE	SE
Linearized	58.82	0.0042	0.9732	861.42	8.85	9.78
Non-linearized	51.23	0.0074	0.7069	781.46	8.43	9.31

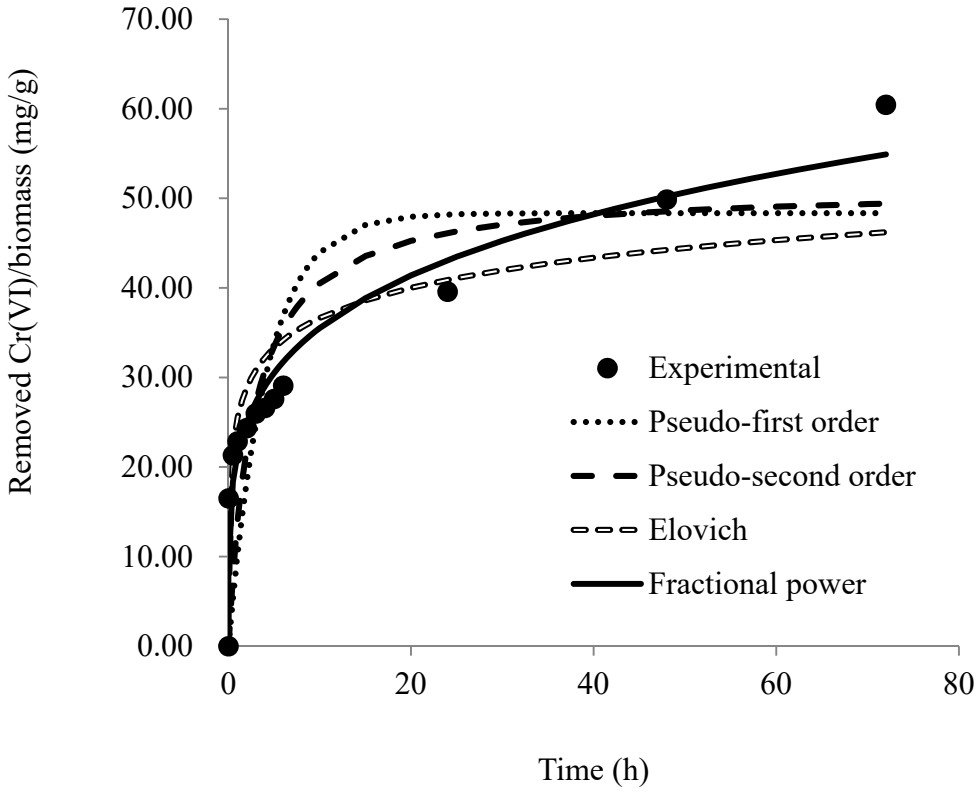

Figure 6.17 Non-linearized kinetic models for Cr(VI) removal by *Mucor rouxii* (25℃).

Table 6.4 Comparison of parameters obtained from the non-linearized kinetic models for Cr(VI) removal by *Mucor rouxii* (25℃).

Models		
Pseudo-first order	q_e (mg/g)	48.35
	k_1 (h^{-1})	0.2406
	r^2	0.6083
	SSE	1044.48
	RMSE	9.74
	SE	10.77
Pseudo-second order	q_e (mg/g)	51.23
	k_2 (g/mg-h)	0.00738
	r^2	0.7069
	SSE	781.46
	RMSE	8.43
	SE	9.32
Elovich	α (mg/g-h)	943
	β (g/mg)	0.2066
	r^2	0.8148
	SSE	493.79
	RMSE	6.70
	SE	7.41
Fractional power	k (mg/g-h^v)	21.38
	v	0.2205
	r^2	0.9479
	SSE	138.76
	RMSE	3.55
	SE	3.93

6.5 Effect of temperature

Changes in temperature may affect the kinetics of Cr(VI) removal process. Figs. 6.18a-c show the Cr concentration profiles at 20, 25 and 40℃, respectively. After 24 hours, the percentage removal of Cr(VI) at 20, 25 and 40℃ were 36.95, 40.99 and 45.16%, respectively. At the same time, the Cr(III) concentration in aqueous solution generally increased with increasing temperature. The increase in Cr(VI) removal and Cr(III) concentration might be due to the increase in the chance of collision between Cr(VI) ions and the functional groups on the biomass surface at higher temperatures. Hence, the adsorption and reduction of Cr(VI) were enhanced as the temperature increased. The concentration of total Cr decreased sharply within the first few hours and reached equilibrium after 24 hours. On the other hand, the contact time for Cr(VI) and Cr(III) to reach equilibrium were much longer than for that of the total Cr. The adsorption of anionic Cr(VI) onto the positively-charged biomass surface (PZC = 3.5) should be very rapid, therefore, the reduction of Cr(VI) to Cr(III) might be the rate determining step in the removal of Cr(VI) from the aqueous solution by *Mucor rouxii* . The kinetic data of the removed Cr(VI) obtained at 20, 25 and 40℃ were simulated by four kinetic models and the results are tabulated in Table 6.5. The

fractional power equation provided the best correlation with the kinetic data obtained at different temperatures with the highest correlation coefficients and the lowest error values, followed by the Elovich, the non-linearized pseudo-second order and the non-linearized pseudo-first order equations. The fractional power plots of Cr(VI) removal at different temperatures are illustrated in Fig. 6.19.

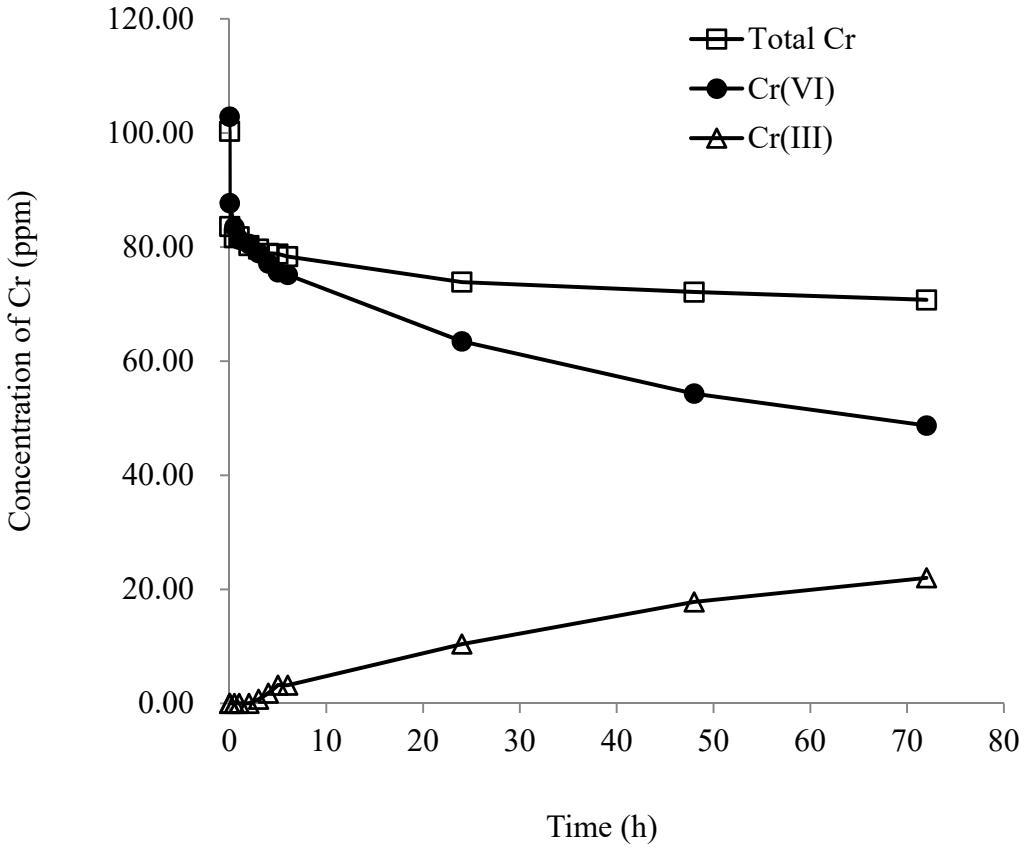

Figure 6.18a Cr concentration profiles during the removal of Cr(VI) from aqueous solution by *Mucor rouxii* (20℃).

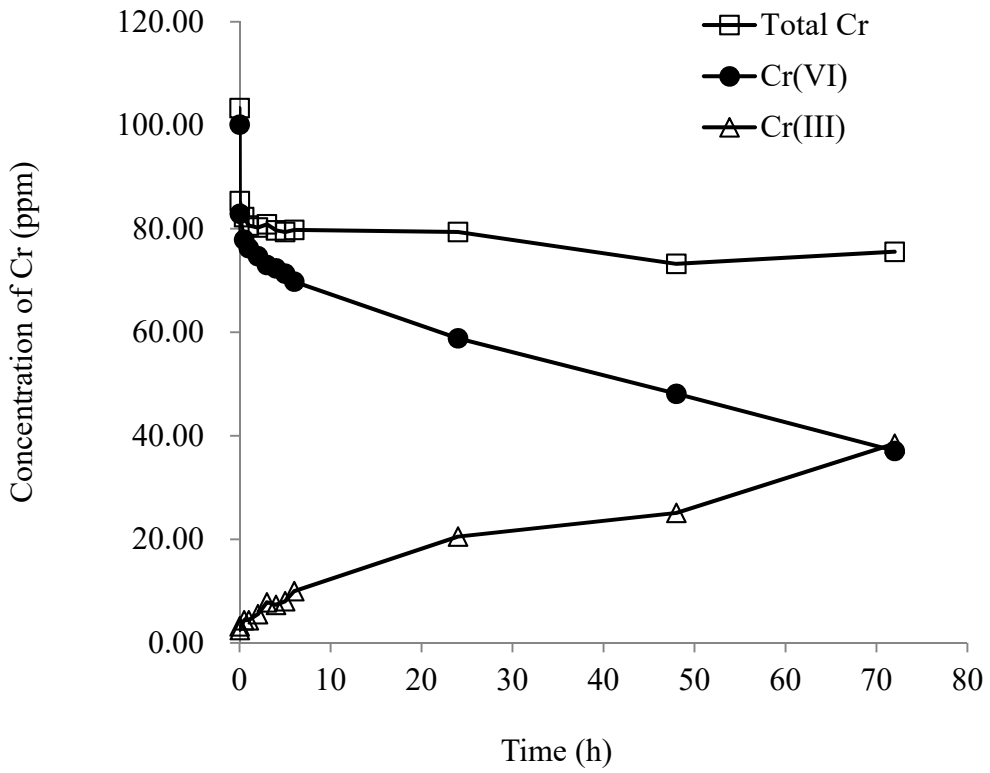

Figure 6.18b Cr concentration profiles during the removal of Cr(VI) from aqueous solution by *Mucor rouxii* (25℃)

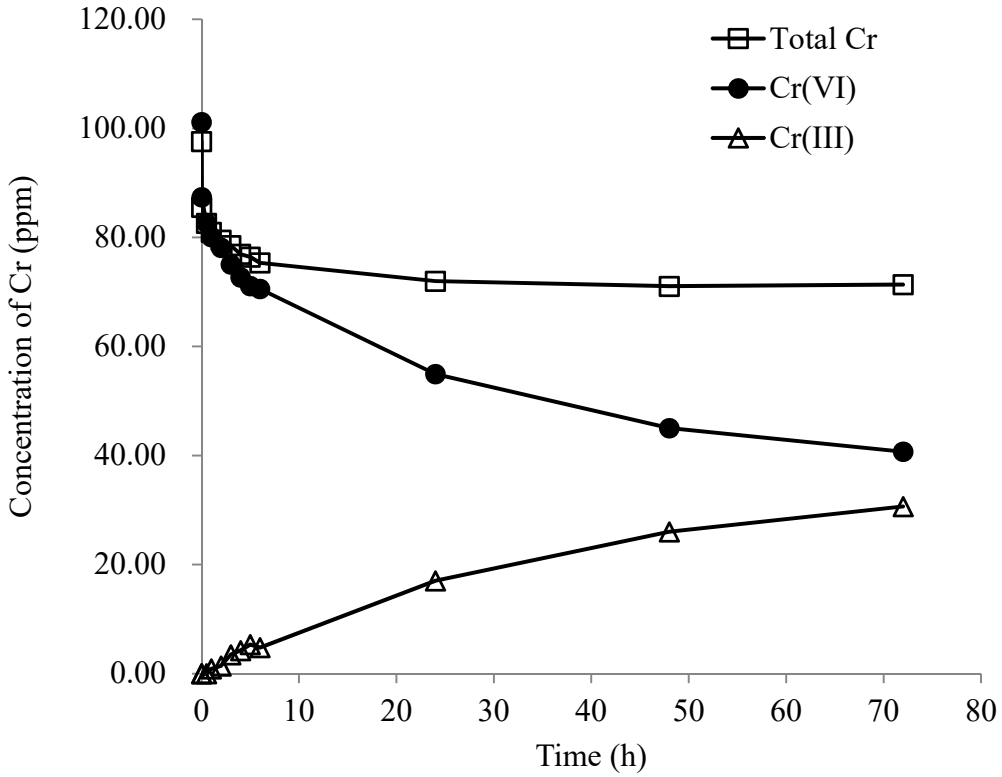

Figure 6.18c Cr concentration profiles during the removal of Cr(VI) from aqueous solution by *Mucor rouxii* (40℃).

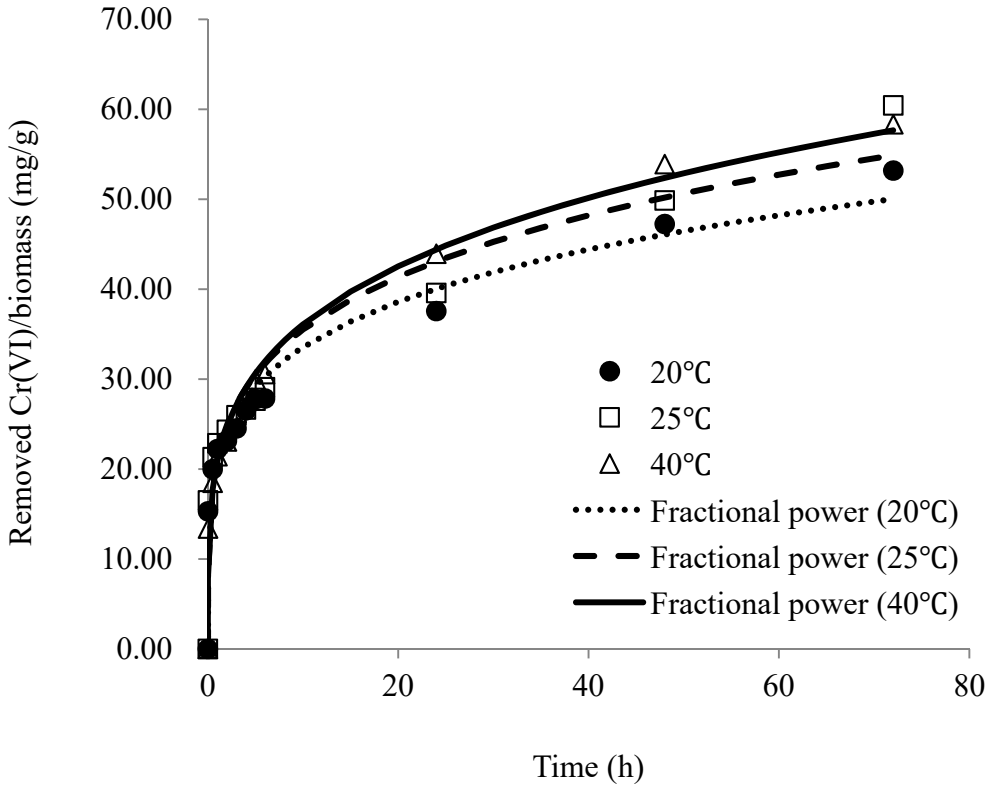

Figure 6.19 Fractional power plot of Cr(VI) removal by *Mucor rouxii* (20, 25, and 40℃).

Table 6.5 Comparison of parameters obtained from the non-linearized kinetic models for Cr(VI) removal by *Mucor rouxii* (20, 25 and 40℃).

Models		20℃	25℃	40℃
Pseudo-first order	q_e (mg/g)	44.00	48.35	50.93
	k_1 (h^{-1})	0.2788	0.2406	0.2245
	r^2	0.6226	0.6083	0.7742
	SSE	818.48	1044.48	678.32
	RMSE	8.63	9.74	7.85
	SE	9.54	10.77	8.68
Pseudo-second order	k_2 (g/mg-h)	46.01	51.23	54.6
	q_e (mg/g)	0.01039	0.00738	0.00599
	r^2	0.7295	0.7069	0.8424
	SSE	586.60	781.46	473.34
	RMSE	7.30	8.43	6.56
	SE	8.07	9.32	7.25
Elovich	β (g/mg)	1097	943	489.6

	α (mg/g-h)	0.2268	0.2066	0.1797
	r^2	0.8571	0.8148	0.8643
	SSE	309.80	493.79	407.68
	RMSE	5.31	6.70	6.09
	SE	5.87	7.41	6.73
Fractional power	k (mg/g-h^v)	21.06	21.38	20.89
	v	0.2023	0.2205	0.2374
	r^2	0.9664	0.9479	0.9863
	SSE	72.85	138.76	41.05
	RMSE	2.57	3.55	1.93
	SE	2.85	3.93	2.14

6.6 Intraparticle diffusion

The adsorption process mainly consists of three steps: (1) mass transfer of metal ions from bulk solution to the surface of the biomass particle; (2) pore diffusion of metal ions to the adsorption sites; (3) adsorption of metal ions onto the active sites. The third step should be the fastest. Therefore, the adsorption of metal ions onto the biomass surface is controlled by either boundary layer diffusion (step 1) or intraparticle diffusion (step 2), or by both steps (Hameed and EI-Khaiary 2008; Cheung et al. 2007).

The intraparticle diffusion equation is shown in Equation 5.27. Fig. 6.20 depicts the plots of q versus square root of t at different temperatures. If the intraparticle diffusion was the only rate determining step, the plot should pass through the origin; if not, the external mass transfer also controlled the biosorption to some extent. As shown in the figure, the plot did not pass through the origin, suggesting that besides the intraparticle diffusion, the external mass transfer also controlled the biosorption to some degree. The rate constants were obtained from the slopes of the plots and they are tabulated in Table 6.6. The rate constants increased with increasing temperature, indicating that the removal of the Cr(VI) ions from the bulk solution was enhanced by a higher temperature.

The intraparticle diffusion equation (r^2 = 0.98-0.99, SE = 0.93-1.85) could even provide a better correlation with the kinetic data than the fractional power equation (r^2 = 0.95-0.99, SE = 2.14-3.93). Both sections 6.5 and 6.6 show that the removal of Cr increased with increasing temperature.

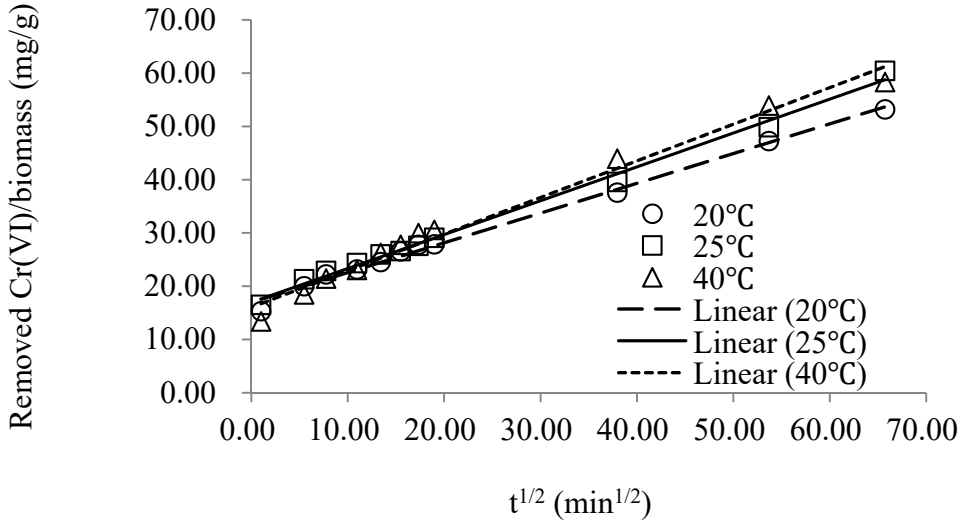

Figure 6.20 Intraparticle diffusion model for Cr(VI) removal by *Mucor rouxii* at different temperatures.

Table 6.6 Parameters obtained from intraparticle diffusion model for Cr(VI) removal by *Mucor rouxii* at different temperatures.

	Temperature (℃)		
	20	25	40
k_{p1} (mg/g-min$^{1/2}$)	0.5585	0.6356	0.6875
c	17.00	16.93	16.07
r^2	0.9936	0.9943	0.9836
SSE	8.69	10.13	34.29
RMSE	0.89	0.96	1.77
SE	0.93	1.01	1.85

6.7 Effect of agitation speed

Changes in agitation speed may affect the kinetics of Cr(VI) removal process. Figs. 6.21a-c show the effect of agitation speed (50, 250 and 500 rpm) on Cr concentration profiles during the removal of Cr(VI) from an aqueous solution. It could be observed that the concentration of Cr(VI) generally decreased with increasing agitation speed. At a higher agitation speed, the transport of Cr(VI) ions from the aqueous solution to the biomass surface was enhanced since the thickness of the boundary layer around the biomass particle was reduced. Thus, the adsorption of Cr(VI) ions was enhanced and more Cr(VI) ions could be removed as the agitation speed increased. On the other hand, the concentration of Cr(III) increased with increasing rotational speed. As the agitation speed increased, the chance of collision between the Cr(VI) ions and the electron-donating groups on the biomass surface increased, enhancing the rate of Cr(VI) reduction. These results indicated that higher agitation speeds could enhance the transport of Cr(VI) from the aqueous solution to the biomass surface, resulting in higher Cr(VI) removal and facilitating the reduction of Cr(VI) to Cr(III).

The kinetic data of the removed Cr(VI) obtained at 50, 250 and 500 rpm

were simulated by four kinetic models and the results are summarized in Table 6.7. The fractional power equation provided the best correlation with the kinetic data obtained at different agitation speeds with the highest correlation coefficients and the lowest error values, followed by the Elovich, the non-linearized pseudo-second order and the non-linearized pseudo-first order equations. The fractional power plots of Cr(VI) removal at different temperatures are illustrated in Fig. 6.22.

The intraparticle diffusion plots at different agitation speeds are shown in Fig. 6.23 and the model parameters are summarized in Table 6.8. The plot did not pass through the origin, suggesting that other than the intraparticle diffusion the external mass transfer also controlled the removal process to some extent. As seen in Table 6.8, the values of k_{p1} increased with increasing rotational speed, suggesting that a higher agitation speed may enhance the Cr(VI) removal. The intraparticle diffusion equation (r^2 = 0.98-1.00, SE = 0.97-1.29) could provide a better correlation with the kinetic data than the fractional power equation (r^2 = 0.95-0.97, SE = 2.33-3.93).

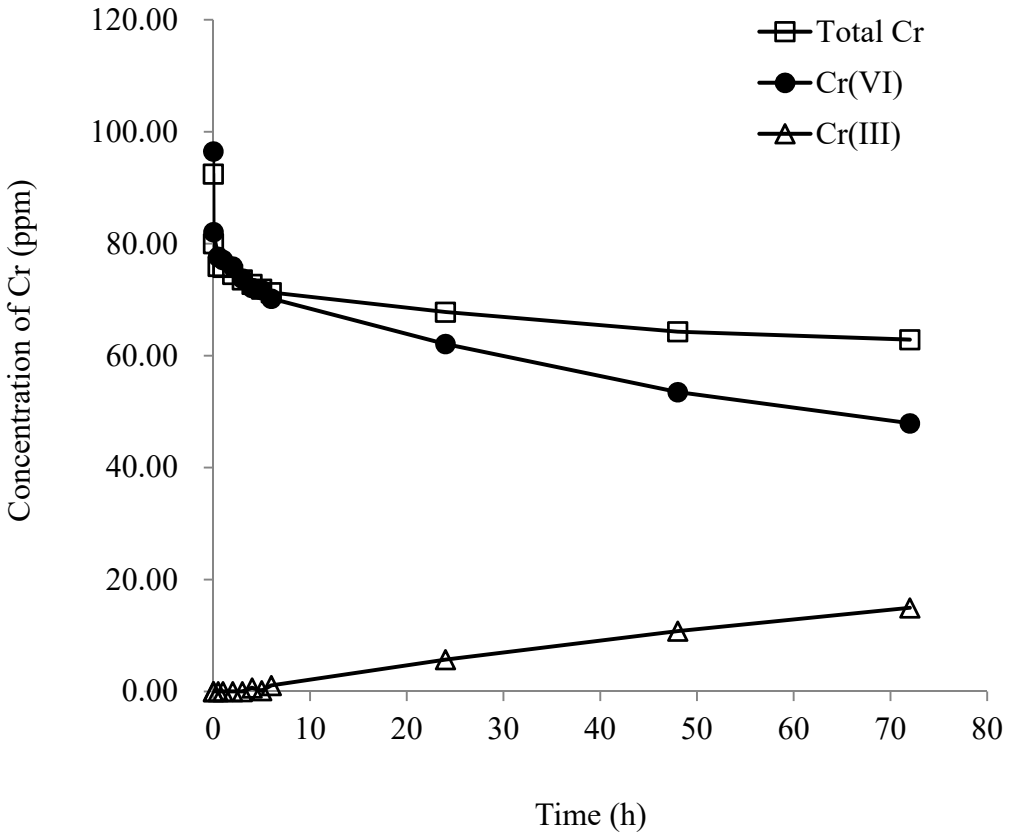

Figure 6.21a Cr concentration profiles during the removal of Cr(VI) from aqueous solution by *Mucor rouxii* (50 rpm).

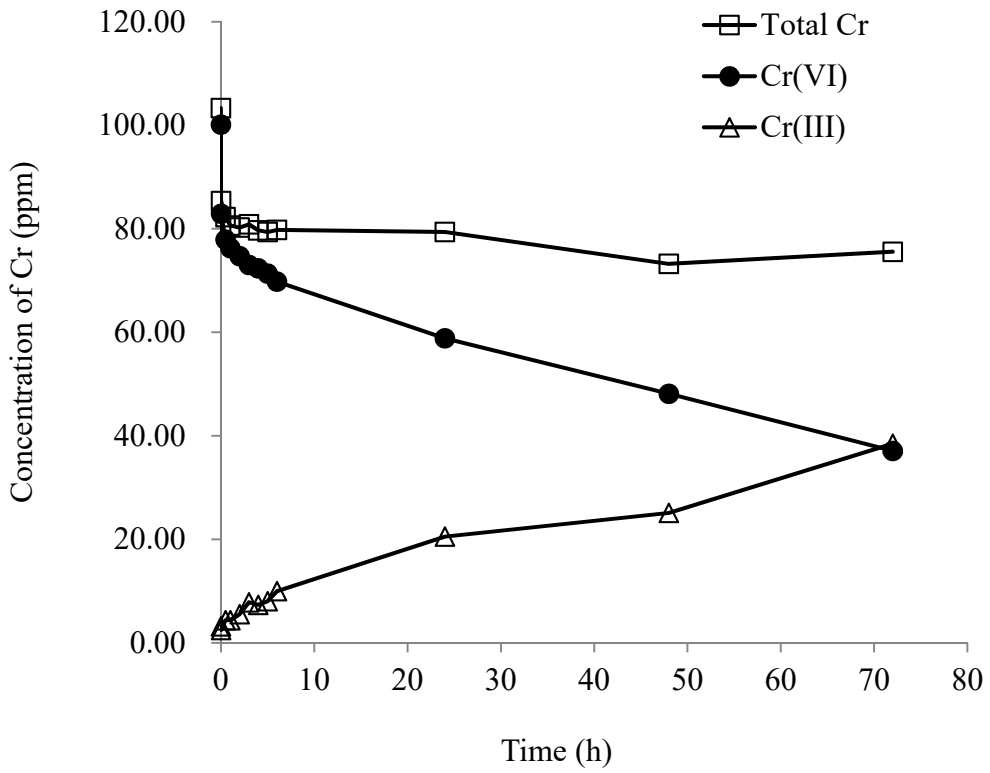

Figure 6.21b Cr concentration profiles during the removal of Cr(VI) from aqueous solution by *Mucor rouxii* (250 rpm).

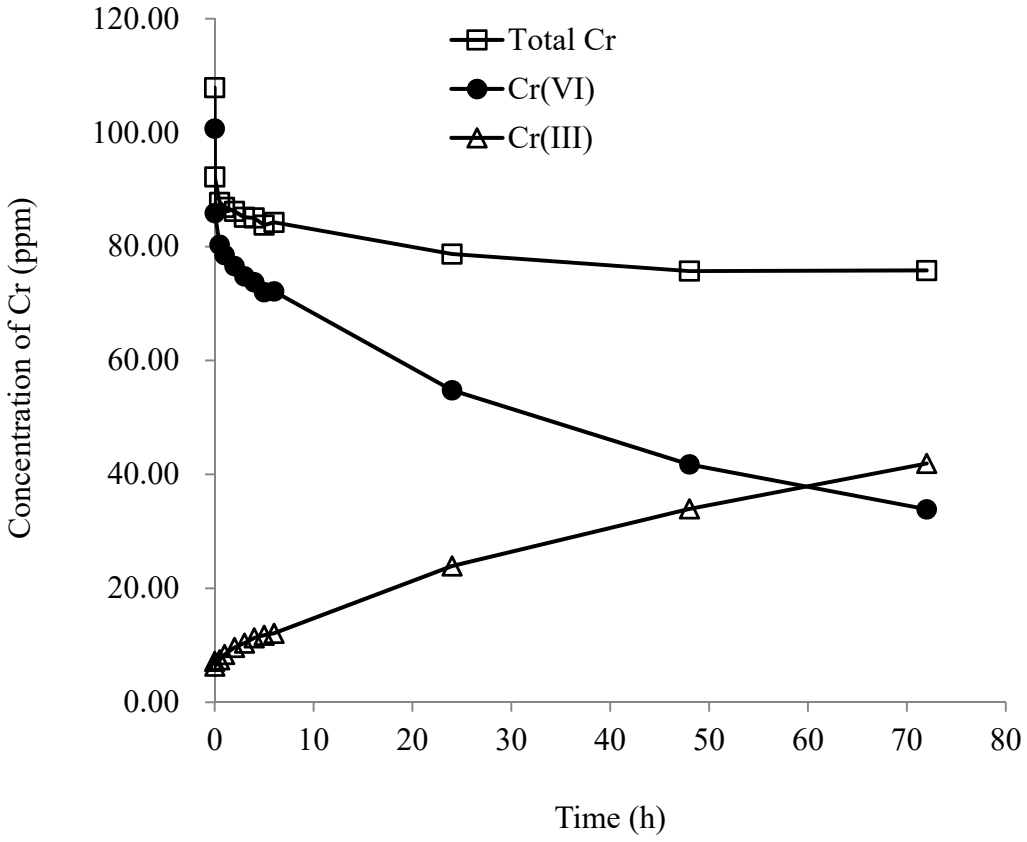

Figure 6.21c Cr concentration profiles during the removal of Cr(VI) from aqueous solution by *Mucor rouxii* (500 rpm).

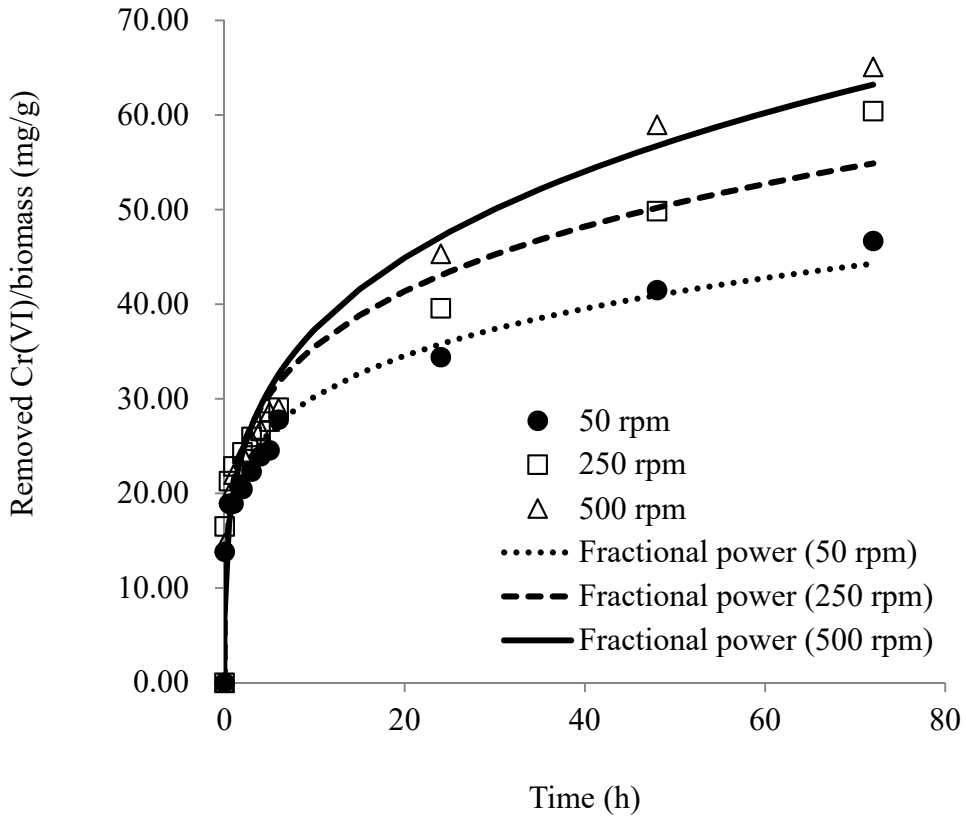

Figure 6.22 Fractional power plots of Cr(VI) removal by *Mucor rouxii* (50, 250 and 500 rpm).

Table 6.7 Comparison of parameters obtained from the non-linearized kinetic models for Cr(VI) removal by *Mucor rouxii* (50, 250 and 500 rpm).

		Cr(VI)		
		50 rpm	250 rpm	500 rpm
Pseudo-first order	q_e (mg/g)	39.12	48.35	56.06
	k_1 (h^{-1})	0.2958	0.2406	0.1788
	r^2	0.6404	0.6083	0.7439
	SSE	607.15	1044.48	940.51
	RMSE	7.43	9.74	9.25
	SE	8.21	10.77	10.22
Pseudo-second order	q_e (mg/g)	40.79	51.23	61.46
	k_2 (g/mg-h)	0.0127	0.00738	0.003836
	r^2	0.7424	0.7069	0.8092
	SSE	434.94	781.46	700.57
	RMSE	6.29	8.43	7.98
	SE	6.95	9.32	8.82

Elovich	α (mg/g-h)	1127	943	423.5
	β (g/mg)	0.2573	0.2066	0.1663
	r^2	0.8727	0.8148	0.8034
	SSE	214.92	493.79	721.99
	RMSE	4.42	6.70	8.10
	SE	4.89	7.41	8.96
Fractional power	k (mg/g-h^{ν})	19.36	21.38	20.19
	ν	0.1936	0.2205	0.2669
	r^2	0.9710	0.9479	0.9686
	SSE	48.91	138.76	115.46
	RMSE	2.11	3.55	3.24
	SE	2.33	3.93	3.58

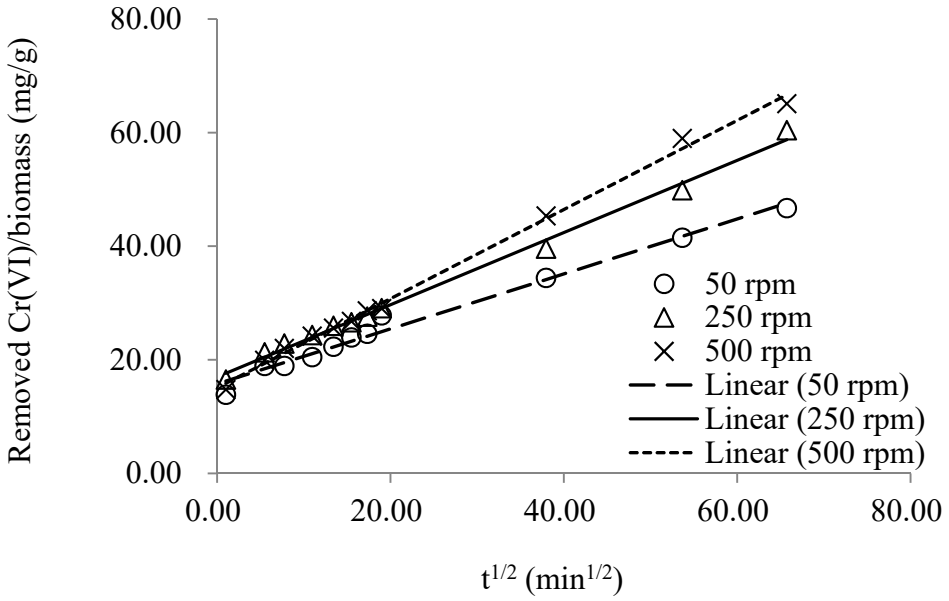

Figure 6.23 Intraparticle diffusion model for Cr(VI) removal by *Mucor rouxii* at different agitation speeds.

Table 6.8 Parameters obtained from the intraparticle diffusion model for Cr(VI) removal by *Mucor rouxii* at different agitation speeds.

	Agitation speed (rpm)		
	50	250	500
k_{p1} (mg/g-min$^{1/2}$)	0.4841	0.6356	0.7845
c	15.77	16.98	15.09
r^2	0.9840	0.9943	0.9965
SSE	16.55	10.13	9.40
RMSE	1.23	0.96	0.92
SE	1.29	1.01	0.97

6.8 Cr(VI) reduction kinetics

In Section 6.5, the biosorption-based kinetic models were used to simulate Cr(VI) removal process. From the previous analysis, both biosorption and reduction were involved in Cr(VI) removal by *Mucor rouxii*. Hence, in this section, kinetic models based on reduction were also applied to simulate the Cr(VI) removal process. The Cr(VI) reduction kinetics in aqueous solution were simulated by four different reduction kinetic models and the fitness of the models was evaluated by the correlation coefficient (r^2) and error analyses (SSE, RMSE and SE).

6.8.1 Park model

Park et al. (2005b) developed a reduction kinetic equation to describe the Cr(VI) removal mechanism and the equation was formulated based on three assumptions. First, the organic compounds on the biomass surface are responsible for reducing Cr(VI). Second, only one type of organic compound is capable of reducing Cr(VI). Third, the Cr(VI) reduction rate follows first-order kinetics. The reduction rate of Cr(VI) is expressed as follows:

$$\frac{d[Cr(VI)]}{dt} = -k_p\,[OC][Cr(VI)] \quad (mmol/l^{-1}\,h^{-1}) \qquad \text{(Equation 6.3)}$$

where OC (mmol/l) is the equivalent organic compound capable of reducing Cr(VI) and k_p (L/mmol-h) is the rate constant. The concentration of OC at a

given time is formulated as follows:

$$[OC] = [OC]_0 (1 - F) \quad (mmol/l) \qquad \text{(Equation 6.4)}$$

where F is the fraction of OC oxidized and $F = \frac{[Cr(VI)]_0 - [Cr(VI)]}{[OC]_0}$

The initial concentration of $[OC]_0$ can be expressed as follows:

$$[OC]_0 = C^*_{OC}\,[B] \quad (mmol/l) \qquad \text{(Equation 6.5)}$$

where C^*_{OC} (mmol/g) is the content of equivalent organic compound per gram of biomass and B is the biomass. By combining Equations 6.3-6.5, Equation 6.6 is yield:

$$\frac{d[Cr(VI)]}{dt} = -k_p\,[Cr(VI)]([Cr(VI)] + C^*_{OC}\,[B] - [Cr(VI)]_0) \quad (mmol\,l^{-1}\,h^{-1})$$

(Equation 6.6)

By integrating Equation 6.6, Equation 6.7 is yield:

$$[Cr(VI)] = \frac{C^*_{OC}\,[B][Cr(VI)]_0 - [Cr(VI)]_0^2}{C^*_{OC}\,[B]\exp\left(k_p\,(C^*_{OC}\,[B] - [Cr(VI)]_0)\,t\right) - [Cr(VI)]_0} \qquad \text{(Equation 6.7)}$$

The experimental data obtained at different temperatures and agitation speeds were simulated by the Park model and the plots are displayed in Figs. 6.24a-f. The model parameters are summarized in Table 6.9 and the results showed that the kinetic data could not be well simulated by the model since the correlation coefficients were low (r^2 = 0.65-0.82) and the error values were high (SE = 12.76-20.91). It could be observed that the model initially overestimated the Cr(VI) concentration in aqueous solution. The overestimation may be due to the

model assumption that only one kind of organic compound is capable of reducing Cr(VI). However, there may be more than one type of function groups that is able to reduce Cr(VI) ions. Thus, the model curves deviated from the experimental data.

Park et al. (2007b) have proposed another model for Cr(VI) reduction kinetics and the equation is formulated as:

$y = m\,t$ (Equation 6.8)

where $y = \ln\left(\frac{[Cr(VI)]_0\,([B] - [Cr(VI)]_0 + [Cr(VI)]}{[B][Cr(VI)]}\right)$

$m = k_M\,([B] - [Cr(VI)]_0)$

where B represents the fungal biomass and k_M (mg/L-h) is the overall rate coefficient of Cr(VI) reduction.

The values of k_M were calculated from the slope of the plot of y versus t. The experimental data obtained at different temperatures and agitation speeds were simulated by the modified model and the plots are shown in Fig. 6.25. As listed in Table 6.9, the model could not satisfactorily simulate the kinetic data since the error values were generally large (SE = 19.20-21.38).

6.8.2 Pseudo-first order reduction equation

The pseudo-first order reduction equation is expressed as:

$\ln C_t = \ln C_0 - K_1\,t$ (Equation 6.9)

where C_t is the Cr(VI) concentration at time t, C_0 is the initial Cr(VI) concentration and K_1 is the rate constant.

6.8.3 Pseudo-second order reduction equation:

The equation is shown below:

$$\frac{1}{C_t} = K_2\, t + \frac{1}{C_0} \qquad \text{(Equation 6.10)}$$

where C_t is the Cr(VI) concentration at time t, C_0 is the initial Cr(VI) concentration and K_2 is the rate constant.

The plots of the pseudo-first order and pseudo-second order reduction models are illustrated in Figs. 6.26 and 6.27, respectively. Table 6.9 summarizes the model parameters and the results showed that the pseudo-second order reduction equation generally provided better simulation to the kinetic data with higher correlation coefficients (r^2 = 0.91-0.99) and lower error values (SE = 3.97-7.30) than the pseudo-first order reduction equation (r^2 = 0.84-0.93, SE = 6.20-7.56). In the case of biomass concentration of 10 g/L, the pseudo-first order reduction equation could better simulate the kinetic data with a higher coefficient and a lower error value than the pseudo-second order reduction equation. The values of rate constants, K_2, generally increased with increasing temperatures, agitation speeds and biomass concentrations. The kinetic modeling results obtained from the intraparticle diffusion model were compared

to those obtained from the pseudo-second order reduction equations. The former model could provide a better simulation of the kinetic data with higher correlation coefficients (r^2 = 0.82-1.00) and lower error values (SE = 0.74-1.85) than the later one (r^2 = 0.66-0.99, SE = 6.28-31.78). In the case of biomass concentration of 5 g/L, the pseudo-second order reduction equation could better simulate the kinetic data with higher correlation coefficients and lower error values than the intraparticle diffusion model.

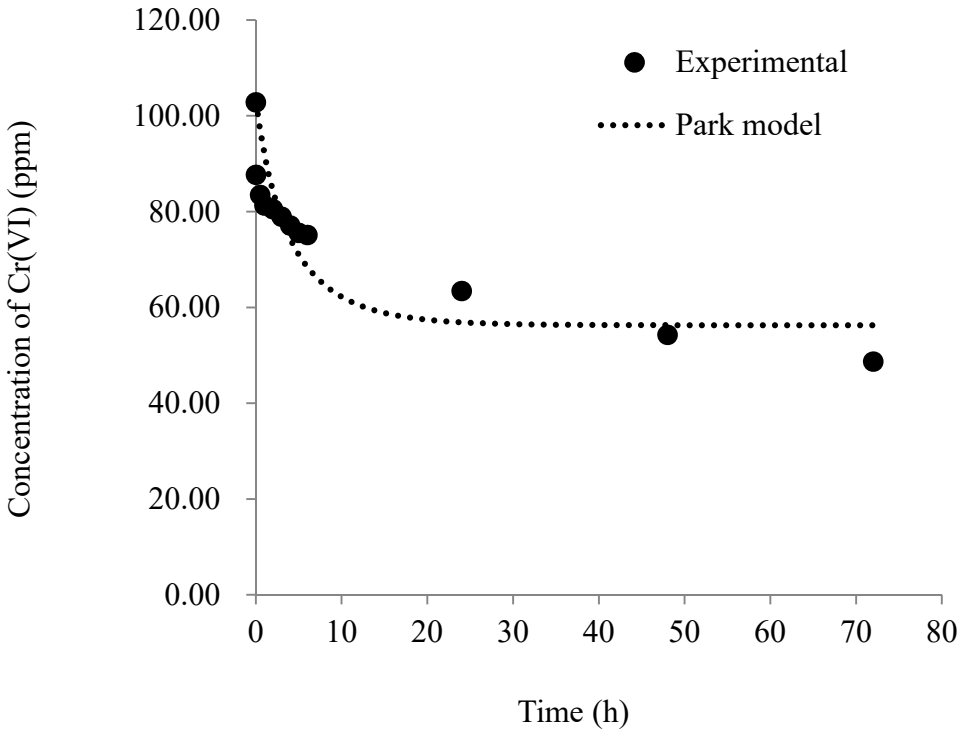

Figure 6.24a Park model for simulating the Cr(VI) removal by *Mucor rouxii* (20 ℃).

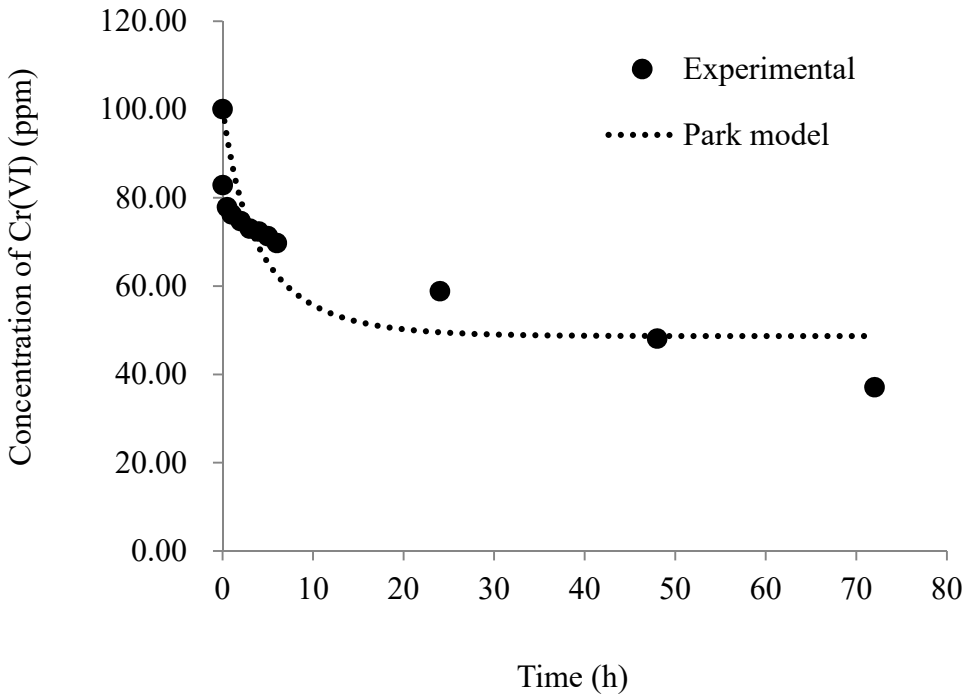

Figure 6.24b Park model for simulating the Cr(VI) removal by *Mucor rouxii* (25 ℃).

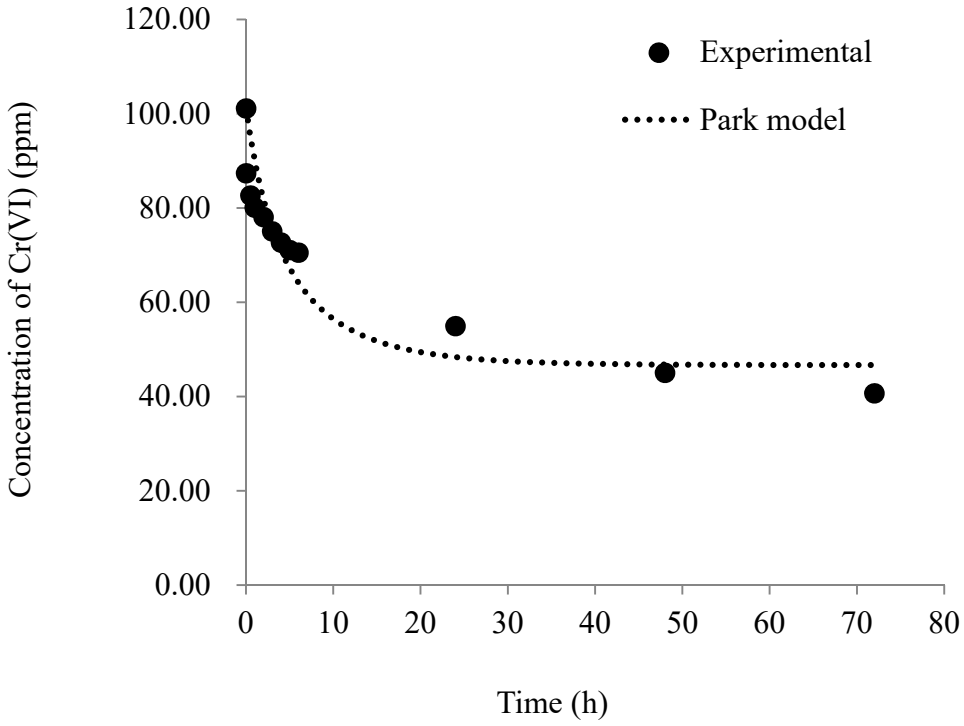

Figure 6.24c Park model for simulating the Cr(VI) removal by *Mucor rouxii* (40 ℃).

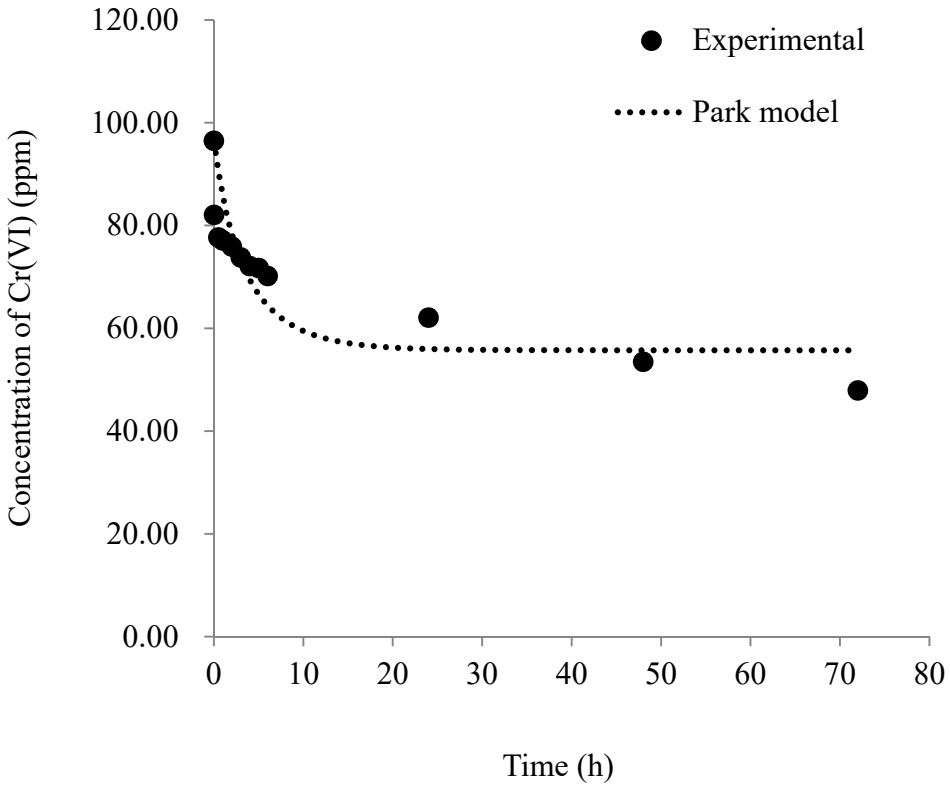

Figure 6.24d Park model for simulating the Cr(VI) removal by *Mucor rouxii* (50 rpm).

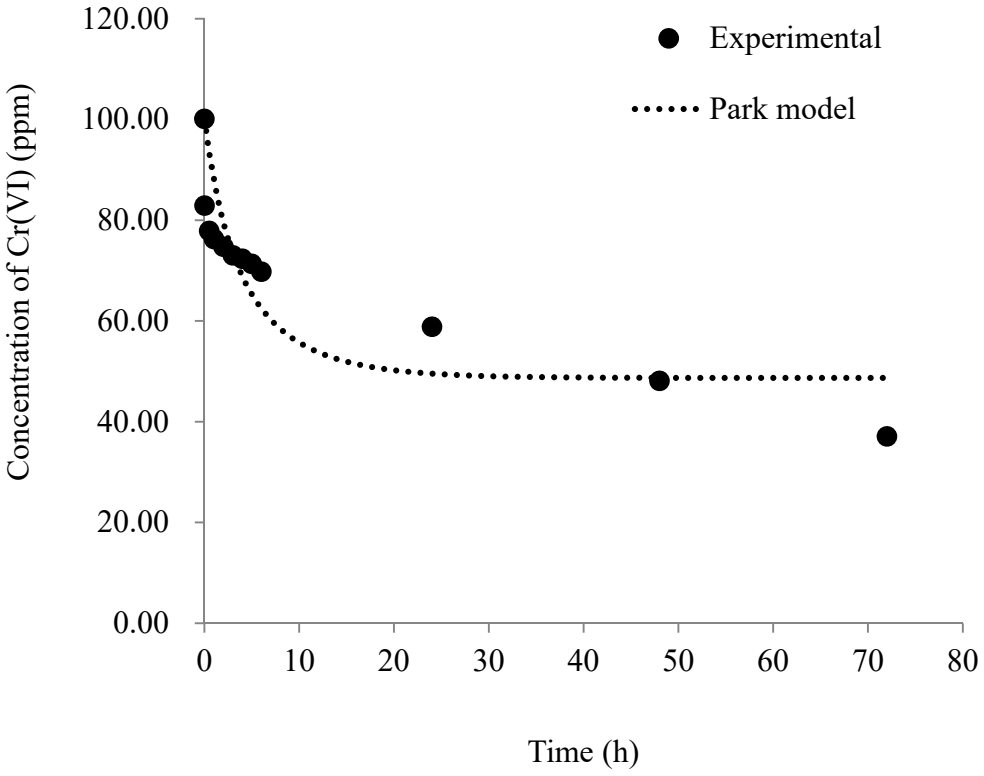

Figure 6.24e Park model for simulating the Cr(VI) removal by *Mucor rouxii* (250 rpm).

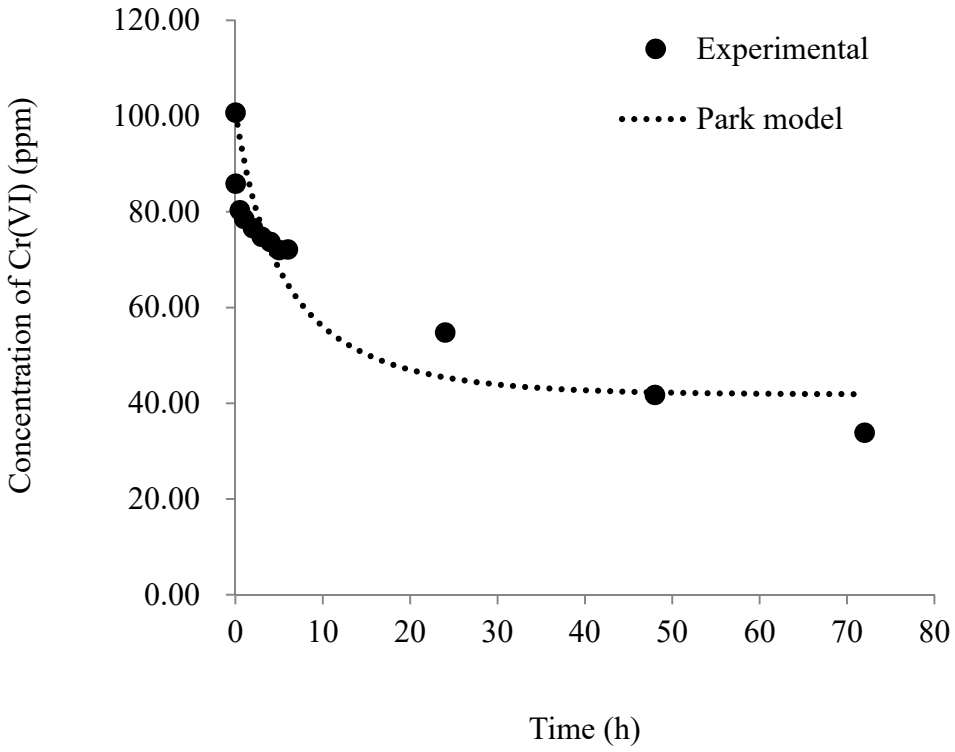

Figure 6.24f Park model for simulating the Cr(VI) removal by *Mucor rouxii* (500 rpm).

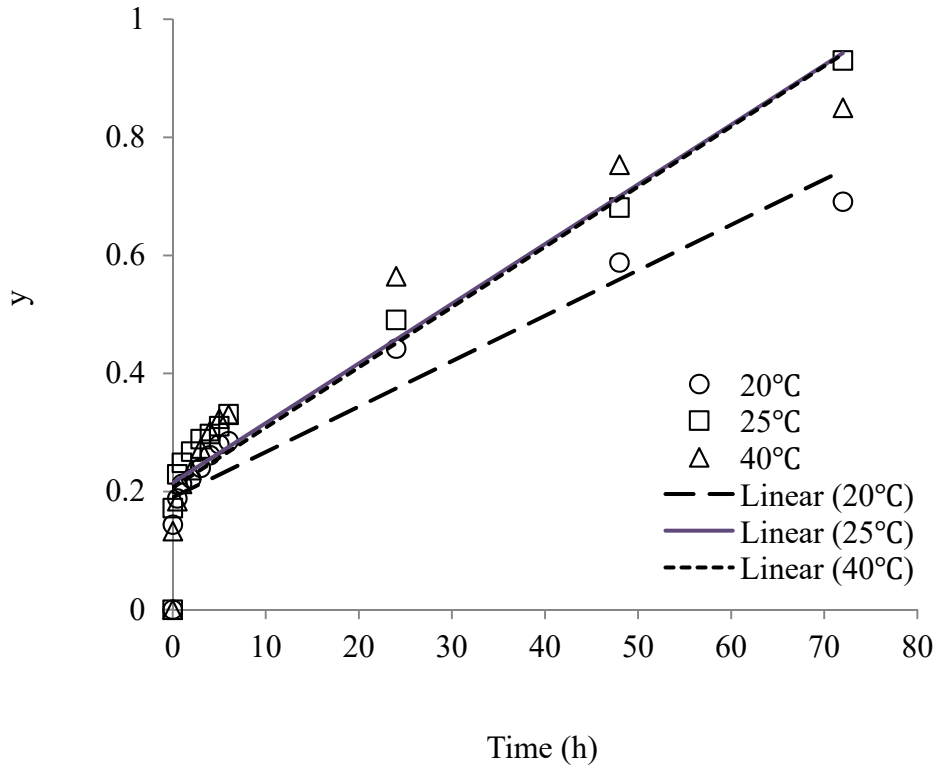

Figure 6.25a The plot of y versus t for Cr(VI) reduction at different temperatures.

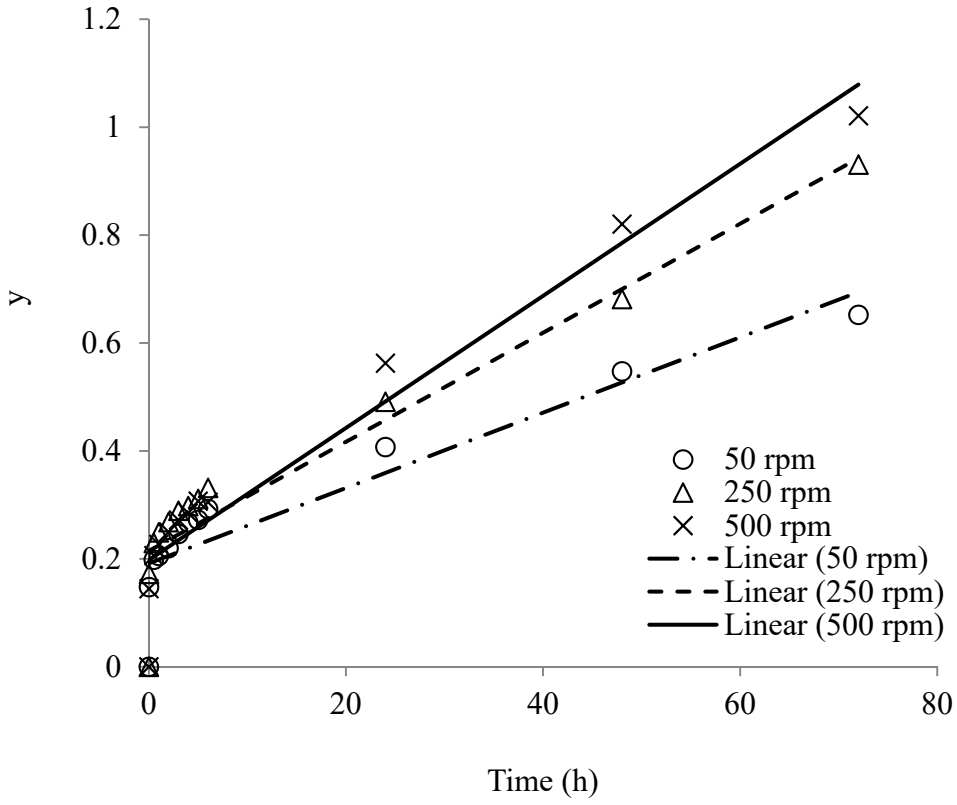

Figure 6.25b The plot of y versus t for Cr(VI) reduction at different agitation speeds.

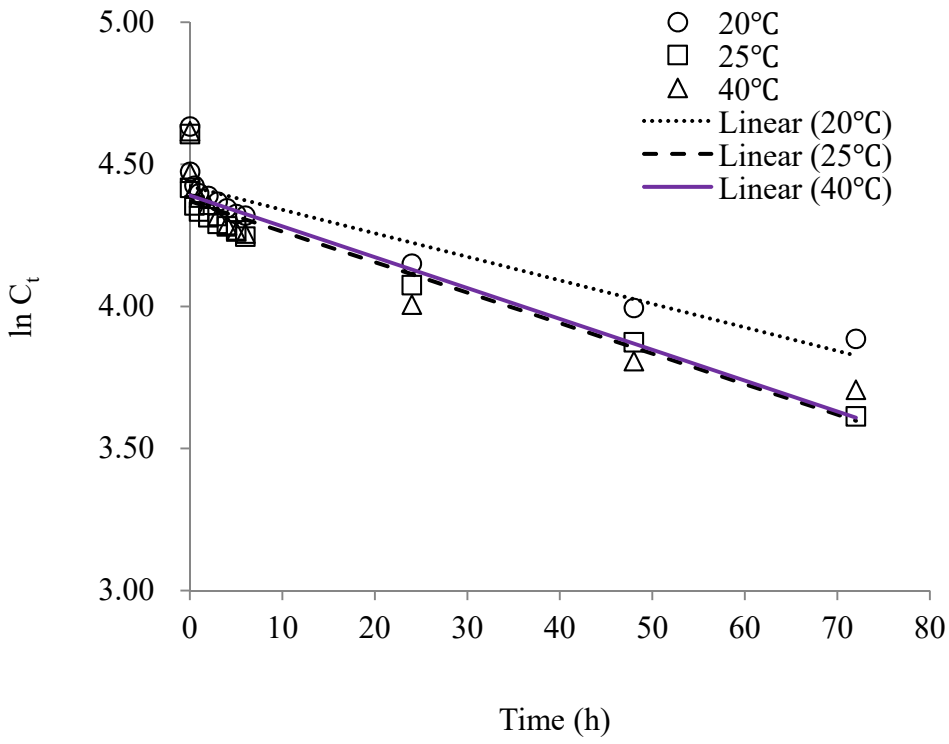

Figure 6.26a Pseudo-first order reduction plot of Cr(VI) by *Mucor rouxii* at different temperatures.

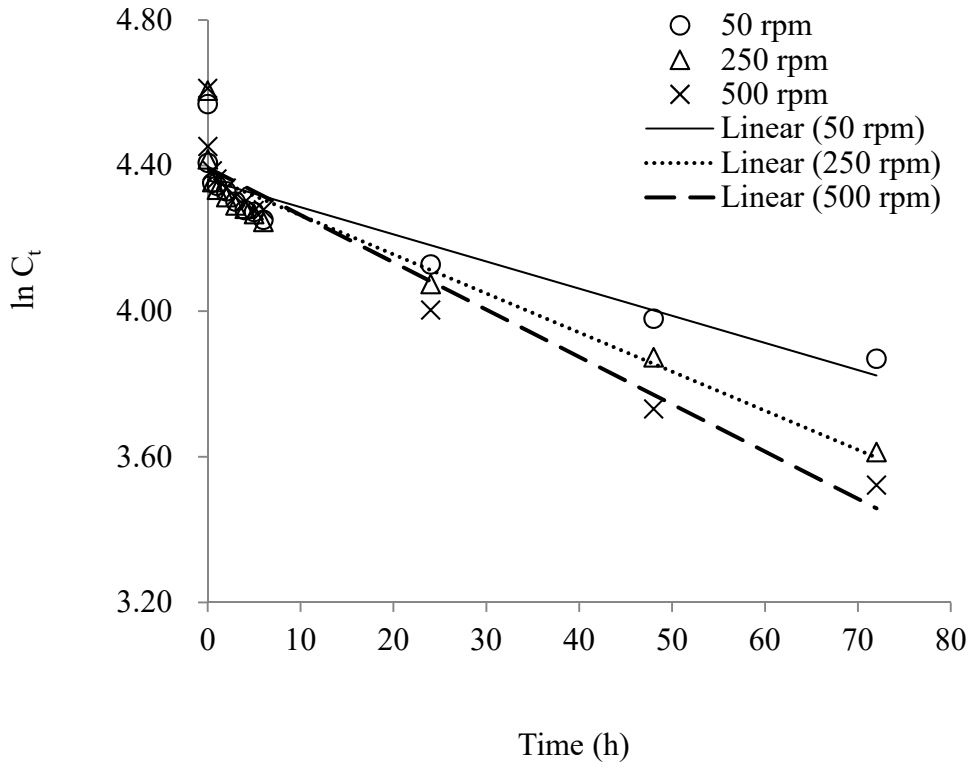

Figure 6.26b Pseudo-first order reduction plot of Cr(VI) by *Mucor rouxii* at different agitation speeds.

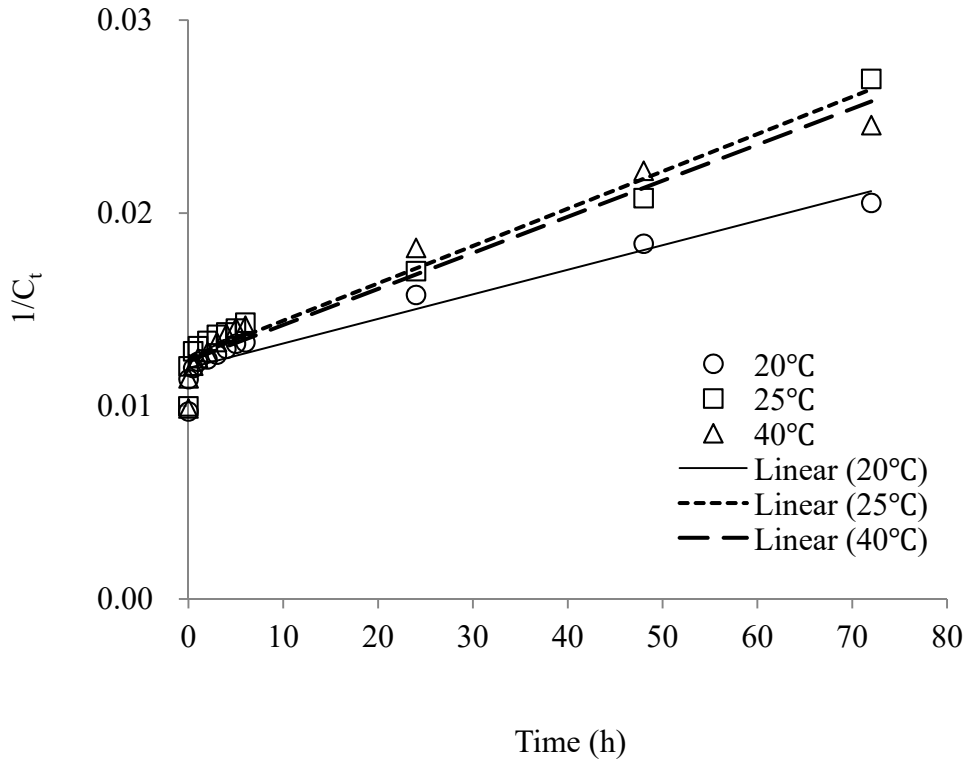

Figure 6.27a Pseudo-second order reduction plot of Cr(VI) by *Mucor rouxii* at different temperatures.

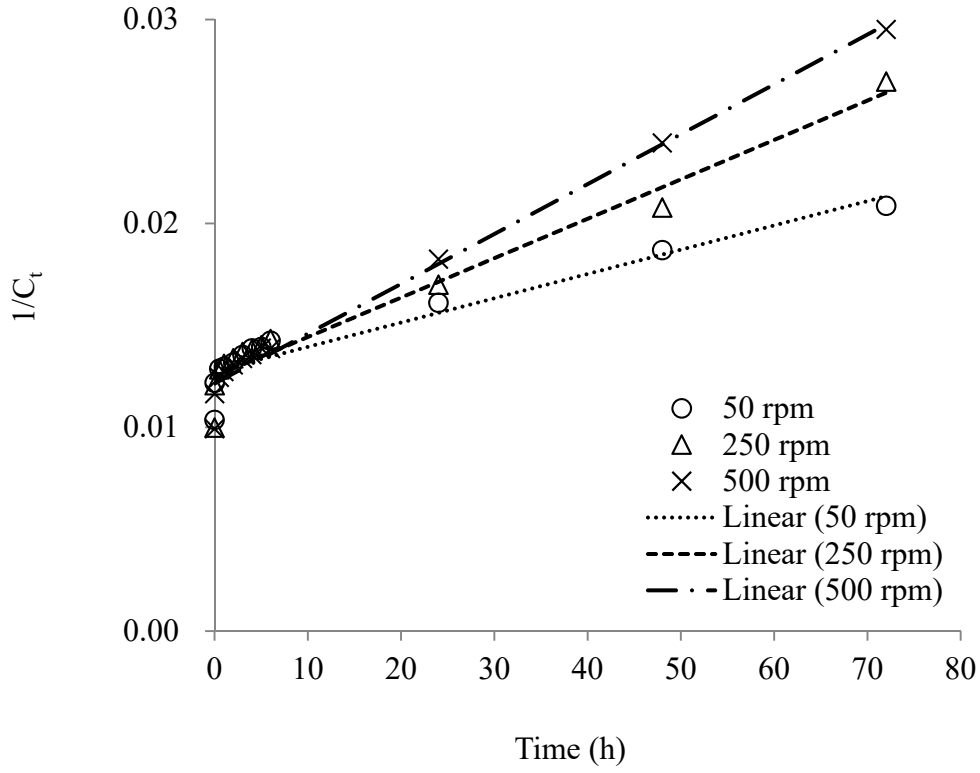

Figure 6.27b Pseudo-second order reduction plot of Cr(VI) by *Mucor rouxii* at different agitation speeds.

Table 6.9 Kinetic parameters obtained from Cr(VI) reduction kinetic models.

		Temperature (℃)			Agitation speed (rpm)			Biomass conc. (g/L)		
Model		20	25	40	50	250	500	1	5	10
Park model	k_P (L/mmol-h)	0.1437	0.1500	0.1261	0.1770	0.1500	0.1039	0.1500	45.26	33.19
	C^*_{OC} (mmol/g)	0.9045	0.9517	1.008	0.7540	0.9517	1.121	0.9517	0.2629	0.1570
	r^2	0.7000	0.6508	0.8222	0.6580	0.6508	0.7758	0.6508	0.7906	0.8259
	SSE	2064.12	2638.86	2874.70	1464.51	2638.86	3933.70	2638.86	1145.5	1291.12
	RMSE	13.70	15.49	16.17	11.54	15.49	18.92	15.49	10.20	10.83
	SE	15.14	17.12	17.87	12.76	17.12	20.91	17.12	11.28	11.98
Park model	k_M (mg/L-h)	8.68E-06	1.07E-05	1.09E-05	7.42E-06	1.07E-05	1.34E-05	1.07E-05	4.86E-06	8.91E-06
(modified)	r^2	0.8646	0.9087	0.8767	0.8452	0.9087	0.9373	0.9087	0.7867	0.9539
	SSE	4097.91	4572.10	4327.07	3643.74	4572.10	3876.45	4572.10	449099	18852
	RMSE	19.30	20.39	19.83	18.20	20.39	18.77	20.39	202.06	41.40
	SE	20.20	21.38	20.80	19.20	21.38	19.69	21.38	223.38	45.77
Pseudo-first order	K_1 (h^{-1})	0.0083	0.0107	0.0109	0.0075	0.0107	0.013	0.0107	0.0210	0.0818
	r^2	0.8585	0.9034	0.8711	0.8394	0.9034	0.9326	0.9034	0.9432	0.9661

	SSE	491.68	531.62	628.70	422.78	531.62	490.69	531.62	1217.60	403.26
	RMSE	6.40	6.66	7.24	5.94	6.66	6.39	6.66	10.52	6.05
	SE	6.69	6.95	7.56	6.20	6.95	6.68	6.95	11.63	6.69
Pseudo-second order	K_2 (L/mg-h)	1.27E-04	1.93E-04	1.87E-04	1.19E-04	1.93E-04	2.45E-04	1.93E-04	0.0011	0.1709
	r^2	0.9267	0.9576	0.9407	0.9111	0.9576	0.9822	0.9576	0.9888	0.6627
	SSE	533.61	475.54	508.22	434.51	475.54	470.56	475.54	141.69	9090.68
	RMSE	6.67	6.30	6.51	6.02	6.30	6.26	6.30	3.59	28.74
	SE	7.30	6.58	6.80	6.28	6.58	6.54	6.58	3.97	31.78

6.9 SEM images and EDAX spectra

The surface morphology changes of the biomass after chromium biosorption were investigated by SEM. The SEM images of biomass exposed in Cr(VI) solution at pH 2 (Figs. 6.28d-f) were compared with those of the virgin biomass (Figs. 6.28a-c). Some small granules were observed on the fungal biomass surface after contact with the Cr(VI) solution; additionally, the biomass surface shrank, an occurrence which may be due to the interaction between the chromium ions and the surface functional groups of the fungal biomass. The EDAX spectrum of the pristine biomass showed that C, N, O and P were present on the raw biomass surface (Fig. 4.20). Peaks of alkali and alkaline earth metal ions (e.g., sodium, potassium, magnesium and calcium ions) commonly found on the surface of algal or other fruit wastes did not appear. Fig. 6.29 shows the EDAX spectrum of the Cr-loaded biomass. Several peaks corresponding to Cr were observed in the figure, revealing the presence of Cr ions on the biomass surface. Comparison of Fig. 4.20 and Fig. 6.29 indicates that the biosorption of Cr ions by the fungal biomass might not be due to an ion exchange reaction between the Cr ions and the alkali and alkaline earth metal ions on cell surface.

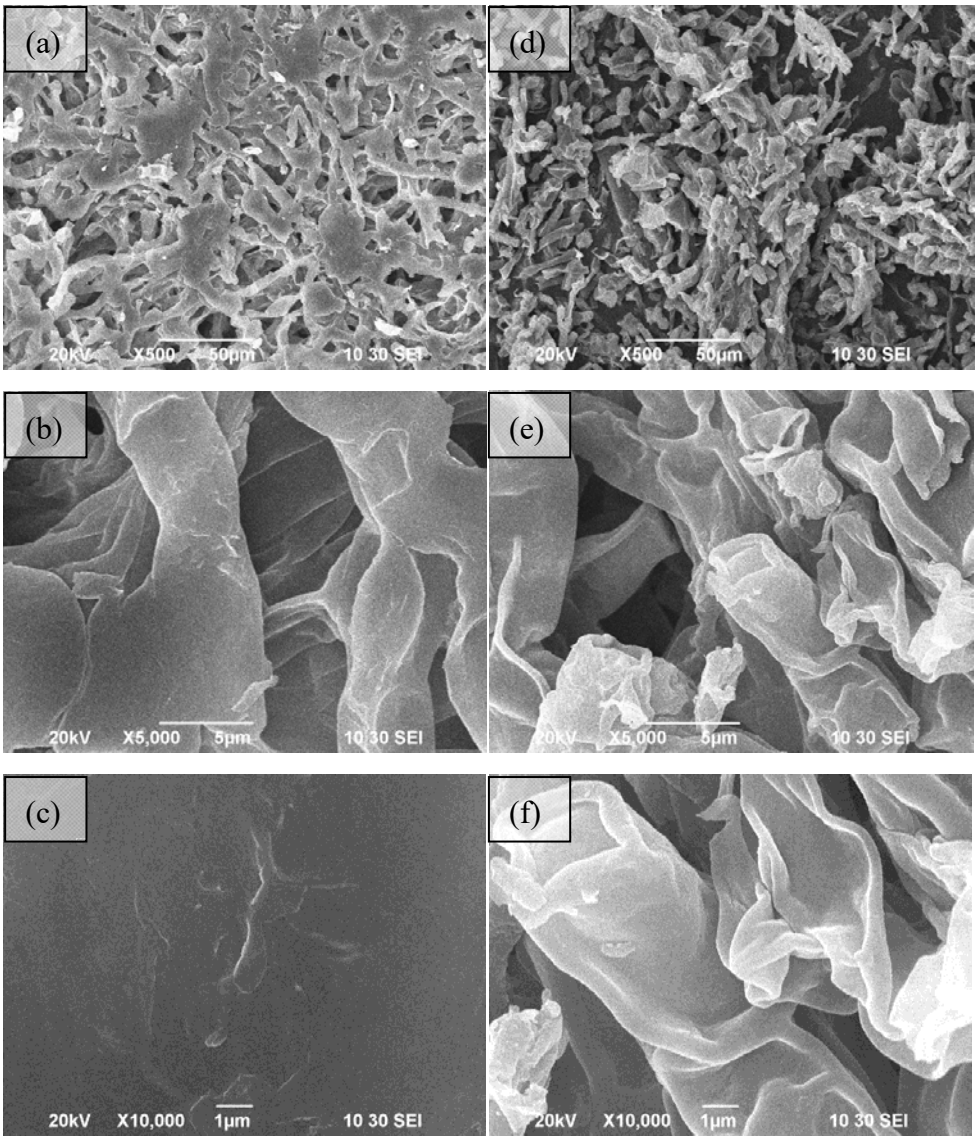

Figure 6.28 SEM images of (a) pristine biomass (500X), (b) pristine biomass (5000X), (c) pristine biomass (10000X), (d) Cr-loaded biomass (500X), (e) Cr-loaded biomass (5000X) and (f) Cr-loaded biomass (10000X)**.**

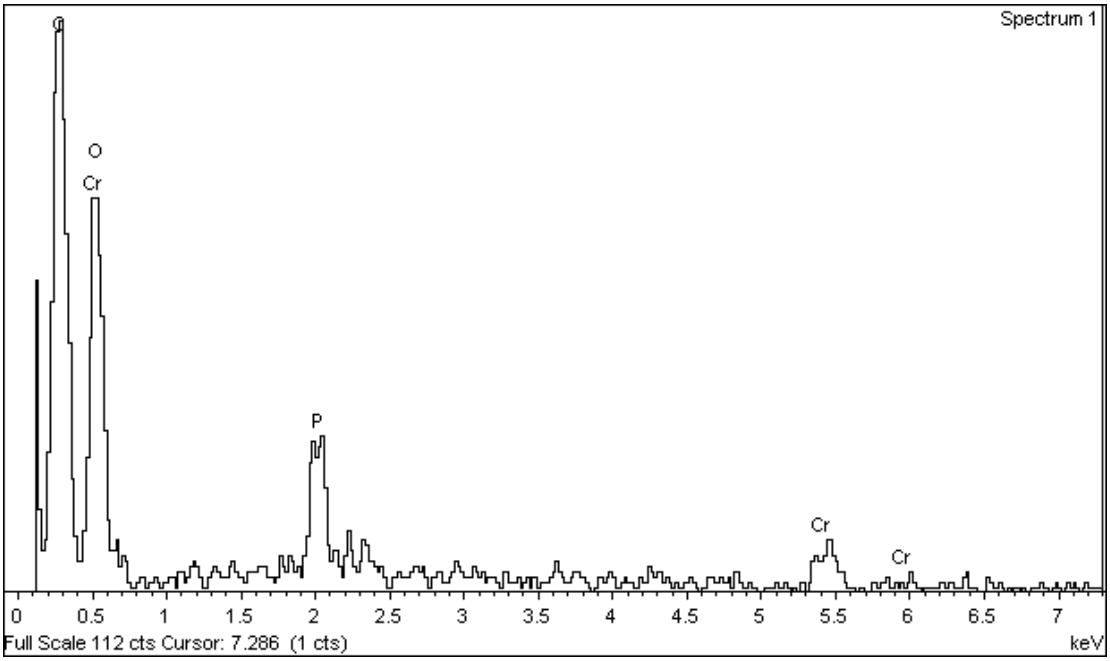

Figure 6.29 EDAX spectrum of Cr-loaded biomass.

6.10 FTIR analysis

The FTIR spectrum of Cr-loaded biomass was compared with that of the pristine biomass, and the changes in wavenumbers of the surface functional groups of the biomass might be useful for elucidating the Cr(VI) removal mechanism. Fig. 6.30 illustrates the FTIR spectra of the pristine and the Cr-loaded biomass. Several changes were observed in the FTIR spectrum of the biomass after contact with the Cr(VI) solution. A band was formed at 3417.0 cm^{-1} which corresponded to the asymmetric stretching of the NH_2 in amines, indicating the involvement of amines groups in Cr(VI) removal. At pH 2.0, the amine group should be in the form of NH_3^+, and thus might be responsible for the adsorption of anionic Cr(VI) from the aqueous solution. The absorption band at 1636.0 cm^{-1} (which may be due to C=O stretching in amide I, NH_2 scissoring in amines or asymmetric stretching in carboxylate ions) shifted to 1652.4 cm^{-1}, revealing the involvement of the amide/amine/carboxylate in Cr(VI) removal. The peak assigned to the stretching vibration of C-O in carboxylic acids shifted from 1264.6 cm^{-1} to 1244.3 cm^{-1}, suggesting that the bioreduced Cr(III) might interact with the carboxylic groups.

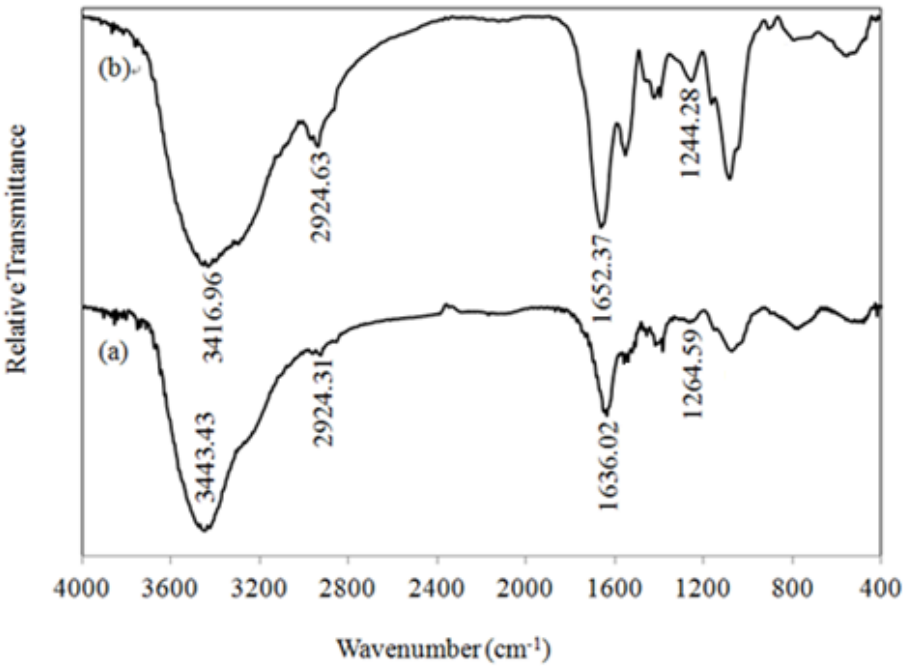

Figure 6.30 FTIR spectra of (a) pristine and (b) Cr-loaded biomass.

6.11 Removal mechanisms of Cr(VI) by *Mucor rouxii*

The cell wall of filamentous *M. rouxii* was reported to consist mainly of chitosan (33% of total dry weight), phosphate (23%), glucuronic acid (12%) and chitin (9%) (Griffin 1994). The functional groups of hydroxyl, phosphate, carboxyl and the amine/amide groups were therefore abundant on the cell wall. Based on the combined results of potentiometric titration, cell wall biochemistry, FTIR and XPS studies, it was proposed that phosphodiester (pK_a = 3.22±0.52), carboxyl (pK_a = 4.92±0.43), hydroxyl (pK_a = 8.77±0.31) and the amine groups (pK_a = 6.79±0.21) were present on the fungal biomass surface that was cultivated in this study. These four types of functional groups (i.e. the phosphodiester, carboxyl, amine and hydroxyl groups) contributed to the surface charge of the biomass. It was observed that when the pH value was below 3.5, the biomass surface exhibited net positive charges, revealing the protonation of surface functional groups (Fig. 4.8). Thus, at low pHs, an electrostatic attraction occurred between the positively-charged functional groups and the anionic Cr(VI) ions. The value of the zeta potential generally decreased as the solution pH went above 3.5 and this was due to the subsequent deprotonation of phosphodiester (pK_a = 3.22±0.52) and carboxyl (pK_a = 4.92±0.43) groups. In Fig. 6.3, it was

noticed that the removal of Cr(VI) decreased significantly when the pH values increased from 4.0 to 7.0. The decrease of Cr(VI) removal was related to the electrostatic repulsion between the negatively-charged surface groups and Cr(VI) ions.

The concentrations of Cr(VI) and Cr(III) in the aqueous solution during the removal of Cr(VI) by the *Mucor rouxii* is illustrated in Fig. 6.12. As shown in the figure, the Cr(VI) concentration decreased rapidly within six hours, while the concentration of Cr(III), which was not initially present in the aqueous solution, increased with increasing contact time. After six hours, the depletion of Cr(VI) was proportional to the appearance of Cr(III), indicating that the reduction of Cr(VI) to Cr(III) was involved in the removal of Cr(VI) from the aqueous solution by the fungal biomass. The results showed that two processes were involved in the removal of Cr(VI) by the fungal biomass. The decrease in Cr(VI) concentration in the aqueous solution could be due to the adsorption of Cr(VI) onto the positively-charged biomass surface and the subsequent reduction of Cr(VI) to Cr(III) ions.

The Cr(VI) removal by the fungal biomass was performed at pH 2.0. At this pH, $HCrO_4^-$ and $Cr_2O_7^{2-}$ were the two dominant species. The fungal biomass surface carried a net positive charge (PZC = 3.5) and the adsorption of anionic

Cr(VI) onto the positively-charged biomass surface was facile. Thus, the concentration of Cr(VI) in the aqueous solution decreased rapidly within the first few hours. On the other hand, the increase in Cr(III) concentration in the aqueous solution was due to the reduction of Cr(VI) to Cr(III). Cr(VI) has a high redox potential and can be easily reduced to Cr(III) by consuming protons and electrons. The reduction of Cr(VI) to Cr(III) can be expressed by the following equations:

$HCrO_4^- + 7H^+ + 3e^- \leftrightharpoons Cr^{3+} + 4H_2O \quad E^0 = +1.35V$ (Equation 6.11)

$Cr_2O_7^{2-} + 14H^+ + 6e^- \leftrightharpoons 2Cr^{3+} + 7H_2O \quad E^0 = +1.33V$ (Equation 6.12)

$H_2CrO_4 + 6H^+ + 3e^- \leftrightharpoons Cr^{3+} + 4H_2O \quad E^0 = +1.33V$ (Equation 6.13)

$CrO_4^{2-} + 8H^+ + 3e^- \leftrightharpoons Cr^{3+} + 4H_2O \quad E^0 = +1.48V$ (Equation 6.14)

As shown in Fig. 6.2, the concentration of bioreduced Cr(III) increased with decreasing pH, indicating the importance of protons in the Cr(VI) reduction process. It was also found that the concentration of Cr(III) increased as the biomass concentration increased (Fig. 6.4) since more electron-donating groups on the biomass surface were available for the reduction of Cr(VI) to Cr(III). Therefore, at pH 2.0, both the biosorption of Cr(VI) onto the fungal biomass and the reduction of Cr(VI) to Cr(III) occurred.

XPS was employed to investigate the oxidation states of Cr bound onto the

fungal biomass surface. High-resolution XPS (Cr2p) spectra of biomass after contact with the Cr(VI) solution at different solution pHs (Fig. 6.31) and different contact time (Fig. 6.32) were recorded. As shown in Figs. 6.31, the peak intensity of Cr decreased with increasing solution pH. On the other hand, the peak intensity of Cr increased with increasing contact time (Fig. 6.32). At pH 7.0 (Fig. 6.31c), no Cr peaks were detected. This might be due to the electrostatic repulsion between anionic Cr(VI) and the negatively-charged biomass surface. The biosorption of Cr(VI) onto the fungal biomass was, therefore, not facile. Significant bands appeared at binding energies of 576.5-579.0 eV ($Cr2p_{3/2}$ orbital) and 586.0-588.5 eV ($Cr2p_{1/2}$ orbital) (Figs. 6.31 and b and Figs. 6.32a and b). The standard Cr(III) compound ($CrCl_3$) appeared at binding energies of 577.4-577.8 eV. The standard Cr(VI) compound ($K_2Cr_2O_7$) exhibited higher binding energies of 579.4-579.9 eV and 588.7 eV (National Institute of Standards and Technology, 2012). The Cr(VI) compound used in this study was Na_2CrO_4. The high-resolution XPS (Cr2p) spectrum of Na_2CrO_4 is shown in Fig. 6.33 and significant bands appeared at binding energies of 578.5-581.5 eV ($Cr2p_{3/2}$ orbital) and 588.0-590.5 eV ($Cr2p_{1/2}$ orbital). These results suggested that mainly Cr(III) was found on the biomass surface at pH 2 and 4 for both 30 min and 24 h exposure times. Thus, the reduction rate might

be rapid (within 30 minutes after the start of biosorption).

Determining the changes in binding energies or atomic concentrations after biosorption is helpful for elucdiating the Cr(VI) removal mechanism by the fungal biomass. High-resolution XPS spectra of C1s, N1s and O1s after Cr(VI) biosorption (at different pHs and contact time) were obtained and are shown in Figs. 6.34-6.36, respectively. The corresponding results are tabulated in Table 6.10. As listed in the table, the atomic concentrations of O=C-O exhibited significant changes after Cr(VI) removal, which might suggest that the reduced Cr(III) ions were bound onto the carboxylic groups (Zheng et al. 2011). Regarding the deconvoluted N1s spectra, the atomic concentrations of the N atom in the two forms showed significant changes after Cr(VI) removal. At low pH, the amine groups should be protonated, and therefore, electrostatic attraction between the anionic Cr(VI) and the positive-charged biomass surface might occur. Shifts of 0.1-0.4 eV in the binding energy of P2p were also observed after Cr(VI) removal, suggesting the involvement of the P-O group in the Cr(VI) removal process.

Based on the results of FTIR and XPS analyses, the amine, carboxylate and phosphodiester groups might involve in the Cr(VI) removal process. The proposed Cr(VI) removal mechanism for the fungal biomass is illustrated in Fig.

6.37. The removal process consisted of three phases. In the first phase, the anionic Cr(VI) was adsorbed onto the protonated fungal biomass surface by electrostatic attraction. Based on the results of potentiometric titration, the amine groups should be protonated at pH 2.0 (pK_a = 6.79). The interactions between Cr(VI) ions and the protonated amine group are proposed below:

$$R\text{-}NH_2 + H^+ \leftrightharpoons R\text{-}NH_3^+ \quad \text{(Equation 6.15)}$$

$$R\text{-}NH_3^+ + HCrO_4^- \leftrightharpoons R\text{-}NH_3^+ \bullet\bullet\bullet HCrO_4^- \quad \text{(Equation 6.16)}$$

$$R\text{-}NH_3^+ + Cr_2O_7^{2-} \leftrightharpoons R\text{-}NH_3^+ \bullet\bullet\bullet Cr_2O_7^{2-} \quad \text{(Equation 6.17)}$$

At pH 2.0, the –COOH and $–PO_4H$ were also easily protonated, facilitating the biosorption of Cr(VI) ions. After biosorption, the adsorbed Cr(VI) could be reduced to Cr(III) in the presence of electron donor groups (e.g. C-N groups) on the biomass surface (Cui et al. 2011). Then, the bioreduced Cr(III) cations were either adsorbed on the carboxylate groups through ion exchange with protons from carboxyl groups or released into the aqueous solution by electrostatic repulsion between the positively-charged biomass surface and the Cr(III) cations (Sun et al. 2010; Deng and Ting 2005).

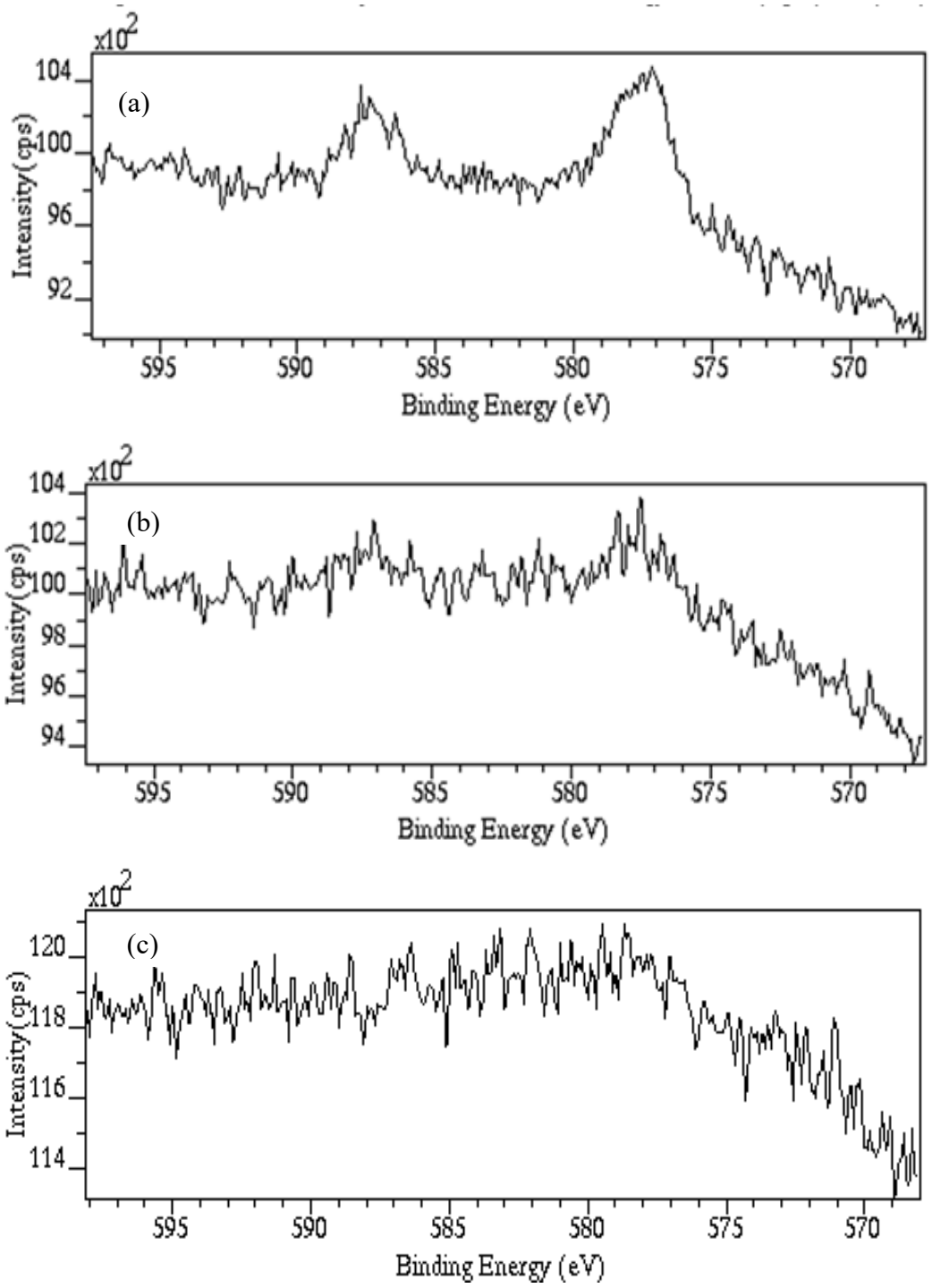

Figure 6.31 High resolution XPS (Cr 2p) spectra of Cr-loaded biomass (a) pH 2; 24 h, (b) pH 4; 24 h and (c) pH 7; 24 h.

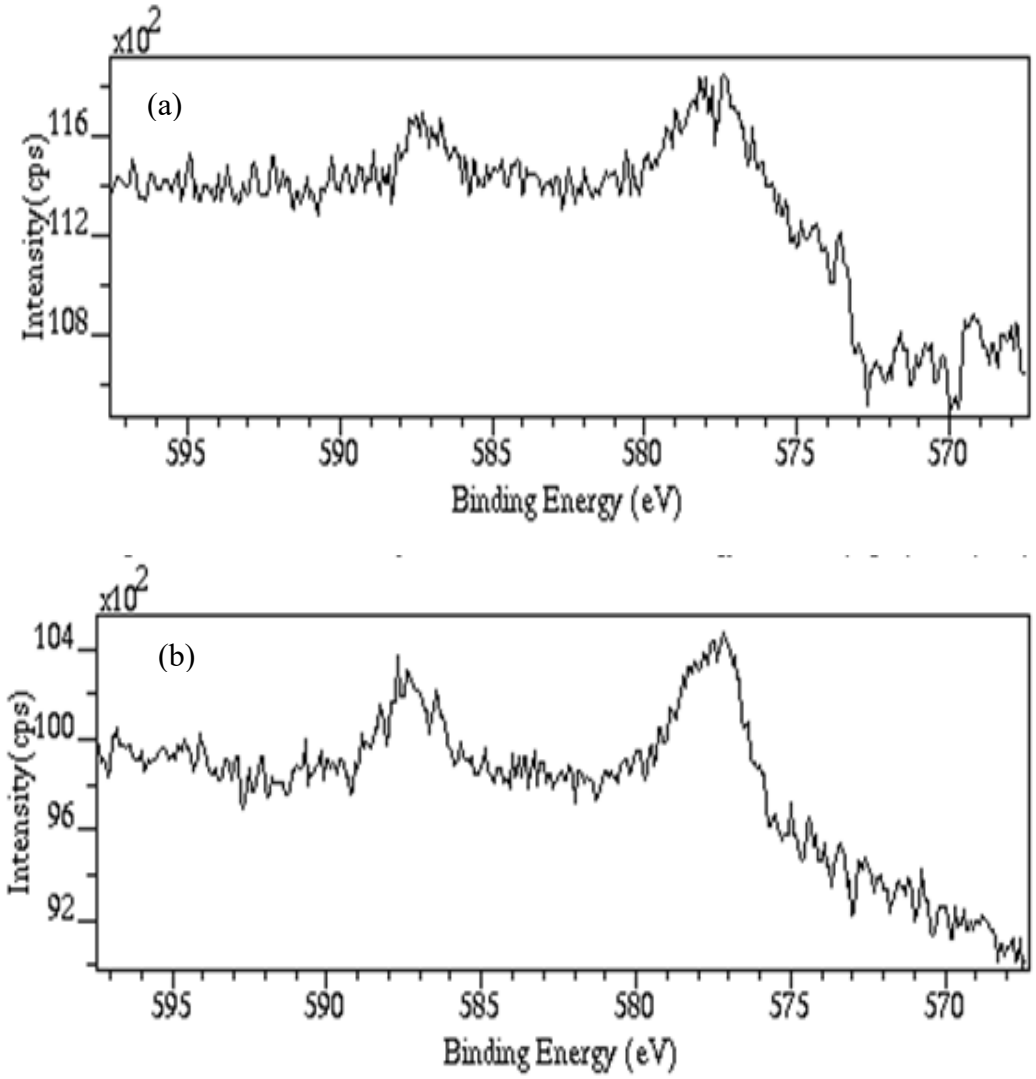

Figure 6.32 High resolution XPS (Cr 2p) spectrum of Cr-loaded biomass (a) 30 min; pH 2 and (b) 24 h; pH 2.

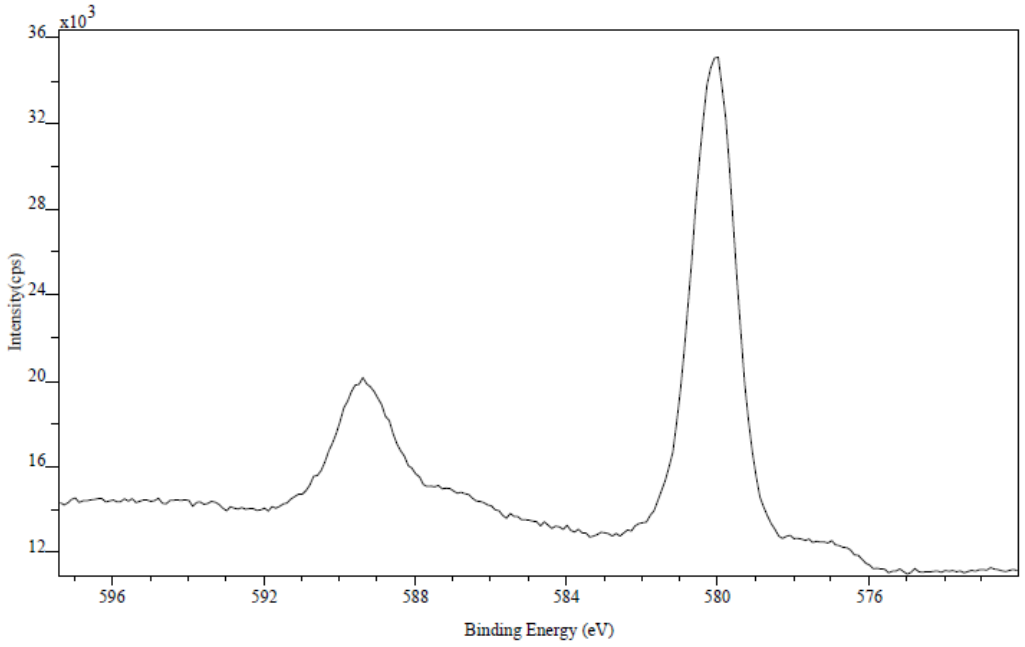

Figure 6.33 High resolution XPS (Cr 2p) spectrum of Na_2CrO_4.

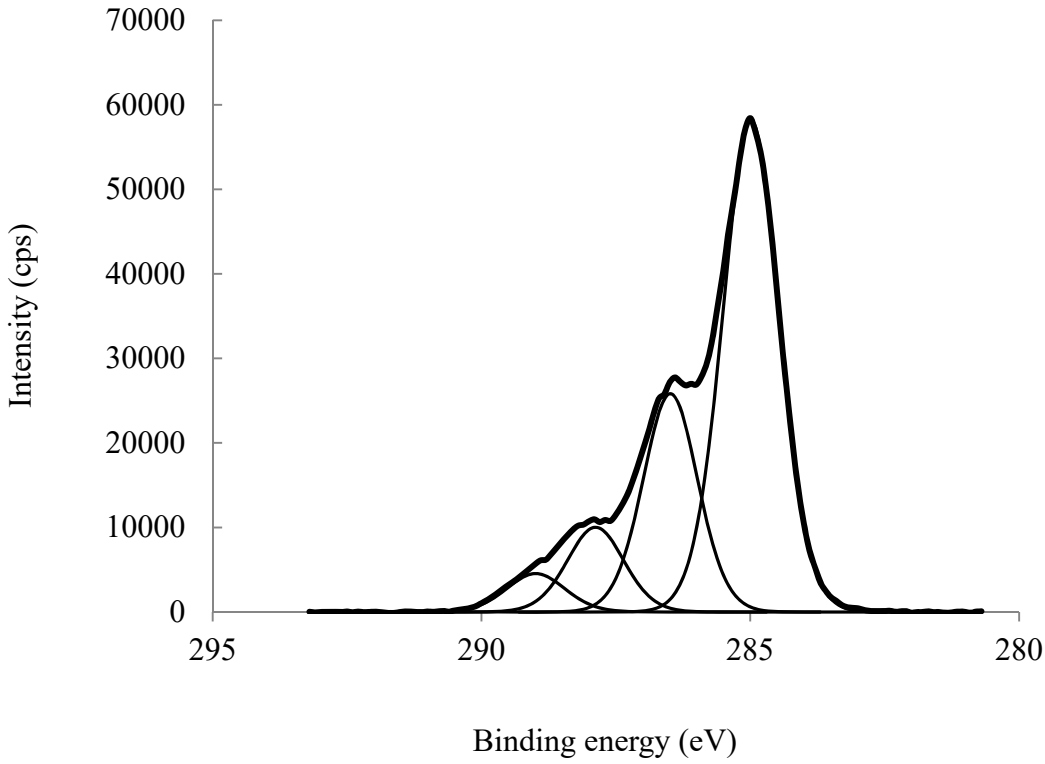

Figure 6.34a High resolution XPS (C1s) spectrum of Cr-loaded biomass (pH 2; 30 min).

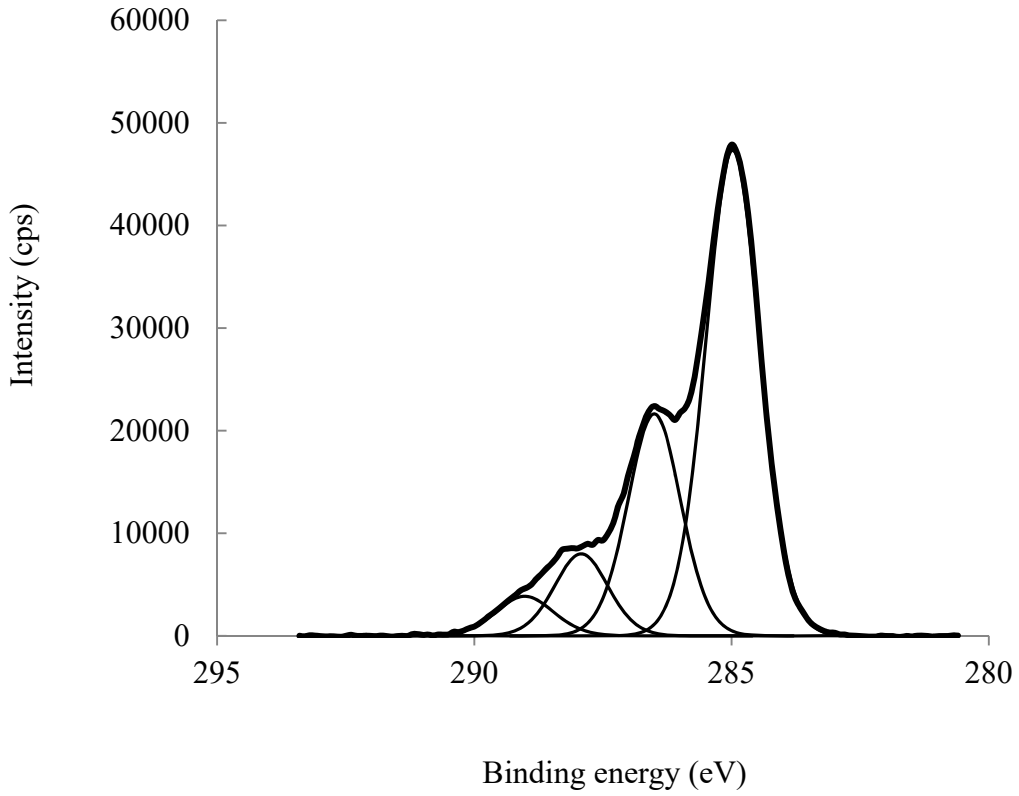

Figure 6.34b High resolution XPS (C1s) spectrum of Cr-loaded biomass (pH 2; 24 h).

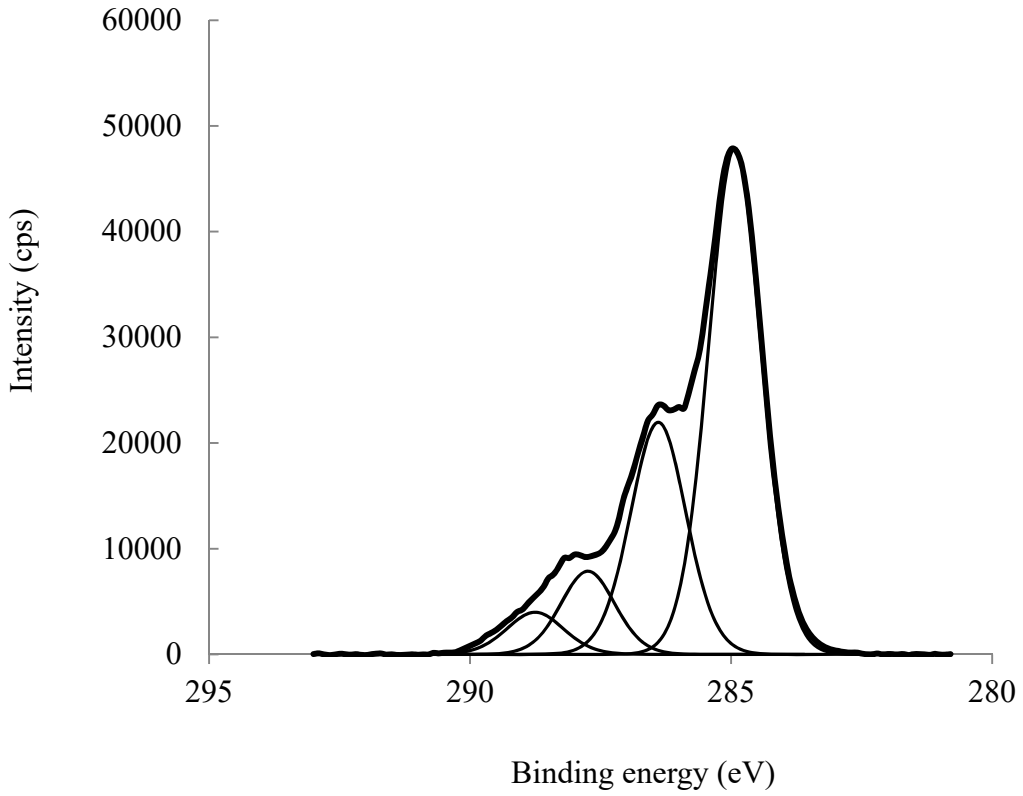

Figure 6.34c High resolution XPS (C1s) spectrum of Cr-loaded biomass (pH 4; 24 h).

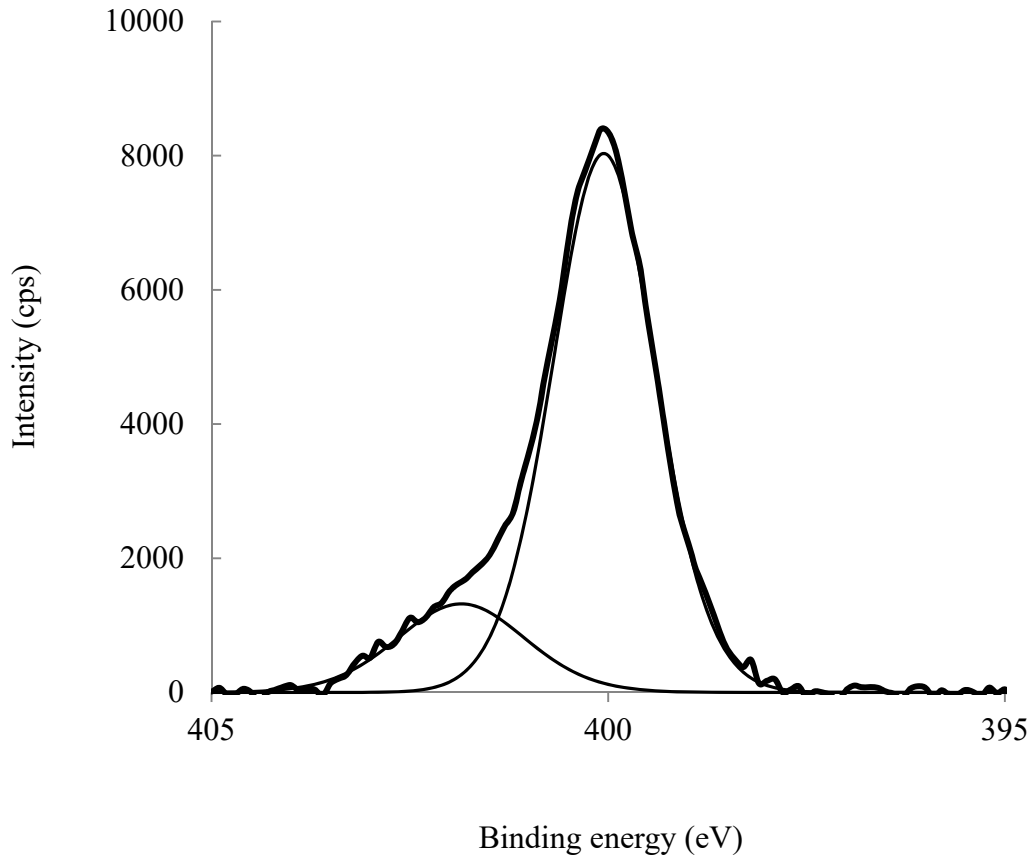

Figure 6.35a High resolution XPS (N1s) spectrum of Cr-loaded biomass (pH 2; 30 min).

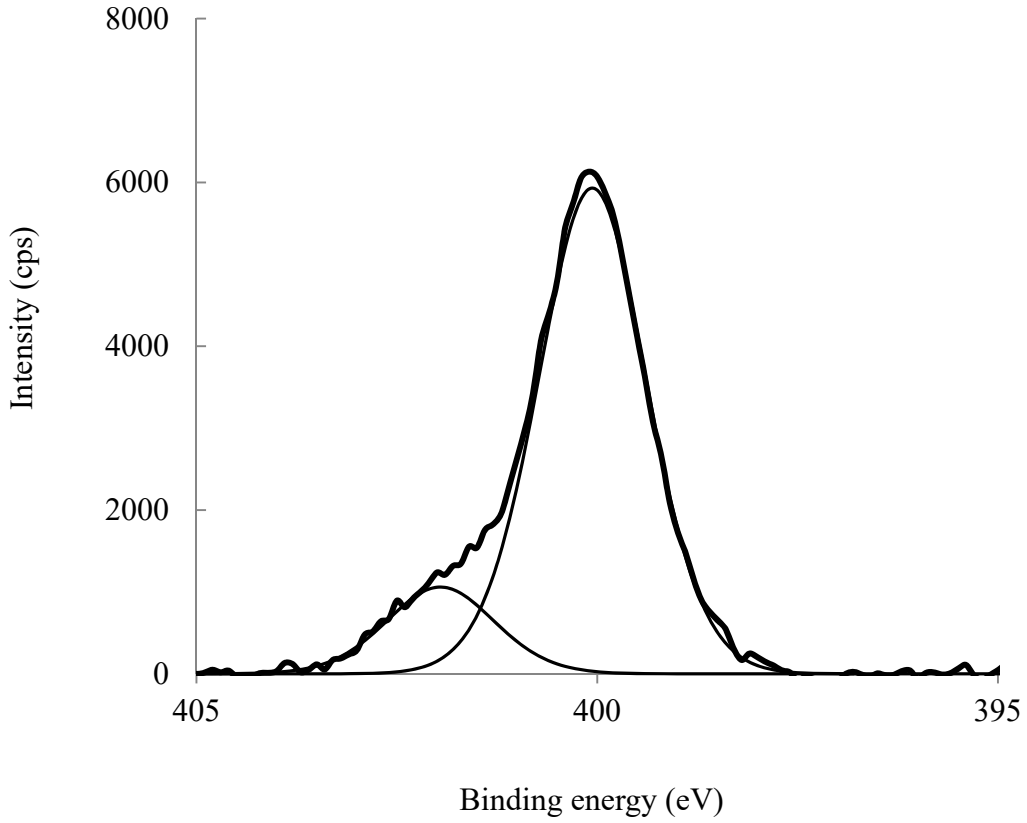

Figure 6.35b High resolution XPS (N1s) spectrum of Cr-loaded biomass (pH 2; 24 h).

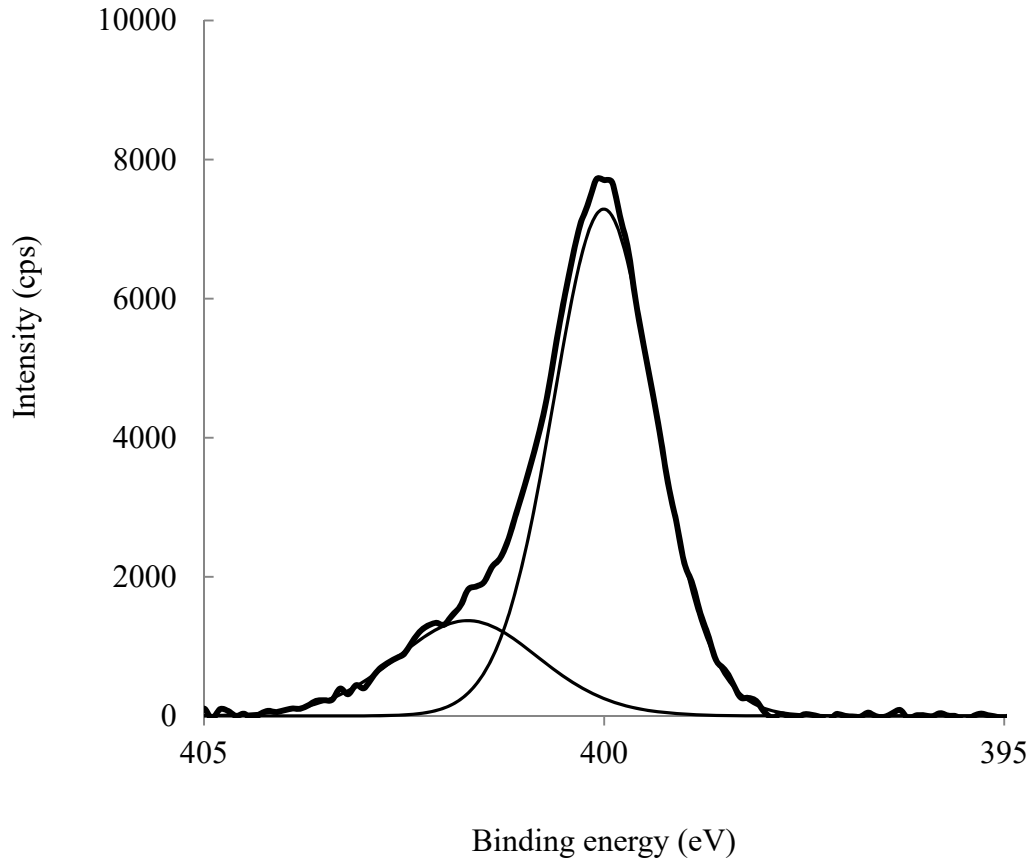

Figure 6.35c High resolution XPS (N1s) spectrum of Cr-loaded biomass (pH 4; 24 h).

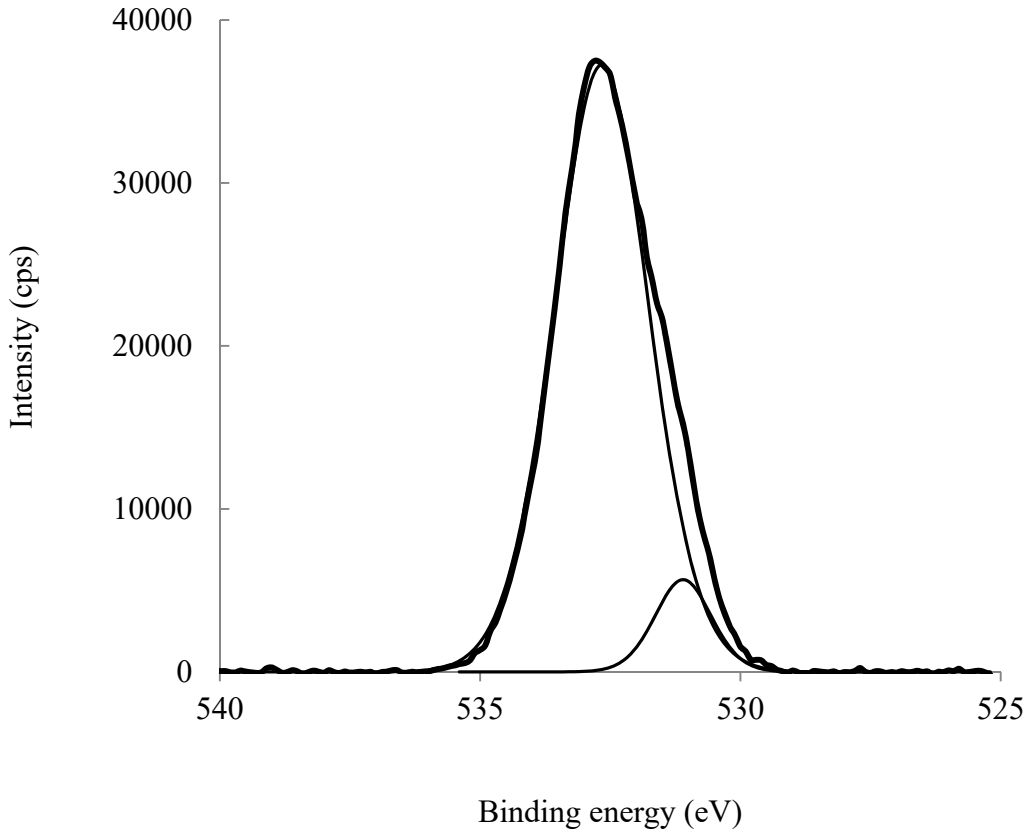

Figure 6.36a High resolution XPS (O1s) spectrum of Cr-loaded biomass (pH 2; 30 min).

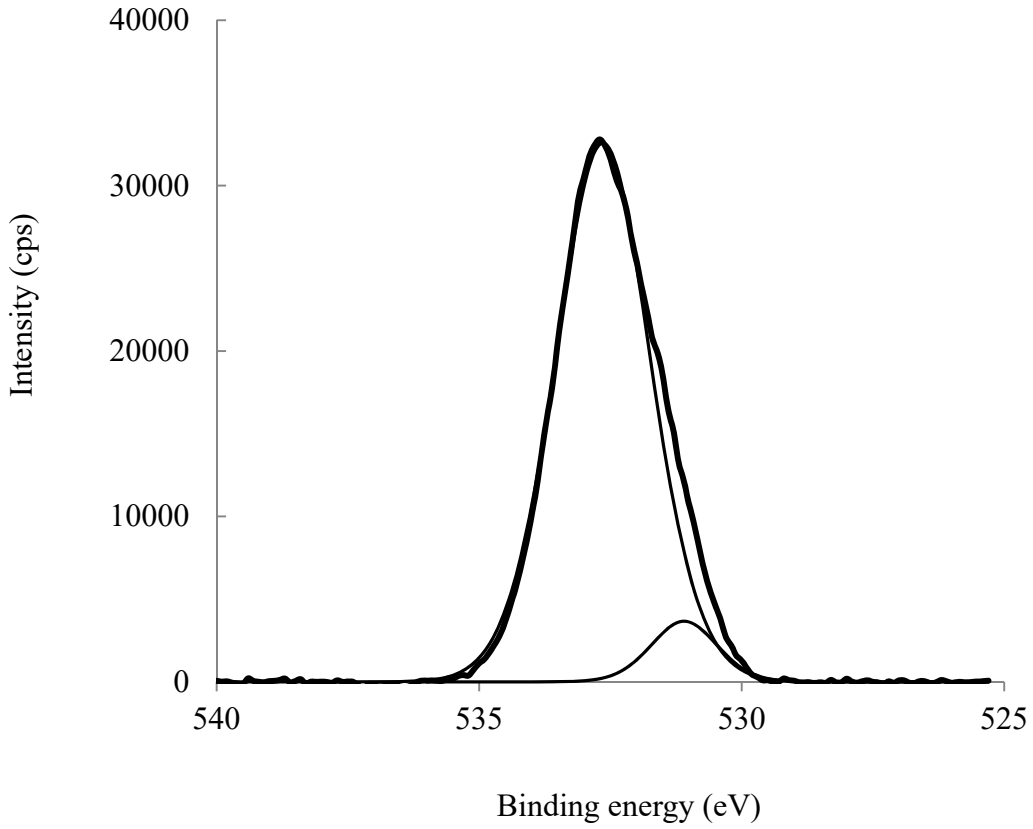

Figure 6.36b High resolution XPS (O1s) spectrum of Cr-loaded biomass (pH 2; 24 h).

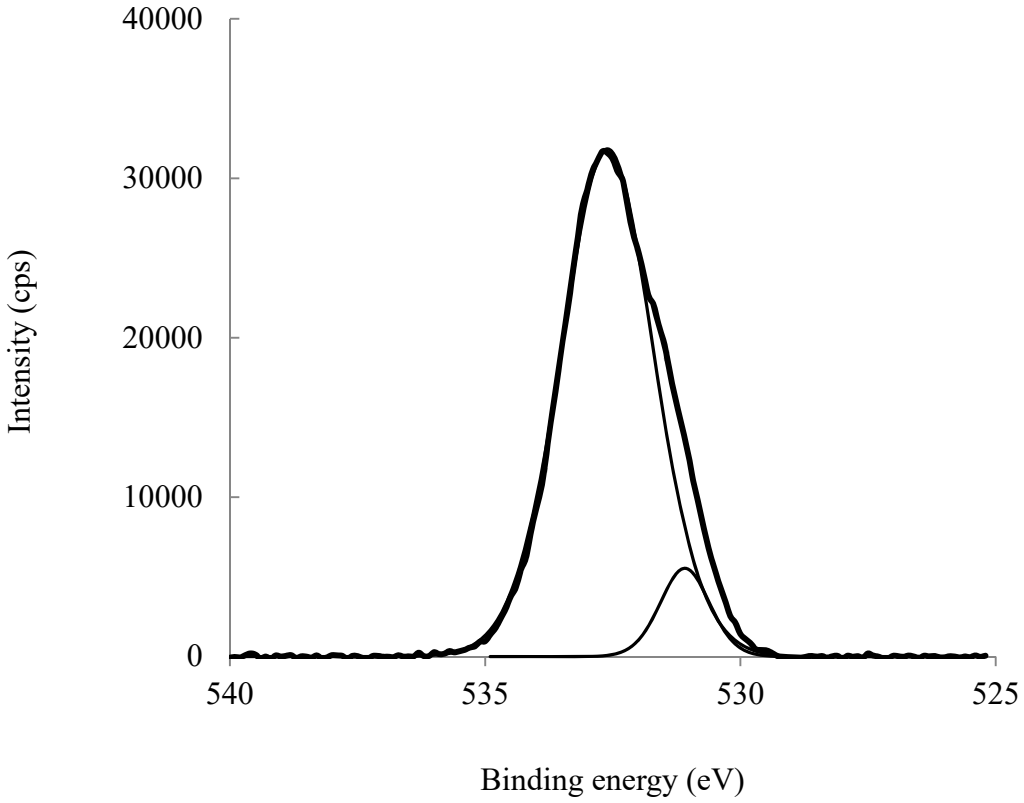

Figure 6.36c High resolution XPS (O1s) spectrum of Cr-loaded biomass (pH 4; 24 h).

Table 6.10 Comparison of binding energies and atomic concentrations of elements before and after Cr(VI) removal.

				30 min		24 h			
		Raw		pH 2		pH 2		pH 4	
Element	Assignment	Binding energy (eV)	Atomic concentration (%)	Binding energy (eV)	Atomic concentration (%)	Binding energy (eV)	Atomic concentration (%)	Binding energy (eV)	Atomic concentration (%)
C1s	C-(C, H)	284.950	55.18	284.967 (0.017)	59.23	284.990 (0.040)	58.65	284.950 (0.000)	57.30
C1s	C-(O, N)	286.372	30.66	286.47 (0.098)	25.63	286.511 (0.139)	26.36	286.373 (0.001)	27.82
C1s	C=O	287.859	10.14	287.868 (0.009)	10.33	287.901 (0.042)	9.87	287.721 (0.138)	9.70
C1s	O=C-O	288.957	4.03	289.000 (0.043)	4.82	289.043 (0.086)	5.12	288.740 (0.217)	5.17
N1s	NH_2	399.988	78.01	400.073 (0.085)	82.93	400.067 (0.079)	84.83	400.007 (0.019)	79.22
N1s	NH_3^+	401.795	21.99	401.877 (0.082)	17.07	401.956 (0.161)	15.17	401.728 (0.067)	20.78

O1s	O-C	532.694	92.44	532.682 (0.012)	91.64	532.622 (0.072)	92.70	532.610 (0.084)	91.43
O1s	O=C	531.018	7.56	531.116 (0.098)	8.36	531.076 (0.058)	7.30	531.089 (0.071)	8.57
P2p	P-O	133.900	100.00	133.800 (0.100)	100.00	134.100 (0.200)	100.00	133.600 (0.300)	100.00

Note: The values in brackets are the binding energy differences between raw and Cr-loaded biomass.

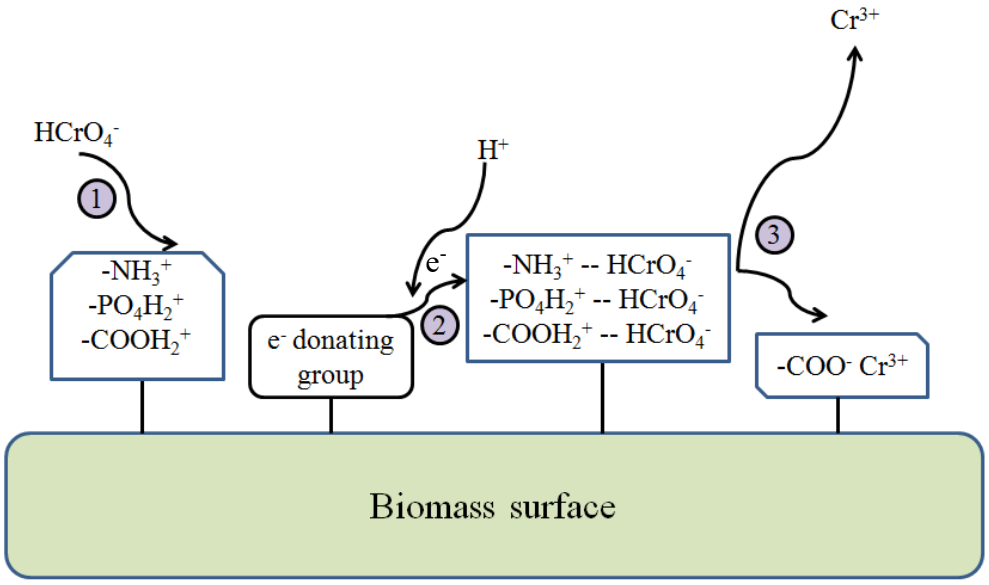

Figure 6.37 Schematic diagram for the Cr(VI) removal by *Mucor rouxii*.

Chapter 7

Conclusions

Mucor rouxii, a low-cost filamentous fungal biomass, was reported earlier to be an outstanding biosorbent for removing Pb(II) ions from an aqueous solution. However, information on the biosorption capacities of the fungal biomass towards other heavy metal ions and the biosorption mechanisms is scarce. Therefore, the aims of this study were to investigate the applicability of the fungal biomass for removing Cd(II), Cr(VI) and Cr(III) ions from the aqueous solution and to elucidate the mechanisms involved. In the preliminary studies, the fungal biomass exhibited outstanding removal abilities towards Cd(II) and Cr(VI) ions when compared with other studies. Hence, the main focuses of this study were to evaluate the experimental parameters that affected the Cd(II) and Cr(VI) removal performances and to elucidate the Cd(II) and Cr(VI) removal mechanisms of the fungal biomass.

The optimization of growth conditions of the fungal biomass were investigated. The results showed that the high incubation temperature and excessive incubation period might inhibit the growth of the fungal biomass.

The surface properties of the fungal biomass were characterized by zeta potential measurement, SCM and spectroscopic studies (SEM/EDAX, FTIR and XPS). Based on the zeta potential measurement, the zero point charge of the fungal biomass was found to be 3.5. The results implied that cations biosorption onto the fungal biomass was more facile when the pH value was above 3.5. The surface

complexation modeling (SCM) of the high-resolution potentiometric titration indicated the presence of four types of surface functional groups on the fungal biomass (phosphodiester, carboxyl, hydroxyl and amine groups). The SEM images of the pristine biomass illustrated that the surface of the fungal biomass was smooth and filamentous. The main surface compositions of the fungal biomass were revealed by EDAX, which were C, N, O and P. Results of FTIR and XPS analyses were consonant with the SCM results.

The batch biosorption results showed that the experimental parameters, including pH, biomass concentration, initial metal concentration, contact time, agitation speed and temperature, were highly correlated to the Cd(II) sorption performance of the fungal biomass. The equilibrium and kinetic data of Cd(II) correlated well with the Sips and the pseudo-second order model, respectively. The intraparticle diffusion analysis suggested that besides intraparticle diffusion external mass transfer might also control the Cd(II) removal process to some extent. The thermodynamic studies demonstrated that the Cd(II) biosorption process were endothermic in nature, thermodynamically feasible and spontaneous. Additional peaks of Cd were observed on the EDAX spectrum after biosorption, indicating the adsorption of Cd ions on the biomass surface. FTIR and XPS studies revealed that phosphodiester, carboxyl and amine groups were involved in Cd(II) biosorption. The surface

complexation models for Cd(II) biosorption showed that two-site-two-pK_a model well simulated the biosorption edge data. The average Cd-carboxyl and Cd-phosphodiester log stability constants were 1.19±0.23 and 6.87±0.51, respectively.

The effect of pH, biomass concentration, initial metal concentration, contact time, agitation speed and temperature on Cr(VI) removal by the fungal biomass were also investigated. The percentage removal of Cr(VI) increased with decreasing pH and initial metal concentration, but increased with increasing biomass concentration, contact time, temperature and agitation speed. The isotherm data were well simulated by the non-linearized Langmuir, Redlich-Peterson and Sips models. The intraparticle diffusion analysis suggested that besides intraparticle diffusion external mass transfer might also control the Cr removal to some degree. The Cr(VI) removal kinetics could be simulated very well by the intraparticle diffusion equation. In the EDAX analysis, additional peaks of Cr were observed after biosorption, indicating the presence of Cr ions on the biomass surface. XPS was used to determine the oxidation states of Cr bound on the biomass surface, and revealed that the dominant specie bound on it was Cr(III), indicating that most of the Cr(VI) ions were reduced to Cr(III) by the fungal biomass. The bio-reduced Cr(III) ions appeared in the aqueous solution or were partly bound onto the biomass surface. High-resolution XPS spectra showed that phosphodiester, amine and carboxyl groups

were involved in Cr(VI) removal. The FTIR analysis also indicated that carboxyl and amine groups were involved in the removal of Cr(VI) from the aqueous solution. The Cr(VI) removal by the fungal biomass was accomplished by biosorption coupled with reduction. This study demonstrated that *Mucor rouxii* is an effective biosorbent for removing Cd(II) and Cr(VI) ions from contaminated water and wastewater.

Chapter 8

Further Studies

The following areas are suggested for further investigation:

1.) Chemical modifications such as the blocking of amine, carboxyl and phosphodiester groups can be researched in order to provide additional evidences for further elucidations of Cd(II) and Cr(VI) removal mechanisms.

2.) The separation of the fungal biomass from the metal-biomass solution mixture is costly, tedious and time-consuming. Immobilization of the biomass in a supporting material can simplify the separation process. Common supporting materials are silica and alginates.

3.) Desorption studies can be conducted to evaluate the reusability of the fungal biomass by using desorbing agents such as citric acid, sodium hydroxide and EDTA solution.

4.) Real industrial effluents usually contain more than one type of heavy metal ions. Hence, the multi-metal solution system and real wastewater can be used to evaluate the metal removal abilities of the fungal biomass when it is used to treat real wastewater.

Appendix 1A. One-way analysis of variance and unpaired Student's t-test for the effect of incubation temperature on the yield of *Mucor rouxii*

	Yield		
	One-way analysis of variance		
Temp (℃)	F	F_{crit}	Interpretation
25	14.69	9.55	$F>F_{crit}$, significant difference
30			
37			
	Yield		
	Unpaired student's t test		
Temp (℃)	t_{stat}	t_{crit}	Interpretation
25 vs 30	0.41	4.30	$t_{stat}<t_{crit}$, no significant difference
25 vs 37	4.48	4.30	Significant difference

Appendix 1B. One-way analysis of variance and unpaired Student's t-test for the effect of incubation temperature on biosorption capacities of *Mucor rouxii*.

	Cd(II)			Cr(VI)		
	One-way analysis of variance			One-way analysis of variance		
Temp (℃)	F	F_{crit}	Interpretation	F	F_{crit}	Interpretation
25 30 37	96.29	9.55	Significant difference	3.57	9.55	No significant difference
	Cd(II)			Cr(VI)		
	Unpaired student's t test			Unpaired student's t test		
Temp (℃)	t_{stat}	t_{crit}	Interpretation	t_{stat}	t_{crit}	Interpretation
25 vs 30	1.05	4.30	No significant difference	1.90	4.30	No significant difference
25 vs 37	10.20	4.30	Significant difference	-2.45	4.30	No significant difference

Appendix 2. Summary of equivalence points and total surface site concentration of *Mucor rouxii*.

System	Equivalence point	Total surface site concentration (mmol/g)
1 g/L, 0.01M, trial 1	4.4	2.679
1 g/L, 0.01M, trial 2	4.3	2.725
1 g/L, 0.1M, trial 1	4.0	2.167
1 g/L, 0.1M, trial 2	4.3	2.434
2 g/L, 0.01M, trial 1	3.5	2.686
2 g/L, 0.01M, trial 2	3.4	2.479
2 g/L, 0.1M, trial 1	3.3	2.726
2 g/L, 0.1M, trial 2	3.2	2.546

Appendix 3A. The plot of TOTH verus pH (1 g/L, 0.1M $NaNO_3$).

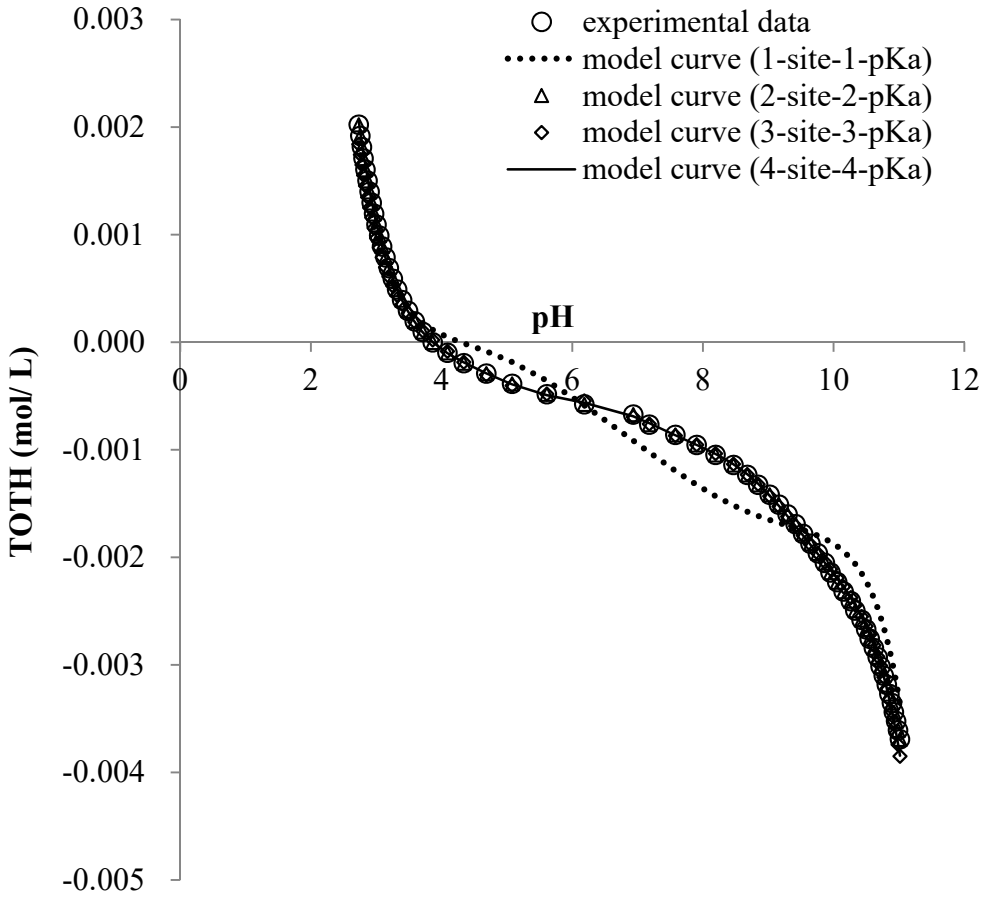

Appendix 3B. The plot of TOTH verus pH (1 g/L, 0.01MNaNO$_3$).

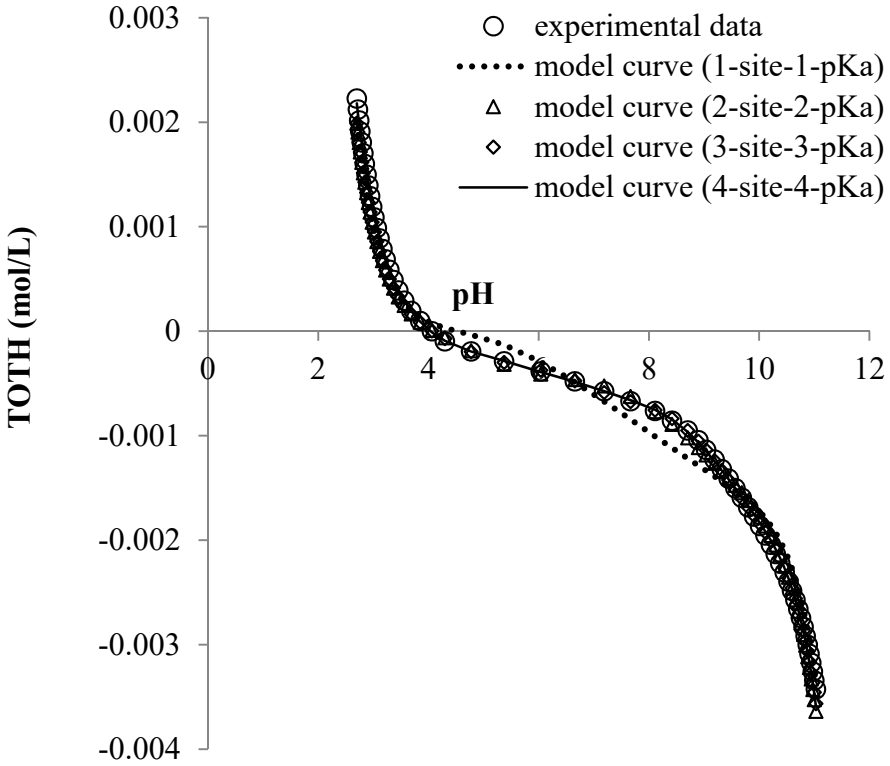

Appendix 3C. The plot of TOTH verus pH (2 g/L, 0.1M $NaNO_3$).

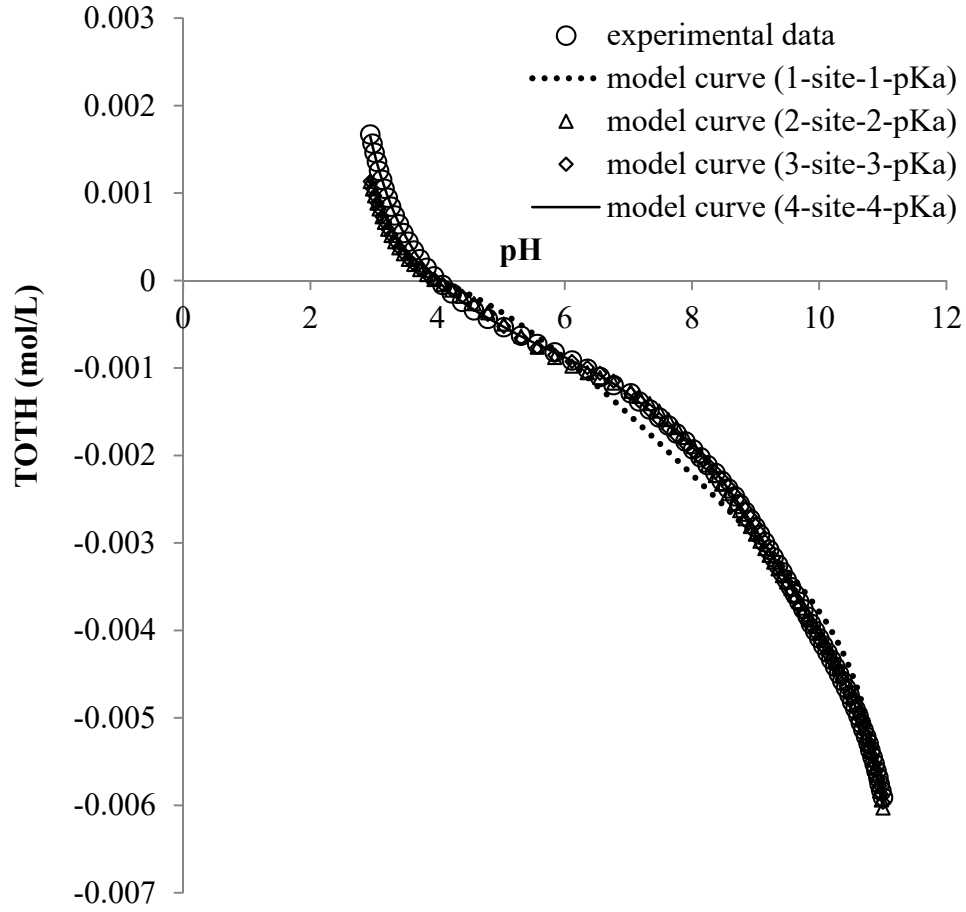

Appendix 3D. The plot of TOTH verus pH (2 g/L, 0.01M $NaNO_3$).

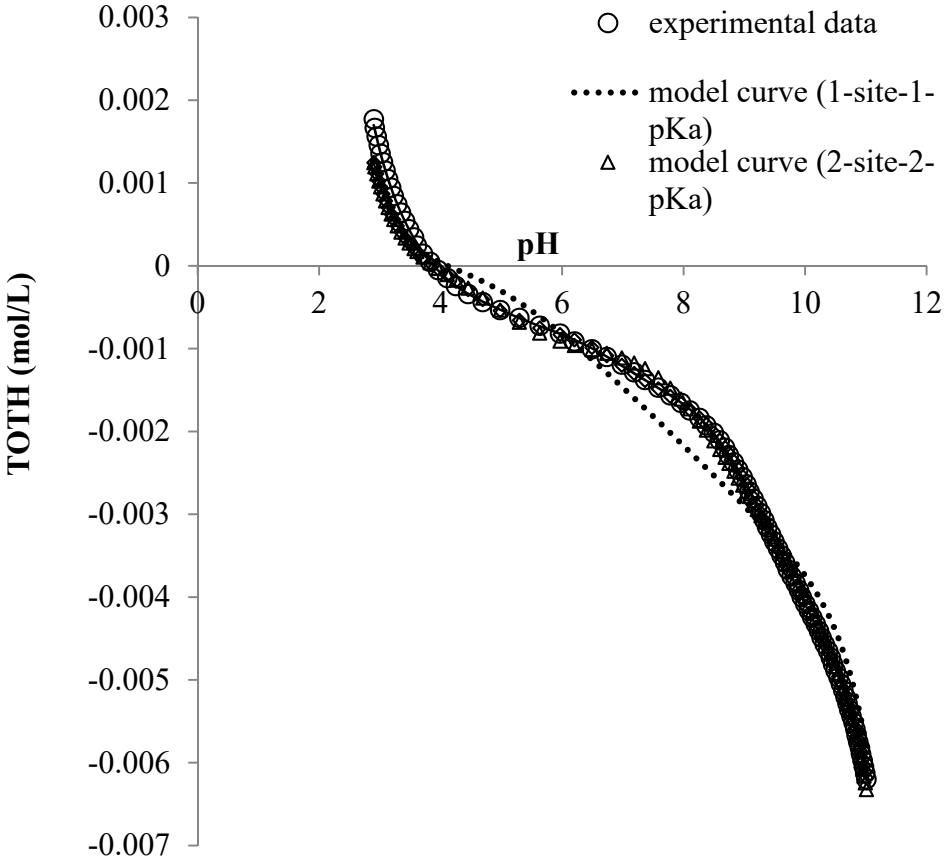

Appendix 4. Cr concentration profiles during the removal of Cr(VI) from aqueous solution by *Mucor rouxii* (A) 1 g/L, (B) 5 g/L and (C) 10 g/L.

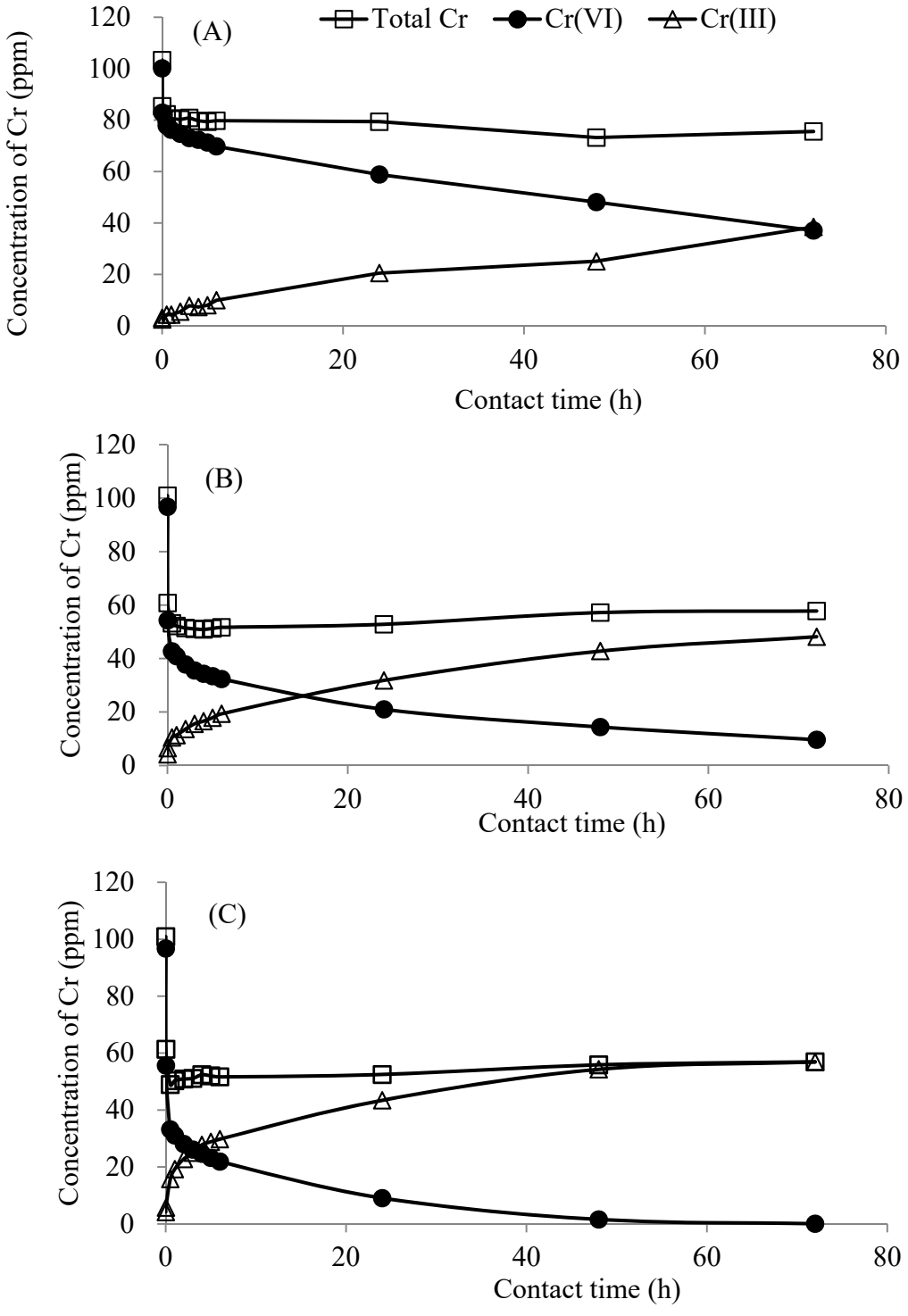

Appendix 5. Comparison of parameters obtained from non-linearized kinetic models for Cr(VI) removal by *Mucor rouxii* (1, 5 and 10 g/L).

Models		1 g/L	5 g/L	10 g/L
Pseudo-first order	q_e (mg/g)	48.35	13.66	8.159
	k_1 (h^{-1})	0.2406	60.78	45.86
	r^2	0.6083	0.7906	0.8258
	SSE	1044.48	48.30	14.57
	RMSE	9.74	2.10	1.15
	SE	10.77	2.32	1.27
Pseudo-second order	q_e (mg/g)	51.23	13.76	8.243
	k_2 (g/mg-h)	0.00738	6.705	7.115
	r^2	0.7069	0.8007	0.8396
	SSE	781.46	45.97	13.41
	RMSE	8.43	2.04	1.10
	SE	9.32	2.26	1.22
Elovich	β (g/mg)	943	60715	14226
	α (mg/g-h)	0.2066	0.9172	1.421
	r^2	0.8148	0.9741	0.9911
	SSE	493.79	5.968	0.7469
	RMSE	6.70	0.74	0.26
	SE	7.41	0.81	0.29
Fractional power	k (mg/g-h^v)	21.38	11.57	6.801
	v	0.2205	0.09382	0.09783
	r^2	0.9479	0.9919	0.9961
	SSE	138.76	1.877	0.3259
	RMSE	3.55	0.41	0.17
	SE	3.93	0.46	0.19
Intraparticle diffusion	k_{p1} (mg/g-$min^{1/2}$)	0.6356	0.1228	0.0723
	c	16.93	10.45	6.185
	r^2	0.9943	0.9291	0.8234
	SSE	10.13	5.00	4.88
	RMSE	0.96	0.67	0.67
	SE	1.01	0.75	0.74

Appendix 6. pH effect on Cr(III) biosorption by *Mucor rouxii*.

(Conditions: 100 ppm Cr(III); 1 g/L biomass)

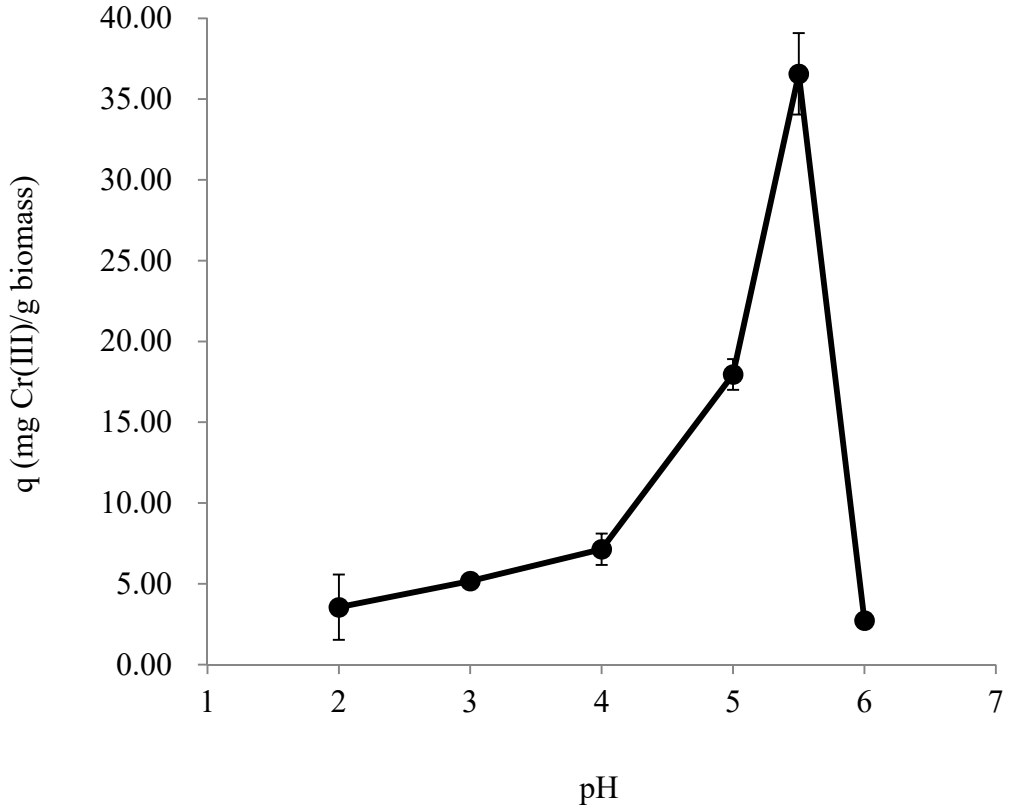

Appendix 7. Initial metal concentration effect on Cr(III) biosorption by *Mucor rouxii*. (Conditions: pH 5.5; 1 g/L)

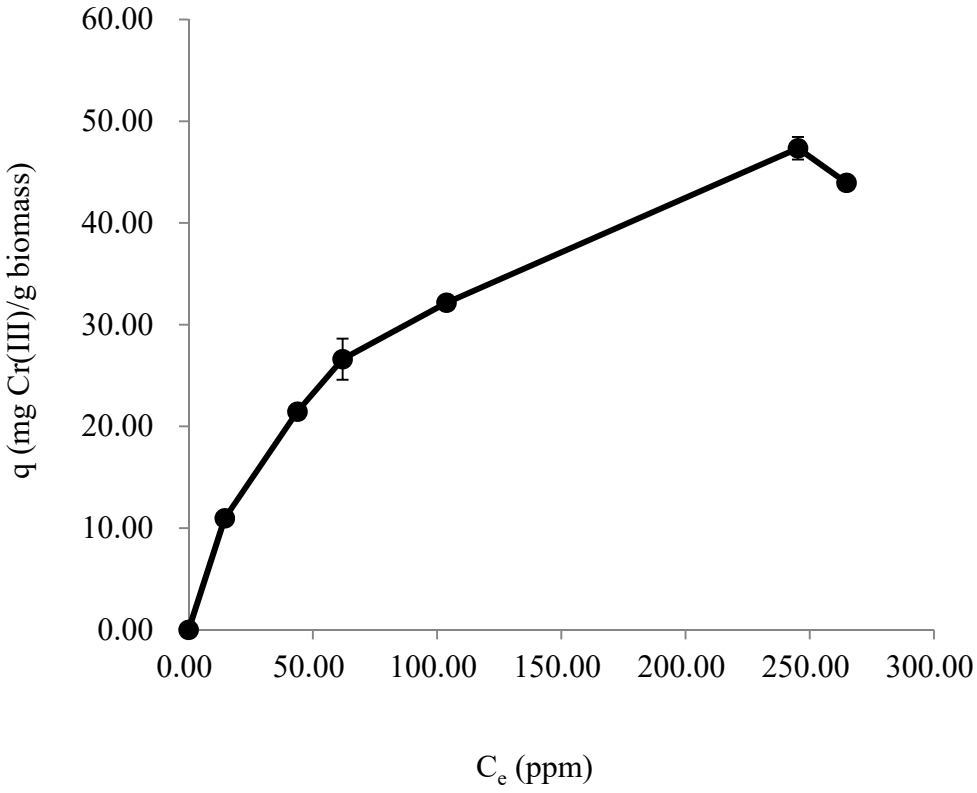

References

Agarwal, G. S., Bhuptawat, H. K. and Chaudhari, S. (2006) 'Biosorption of chromium(VI) by *Tamarindus indica* seeds', *Bioresource Technology*, 97, 949-956.

Ahluwalia, S. S. and Goyal, D. (2007) 'Microbial and plant derived biomass for removal of heavy metals from wastewater', *Bioresource Technology*, 98(12), 2243-2257.

Akar, T., Tunali, S. and Cabuk, A. (2007) 'Study on the characterization of lead (II) biosorption by fungus *Aspergillus parasiticus*', *Applied Biochemistry and Biotechnology*, 136(3), 389-405.

Aksu, Z., Acikel, U. and Kutsal, T. (1999) ' Investigation of simultaneous biosorption of copper(II) and chromium(VI) on dried *Chlorella Vulgaris* from binary metal mixtures: Application of multicomponent adsorption isotherms', *Separation Science and Technology*, 34(3), 501-524.

Aksu, Z., Ertugrul, S. and Donmez, G. (2009) 'Single and binary chromium(VI) and Remazol Black B biosorption properties of *Phormidium* sp.', *Journal of Hazardous Materials*, 168, 310-318.

Allouche, F. N., Mameri, N. and Guibal, E. (2011) 'Pb(II) biosorption on *Posidonia oceanica* biomass', *Chemical Engineering Journal*, 168(3), 1174-1184.

American Public Health Association (1998) 'Standard methods for the examination of water and wastewater', 20th ed., Washington, DC: American Public Health Association.

Andersen, O. (1984) 'Chelation of cadmium', *Environmental Health Perspectives*, 54, 249-266.

Anirudhan, T. S., Radhakrishnan, P. G. (2008) 'Thermodynamics and kinetics of adsorption of Cu(II) from aqueous solutions onto a new cation exchanger derived from tamarind fruit shell', *Journal of Chemical Thermodynamics*, 40(4), 702-709.

Aoyama, M. and Tsuda, M (2001) ‘Removal of Cr(VI) from aqueous solutions by larch bark’, *Wood Science and Technology*, 35, 425-434.

Apiratikul, R. and Pavasant, P. (2008) ‘Batch and column studies of biosorption of heavy metals by *Caulerpa lentillifera*’, *Bioresource Technology*, 99(8), 2766-2777.

Aravindhan, R., Madhan, B., Rao, J. R., Nair, B. U. and Ramasami, T. (2004) 'Bioaccumulation of chromium from tannery wastewater: An approach for chrome recovery and reuse', *Environmental Science & Technology*, 38(1), 300-306.

Areco, M. M. and Afonso, M. D. (2010) 'Copper, zinc, cadmium and lead biosorption by *Gymnogongrus torulosus*: Thermodynamics and kinetics studies', *Colloids and Surfaces B-Biointerfaces*, 81(2), 620-628.

Argun, M. E., Dursun, S., Ozdemir, C. and Karatas, M. (2007) 'Heavy metal adsorption by modified oak sawdust: Thermodynamics and kinetics', *Journal of Hazardous Materials*, 141(1), 77-85.

Arica, M. Y. and Bayramoglu, G. (2005) ‘Cr(VI) biosorption from aqueous solutions using free and immobilized biomass of *Lentinus sajor-caju*: Preparation and kinetic characterization’, *Colloids and Surfaces A: Physicochem. Eng. Aspects*, 253, 203-211.

Arief, V. O., Trilestari, K., Sunarso, J., Indraswati, N. and Ismadji, S. (2008) 'Recent progress on biosorption of heavy metals from liquids using low cost biosorbents: Characterization, biosorption parameters and mechanism studies', *Clean-Soil Air Water*, 36(12), 937-962.

Ashkenazy, R., Gottlieb, L. and Yannai, S. (1996) ‘Characterization of acetone-washed yeast biomass functional groups involved in lead biosorption’, *Biotechnology and Bioengineering*, 55(1), 1-10.

Atkins, P. W. (2002) ‘Atkins' Physical chemistry’, Peter Atkins, Julio de Paula, Oxford [England]: Oxford England: Oxford University Press.

Aytas, S., Turkozu, D. A. and Gok, C. (2011) 'Biosorption of uranium(VI) by

bi-functionalized low cost biocomposite adsorbent', *Desalination*, 280(1-3), 354-362.

Azouaou, N., Sadaoui, Z., Djaafri, A. and Mokaddem, H. (2010) 'Adsorption of cadmium from aqueous solution onto untreated coffee grounds: Equilibrium, kinetics and thermodynamics', *Journal of Hazardous Materials*, 184(1-3), 126-134.

Bai, H. J., Zhang, Z. M., Yang, G. E. and Li, B. Z. (2008) 'Bioremediation of cadmium by growing *Rhodobacter sphaeroides*: Kinetic characteristic and mechanism studies', *Bioresource Technology*, 99(16), 7716-7722.

Bartnicki-Garica, S. (1963) 'Symposium on biochemical bases of morphogenesis in fungi III. Mold-yeast dimorphism of *Mucor*', *Bacteriology Reviews*, 27(3), 293-304.

Bayramoglu, G., Bektas, S. and Arica, M. Y. (2003) 'Biosorption of heavy metal ions on immobilized white-rot fungus *Trametes versicolor*', *Journal of Hazardous Materials,* 101(3), 285-300.

Bayramoglu, G., Celik, G., Yalcin, E., Yilmaz, M. and Arica, M. Y. (2005) 'Modification of surface properties of *Lentinus sajor-caju* mycelia by physical and chemical methods: Evaluation of their Cr^{6+} removal efficiencies from aqueous medium', *Journal of Hazardous Materials*, 119(1-3), 219-229.

Benguella, B. and Benaissa, H. (2002) 'Cadmium removal from aqueous solutions by chitin: kinetic and equilibrium studies', *Water Research*, 36(10), 2463-2474.

Bettina, B. (2015) ‘Dipolar correlation spectroscopy: Higher-order correlation terms in three-spin double electron-electron resonance (DEER)’, Wiesbaden:Springer Spektrum.

Bingol, A., Ucun, H., Bayhan, Y. K., Karagunduz, A., Cakici, A. and Keskinler, B. (2004) 'Removal of chromate anions from aqueous stream by a cationic surfactant-modified yeast', *Bioresource Technology*, 94(3), 245-249.

Boddu, V. M., Abburi, K., Talbott, J. L. and Smith, E. D. (2003) 'Removal of hexavalent chromium from wastewater using a new composite chitosan

biosorbent', *Environmental Science & Technology*, 37(19), 4449-4456.

Cesur, H. and Balkaya, N. (2007) 'Zinc removal from aqueous solution using an industrial by-product phosphogypsum', *Chemical Engineering Journal*, 131(1-3), 203-208.

Chen, J. P. and Yang, L. (2006) 'Study of a heavy metal biosorption onto raw and chemically modified *Sargassum* sp. via spectroscopic and modeling analysis', *Langmuir*, 22(21), 8906-8914.

Chen, X. C., Shi, J. Y., Chen, Y. X., Xu, X. J., Chen, L. T., Wang, H. and Hu, T. D. (2007) 'Determination of copper binding in *Pseudomonas putida* CZ1 by chemical modifications and X-ray absorption spectroscopy', *Applied Microbiology and Biotechnology*, 74(4), 881-889.

Chen, Z., Huang, Z. P., Cheng, Y. J., Pan, D. M., Pan, X. H., Yu, M. J., Pan, Z. Y., Lin, Z., Guan, X. and Wu, Z. Y. (2012) 'Cr(VI) uptake mechanism of *Bacillus cereus*', *Chemosphere*, 87(3), 211-216.

Cheung, W. H., Szeto, Y. S. and McKay, G. (2007) 'Intraparticle diffusion processes during acid dye adsorption onto chitosan', *Bioresource Technology,* 98(15), 2897-2904.

Choi, S. B. and Yun, Y. S. (2006) 'Biosorption of cadmium by various types of dried sludge: An equilibrium study and investigation of mechanisms', *Journal of Hazardous Materials*, 138(2), 378-383.

Choy, K. K. H., Ko, D. C. K., Cheung, C. W., Porter, J. F. and McKay, G. (2004) 'Film and intraparticle mass transfer during the adsorption of metal ions onto bone char', *Journal of Colloid and Interface Science,* 271(2), 284-295.

Cox, J. S., Smith, D. S., Warren, L. A. and Ferris, F. G. (1999) 'Characterizing heterogeneous bacterial surface functional groups using discrete affinity spectra for proton binding', *Environmental Science & Technology*, 33(24), 4514-4521.

Cui, H. J., Fu, M. L., Yu, S. and Wang, M. K. (2011) 'Reduction and removal of Cr(VI) from aqueous solutions using modified byproducts of beer production',

Journal of Hazardous Materials, 186(2-3), 1625-1631.

Das, N., Charumathi, D. and Vimala, R. (2007) 'Effect of pretreatment on Cd^{2+} biosorption by mycelial biomass of *Pleurotus florida*', African Journal of *Biotechnology*, 6(22), 2555-2558.

Das, S. K., Das, A. R. and Guha, A. K. (2007) 'A study on the adsorption mechanism of mercury on *Aspergillus versicolor* biomass', *Environmental Science & Technology*, 41(24), 8281-8287.

Das, S. K. and Guha, A. K. (2007) 'Biosorption of chromium by *Termitomyces clypeatus*', *Colloids and Surfaces B-Biointerfaces*, 60(1), 46-54.

Daughney, C. J., Fowle, D. A. and Fortin, D. E. (2001) 'The effect of growth phase on proton and metal adsorption by *Bacillus subtilis*', *Geochimica Et Cosmochimica Acta*, 65(7), 1025-1035.

Davis, T. A., Volesky, B. and Mucci, A. (2003) 'A review of the biochemistry of heavy metal biosorption by brown algae', *Water Research*, 37(18), 4311-4330.

Deng, L. P., Su, Y. Y., Hua, S., Wang, X. T. and Zhu, X. B. (2007) 'Sorption and desorption of lead (II) from wastewater by green algae *Cladophora fascicularis*', *Journal of Hazardous Materials*, 143(1-2), 220-225.

Deng, S. B. and Ting, Y. P. (2005) 'Polyethylenimine-modified fungal biomass as a high-capacity biosorbent for Cr(VI) anions: Sorption capacity and uptake mechisms', *Environmental Science & Technology*, 39(21), 8490-8496.

Dhankhar, R. and Hooda, A. (2011) 'Fungal biosorption - an alternative to meet the challenges of heavy metal pollution in aqueous solutions', *Environmental Technology*, 32(5), 467-491.

Doshi, H., Ray, A. and Kothari, I. L. (2007) 'Biosorption of cadmium by live and dead *Spirulina*: IR spectroscopic, kinetics, and SEM studies', *Current Microbiology*, 54(3), 213-218.

Du, Q., Sun, Z. X., Forsling, W. and Tang, H. X. (1997) 'Acid-base properties of

aqueous illite surfaces', J*ournal of Colloid and Interface Science*, 187(1), 221-231.

Do, D. D. (1998) 'Adsorption analysis: equilibria and kinetics', Imperial College Press, 519-602.

Dzombak, D. A. and Morel, F. M. M. (1990) 'Surface complexation modeling: hydrous ferric oxide', John Wiley & Sons, Inc.

Eccles, H. (1999) 'Treatment of metal-contaminated wastes: Why select a biological process?', *Trends in Biotechnology*, 17(12), 462-465.

El-Naggar, M. R., El-Kamash, A. M., El-Dessouky, M. I. and Ghonaim, A. K. (2008) 'Two-step method for preparation of NaA-X zeolite blend from fly ash for removal of cesium ions', *Journal of Hazardous Materials,* 154(1-3), 963-972.

Elangovan, R., Philip, L. and Chandraraj, K. (2008) 'Biosorption of chromium species by aquatic weeds: Kinetics and mechanism studies', *Journal of Hazardous Materials*, 152(1), 100-112.

Elkady, M. F., Ibrahim, A. M. and Abd El-Latif, M. M. (2011) 'Assessment of the adsorption kinetics, equilibrium and thermodynamic for the potential removal of reactive red dye using eggshell biocomposite beads', *Desalination*, 278(1-3), 412-423.

Environmental Protection Department (1997) 'Technical memorandum on effluent standards', available: http://www.legislation.gov.hk/blis_pdf.nsf/6799165D2FEE3FA94825755E0033E532/569E03D57CCBAE69482575EE006FF774/$FILE/CAP_358AK_e_b5.pdf [assessed 30 June 1997].

Ertugay, N. and Bayhan, Y. K. (2008) 'Biosorption of Cr(VI) from aqueous solutions by biomass of *Agaricus bisporus*', *Journal of Hazardous Materials*, 154, 432-439.

Fein, J. B., Daughney, C. J., Yee, N. and Davis, T. A. (1997) 'A chemical equilibrium model for metal adsorption onto bacterial surfaces', *Geochimica Et Cosmochimica Acta*, 61(16), 3319-3328.

Fein, J. B., Martin, A. M. and Wightman, P. G. (2001) 'Metal adsorption onto bacterial surfaces: Development of a predictive approach', *Geochimica Et Cosmochimica Acta,* 65(23), 4267-4273.

Gallios, G. P. and Vaclavikova, M. (2008) 'Removal of chromium (VI) from water streams: a thermodynamic study', *Environmental Chemistry Letters*, 6(4), 235-240.

Gabr, R. M., Gad-Elrab, S. M. F., Abskharon, R. N. N., Hassan, S. H. A. and Shoreit, A. A. M. (2009) 'Biosorption of hexavalent chromium using biofilm of *E. coli* supported on granulated activated carbon', *World Journal of Microbiology and Biotechnology*, 25, 1695-1703.

Garcia-Reyes, R. B. and Rangel-Mendez, J. R. (2010) 'Adsorption kinetics of chromium(III) ions on agro-waste materials', *Bioresource Technology*, 101(21), 8099-8108.

Gardea-Torresdey, J. L., de la Rosa, G. and Peralta-Videa, J. R. (2004) 'Use of phytofiltration technologies in the removal of heavy metals: A review', *Pure and Applied Chemistry*, 76(4), 801-813.

Gao, Y. and Mucci, A. (2001) 'Acid base reactions, phosphate and arsenate complexation, and their competitive adsorption at the surface of goethite in 0.7 M NaCl solution', *Geochimica et Cosmochimica Acta*, 65(14), 2361-2378.

Ghosh, D., Saha, R., Ghosh, A., Nandi, R. and Saha, B. (2015) 'A review on toxic cadmium biosorption from contaminated wastewater', *Desalination and Water Treatment*', 53, 413-420.

Gonzalez, M. H., Araujo, G. C. L., Pelizaro, C. B., Menezes, E. A., Lemos, S. G., de Sousa, G. B. and Nogueira, A. R. A. (2008) 'Coconut coir as biosorbent for Cr(VI) removal from laboratory wastewater', *Journal of Hazardous Materials*, 159(2-3), 252-256.

Green-Ruiz, C., Rodriguez-Tirado, V. and Gomez-Gil, B. (2008) 'Cadmium and zinc removal from aqueous solutions by *Bacillus jeotgali*: pH, salinity and

temperature effects', *Bioresource Technology*, 99(9), 3864-3870.

Griffin, D. H. (1994) *Fungal physiology,* 2nd ed., New York: Wiley-Liss.

Gunay, A., Arslankaya, E. and Tosun, I. (2007) 'Lead removal from aqueous solution by natural and pretreated clinoptilolite: Adsorption equilibrium and kinetics', *Journal of Hazardous Materials*, 146(1-2), 362-371.

Gupta, R., Ahuja, P., Khan, S., Saxena, R. K. and Mohapatra, H. (2000) 'Microbial biosorbents: Meeting challenges of heavy metal pollution in aqueous solutions', *Current Science*, 78(8), 967-973.

Gupta, V. K. and Rastogi, A. (2009) 'Biosorption of hexavalent chromium by raw and acid-treated green alga *Oedogonium hatei* from aqueous solutions', *Journal of Hazardous Materials*, 163(1), 396-402.

Hameed, B. H. and El-Khaiary, M. I. (2008) 'Sorption kinetics and isotherm studies of a cationic dye using agricultural waste: Broad bean peels', *Journal of Hazardous Materials,* 154(1-3), 639-648.

Han, X., Wong, Y. S. and Tam, N. F. Y. (2006) 'Surface complexation mechanism and modeling in Cr(III) biosorption by a microalgal isolate, *Chlorella miniata*', *Journal of Colloid and Interface Science*, 303(2), 365-371.

Holman, H. Y. N., Perry, D. L., Martin, M. C., Lamble, G. M., McKinney, W. R. and Hunter-Cevera, J. C. (1999) 'Real-time characterization of biogeochemical reduction of Cr(VI) on basalt surfaces by SR-FTIR imaging', *Geomicrobiology Journal*, 16(4), 307-324.

Hydari, S., Sharififard, H., Nabavinia, M. and Parvizi, M. R. (2012) 'A comparative investigation on removal performances of commerical activated carbon, chitosan biosorbent and chitosan/activated carbon composite for cadmium', *Chemical Engineering Journal*, 193, 276-282.

Iddou, A. and Ouali, M. S. (2008) 'Waste-activated sludge (WAS) as Cr(III) sorbent biosolid from wastewater effluent', *Colloids and Surfaces B-Biointerfaces*, 66(2), 240-245.

Kapoor, A. and Viraraghavan, T. (1995) 'Fungal biosorption - An alternative treatment option for heavy metal bearing wastewaters: A review', *Bioresource Technology*, 53(3), 195-206.

Kapoor, A., Viraraghavan, T. and Cullimore, D. R. (1999) 'Removal of heavy metals using the fungus *Aspergillus niger*', *Bioresource Technology*, 70(1), 95-104.

Karthikeyan, T., Rajgopal, S. and Miranda, L. R. (2005) 'Chromium(VI) adsorption from aqueous solution by *Hevea Brasilinesis* sawdust activated carbon', *Journal of Hazardous Materials*, 124(1-3), 192-199.

Kazy, S. K., D'Souza, S. F. and Sar, P. (2009) 'Uranium and thorium sequestration by a *Pseudomonas* sp.: Mechanism and chemical characterization', *Journal of Hazardous Materials*, 163(1), 65-72.

Kratochvil, D., Pimentel, P. and Volesky, B. (1998a) 'Removal of trivalent and hexavalent chromium by seaweed biosorbent', *Environmental Science & Technology*, 32(18), 2693-2698.

Kratochvil, D. and Volesky, B. (1998b) 'Advances in the biosorption of heavy metals', *Trends in Biotechnology*, 16(7), 291-300.

Krishnani, K. K., Meng, X. G., Christodoulatos, C. and Boddu, V. M. (2008) 'Biosorption mechanism of nine different heavy metals onto biomatrix from rice husk', *Journal of Hazardous Materials*, 153(3), 1222-1234.

Koningsberger, D. C. and Prins, R. (1988) ‘X-ray absorption: Principles, applications, techniques of EXAFS, SEXAFS, and XANES. New York:Wiley.

Kurniawan, T. A., Chan, G. Y. S., Lo, W. H. and Babel, S. (2006a) 'Comparisons of low-cost adsorbents for treating wastewaters laden with heavy metals', *Science of the Total Environment*, 366(2-3), 409-426.

Kurniawan, T. A., Chan, G. Y. S., Lo, W. H. and Babel, S. (2006b) 'Physico-chemical treatment techniques for wastewater laden with heavy metals',

Chemical Engineering Journal, 118(1-2), 83-98.

Kumar, R., Bishnoi, N. R., Garima and Bishnoi, K. (2008) ‘Biosorption of Cr(VI) from aqueous solution and electroplating wastewater using fungal biomass’, *Chemical Engineering Journal*, 135(3), 202-208.

Kushwaha, S., Sreedhar, B. and Padmaja, P. (2010) 'Sorption of phenyl mercury, methyl mercury, and inorganic mercury onto chitosan and barbital immobilized chitosan: Spectroscopic, potentiometric, kinetic, equilibrium, and selective desorption studies', *Journal of Chemical and Engineering Data*, 55(11), 4691-4698.

Lei, W., Chua, H., Lo, W. H., Yu, P. H. F., Zhao, Y. G. and Wong, P. K. (2000) 'A novel magnetite-immobilized cell process for heavy metal removal from industrial effluent', *Applied Biochemistry and Biotechnology,* 84-6, 1113-1126.

Leone, L., Ferri, D., Manfredi, C., Persson, P., Shchukarev, A., Sjoberg, S. and Loring, J. (2007) 'Modeling the acid-base properties of bacterial surfaces: A combined spectroscopic and potentiometric study of the gram-positive bacterium *Bacillus subtilis*', *Environmental Science & Technology*, 41(18), 6465-6471.

Leung, W. C., Chua, H. and Lo, W. H. (2001) 'Biosorption of heavy metals by bacteria isolated from activated sludge', *Applied Biochemistry and Biotechnology*, 91-3, 171-184.

Leung, W. C., Wong, M. F., Chua, H., Lo, W., Yu, P. H. F. and Leung, C. K. (2000) 'Removal and recovery of heavy metals by bacteria isolated from activated sludge treating industrial effluents and municipal wastewater', *Water Science and Technology,* 41(12), 233-240.

LeyvaRamos, R., RangelMendez, J. R., MendozaBarron, J., FuentesRubio, L. and GuerreroCoronado, R. M. (1997) 'Adsorption of cadmium(II) from aqueous solution onto activated carbon', *Water Science and Technology*, 35(7), 205-211.

Lin, Y. C. and Wang, S. L. (2012) 'Chromium(VI) reactions of polysaccharide biopolymers', *Chemical Engineering Journal*, 181, 479-485.

Lin, Z. Y., Zhou, C. H., Wu, J. M., Zhou, J. Z. and Wang, L. (2005) 'A further insight into the mechanism of Ag^{+} biosorption by *Lactobacillus* sp strain A09', *Spectrochimica Acta Part a-Molecular and Biomolecular Spectroscopy*, 61(6), 1195-1200.

Liu, C. C., Wang, M. K., Chiou, C. S., Li, Y. S., Lin, Y. A. and Huang, S. S. (2006) 'Chromium removal and sorption mechanism from aqueous solutions by wine processing waste sludge', *Industrial & Engineering Chemistry Research*, 45(26), 8891-8899.

Liu, N., Liao, J., Yang, Y., Luo, S., Luo, Q., An, Z., Duan, Y., Liu, M. and Zhao, P. (2008) 'Biosorption of ^{241}Am by *Saccharomyces cerevisiae*: Preliminary investigation on mechanism', *Journal of Radioanalytical and Nuclear Chemistry*, 275(1), 173-180.

Liu, R. X., Tang, H. X. and Lo, W. H. (2002) 'Advances in biosorption mechanism and equilibrium modeling for heavy metals on biomaterials', *Progress in Chemistry,* 14(2), 87-92.

Liu, Y. (2008) 'Biosorption isotherms, kinetics and thermodynamics', Separation and Purification Technology, 61(3), 229-242.

Lo, W., Chua, H., Wong, M. F. and Yu, P. (2003a) 'Bacterial biosorbent for removing and recovering copper from electroplating effluents', *Water Science and Technology*, 47(1), 251-256.

Lo, W. H., Chua, H., Lam, K. H. and Bi, S. P. (1999) 'A comparative investigation on the biosorption of lead by filamentous fungal biomass', *Chemosphere*, 39(15), 2723-2736.

Lo, W. H., Ng, L. M., Chua, H., Yu, P. H. F., Sin, S. N. and Wong, P. K. (2003b) 'Biosorption and desorption of copper(II) ions by *Bacillus* sp', *Applied Biochemistry and Biotechnology,* 105, 581-591.

Luo, J. M., Xiao, X. A. and Luo, S. L. (2010) 'Biosorption of cadmium(II) from aqueous solutions by industrial fungus *Rhizopus cohnii*', *Transactions of Nonferrous Metals Society of China*, 20(6), 1104-1111.

Majumdar, S. S., Das, S. K., Chakravarty, R., Saha, T., Bandyopadhyay, T. S. and Guha, A. K. (2010) 'A study on lead adsorption by *Mucor rouxii* biomass', *Desalination*, 251(1-3), 96-102.

Malkoc, E. (2006) 'Ni(II) removal from aqueous solutions using cone biomass of *Thuja orientalis*', *Journal of Hazardous Materials*, 137(2), 899-908.

Marin, A. B. P., Aguilar, M. I., Meseguer, V. F., Ortuno, J. F., Saez, J. and Llorens, M. (2009) 'Biosorption of chromium (III) by orange (*Citrus cinensis*) waste: Batch and continuous studies', *Chemical Engineering Journal*, 155(1-2), 199-206.

Martinez, R. E. and Ferris, F. G. (2001) 'Chemical equilibrium modeling techniques for the analysis of high-resolution bacterial metal sorption data', *Journal of Colloid and Interface Science*, 243(1), 73-80.

Mata, Y. N., Blazquez, M. L., Ballester, A., Gonzalez, F. and Munoz, J. A. (2008) 'Characterization of the biosorption of cadmium, lead and copper with the brown alga *Fucus vesiculosus*', *Journal of Hazardous Materials*, 158(2-3), 316-323.

Merroun, M. L., Omar, N. B., Gonzalez-Munoz, M. T. and Arias, J. M. (1998) '*Myxococcus xanthus* biomass as biosorbent for lead', *Journal of Applied Microbiology*, 84, 63-67.

Mohan, D. and Pittman, C. U. (2006) 'Activated carbons and low cost adsorbents for remediation of tri- and hexavalent chromium from water', *Journal of Hazardous Materials*, 137(2), 762-811.

Naja, G., Mustin, C., Volesky, B. and Berthelin, J. (2005) 'A high-resolution titrator: a new approach to studying binding sites of microbial biosorbents', *Water Research*, 39(4), 579-588.

Nakajima, A. and Baba, Y. (2004) 'Mechanism of hexavalent chromium adsorption by persimmon tannin gel', *Water Research*, 38(12), 2859-2864.

Nakamoto, K. (2009) 'Infrared and raman spectra of inorganic and coordination compounds part b: applications in coordination, organometallic, and bioinorganic

chemistry', John Wiley & Sons, Inc., Hoboken, New Jersey.

National Institute of Standards and Technology (2012) 'NIST X-ray Photoelectron Spectroscopy Database', available: http://srdata.nist.gov/xps/EngElmSrchQuery.aspx?EType=PE&CSOpt=Retri_ex_dat&Elm=Cr [assessed 15 Sep 2012].

Ngwenya, B. T., Tourney, J., Magennis, M., Kapetas, L. and Olive, V. (2009) 'A surface complexation framework for predicting water purification through metal biosorption', *Desalination*, 248(1-3), 344-351.

Nordic Council of Ministers (2003) 'Cadmium review', available: http://www.who.int/ifcs/documents/forums/forum5/nmr_cadmium.pdf [assessed 28 Jan 2003].

Ojeda, J. J., Romero-Gonzalez, M. E., Bachmann, R. T., Edyvean, R. G. J. and Banwart, S. A. (2008) 'Characterization of the cell surface and cell wall chemistry of drinking water bacteria by combining XPS, FTIR spectroscopy, modeling, and potentiometric titrations', *Langmuir*, 24(8), 4032-4040.

Oura, K., Lifshits, V. G., Saranin, A. A., Zotov, A. V., Katayama, M. (2003) 'Surface science: an introduction. ', Springer.

Ozcan, A., Oncu, E. M. and Ozcan, A. S. (2006) 'Adsorption of Acid Blue 193 from aqueous solutions onto DEDMA-sepiolite', *Journal of Hazardous Materials*, 129(1-3), 244-252.

Ozdemir, S., Kilinc, E., Poli, A., Nicolaus, B. and Guven, K. (2009) 'Biosorption of Cd, Cu, Ni, Mn and Zn from aqueous solutions by thermophilic bacteria, *Geobacillus toebii* sub.sp *decanicus* and *Geobacillus thermoleovorans* sub.sp *stromboliensis*: Equilibrium, kinetic and thermodynamic studies', *Chemical Engineering Journal*, 152(1), 195-206.

Ozer, A. and Ozer, D. (2003) ‘Comparative study of the biosorption of Pb(II), Ni(II) and Cr(VI) ions onto *S. cerevisiae*: Determination of biosorption heats’, *Journal of Hazardous Materials*, B100, 219-229.

Pan, J. H., Liu, R. X. and Tang, H. X. (2007) 'Surface reaction of *Bacillus cereus* biomass and its biosorption for lead and copper ions', *Journal of Environmental Sciences-China*, 19(4), 403-408.

Panda, G. C., Das, S. K., Chatterjee, S., Maity, P. B., Bandopadhyay, T. S. and Guha, A. K. (2006) 'Adsorption of cadmium on husk of *Lathyrus sativus*: Physico-chemical study', *Colloids and Surfaces B-Biointerfaces*, 50(1), 49-54.

Park, D., Lim, S. R., Yun, Y. S. and Park, J. M. (2007a) 'Reliable evidences that the removal mechanism of hexavalent chromium by natural biomaterials is adsorption-coupled reduction', *Chemosphere,* 70(2), 298-305.

Park, D., Yun, Y. S., Ahn, C. K. and Park, J. M. (2007b) 'Kinetics of the reduction of hexavalent chromium with the brown seaweed *Ecklonia* biomass', *Chemosphere,* 66(5), 939-946.

Park, D., Yun, Y. S., Jo, J. H. and Park, J. M. (2005a) 'Mechanism of hexavalent chromium removal by dead fungal biomass of *Aspergillus niger*', *Water Research*, 39(4), 533-540.

Park, D., Yun, Y. S. and Park, J. M. (2004) 'Reduction of hexavalent chromium with the brown seaweed *Ecklonia* biomass', *Environmental Science & Technology*, 38(18), 4860-4864.

Park, D., Yun, Y. S. and Park, J. M. (2005b) 'Use of dead fungal biomass for thedetoxification of hexavalent chromium: screening and kinetics', *Process Biochemistry,* 40(7), 2559-2565.

Parsons, J. G., Hejazi, M., Tiemann, K. J., Henning, J. and Gardea-Torresdey, J. L. (2002) 'An XAS study of the binding of copper(II), zinc(II), chromium(III) and chromium(VI) to hops biomass', *Microchemical Journal*, 71(2-3), 211-219.

Patron-Prado, M., Casas-Valdez, M., Serviere-Zaragoza, E., Zenteno-Savin, T., Lluch-Cota, D. B. and Mendez-Rodriguez, L. (2011) 'Biosorption capacity for cadmium of brown seaweed *Sargassum sinicola* and *Sargassum lapazeanum* in the gulf of California', *Water Air and Soil Pollution*, 221(1-4), 137-144.

Perez-Marin, A. B., Zapata, V. M., Ortuno, J. F., Aguilar, M., Saez, J. and Llorens, M. (2007) 'Removal of cadmium from aqueous solutions by adsorption onto orange waste', *Journal of Hazardous Materials*, 139(1), 122-131.

Pethkar, A. V., Kulkarni, S. K. and Paknikar, K. M. (2001) 'Comparative studies on metal biosorption by two strains of *Cladosporium cladosporioides*', *Bioresource Technology*, 80(3), 211-215.

Prabhakaran, S. K., Vijayaraghavan, K. and Balasubramanian, R. (2009) 'Removal of Cr(VI) ions by spent tea and coffee dusts: Reduction to Cr(III) and biosorption', *Industrial & Engineering Chemistry Research*, 48, 2113-2117.

Preetha, B. and Viruthagiri, T. (2007) 'Batch and continuous biosorption of chromium(VI) by *Rhizopus arrhizus*', *Separation and Purification Technology*, 57, 126-133.

Raize, O., Argaman, Y. and Yannai, S. (2004) 'Mechanisms of biosorption of different heavy metals by brown marine macroalgae', *Biotechnology and Bioengineering*, 87(4), 451-458.

Ramrakhiani, L., Majumder, R. and Khowala, S. (2011) 'Removal of hexavalent chromium by heat inactivated fungal biomass of *Termitomyces clypeatus*: Surface characterization and mechanism of biosorption', *Chemical Engineering Journal*, 171(3), 1060-1068.

Saeed, A., Iqbal, M. and Holl, W. H. (2009) 'Kinetics, equilibrium and mechanism of Cd^{2+} removal from aqueous solution by mungbean husk', *Journal of Hazardous Materials*, 168(2-3), 1467-1475.

Safa, Y. and Bhatti, H. N. (2011) 'Kinetic and thermodynamic modeling for the removal of Direct Red-31 and Direct Orange-26 dyes from aqueous solutions by rice husk', *Desalination*, 272(1-3), 313-322.

Saha, B. and Orvig, C. (2010) 'Biosorbents for hexavalent chromium elimination from industrial and municipal effluents', *Coordination Chemistry Reviews*, 254(23-24), 2959-2972.

Saha, R., Nandi, R. and Saha, B. (2011) ‘Sources and toxicity of hexavlent chromium’, *Journal of Coordination Chemistry*, 64(10), 1782-1806.

Sari, A. and Tuzen, M. (2008) 'Biosorption of cadmium(II) from aqueous solution by red algae (*Ceramium virgatum*): Equilibrium, kinetic and thermodynamic studies', *Journal of Hazardous Materials*, 157(2-3), 448-454.

Sarkar, M. and Majumdar, P. (2011) 'Application of response surface methodology for optimization of heavy metal biosorption using surfactant modified chitosan bead', *Chemical Engineering Journal*, 175, 376-387.

Say, R., Denizli, A. and Arica, M. Y. (2001) 'Biosorption of cadmium(II), lead(II) and copper(II) with the filamentous fungus *Phanerochaete chrysosporium*', *Bioresource Technology*, 76(1), 67-70.

Say, R., Yilmaz, N. and Denizli, A. (2004) ‘Removal of chromium(VI) ions from synthetic solutions by the fungus *Penicillium purpurogenum*’, *Engineering in Life Sciences*, 4(3), 276-280.

Schiewer, S. and Patil, S. B. (2008) 'Pectin-rich fruit wastes as biosorbents for heavy metal removal: Equilibrium and kinetics', *Bioresource Technology*, 99(6), 1896-1903.

Shashirekha, V., Sridharan, M. R. and Swamy, M. (2008) 'Biosorption of trivalent chromium by free and immobilized blue green algae: Kinetics and equilibrium studies', *Journal of Environmental Science and Health Part a-Toxic/Hazardous Substances & Environmental Engineering*, 43(4), 390-401.

Shen, Y. S., Wang, S. L., Huang, S. T., Tzou, Y. M. and Huang, J. H. (2010) 'Biosorption of Cr(VI) by coconut coir: Spectroscopic investigation on the reaction mechanism of Cr(VI) with lignocellulosic material', *Journal of Hazardous Materials*, 179(1-3), 160-165.

Shin, E. W., Karthikeyan, K. G. and Tshabalala, M. A. (2007) 'Adsorption mechanism of cadmium on juniper bark and wood', *Bioresource Technology*, 98(3), 588-594.

Shroff, K. A. and Vaidya, V. K. (2011) 'Kinetics and equilibrium studies on biosorption of nickel from aqueous solution by dead fungal biomass of *Mucor hiemalis*', *Chemical Engineering Journal*, 171(3), 1234-1245.

Smart, L. E. and Moore, E. A. (2012) 'Solid state chemistry: an introduction', Boca Raton : CRC Press.

Smith, B. C. (1999) 'Infrared spectral interpretation: A systematic approach', Brian Smith, Boca Raton, Fla.: Boca Raton, Fla.: CRC Press.

Srinath, T., Verma, T., Ramteke, P. W. and Garg, S. K. (2002) 'Chromium(VI) biosorption and bioaccumulation by chromate resistant bacteria', *Chemosphere*, 48, 427-435.

Srivastava, P. and Hasan, S. H. (2011) 'Biomass of *Mucor heimalis* for the biosorption of cadmium from aqueous solutions: Equilibrium and kinetic studies', *Bioresources*, 6(4), 3656-3675.

Suksabye, P., Nakajima, A., Thiravetyan, P., Baba, Y. and Nakbanpote, W. (2009) 'Mechanism of Cr(VI) adsorption by coir pith studied by ESR and adsorption kinetic', *Journal of Hazardous Materials*, 161(2-3), 1103-1108.

Sulaymon, A. H., Mohammed, A. A. and Al-Musawi, T. J. (2013) 'Removal of lead, cadmium, copper, and arsenic ions using biosorption: equilibrium and kinetic studies', *Desalination and Water Treatment*, 51, 4424-4434.

Sun, X. F., Ma, Y., Liu, X. W., Wang, S. G., Gao, B. Y. and Li, X. M. (2010) 'Sorption and detoxification of chromium(VI) by aerobic granules functionalized with polyethylenimine', *Water Research*, 44(8), 2517-2524.

Synowiecki, J. and Al-Khateeb, N. A. (2003) 'Production, properties, and some new applications of chitin and its derivatives', *Critical Reviews in Food Science and Nutrition*, 43(2), 145-171.

Synowiecki, J. and Al-Khateeb, N. (1997) 'Mycelia of *Mucor rouxii* as a source of chitin and chitosan', *Food Chemistry*, 60(4), 605-610.

Tan, G. Q., Yuan, H. Y., Liu, Y. and Xiao, D. (2011) 'Removal of cadmium from aqueous solution using wheat stem, corncob, and rice husk', *Separation Science and Technology*, 46(13), 2049-2055.

Ting, Y. P. and Sun, G. (2000) 'Comparative study on polyvinyl alcohol and alginate for cell immobilization in biosorption', *Water Science and Technology,* 42(5-6), 85-90.

Uluozlu, O. D., Sari, A., Tuzen, M. and Soylak, M. (2008) 'Biosorption of Pb(II) and Cr(III) from aqueous solution by lichen (*Parmelina tiliaceae*) biomass', *Bioresource Technology*, 99(8), 2972-2980.

United States Environmental Protection Agency (1998) 'Toxicological review of hexavalent chromium', available: http://www.epa.gov/iris/toxreviews/0144tr.pdf [accessed Aug 1998]

VanderVegte, E. W. and Hadziioannou, G. (1997) 'Acid-base properties and the chemical imaging of surface-bound functional groups studied with scanning force microscopy', Journal of Physical Chemistry B, 101(46), 9563-9569.

Veglio, F. and Beolchini, F. (1997) ‘Removal of metals by biosorption: A review’, *Hydrometallurgy*, 44, 301-316.

Vijayaraghavan, K. and Balasubramanian, R. (2010) ‘Single and binary biosorption of cerium and europium onto crab shell particles’, *Chemical Engineering Journal*, 163(3), 337-343.

Vijayaraghavan, K., Padmesh, T. V. N., Palanivelu, K. and Velan, M. (2006) 'Biosorption of nickel(II) ions onto *Sargassum wightii*: Application of two-parameter and three-parameter isotherm models', *Journal of Hazardous Materials*, 133(1-3), 304-308.

Vimala, R. and Das, N. (2009) 'Biosorption of cadmium (II) and lead (II) from aqueous solutions using mushrooms: A comparative study', *Journal of Hazardous Materials, 168(1), 376-382.*

Volesky, B. (2001) 'Detoxification of metal-bearing effluents: Biosorption for the

next century', *Hydrometallurgy*, 59(2-3), 203-216.

Volesky, B. and Holan, Z. R. (1995) 'Biosorption of heavy metals', *Biotechnology Progress,* 11(3), 235-250.

Warren, L. A. and Haack, E. A. (2001) 'Biogeochemical controls on metal behavior in freshwater environments', *Earth-Science Reviews*, 54, 261-320.

Wang, J. L. and Chen, C. (2009) 'Biosorbents for heavy metals removal and their future', *Biotechnology Advances*, 27, 195-226.

Wang, L., Chua, H., Wong, P. K., Lo, W. H. and Yu, P. H. F. (2003a) 'Ni^{2+} removal and recovery from electroplating effluent by *Pseudomonas putida* 5-x cell biomass', *Journal of Environmental Science and Health Part a-Toxic/Hazardous Substances & Environmental Engineering,* 38(3), 521-531.

Wang, L., Chua, H., Wong, P. K., Lo, W. H., Yu, P. H. F. and Zhao, Y. G. (2000) 'An optimal magnetite immobilized *Pseudomonas-putida* 5-x cellsystem for Cu^{2+} removal from industrial waste effluent', *Water Science and Technology,* 41(12), 241-246.

Wang, L., Chua, H., Zhou, Q., Wong, P. K., Sin, S. N., Lo, W. H. and Yu, P. H. (2003b) 'Role of cell surface components on Cu^{2+} adsorption by *Pseudomonas putida* 5-x isolated from electroplating effluent', *Water Research,* 37(3), 561-568.

Wang, L., Zhou, Q. and Zheng, G. H. (2005) 'Optimizing cell preparation technique to enhance adsorption capacity of *Pseudomonas putida* 5-X to heavy metal ions', *Journal of Environmental Science and Health*, 40, 2041-2055.

Wang, X. S., Chen, L. F., Li, F. Y., Chen, K. L., Wan, W. Y. and Tang, Y. J. (2010) 'Removal of Cr(VI) with wheat-residue derived black carbon: Reaction mechanism and adsorption performance', *Journal of Hazardous Materials*, 175(1-3), 816-822.

Water Research Foundation (2012) 'State of the science of hexavalent chromium in drinking water', available: http://www.waterrf.org/resources/Lists/PublicProjectPapers/Attachments/2/4404_

ProjectPaper.pdf [accessed May 2012].

Watts, J. F. (2003) ‘An introduction to surface analysis by XPS and AES’, Chichester, UK : J.Wiley.

Wong, M. F., Chua, H., Lo, W. H., Leung, C. K. and Yu, P. H. F. (2001) 'Removal and recovery of copper (II) ions by bacterial biosorption', *Applied Biochemistry and Biotechnology*, 91-3, 447-457.

World Health Organization (2003) 'Cadmium in drinking-water. Background document for preparation of WHO Guidelines for drinking-water quality', Geneva, World Health Organization (WHO/SDE/WSH/03.04/80).

Yan, C. and Viraraghavan, T. (2008) 'Mechanism of biosorption of heavy metals by *Mucor rouxii*', *Engineering in Life Sciences*, 8(4), 363-371.

Yang, J. B. and Volesky, B. (1999) 'Cadmium biosorption rate in protonated *Sargassum* biomass', *Environmental Science & Technology,* 33(5), 751-757.

Yee, N., Benning, L. G., Phoenix, V. R. and Ferris, F. G. (2004) 'Characterization of metal-cyanobacteria sorption reactions: A combined macroscopic and infrared spectroscopic investigation', *Environmental Science & Technology*, 38(3), 775-782.

Yee, N. and Fein, J. B. (2003) 'Quantifying metal adsorption onto bacteria mixtures: A test and application of the surface complexation model', *Geomicrobiology Journal*, 20(1), 43-60.

Yin, H., He, B., Peng, H., Ye, J., Yang, F. and Zhang, N. (2008) 'Removal of Cr(VI) and Ni(II) from aqueous solution by fused yeast: Study of cations release and biosorption mechanism', *Journal of Hazardous Materials*, 158(2-3), 568-576.

Yipmantin, A., Maldonado, H. J., Ly, M., Taulemesse, J. M. and Guibal, E. (2011) 'Pb(II) and Cd(II) biosorption on *Chondracanthus chamissoi* (a red alga)', *Journal of Hazardous Materials*, 185(2-3), 922-929.

Yun, Y. S., Park, D., Park, J. M. and Volesky, B. (2001) 'Biosorption of trivalent

chromium on the brown seaweed biomass', *Environmental Science & Technology*, 35(21), 4353-4358.

Zawisza, B. and Sitko, R. (2013). 'Pre-concentration procedure based on chitosan combined with ionic liquid for the determination of cobalt, nickel, and copper in water samples', *Applied Spectroscopy*, 67(5), 536-541.

Zeng, X. X., Tang, J. X., Yin, H. Q., Liu, X. D., Jiang, P. and Liu, H. W. (2010) 'Isolation, identification and cadmium adsorption of a high cadmium-resistant *Paecilomyces lilacinus*', *African Journal of Biotechnology*, 9(39), 6525-6533.

Zhang, Y. S., Liu, W. G., Xu, M., Zheng, F. and Zhao, M. J. (2010) 'Study of the mechanisms of Cu^{2+} biosorption by ethanol/caustic-pretreated baker's yeast biomass', *Journal of Hazardous Materials*, 178(1-3), 1085-1093.

Zheng, Y. M., Liu, T., Jiang, J. W., Yang, L., Fan, Y. P., Wee, A. T. S. and Chen, J. P. (2011) 'Characterization of hexavalent chromium interaction with *Sargassum* by X-ray absorption fine structure spectroscopy, X-ray photoelectron spectroscopy, and quantum chemistry calculation', *Journal of Colloid and Interface Science*, 356(2), 741-748.